

N92-17546

CONFIDENTIAL

LIBRARY COPY

SEP 14 1993

LANGLEY RESEARCH CENTER  
LIBRARY NASA  
HAMPTON, VIRGINIA

A Service of:



National Aeronautics and  
Space Administration

Scientific and Technical  
Information Office





NASA Technical Memorandum 105397

1N-07  
67273  
p 214

# Experiments and Analysis Concerning the Use of External Burning to Reduce Aerospace Vehicle Transonic Drag

Charles J. Trefny  
*Lewis Research Center*  
*Cleveland, Ohio*

(NACA-TM-105397) EXPERIMENTS AND ANALYSIS  
CONCERNING THE USE OF EXTERNAL BURNING TO  
REDUCE AEROSPACE VEHICLE TRANSONIC DRAG  
PH.D. Thesis - Maryland Univ., 1991 (NACA)  
294 p

NP2-17346

Unclass

COOL 21E 08/07 0000273

January 1992

**NASA**





EXPERIMENTS AND ANALYSIS CONCERNING THE USE OF EXTERNAL  
BURNING TO REDUCE AEROSPACE VEHICLE TRANSONIC DRAG

Charles J. Trefny  
National Aeronautics and Space Administration  
Lewis Research Center  
Cleveland, Ohio 44135

ABSTRACT

The external combustion of hydrogen to reduce transonic drag has been investigated. A control volume analysis is developed and indicates that the specific impulse performance of external burning is competitive with other forms of airbreathing propulsion and depends on the fuel-air ratio, freestream Mach number, and the severity of the base drag. A method is presented for sizing fuel injectors for a desired fuel-air ratio in the unconfined stream.

A two-dimensional Euler analysis is also presented which indicates that the total axial force generated by external burning depends on the total amount of energy input and is independent of the transverse and streamwise distribution of heat addition. Good agreement between the Euler and control volume analysis is demonstrated. Features of the inviscid external burning flowfield are discussed. Most notably, a strong compression forms at the sonic line within the burning stream which may induce separation of the plume and prevent realization of the full performance potential.

An experimental program was conducted in a Mach 1.26 free-jet to demonstrate drag reduction on a simple expansion ramp geometry, and verify hydrogen-air stability limits at external burning conditions. Stable combustion appears feasible to Mach numbers of between 1.4 and 2 depending on the vehicle flight trajectory. Drag reduction is demonstrated on the expansion ramp at Mach 1.26, however force levels showed little dependence on fuel pressure or altitude in contrast to control volume analysis predictions. Various facility interference mechanisms and scaling issues were studied and are discussed.

## ACKNOWLEDGEMENTS

The author gratefully acknowledges the work of the engineers and technicians at the Propulsion Systems Lab at Lewis Research Center. Their dedication carried the experimental program through many trials and tribulations to a successful conclusion.

Also acknowledged is the encouragement and guidance of Dr. John Anderson throughout the time I spent at the University of Maryland as well as the past four years at Lewis.

Numerous technical discussions with Dr. Fred Billig at the Applied Physics Lab were invaluable in the planning and execution of the program. I will always be grateful for having had the opportunity to work with Dr. Billig.

Thanks are also due to my supervisors at NASA Lewis for their technical and administrative support. In particular, to Mr. Robert Coltrin and Mr. Bernard Blaha for providing me sufficient latitude to complete this study.



## TABLE OF CONTENTS

<u>Section</u>	<u>Page</u>
List of Tables	viii
List of Figures	ix
List of Symbols	xvi
Chapter I - Introduction	1
Single-Stage to Orbit Airbreathing Nozzle Operation	2
Application of External Burning	3
Previous Work in External Burning	5
Objectives of Current Work	13
Chapter II - Control Volume Analysis	15
Background	15
Development	20
Three-Dimensional Relief Approximation	27
Equations For a Perfect Gas	30
Equations At Zero Drag	30
Performance Parameter Definitions	31
Results	33
Fuel Injection Considerations	37
Jet Penetration Model and Equivalence Ratio Approximation	37
Fuel Injection Design Example	40
Performance at Constant Fuel Conditions	42
Control Volume Analysis Summary	45
Chapter III - Euler Analysis	46
Background	46
Development	48
Euler Equations in Conservation Form	48
Method of Solution	50
Artificial Damping	51
Assignment of Heat Addition Distribution	52
Boundary Conditions	54
Results	55
Effect of Heat Addition Distribution	55
Effect of Artificial Damping	60

Effect of Grid Refinement	61
Effect of Freestream Mach Number	62
Euler Analysis Summary	63
Chapter IV - Experimental Program	65
Background	65
Hydrogen-Air Flameholding Previous Work	67
Facility Description	74
Spraybar Test Apparatus and Procedure	76
Equivalence Ratio Estimate	77
Fuel Injector Sizing	78
Instrumentation	80
Ignition System	81
Test Procedure	82
Results	83
Spraybar Base Pressure Measurements	83
Flame Stability	84
Effect of Elevated Temperature	86
Scaling of Small-Scale Test Results	87
Expansion Ramp Test Apparatus and Procedure	92
Fuel Injector Sizing	94
Flameholder Sizing	95
Test Procedure	96
Expansion Ramp Test Results	97
Baseline Performance	97
Comparison to Control Volume Analysis	102
Facility Interaction Studies	106
Effect of Exhaust Collector Modification	108
Effect of Plume Boundary Simulator	109
Effect of Free-Jet Boundary	113
Alternate Flame-Holder and Fuel Injector Configurations	118
Results with Heated Freestream	124
Effect of Upper Sidewalls	125
Expansion Ramp Flameholding	126
Expansion Ramp Performance Assessment	127
Chapter V - Summary and Conclusions	130
Appendix A - Hydrogen-Air Equilibrium Scheme	135
Appendix B - Euler Analysis Test Cases	142
Appendix C - Water-Cooled Total Temperature Probe Data Reduction	153

Appendix D - Expansion Ramp Fuel Injector and Flameholders Configurations	158
--	-----

References	163
------------	-----

## LIST OF TABLES

3-1	Summary of Euler Analysis Runs	168
4-1	Summary of Expansion Ramp Configurations	169
4-2	Perfect Gas Equivalence Ratios	170



## LIST OF FIGURES

1-1	Artist's conception of a single-stage-to-orbit vehicle.	171
1-2	Single expansion ramp nozzle design and operation. a) On-design at high speed. b) Over-expanded at transonic conditions.	172
1-3	Cowl flap deflection to prevent internal over-expansion.	173
1-4	External burning concept applied to single expansion ramp nozzle.	173
2-1	Control volume nomenclature.	174
2-2	Results at zero drag along a $Q_0=1000$ psfa trajectory. a) Ratio of inflow stream height to base height. b) Fuel flow per unit base area. c) Normalized specific impulse.	175
2-3	Trajectory of 1/2% fuel volume concentration from correlation of reference 50 for various fuel pressure ratios.	177
2-4	Fuel schedule required to maintain zero thrust at stoichiometric conditions with a fixed orifice geometry; $Q_0=1000$ psfa, $d^*/w=.005824$ , $S/d^*=9.485$ , $C_v=.9$ , $T_f=518^\circ\text{R}$ .	177
2-5	Results at constant fuel conditions for a fixed orifice geometry; $Q_0=1000$ psfa, $d^*/w=.005824$ , $S/d^*=9.485$ , $C_v=.9$ , $T_f=518^\circ\text{R}$ . a) Ratio of inflow stream height to base height. b) Equivalence ratio. c) Thrust coefficient for various expansion assumptions; $y_b/L=3.732$ , $w/y_b=2.5$ . d) Specific impulse.	178
3-1	Euler analysis schematic.	180
3-2	80 by 40 grid.	181
3-3	Case 1 heat addition distribution and streamlines.	181
3-4	Case 2 heat addition distribution, Gaussian in axial direction, constant in transverse. a) Heat addition contours and streamlines. b) Gaussian axial distribution function.	182

3-5	Case 3 heat addition distribution, Gaussian in axial direction, parabolic in transverse. a) Heat addition contours and streamlines. b) Parabolic transverse distribution function.	183
3-6	Euler results for case 1 heat addition; $M_0=1.4$ . a) Mach number contours (.05 contour intervals). b) Wall Mach number distribution. c) Wall pressure distribution.	184
3-7	Euler results for case 2 heat addition; $M_0=1.4$ . a) Mach number contours (.05 contour intervals). b) Wall Mach number distribution. c) Wall pressure distribution.	185
3-8	Euler results for case 3 heat addition; $M_0=1.4$ . a) Mach number contours (.05 contour intervals). b) Wall Mach number distribution. c) Wall pressure distribution.	186
3-9	Velocity profiles at ramp trailing edge.	187
3-10	Effect of artificial damping on Euler results. Mach number contours (.05 contour intervals); $M_0=1.4$ , 80 x 40 grid, case 2 heat addition. a) $C_d=.0125$ . b) $C_d=.025$ . c) $C_d=.05$ .	188
3-11	Effect of grid refinement on Euler results. Mach number contours (.05 contour intervals); $M_0=1.4$ , $C_d=.025$ , case 2 heat addition. a) 50 x 25 grid. b) 80 x 40 grid. c) 100 x 50 grid.	189
3-12	Effect of grid density on wall pressure distributions.	190
3-13	Mach number contours at various freestream Mach numbers (.05 contour increment); 80 x 40 grid, $C_d=.025$ , case 2 heat addition. a) $M_0=1.2$ . b) $M_0=1.6$ . c) $M_0=2.0$ . d) $M_0=2.4$ .	191
3-14	Wall Mach number distributions at various freestream Mach numbers; 80 x 40 grid, $C_d=.025$ , case 2 heat addition.	193
3-15	Wall pressure distributions at various freestream Mach numbers; 80 x 40 grid, $C_d=.025$ , case 2 heat addition.	193

3-16	Comparison of Euler and control volume analysis thrust coefficient predictions.	194
4-1	Combination spraybar-flameholder concept	195
4-2	Flame stability for a pre-mixed, subsonic hydrogen-air stream (reproduced from reference 57).	196
4-3	Flame stability along flight trajectories for a 1" dia. disk.	196
4-4	Non pre-mixed, and supersonic stability limits from reference 59 in terms of DeZubay parameter.	197
4-5	Propulsion Systems Lab Cell 4 after hypersonic modifications (reproduced from reference 60).	198
4-6	Spraybar mounted in free-jet with spark ignitor and water-cooled probe in extended positions.	199
4-7	Details of piloted spraybar.	200
4-8	Piloted spraybar operating envelopes at Mach 1.26.	201
4-9	Field of view for optical instrumentation and location of translating water-cooled total temperature probe.	202
4-10	Schlieren images at various free-jet exit pressure ratios; $p_0$ (free-jet exit pressure) held constant at 8 psia. a) Over-expanded, $p_0/p_a=.8$ . b) On design, $p_0/p_a=1.0$ . c) Under-expanded, $p_0/p_a=1.2$ .	203
4-11	Effect of free-jet exit pressure ratio on spraybar base pressure; $p_0$ (free-jet exit pressure) held constant at 8 psia.	205
4-12	Spraybar base pressure with external burning.	205
4-13	Flame stability for piloted spraybar.	206
4-14	Plume characteristics at nominal temperature and pressure; $T_{t,0}=540^\circ\text{R}$ , $p_0=6$ psia, $Re=4.9 \times 10^6/\text{ft}$ . a) Infra-red image; $p_t=250$ psia, $y_p=1.0"$ , $\phi_{pxs}=.63$ . b) Infra-red image; $p_t=350$ psia, $y_p=1.2"$ , $\phi_{pxs}=.75$ . c) Total temperature profiles.	207
4-15	Plume characteristics at increased temperature and pressure; $T_{t,0}=960^\circ\text{R}$ , $p_0=12$ psia, $Re=4.9 \times 10^6/\text{ft}$ . a) Infra-red image; $p_t=250$ psia, $y_p=.72"$ , $\phi_{pxs}=.58$ . b) Infra-red image; $p_t=350$ psia, $y_p=.85"$ , $\phi_{pxs}=.69$ . c) Total temperature profiles.	209

4-16	Relation of expansion ramp models to vehicle base.	211
4-17	Expansion ramp model details.	212
4-18	Expansion ramp mounted in free-jet.	213
4-19	Flame stability envelopes for 26 injector model; $4 < p_0 < 12$ psia, $50 < p_f < 375$ psia.	214
4-20	Fuel-off static pressure distributions; configuration 1. a) $p_0=12$ psia b) $p_0=8$ psia c) $p_0=4$ psia	215
4-21	Effect of fuel mass addition on centerline static pressure distributions; configuration 1. a) $p_0=12$ psia b) $p_0=8$ psia c) $p_0=4$ psia	217
4-22	Effect of external burning on centerline static pressure distributions; configuration 1. a) $p_0=12$ psia b) $p_0=8$ psia c) $p_0=4$ psia	220
4-23	Schlieren images of external burning (configuration 10). a) Fuel-off. b) Low equivalence ratio; $p_f=250$ psia, $p_0=12$ psia ( $\phi_{pxs}=.56$ , $y_p=.25''$ ). c) High equivalence ratio; $p_f=375$ psia, $p_0=4$ psia ( $\phi_{pxs}=1.24$ , $y_p=.51''$ ).	223
4-24	Total temperature profiles; configuration 1. a) $p_0=12$ psia b) $p_0=8$ psia c) $p_0=4$ psia	226
4-25	Infra-red images of external burning plume; configuration 1. a) Low equivalence ratio; $p_f=200$ psia, $p_0=12$ psia ( $\phi_{pxs}=.51$ , $y_p=.22''$ ). b) Medium equivalence ratio; $p_f=250$ psia, $p_0=8$ psia ( $\phi_{pxs}=.70$ , $y_p=.30''$ ). c) High equivalence ratio; $p_f=375$ psia, $p_0=4$ psia ( $\phi_{pxs}=1.24$ , $y_p=.51''$ ).	229
4-26	Average plume temperature correlation. a) Equivalence ratio based on penetration times spacing method with $x/d=30$ . b) Equivalence ratio and inflow stream height based on correlation of average measured plume temperature.	230

4-27	Thrust coefficient; configuration 1. a) Equivalence ratio based on penetration times spacing method with $x/d=30$ . b) Equivalence ratio and inflow stream height based on correlation of average measured plume temperature.	232
4-28	Facility interactions suspected of causing low performance.	234
4-29	PSL-4 Facility exhaust collector layout.	234
4-30	Effect of altitude on exhaust collector pressure distributions during external burning; $p_f=375$ psia.	235
4-31	Effect of auxiliary air flow on exhaust collector pressure distributions; $p_0=4$ psia, fuel off.	235
4-32	Effect of exhaust collector modification on thrust coefficient; configuration 1.	236
4-33	Plume boundary simulator installation; configuration 2.	237
4-34	Gaussian axial heat addition distribution function.	238
4-35	2-D Euler grids used to validate use of plume boundary simulator. a) Solid wall boundary, 100 x 50 nodes. b) Freestream boundary, 100 x 70 nodes.	239
4-36	Comparison of streamlines, total heat added corresponds to $\phi_{corr}=.45$ , $y_0/y_b=.20$ . a) Solid wall boundary. b) Freestream boundary.	240
4-37	Comparison of Mach number contours (.05 contour increment), total heat added corresponds to $\phi_{corr}=.45$ , $y_0/y_b=.20$ . a) Solid wall boundary. b) Freestream boundary.	241
4-38	Comparison of wall pressure distributions, total heat added corresponds to $\phi_{corr}=.45$ , $y_0/y_b=.20$ .	242
4-39	Effect of plume boundary simulator on centerline pressure distributions. a) Fuel off; $p_0=8$ psia. b) $p_f=250$ psia, $p_0=12$ psia ( $\phi_{corr}=.30$ ). c) $p_f=375$ psia, $p_0=8$ psia ( $\phi_{corr}=.67$ ). d) $p_f=375$ psia, $p_0=4$ psia ( $\phi_{corr}=1.36$ ).	243
4-40	Total temperature profiles with plume boundary simulator installed; configuration 2.	245

4-41	Effect of plume boundary simulator on thrust coefficient.	246
4-42	Grid used to evaluate effects of free-jet boundary (100 x 80 nodes).	247
4-43	Fuel-off Euler results with free-jet boundary. a) Mach number contours (.05 contour increment) b) Wall pressure distribution.	248
4-44	Effect of free-jet boundary on calculated external burning thrust coefficient.	249
4-45	Comparison of Mach number contours at low heat addition corresponding to $\phi_{corr}=.25$ , $y_o/y_b=.20$ . a) Flight boundary. b) Free-jet boundary.	250
4-46	Comparison of Mach number contours at medium heat addition corresponding to $\phi_{corr}=.66$ , $y_o/y_b=.20$ . a) Flight boundary. b) Free-Jet boundary.	251
4-47	Comparison of Mach number contours at high heat addition corresponding to $\phi_{corr}=1.38$ , $y_o/y_b=.20$ . a) Flight boundary. b) Free-jet boundary.	252
4-48	Results for 56 injector model; configuration 3. a) Centerline pressure distributions. b) Total temperature profiles	253
4-49	26 injector model with upstream injection and flameholding; configuration 7.	255
4-50	Results with upstream injection and flameholding; configuration 7. a) Centerline pressure distributions. b) Total temperature profiles.	256
4-51	26 injector model with leading edge extension installed (flameholder not installed).	258
4-52	Effect of leading edge extension and upstream injection (configurations 2 and 8) a) Comparison of centerline pressure distributions with fuel off; $p_o=8$ psia. b) Comparison of centerline pressure distributions with external burning; $p_t=375$ psia, $p_o=8$ psia ( $\phi_{corr}=.65$ ). c) Comparison of total temperature profiles; $p_t=375$ psia, $p_o=8$ psia ( $\phi_{corr}=.65$ ).	259

4-53	1/4" Serrated flameholder; configuration 10.	261
4-54	Results with 1/4" serrated flameholder; configuration 10. a) Centerline pressure distributions. b) Total temperature profiles.	262
4-55	Thrust coefficient comparison for alternate configurations.	264
4-56	Results for configuration 10 with heated freestream; $T_{\infty,0}=960^{\circ}\text{R},$ a) Centerline pressure distributions. b) Total temperature profiles. c) Thrust coefficient.	265
4-57	Upper sidewall installation (baseline flameholder shown).	268
4-58	Effect of upper sidewalls on configuration 10 performance. a) Comparison of centerline pressure distributions with fuel off; $p_0=8$ psia. b) Comparison of centerline pressure distributions with external burning; $p_t=375$ psia, $p_0=4$ psia ( $\phi_{\text{corr}}=1.33$ ). c) Comparison of total temperature profiles; $p_t=375$ psia, $p_0=4$ psia ( $\phi_{\text{corr}}=1.33$ ). d) Comparison of thrust coefficients.	269
4-59	Expansion ramp flameholding, all flameholder configurations.	272
4-60	Demonstrated performance for configuration 10. a) Thrust coefficient. b) Specific impulse.	273

## LIST OF SYMBOLS

$a$	speed of sound
$A$	cross-sectional or projected area
$C_p$	pressure coefficient
$C_T$	thrust coefficient (force / $Q_0 A_0$ )
$C_v$	orifice flow coefficient
$C_x, C_y, C_d$	coefficients in artificial damping scheme
$C_{2D}$	2-D Courant number
$d$	orifice diameter
$dx$	incremental distance in x-direction
$dy$	incremental distance in y-direction
$d\vec{s}$	area increment vector
$D$	disk diameter in flameholding correlation
$e$	internal energy per unit mass
$E_{tot}$	total energy per unit mass ( $\rho(e+V_2/2)$ )
$F_1, F_2$	fuel injection constants
$g_c$	proportionality factor (32.17 ft-lb <sub>m</sub> /lb <sub>f</sub> -sec <sup>2</sup> in english system)
$h$	enthalpy per unit mass
$H$	effective height of flameholder
$H_2$	hydrogen fuel
$I_{sp}$	specific impulse (force per unit fuel flow) (lb <sub>f</sub> -sec/lb <sub>m</sub> )
$I_{sp,tot}$	specific impulse based on total force (lb <sub>f</sub> -sec/lb <sub>m</sub> )
$J$	jacobian of transformation
$L$	length of expansion ramp in x-direction
$l$	length of computational plane in x-direction



LHV	lower heating value (taken to be 52000 BTU/lb <sub>m</sub> for H <sub>2</sub> )
M	Mach number
$\dot{m}$	mass flowrate
P	pressure
P <sub>a</sub>	test cell or ambient pressure
Q	dynamic pressure
q	heat added per unit mass of air
$\dot{Q}$	heat added per unit volume per unit time
R	specific gas constant
Re	Reynold's number
S	distance between fuel injection orifice centerlines
t	time
T	temperature
u	x-component of velocity
v	y-component of velocity
$\vec{V}$	velocity vector
V <sub>B.O.</sub>	blow-off velocity
w	width
x	distance in streamwise or x-direction
y	height or distance in transverse or y-direction

greek

$\Delta y_{3D}$	three-dimensional stream surface deflection
$\Delta x$	grid spacing in x direction
$\Delta y$	grid spacing in y direction

$\Delta y$	time step
$\rho$	mass per unit volume
$\tau$	ignition delay time
$\xi$	x-coordinate in computational plane
$\eta$	y-coordinate in computational plane
$\theta$	shock wave angle
$\phi$	equivalence ratio (fraction of stoichiometric fuel-air ratio)
$\mu$	Mach angle
$\gamma$	ratio of specific heats

#### subscripts

a	air, or ambient
b	base
corr	based on data correlation
eb	effective back pressure
f	fuel
N-S	downstream of a normal shock
p	jet penetration
pxs	based on penetration times spacing
s	streamline
t	stagnation
w	wall surface
x	x-component, or derivative with respect to x
y	y-component, or derivative with respect to y
2	station 2, outflow
0	station 0, freestream or inflow

superscripts

- \* sonic, or non-dimensional quantity
- 0 fuel off

miscellaneous

- <> indicates dimensional quantity



## CHAPTER I - INTRODUCTION

Interest in "transatmospheric" or "aerospace" vehicles has been revived in the United States following almost two decades of relative inactivity. Evolutionary advances in "scramjet" propulsion, materials, and computer modeling, along with current political support have set the stage for an aggressive program (the National Aerospace-Plane, or NASP) to develop a revolutionary aircraft capable of flying into orbit following take-off from a conventional runway. Ready access to space, and very high speed earth transportation are two of the obvious benefits of this technology. The single stage to orbit (SSTO) concept is very attractive due to its operational simplicity, flexibility and its potential for reducing the cost of putting payload into orbit. The technical challenges facing the aerospace community are numerous, many of them related to the airbreathing propulsion system required to achieve orbit in a single stage. Liquid hydrogen fuel is widely accepted as the fuel of choice for hypersonic airbreathing propulsion due to its high heat capacity for engine and airframe cooling, and a heat of combustion more than twice that of hydrocarbon fuels. One drawback of hydrogen is its low molecular weight which results in a large cryogenic volume that must be highly integrated with the airframe and propulsion system. An artist's conception of an SSTO vehicle appears in figure 1-1 which illustrates the highly integrated nature of the design. The entire aft end of the vehicle acts as a single expansion ramp nozzle, providing a very high area ratio which is exploited at the high nozzle pressure ratios associated with high Mach number and

altitude. This large aft-facing area becomes a great liability however at transonic and low supersonic speeds where low airbreathing engine pressure ratios result in a highly overexpanded nozzle. Since the nozzle exit area is largely fixed at the vehicle cross-sectional area, the amount of variable geometry that can be employed is a small fraction of that required to keep the nozzle "on-design" over this speed range.

#### Single-Stage to Orbit Airbreathing Nozzle Operation

A qualitative discussion of nozzle design and operation follows which illustrates overexpanded operation and the application of external burning to an SSTO nozzle geometry. At hypersonic speeds, with the engine operating as a supersonic combustion ramjet or "scramjet", the combustor exit (nozzle inlet) Mach number is supersonic and one could envision a minimum length shock-free design with expansion to freestream ambient pressure at a given design point. The resulting hypothetical design and associated flowfield appear schematically in figure 1-2a. Note that the cowl and shear layer of the single expansion ramp nozzle can be thought of as the symmetry plane of a symmetric two-dimensional nozzle. The nozzle is perfectly expanded and the limiting characteristic in the exhaust flow emanating from the trailing edge of the cowl intersects the expansion surface at the trailing edge. At this point, the nozzle is performing optimally, and the freestream Mach number has little effect on nozzle performance. In figure 1-2b, the nozzle pressure ratio and freestream Mach number have been reduced to a point representative of a transonic

flight condition where the engine operates as a ramjet with a choked throat. The portion of the nozzle enclosed by the cowl (referred to as the internal nozzle) has a significant area ratio and at low nozzle pressure ratios is itself overexpanded to less than freestream pressure. Upon leaving the internal nozzle, the exhaust stream adjusts to the local base pressure through the familiar "shock diamond" wave structure. The local base pressure to which the exhaust flow eventually equalizes, is lower than freestream due to the fact that the exhaust stream "fills" only a small part of the large nozzle exit area. Nozzle drag results from overexpansion in the internal nozzle, and the exhaust stream's subsequent inability to fully recompress to freestream pressure due to the low overall vehicle base pressure. The transonic nozzle drag problem can thus be thought of as similar to any other base drag problem, being complicated by the fact that the effective base pressure will be a function of the exhaust stream's ability to fill the base.

#### Application of External Burning

The nozzle pictured in fig 1-2 is a high Mach number, minimum length design employing a sharp expansion at the nozzle throat, with a resulting geometric area ratio in the internal nozzle. In the preceding discussion, no attempt was made to vary the geometry over the range of operating conditions, although one could envision deflecting the trailing edge of the cowl upwards as shown in figure 1-3 to prevent internal overexpansion of the exhaust flow. Freestream pressure may be maintained in the

internal nozzle, but would be offset by boattail drag on the deflected flap. With respect to the reduced pressure on the deflected cowl boattail, the internal nozzle is underexpanded, so the propulsive stream expands to the local base pressure through a wave structure. Ultimately, the propulsive stream expands to nearly the same cross-sectional area as before with the cowl undeflected, so that the overall base pressure in this region is unchanged. The cowl flap deflection concept can prevent internal overexpansion and also reduce the strength of the external wave structure, but results in no significant net drag reduction.

The deflected cowl does however transfer the low pressure region which existed on the inner expansion surface to the external flap, which makes the use of external burning an attractive possibility. Shown conceptually in figure 1-4, hydrogen would be injected upstream of the deflected cowl and burn adjacent to the nozzle, pressurizing the entire base region thereby eliminating cowl flap drag and the external overexpansion of the exhaust flow.

The effect of external burning on a nozzle of this type at first seems to be complicated by detailed interactions between the freestream, the external burning plume, and the exhaust flow. The strategy adopted herein is to consider the deflected flap and exhaust shear layer together as a surface upon which external burning acts. Obviously, any pressurization of the shear layer by external burning does not act directly on a vehicle surface, but must be transmitted through the exhaust stream. This is seen as a second-order effect though, with regard to the main objective of the



present work which is to investigate the feasibility of using hydrogen external burning to reduce transonic drag. If the concept is workable in the preceding simplified sense, extension to the actual airbreathing propulsion system seems straightforward.

### Previous Work in External Burning

A review of the literature reveals that work related to this area falls roughly into two categories, "base burning" and "external burning". Although both use external, or unconfined combustion to increase pressure on a surface, important differences exist in the mechanics of the processes, and the analysis methods used. Base burning is characterized by direct fuel injection and combustion in the wake of a blunt based aerodynamic body (such as a projectile) to reduce drag. The recirculating base flow acts as the flameholder, with fuel injection and combustion modifying the base flow pattern in such a manner as to increase the base pressure. The fuel mass addition itself can often account for a significant part of the total drag reduction. The analysis of base burning must include the complex viscous effects which dominate the base flow phenomena and as a result, integral theories have been widely used. The majority of work in base flow phenomena including base injection and burning is summarized by Murthy, et al.<sup>1</sup> which includes a bibliography with over 350 references. In contrast to base burning where the surface to be pressurized acts as a flameholder, the present application tends more toward external burning in which heat is released in the inviscid portion

of the flowfield adjacent to the surface on which the pressure is to be increased. This process has been proposed to reduce drag, provide control forces and even provide primary propulsion. By it's very definition, external burning is primarily an inviscid phenomena, and a number of theoretical approaches to solving flows with heat addition have been used such as the diabatic method of characteristics, linearized flow with heat addition, and the "planar heater" where heat addition is confined to a thin, constant area region. These techniques have been summarized by Billig<sup>2</sup> who published an unclassified, unlimited review of theoretical and experimental external burning work done from 1945 to 1964. Highlights of experimental work done during this period and subsequently are given in the following paragraphs.

In 1955, Davis<sup>3</sup> et. al., at Texaco Experiment Inc. tested hydrogen external burning on a small flat plate model with various fuel injection and flameholder configurations including oxygen piloting. The experiments were conducted in a Mach 1.7, 1.62" diameter free-jet at nominally standard temperature and pressure. Encouraging results were obtained, but due to the large flameholders required to stabilize the hydrogen flame (with respect to the tiny models), no conclusions on performance were drawn.

A series of external combustion tests at the NACA Lewis Flight Propulsion Laboratory (now The NASA Lewis Research Center) was also initiated in 1955. Fletcher<sup>4</sup>, et. al. demonstrated stable combustion of aluminum borohydride in a small (3.84" by 10") supersonic wind tunnel at sub-

ambient pressure and temperature without the use of a flameholder from Mach 1.5 to 4. The pyrophoric liquid fuel was injected from the 3.84" wide tunnel ceiling. The effect of combustion on the tunnel ceiling static pressure distribution was reported in reference 5 as "significant" which prompted subsequent tests of various aerodynamic shapes including flat plates, a body of revolution, and a two-dimensional supersonic wing in a 1' by 1' Mach 2.46 tunnel<sup>6-8</sup>. These tests demonstrated levels of performance commensurate with theoretical predictions with combustion having doubled the L/D of the wing model, and nearly eliminating base drag on the body of revolution, but results were said to be subject to "undetermined wind tunnel effects" which were thought to be wave reflections from the tunnel walls. In order to assess these interference effects, the flat plate model tests were repeated in the 10' by 10' supersonic tunnel at Lewis by Dorsch<sup>9</sup> et. al. Results indicated that significant interference occurred only on a long (25" chord) flat plate model, and much of the data taken during the small tunnel tests was free of interference.

Billig<sup>2,10</sup> conducted numerous experiments at Mach 5 on flat plate and wedge models using pyrophoric aluminum-alkyl fuels including work in support of an external burning ramjet program<sup>11</sup>. Stable combustion was attained without flameholders at Mach 5, but performance in terms of lift and thrust was somewhat lower than predicted. A composite plot in reference 2 which shows results of many tests, indicates that external burning performance is generally lower than that predicted by a constant pressure analysis. Billig concludes that the process is reaction-rate limited and

that lengths on the order of feet rather than inches would be required for complete combustion.

The work of Townend and Reid<sup>12</sup>, reported in 1964 was not included in Billig's review and was clearly a base burning test, but is relevant to the present study since hydrogen fuel was used successfully to alleviate base drag on an axisymmetric cone-cylinder model at a relatively low Mach number. The 1" diameter model was mounted in the center of a 5.5" square test section. Test conditions were Mach 2.14, at a static pressure of 2 atmospheres, and ambient total temperature. Two methods of fuel injection were tried, direct bleeding into the base, and peripheral injection through a slot upstream of the base. Hydrogen combustion in the wake increased the base pressure to slightly higher than ambient pressure in either case. The similarity in results of both injection methods suggested that fuel issuing from the peripheral slot simply burned in the wake in the same manner as fuel which was bled into the wake directly. 30 and 22.5 degree cone-cylinder afterbodies were tested and resulted in little difference from the blunt base results. The objective of this work was to study the effects of stable combustion in the wake or base burning, the peripheral injection being used only to enhance mixing. This configuration however bears a close resemblance to an external burning scheme suggested by Strahle<sup>13</sup> four years later in which fuel would be injected transversely and burn in the inviscid stream adjacent to the wake supposedly yielding much higher performance.

In 1968, Strahle noted that previous base burning results were "somewhat

"disappointing" being limited to base pressures less than or equal to freestream static pressure. He proposed using external burning outside but adjacent to the viscous wake to pressurize the dividing streamline and thereby the base surface by communication through the elliptic recirculation zone. In effect, the wake was to act as an afterbody pressurized by external burning. He reasons that the pressure rise due to external burning is not constrained to freestream pressure, and that higher performance than that of base burning alone would be possible. He evaluated this concept analytically using an integral analysis for the recirculating wake flow, and a composite approach for the external burning heat addition region which combined 2-D planar linear theory and one-dimensional flow. The conclusion drawn from the analysis was that indeed, there is no limit to the base pressure rise and the rise is monotonic in combustion zone strength. Boundary layer separation upstream of the base, and the breakdown of supersonic flow in the heat addition region were mentioned as two possible limiting factors. The latter concern was addressed in 1970 by Strahle in reference 14. He performs a more detailed analysis of the transonic external burning process on a flat plate using 2-D velocity potential formulation. The conclusion is that a positive pressure coefficient can be maintained on the surface even after the transition to subsonic flow. If the outer, supersonic flow breaks down however, as may be the case if a transonic flow is turned through too great an angle, he concludes that useful force generation cannot be realized. Strahle's application of external burning to wake pressurization served as the basis for several subsequent external burning studies.

In the early 1970's, Fuhs<sup>15</sup> at the Naval Postgraduate School extended Strahle's analysis to axisymmetric, annular heat addition geometries and proposed a number of applications for external burning. One was that of transonic drag reduction on an axisymmetric plug nozzle. He proposed the addition of heat on the cowl boattail surface to reduce the Mach number, ultimately resulting in subsonic flow downstream of the cowl trailing edge. Drag reduction on the boattail is secondary to a "wave trapping" effect where waves reflected from the plug surface are now reflected back as compressions from the subsonic boundary. Large gains in thrust at very modest fuel consumption are demonstrated by an initial analysis.

A group of graduate students led by Fuhs<sup>16-19</sup> performed projectile drag reduction experiments based on Strahle's concept in a Mach 2 free-jet. A projectile base was mounted concentrically in the free-jet, and the nozzle exit was contoured to generate compression waves which simulated external burning. The location and strength of the simulated heat release was varied using different nozzle geometries, to arrive at an optimum configuration. Compression waves focused on the wake did produce the expected increase in base pressure, but the practicality of forcing combustion to occur at the desired location and with the desired intensity was not addressed.

Strahle, Hubbartt and Neale<sup>20-25</sup> performed a series of experiments in a 6" diameter, Mach 3 tunnel with a concentrically mounted 2.25" diameter model. Following Fuhs, tests were run with simulated external burning in which detailed wake measurements were made. Base bleed and hydrogen base

burning with simulated external compression was then studied followed by an attempt at hydrogen external burning using subsonic, radial fuel injection just upstream of the base. It was found that this external burning configuration performed very similarly to base burning where the fuel was bled axially into the wake. It was concluded that extra jet penetration of the fuel was needed, and the orifices were re-drilled to provide supersonic injection. The extra jet penetration however, rendered stable combustion impossible. The projectile base recirculation zone which had been acting as the flameholder was no longer entraining fuel and supporting a pilot flame. The Mach 3, 35000 ft. test conditions were simply too severe to expect flameholding by the fuel jet only. The strong disturbance created by the supersonic injection also caused significant interference within the tunnel. These results exemplify the practical difficulty associated with obtaining "true" external burning in the inviscid stream with non-pyrophoric fuels such as hydrogen.

Schadow<sup>26-28</sup> performed a parallel series of experiments combining base and external burning in the late 1970's on both two-dimensional and axisymmetric base geometries at Mach 2, sea level conditions using fuel-rich solid rocket exhaust as fuel. Schadow's tests were run in a free-jet, and were not susceptible to tunnel choking and wall interference effects. In fact, Strahle in reference 25 notes that waves reflected from Schadows free-jet boundary would lead to conservative results. Schadow achieved base pressures greater than freestream (base thrust) with combined base and external burning, but as in Strahle's tests, external burning alone did not perform to expectations.

In 1976, Cavalleri<sup>29</sup> reports on an external burning rocket concept in which Strahle's wake pressurization scheme is used to provide propulsion. Tests were run at Mach 2 and 2.5 over a range of altitudes with an 8" diameter base in a 37" diameter test section, which is of significantly larger scale than previous tests. Fuel-rich solid rocket exhaust was injected radially upstream of the base. No base injection or base burning was used in conjunction with the external burning, yet enough thrust to cruise a low drag shape at Mach 2 was obtained. Relatively cool base temperatures measured during the tests indicated that the heat addition was truly in the form of external burning and not base burning of fuel entrained into the wake. Measurements made downstream of the model indicated that a subsonic plume caused by external combustion persisted for 14 radii downstream of the model base. This led to concerns that wave reflections and high pressure in the facility diffuser may have fed forward to influence base pressure. Director<sup>30</sup> analyzes the data further and concludes that the results were not affected by facility interference.

The bulk of past experimental external burning studies have been conducted using pyrophoric fuels with no additional flameholding required. Previous hydrogen external burning studies include Baker's early work which required large flameholders with respect to the tiny model scale, and Strahle's work at Mach 3 with no flameholders in which successful external burning was not achieved. To date, external burning in the inviscid flowfield has been approached only with pyrophoric fuels in Cavalleri's external burning rocket experiment. It seems that true external burning



in the sense meant by Strahle in 1968 will always be elusive, especially with a non-pyrophoric fuel such as hydrogen since an undisturbed, inviscid supersonic flow by definition has not been disrupted by the fueling process, and contains no flameholding sites. The present study is intended to extend the hydrogen external burning knowledge base to transonic conditions, representative of a single stage to orbit airbreathing vehicle trajectory. Some features peculiar to this situation are the need for a flameholder, and the subsonic condition of the plume following external combustion which must be carefully considered in both analysis and experiments.

#### Objectives of Current Work

In the current concept, a flameholder is used to sustain a piloting region near the wall surface, from which combustion can propagate into a fueled stream of somewhat larger proportion. One objective of the present study is thus to characterize the flameholding requirements for hydrogen and air at the transonic, sub-atmospheric pressure conditions of current interest, and to define the flight envelope where external burning is feasible.

Given that the hydrogen-air combustion process can be stabilized over an appropriate range of flight conditions, another objective is to evaluate the performance of external burning on the simplified expansion ramp geometry described earlier at transonic conditions.

To satisfy these objectives, an analytical and experimental study was undertaken. The control volume analysis described in chapter II was performed to estimate the performance potential of hydrogen external burning at the conditions of interest. The control volume analysis was also used to size fuel injection orifices for the experimental program. Results obtained were encouraging and the experimental program described in chapter IV was initiated to characterize the flameholding requirements, and demonstrate drag reduction on the simplified expansion ramp geometry, while providing data for comparison to the control volume results. In chapter III, an Euler analysis is performed which verifies the control volume results in two-dimensions, and provides further insight into the external burning flowfield and supersonic-subsonic transition. The Euler analysis also proved useful in interpreting the experimental results.

## CHAPTER II - CONTROL VOLUME ANALYSIS

### Background

The analysis of external burning in a transonic flow can be a formidable task, depending upon the level of detail required. Features of the flowfield include combustion of an unbounded stream of fuel and air, and the interaction of this stream with the unburned freestream and thrust surface. The details of fuel injection, flameholding, mixing and reaction kinetics could also be considered. To lay the groundwork for more sophisticated multi-dimensional analysis and experimental programs it is useful, if not critical to perform a simple parametric study that includes only the most dominant physical phenomena. The control volume analysis described in this section is a means to this end. It is intended to reveal the important parameters in the external burning process and assess the practicality of the concept as a drag reduction device. Based on the conservation equations, it provides insights into overall performance sensitivities while avoiding complex fuel injection, mixing and combustion modeling.

Before developing the control volume equations, a brief overview of analysis methods used by previous authors is given to provide a rationale for choosing the control volume method. Past analytical approaches to external burning can be divided into roughly three categories:

- 1) Two dimensional linearized, or exact methods which are mentioned here for completeness, but in general do not apply to the transonic problem where heat addition causes a transition to subsonic flow.

Pinkel<sup>31</sup> et. al. developed a graphical approach for obtaining diabatic method of characteristics solutions. This technique was then applied to a supersonic wing under which heat was added to increase the lift/drag ratio<sup>32</sup>. The method never seemed to catch on however due to it's tedious nature.

Tsien and Beilock<sup>33</sup> developed equations for the perturbations caused by a line heat source in a compressible flow. These linear theory results could be superimposed and were used widely by other authors. Schetz<sup>34,35</sup> for example used these results to model external burning adjacent to a turbulent wake as a "flame sheet". A similar method was also used by Fuhs in reference 15 for a number of different external burning examples.

- 2) One dimensional methods which employ equations derivable from Shapiro's<sup>36</sup> influence coefficients. They are generally put in finite difference form and solved by marching downstream while incrementally adding heat. While the equations are valid for subsonic flow, a singularity in the equations exists at Mach one, making the supersonic-subsonic transition difficult numerically. A subsonic outflow would also require multiple iterations in a downstream marching approach.

Vaughan<sup>37</sup> studied the control force generated on a flat plate by jet interaction and subsequent external burning of hydrogen. He limited the heat release to avoid sonic conditions in the burned stream since if the burned stream chokes, he concludes that upstream conditions must change and the assumptions used in deriving the model are violated.

Callens<sup>38</sup> et. al. used the one-dimensional equations to determine external burning propulsion performance for a high Mach upper stage. He further assumes a constant pressure in the burned stream which allowed a closed form integration of the equations (making his method similar to a control volume approach). He states that a limit on the amount of heat that can realistically be added is that the flow remain supersonic. Further reasoning behind this restriction was not given.

3) Control volume methods which ignore the detailed interactions within the heat addition zone, generally requiring information only at the control surfaces. No difficulty arises mathematically with subsonic flow, but assumptions regarding the outflow conditions must be made carefully, since any subsonic region is elliptic in nature. The control surfaces generally include inflow and outflow boundaries joined by two lateral control surfaces through which no flow passes. One of the lateral boundaries is the surface to be pressurized, either a solid surface or wake, the other is the boundary between heated and unheated flow. All injection, mixing, and combustion occurs within the control volume. Often, the entire control volume is assumed to be at constant pressure eliminating pressure-area

terms which can be difficult to evaluate.

Marino<sup>39</sup> used a constant pressure control volume approach to calculate the side force specific impulse of external burning on a flat plate for control purposes. The minimum Mach number considered was two, and since the fuel considered had a heating value of 18000 btu/lb, a subsonic exit condition would probably not occur, and was not discussed.

Harvey<sup>40,41</sup> et. al. used an annular control volume formulation for external burning adjacent to wake flow. In this study, the shape of the control volume was based on shadowgraphs of an external burning experiment and an approximate method of characteristics technique for axisymmetric flow was used to calculate the pressure on the outer control surface based on it's angle with respect to the freestream.

In reference 2, Billig presents a two-dimensional constant pressure control volume approach applicable to high Mach external burning propulsion. He presents experimental data which support the constant pressure assumption. Shock-expansion theory was used to determine the control volume pressure based on the angle of the outer control surface.

Another method used by many authors and summarized in reference 2, is the constant-area approach or planar heat addition model. An infinitely fast heat release rate is assumed such that the heat release takes place in an infinitely thin region and therefore at constant area. One-dimensional relations then apply across the thin control volume bounding the heater.

Normal or oblique heater planes can be treated in combination with normal and oblique shocks to build up the flowfield.

Transonic freestream conditions combined with the high heat of combustion of hydrogen will result in subsonic flow. For this reason, the control volume method was chosen as being the most applicable for the present study. Another more subtle advantage is that the outflow pressure in the elliptic region can be specified, where this would generally be impossible in a one-dimensional marching technique, without some type of iterative procedure. The present formulation differs from that of previous authors in that a constant pressure assumption is not made. The present analysis allows for the outflow pressure to equal the freestream static pressure, yet does not prohibit pressure excursions within the control volume which yield a net thrust or drag. This seems to be an important consideration since by it's elliptic nature, the subsonic plume extending past the outflow plane is influenced by the pressure downstream which quickly returns to freestream behind the vehicle.

In the development to follow, only the axial or thrust force will be considered. A beneficial normal force, proportional to the axial force is also generated which counteracts the high pressure forward of the vehicle center of gravity on the forebody (or inlet compression surface). The benefit of this normal force (which may be a number of times larger than the axial force) cannot be characterized as easily, but it has the synergistic effect of reducing drag by reducing the vehicle wing loading, and required pitching moment trim. The determination of the normal force

is an obvious extension to the control volume analysis once the nozzle chordal angle is specified, and it must be considered in vehicle closure studies, when comparing external burning to other propulsion augmentation options.

### Development

A simple planar expansion ramp geometry is used to model the vehicle base. With some imagination, this can be thought of as a simplified representation of the vehicle afterbody and nozzle system where the nozzle cowl flap and the main engine exhaust flow outer shear layer comprise a solid surface upon which external burning acts. The angle of this control surface and its' projected base area would be functions of the vehicle afterbody and nozzle geometry as well as the main engine nozzle pressure ratio. Implicit in this thinking is that the engine exhaust stream transmits the local pressure on the shear layer directly to the vehicle afterbody.

An important initial step in any control volume analysis is the prudent choice of problem boundaries. Good choices include surfaces through which mass does not pass and surfaces through which mass passes at right angles. All boundaries in the subsequent development fall into one of these categories. Figure 2-1 depicts the control volume nomenclature used. At station zero a uniform stream of air flows into the control volume at freestream conditions. The stream is fueled by injecting gaseous hydrogen



normal to the freestream through a row of sonic orifices. This specification of the injection method is not essential to obtain initial results, but is included so that fuel momentum may be taken into account. Conditions at the outflow plane or station two are also taken as uniform with velocity parallel to the freestream. The expansion ramp or vehicle base on which the change in force will be evaluated comprises the upper control surface. Completing the control volume is the streamline bounding the external burning plume, emanating from a point at station zero above which all of the fuel is confined. Integral forms of the continuity, momentum and energy equations can now be applied to the control volume and with some additional assumptions will result in a system of four equations which can be solved for a choice of four dependent variables.

The applicable form of the integral momentum equation for steady flow with no body or viscous forces is as follows:

$$\oint (\rho \vec{V} \cdot d\vec{s}) \vec{V} + \oint P d\vec{s} = 0 \quad [2-1]$$

Equation 2-1 is split into x and y components, and the integrals are evaluated for each control surface. Beginning with the x component, the inflow and outflow surfaces are easily evaluated with the assumption of uniform, parallel flow, and yield the following terms:

$$\text{inflow:} \quad -\dot{m}_a u_0 - P_0 y_0 \quad [2-2]$$

$$\text{outflow: } (\dot{m}_a + \dot{m}_f) u_2 + P_2 y_2 \quad [2-3]$$

At the upper boundary or wall surface, only a pressure integral exists and is written in terms of the axial thrust coefficient defined as follows:

$$C_t = - \frac{\oint_{\text{wall}} (P_w - P_0) ds_x}{Q_0 y_b} \quad [2-4]$$

The minus sign preceeding this equation is required so that wall pressures above freestream static pressure result in positive thrust (note that the area increment vector  $ds$  points out of the control volume). Using this definition, terms of the x-component of the momentum equation for the wall surface become:

$$\text{wall surface: } -C_t Q_0 y_b - P_0 y_b \quad [2-5]$$

On the bounding streamline or lower control surface, there is no momentum flux and linear theory is used to evaluate the pressure integral. Simply stated, the local pressure coefficient on the streamline is assumed to be a function of the local deflection angle. Assuming small angles the linear theory relation is as follows:

$$C_{p,s} = \frac{P_s - P_0}{Q_0} = \frac{-2\left(\frac{dy}{dx}\right)_s}{\sqrt{M_0^2 - 1}} \quad [2-6]$$

The minus sign is required so that deflections away from the vehicle axis result in positive values of  $C_p$ . It is further assumed that the streamline returns to the freestream direction at station 2 so that the outflow and inflow pressures are equal. Under these assumptions, the x-component of the pressure integral on the streamline becomes:

$$\int_0^2 \left[ P_0 - \frac{2Q_0\left(\frac{dy}{dx}\right)_s}{\sqrt{M_0^2 - 1}} \right] \left(\frac{dy}{dx}\right)_s dx \quad [2-7]$$

The second term in the integrand cannot be evaluated unless the variation of  $dy/dx$  along the streamline is known. This term, which is the pressure increment above freestream times an area increment involves the slope squared and always acts to reduce the thrust coefficient. Since linear theory already restricts the analysis to small deflection angles, it could be neglected which would be tantamount to assuming that freestream pressure acts on the streamline control surface. A more conservative approach is to account for the term at least approximately by assuming a streamline shape. In practice, the shape would depend on the axial heat addition distribution which is beyond the scope of this simple analysis. The assumption used herein is that the slope is constant and equals the total change in elevation of the streamline divided by the ramp length  $L$ .

The first term in equation 2-7 involves the integral of the slope and is evaluated exactly as freestream pressure times the change in elevation along the streamline. The resulting terms of the x-momentum equation on the streamline are as follows:

$$\text{streamline: } P_0(y_0 + y_b - y_2) - \frac{2Q_0}{\sqrt{M_0^2 - 1}} \frac{(y_b - y_2 + y_0)^2}{L} \quad [2-8]$$

Summing the terms in 2-2, 2-3, 2-5, and 2-8, the final x-momentum equation becomes:

$$C_x = 2 \left( \frac{y_0}{y_b} \right) \left[ \left( 1 + \frac{\dot{m}_f}{\dot{m}_a} \right) \left( \frac{u_2}{u_0} \right) - 1 \right] - \frac{2 \left( \frac{y_b}{L} \right)}{\sqrt{M_0^2 - 1}} \left( 1 + \frac{y_0}{y_b} \left( 1 - \frac{y_2}{y_0} \right) \right)^2 \quad [2-9]$$

The second term is the streamline linear theory approximation and is negligible for low deflection angles and thrust coefficients. Note that this is where the effect of the ramp angle appears. From this equation it can be seen that for thrust coefficients near zero (base drag eliminated) the inflow and outflow velocities are nearly equal, only differing by a factor involving the fuel-air ratio. The outflow temperature following hydrogen-air combustion can be almost an order of magnitude greater than the inflow, resulting in a factor of three increase in the speed of sound. The outflow will therefore be subsonic for the range of freestream Mach numbers of interest here.

Evaluating the y-component of momentum on all control surfaces results in equation 2-10:

$$(\dot{m}V)_f = -(PA)_f - \int_0^L P_w dx + \int_0^L P_s dx \quad [2-10]$$

Here it has been assumed that the fuel is injected normal to the freestream. The integrals are evaluated in a manner analagous to those of the x-momentum equation with the additional assumption that the wall surface is straight ( $dy/dx$  is constant). The final form of the y-momentum equation is as follows where  $d^*$  is the diameter of the choked orifices, and  $S$  is the spacing between orifices:

$$C_f = \frac{2\left(\frac{y_b}{L}\right)\left[\frac{y_0}{y_b}\left(\frac{y_2}{y_0}-1\right)-1\right]}{\sqrt{M_0^2-1}} - \frac{(1+C_v\gamma_f)\left(\frac{P_f}{Q_0}\right)\left(\frac{d^*}{y_b}\right)\left(\frac{\pi}{4}\right)}{\left(1+\frac{(\gamma_f-1)}{2}\right)^{\frac{\gamma_f}{\gamma_f-1}}\left(\frac{S}{d^*}\right)\left(\frac{L}{y_b}\right)} \quad [2-11]$$

The second term represents the fuel momentum and acts to reduce thrust. In spite of it's complexity, this term is negligible compared to the inflow momentum and can be ignored.

The continuity equation can be written simply as a statement of mass conservation in the control volume:

$$\dot{m}_a + \dot{m}_f = \dot{m}_2 \quad [2-12]$$

Applying the equation of state for a thermally perfect gas at the inflow and outflow stations, and recalling that the inflow and outflow pressures are equal, results in a relation for the overall control volume area ratio:

$$\frac{y_2}{y_0} = \frac{\left(1 + \frac{\dot{m}_f}{\dot{m}_a}\right) \left(\frac{T_2}{T_0}\right) \left(\frac{R_2}{R_0}\right)}{\left(\frac{u_2}{u_0}\right)} \quad [2-13]$$

To close the system of equations, information about the thermodynamic state of the outflow is needed. This is provided by the energy equation:

$$\oint P \vec{V} \cdot d\vec{S} + \oint \rho \left(e + \frac{V^2}{2}\right) \vec{V} \cdot d\vec{S} = 0 \quad [2-14]$$

Only the inflow and outflow planes, and the normal fuel injection need to be considered here since the dot product of velocity and area is zero everywhere else. Equation 2-15 is the energy balance used.

$$\dot{m}_a \left(h + \frac{V^2}{2}\right)_0 + \dot{m}_f \left(h + \frac{V^2}{2}\right)_f = (\dot{m}_a + \dot{m}_f) \left(h + \frac{V^2}{2}\right)_2 \quad [2-15]$$

This equation is evaluated by assuming that combustion at a given fuel-air

ratio is complete at station 2 and that the combustion products are in equilibrium at freestream static pressure. Ten species are considered in this calculation which is outlined in appendix A. The outflow gas constant needed in the continuity equation is a by-product of the equilibrium energy balance.

Equations 2-9, 2-11, 2-13, and 2-15 are four equations which can be used to solve for four unknowns. In general, the control volume inflow conditions are specified, as well as the inflow stream height and fuel-air ratio. The conservation equations can then be used to determine the control volume area ratio  $y_2/y_0$ , velocity ratio  $u_2/u_0$ , temperature ratio  $T_2/T_0$  and finally, the thrust coefficient  $C_r$ . Some variations of this basic equation set will now be described.

### Three-Dimensional Relief Approximation

A non-zero thrust coefficient implies pressures different from freestream within the control volume which would give rise to a transverse flow. To account for this three-dimensional relieving effect which would tend to lower the magnitude of the thrust coefficient, some additional modeling is introduced which allows for changes in the control volume width from station 0 to station 2. The main assumption here is that all three "sides" (stream surfaces) of the control volume deflect equally. The change in the formulation arises in the x and y-momentum equations where the streamline slope is reduced since the cross-sectional area of the

control volume at station 2 is now accommodated by equal deflections of all three stream surfaces. Similar to the two-dimensional form (2-7), the x-component of the pressure integral on the stream surfaces is:

$$0 = - \int_0^2 \left[ P_0 - 2Q_0 \frac{\left(\frac{dy}{dx}\right)_s}{\sqrt{M_0^2 - 1}} \right] \left( -\frac{dA}{dx} + w \frac{y_b}{L} \right) dx \quad [2-16]$$

The  $dA/dx$  term is the total cross-sectional area change, and  $dy/dx$  is now the three-dimensional slope of all three stream surfaces. As in the two-dimensional case, this slope is assumed to be constant and equal to the total deflection divided by the base length. The final "three-dimensional" form of the x-momentum equation becomes:

$$C_t = 2 \left( \frac{y_0}{y_b} \right) \left[ \left( 1 + \frac{m_f}{m_s} \right) \left( \frac{u_2}{u_0} \right) - 1 \right] - \frac{2 \left( \frac{\Delta y_{3D}}{L} \right)}{\sqrt{M_0^2 - 1}} \left( 1 + \frac{y_0}{y_b} \left( 1 - \frac{A_2}{A_0} \right) \right) \quad [2-17]$$

The three dimensional stream surface deflection is a function of the control volume area ratio  $A_2/A_0$ , the inflow stream height  $y_0/y_b$ , the base aspect ratio  $w/y_b$ , and the ramp angle  $L/y_b$ . Evaluation of this term is purely geometric and is reduced to the quadratic equation below.



$$a\left(\frac{\Delta y_{3D}}{L}\right)^2 + b\left(\frac{\Delta y_{3D}}{L}\right) + c = 0$$

$$a = 2\left(\frac{L}{y_b}\right)^2$$

[2-18]

$$b = 2\left(\frac{L}{y_b}\right)\left[1 + \frac{y_0}{y_b} + \frac{1}{2}\left(\frac{w}{y_b}\right)\right]$$

$$c = \left(\frac{w}{y_b}\right)\left[1 + \left(\frac{y_0}{y_b}\right)\left(1 - \frac{A_2}{A_0}\right)\right]$$

It should be noted that some small pressure-area terms have been neglected in this three-dimensional model since the control volume no longer conforms exactly to the edges of the ramp surface. Since linear theory already restricts angles to small values, inclusion of these small "wedges" is unnecessary.

The three-dimensional y-momentum equation is similar to the two-dimensional form (equation 2-11) except that the 3-D streamline deflection is now used:

$$C_s = -\frac{2\left(\frac{\Delta y_{3D}}{L}\right)}{\sqrt{M_0^2 - 1}} - \frac{(1 + C_v \gamma_f)\left(\frac{P_f}{Q_0}\right)\left(\frac{d^*}{y_b}\right)\left(\frac{\pi}{4}\right)}{\left(1 + \frac{(\gamma_f - 1)}{2}\right)^{\frac{\gamma_f}{\gamma_f - 1}}\left(\frac{S}{d^*}\right)\left(\frac{L}{y_b}\right)} \quad [2-19]$$

The continuity and energy equations are unchanged, with  $y_2/y_0$  interpreted as the cross-sectional area change of the control volume from inflow to outflow.

### Equations for a Perfect Gas

The energy equation can be greatly simplified by neglecting the addition of fuel altogether and assuming that energy is simply added to a perfect gas air stream. The resulting equation (2-20) will be useful in a subsequent section when comparing results from a two-dimensional perfect gas Euler analysis.

$$\frac{T_2}{T_0} = (\gamma_a - 1) M_0^2 \left[ \frac{q}{(u_0^2/g_c)} + \frac{1}{(\gamma_a - 1) M_0^2} - \frac{1}{2} \left( \frac{u_2}{u_0} \right)^2 + \frac{1}{2} \right] \quad [2-20]$$

The energy added per unit mass of air flowing into the control volume ( $q$ ) is assumed equal to the product of fuel-air ratio and the lower heating value of the fuel. Corresponding simplifications to the continuity and momentum equations are readily made by assuming a fuel mass flow of zero and that the outflow and inflow gas constants are identical. If the two-dimensional forms of the  $x$  and  $y$  momentum equations are used (2-9 and 2-11), and the second term in equation 2-11 is neglected, the equation set can be manipulated into a quadratic in  $u_2/u_0$ .

### Equations At Zero Drag

At zero drag, three-dimensional effects are negligible, so the two-dimensional equations are used. Further, the term involving the slope

squared in the x-momentum equation (2-7) can be neglected. The fuel momentum term in the y-momentum equation is ignored so that answers are not specific to the normal injection case. Now, setting the thrust coefficient to zero results in the following forms of the x-momentum, and y-momentum equations.

$$\frac{u_2}{u_0} = \frac{1}{\left(1 + \frac{\dot{m}_f}{\dot{m}_a}\right)} \quad [2-21]$$

$$\frac{y_0}{y_b} = \frac{1}{\left(\frac{y_2}{y_0} - 1\right)} \quad [2-22]$$

The continuity and energy equations are unchanged at zero drag.

### Performance Parameter Definitions

A figure of merit for external burning is needed so that it's performance can be compared to that of other forms of propulsion. An obvious choice would be the specific impulse based on the force generated by external burning:

$$I_{sp} = \frac{\text{AXIAL FORCE INCREASE}}{\dot{m}_f} \quad [2-23]$$

In terms of the external burning parameters used in the preceeding development, this equation becomes:

$$I_{sp} = \frac{(C_r - C_r^0)}{\left(\frac{y_0}{y_b}\right)\left(\frac{\dot{m}_f}{\dot{m}_a}\right)\left(\frac{2g_c}{u_0}\right)} \quad (lb_f\text{-sec}/lb_m) \quad [2-24]$$

Where  $C_r^0$  is the ramp surface force coefficient without external burning and is defined exactly as the thrust coefficient was in equation 2-4. Another definition, which does not involve the fuel off thrust coefficient is obtained by assuming that the pressure on the wall with no external burning is zero. The resulting "total specific impulse" can be written as follows:

$$I_{sp, tot} = \frac{\left(C_r + \frac{2}{\gamma M_0^2}\right)}{\left(\frac{y_0}{y_b}\right)\left(\frac{\dot{m}_f}{\dot{m}_a}\right)\left(\frac{2g_c}{u_0}\right)} \quad (lb_f\text{-sec}/lb_m) \quad [2-25]$$

This definition results in high impulse values, since it is based on the total force instead of the external burning force increment, but can be computed without knowledge of the drag coefficient. The total specific impulse is the sum of the external burning impulse given by equation 2-24 and an impulse attributed to the pressure on the ramp without external burning. It cannot be directly compared to the specific impulse of other propulsion systems, but is useful for examining trends.

At zero thrust coefficient, a "normalized" specific impulse is obtained from equation 2-24.

$$\frac{I_{sp}}{-C_T^0} = \frac{\left(\frac{u_0}{2g_c}\right)}{\left(\frac{y_0}{y_b}\right)\left(\frac{\dot{m}_f}{\dot{m}_a}\right)} = \frac{Q_0}{\left(\frac{\dot{m}_f}{y_b w}\right)} \quad (lb_f\text{-sec}/lb_m) \quad [2-26]$$

This equation illustrates the fact that external burning performance is directly proportional to the severity of the base drag problem.

### Results

The zero-drag form of the equations will be examined first to determine the fuel flow and inflow stream height required to eliminate base drag. If either of these parameters appear to be unreasonably high, the utility of the concept would be in question. The zero drag y-momentum equation (eq. 2-22) states that the inflow stream height depends only on the control volume area ratio. Since this stream must be fueled by a fuel injection system in any practical application, a low value is desirable which translates into a high value for the control volume area ratio. As shown by equation 2-13, the area ratio is mainly a function of the fuel-air ratio chosen since at zero drag, the inflow and outflow velocity ratio is nearly one. Both the temperature and gas constant ratios increase with increasing fuel-air ratio until the maximum equilibrium temperature is reached at a fuel-air equivalence ratio slightly greater than one.

Further increases in the equivalence ratio result in much lesser increases in area ratio as the now decreasing equilibrium temperature compensates for the gas constant and mass addition effects. The equilibrium temperature ratio is affected to a lesser extent by altitude, as the temperature ratio increases with decreasing inflow temperature. The effect of pressure on the equilibrium calculation is negligible at the altitudes considered for transonic flight.

The variation of required inflow stream height at zero drag with fuel equivalence ratio is shown in figure 2-2a over a range of transonic flight Mach numbers on a 1000 psfa dynamic pressure trajectory. Note that since the linear theory terms were ignored in the zero drag equations they can be evaluated below Mach one. The benefit of increasing equivalence ratio is reduced for equivalence ratios greater than one. The curves flatten out at Mach 1.8 as the vehicle climbs into the tropopause and the inflow temperature becomes constant. This is the only effect of trajectory on the inflow stream height; different trajectories would simply cause this flattening to begin at a different Mach number. For a stoichiometric, or fuel rich system, the required stream height is about six to ten percent of the base height over the entire Mach number range.

The inflow stream height and freestream conditions fix the air flowrate into the control volume, so specifying the fuel-air ratio determines the fuel flowrate required. Figure 2-2b shows the required fuel flows at zero drag corresponding to the conditions of figure 2-2a. For equivalence ratios less than one, the increase in fuel flow with fuel-air ratio is

compensated by the reduction in inflow stream height. Thus the curves for equivalence ratios from .5 to 1.0 are nearly coincident. On the fuel-rich side however, the fuel flow does increase with equivalence ratio since the reduction in inflow stream height is relatively small. Unlike the inflow stream height, the fuel flowrate is a strong function of altitude being roughly proportional to the freestream dynamic pressure. Along the 1000 lb/ft<sup>2</sup> trajectory, the required hydrogen flowrate ranges from about .05 to .2 lb/sec per ft<sup>2</sup> of base area for stoichiometric or fuel lean equivalence ratios.

So far, the desire for low inflow stream height requires the highest equivalence ratio possible, tempered by consideration of the fuel flow which increases sharply for equivalence ratios greater than one. The penalty for high fuel flow is shown in figure 2-2c using the "normalized" specific impulse given by equation 2-26. The impulse values decrease with increasing equivalence ratio, but there is relatively little loss in performance for equivalence ratios up to one. Performance degrades quickly however with further increases in equivalence ratio. The specific impulse is nearly invariant with trajectory, since the fuel flow increases proportionately with freestream dynamic pressure, and the ratio of these two appears in equation 2-26; i.e. for a given drag coefficient, the drag force and fuel flow are proportional to dynamic pressure. The increase in specific impulse with Mach number is due to the normalization used and would only occur if the drag coefficient were constant over the Mach number range. To determine the actual  $I_{sp}$  due to external burning, the base drag of the vehicle without external burning must be known. The

determination of a base drag coefficient is a complex problem even for simple projectile shapes, depending on many different parameters such as Reynold's number, Mach number, approach boundary layer thickness and boattail angle. The situation herein is further complicated by the main engine exhaust which has already been simplified. Reference 1 contains a vast number of correlations and models from which an overall flavor of the base drag problem can be obtained. To pick a single drag coefficient applicable over the range of flight conditions would be a gross oversimplification, however for the present discussion, a value of order - .25 puts a lower bound on the specific impulse, reducing the normalized values by a factor of four. Even at this conservative level of base drag, the  $I_{sp}$  at stoichiometric conditions ranges from 1000 to 4000 seconds which exceeds that of a rocket (400 sec) and is competitive with a turbojet installation. Added benefits of an external burning system are its light weight and relative simplicity.

The results at zero drag indicate that the external burning system should be designed to operate at or near stoichiometric conditions. A fuel-lean approach results in slightly lower fuel flows, and higher performance, but would involve distributing less fuel over a larger cross-sectional area. From the practical standpoints of fuel injection and flame stability to be discussed in a subsequent section, equivalence ratios near one are preferred.



### Fuel Injection Considerations

Given the required fuel flowrate and inflow air stream height, the fuel injection scheme can be examined in more detail. A transverse row of sonic orifices injecting gaseous hydrogen fuel normal to the freestream will be considered. More imaginative ways of fueling the stream such as spraybars, vortex mixing, etc. could be considered, but wall injection can be modeled in a relatively straightforward manner and provides a good point of departure for more elaborate schemes. Upon injection from a sonic orifice normal to the freestream, the fuel jet interacts with the oncoming freestream air and is bent downstream in a relatively well-understood inviscid process known as "jet penetration"<sup>42-51</sup>. The "trajectory" of the fuel jet depends largely on the momentum of the two streams. If the freestream momentum is high compared to that of the jet, the fuel is quickly directed downstream and may only penetrate a few orifice diameters into the freestream. This inviscid interaction which results in most of the penetration occurs within about 20 orifice diameters downstream of injection, after which the viscous mixing process transports the fuel further into the freestream at a much slower rate.

### Jet Penetration Model and Equivalence Ratio Approximation

For round, underexpanded, sonic orifices the jet penetration depends on a number of parameters including the orifice diameter, fuel and freestream conditions, and distance downstream of the orifice at which the

penetration is measured. The jet penetration was found to be almost invariant with gas molecular weight and total temperature in reference 48. Povinelli et.al.<sup>50</sup> presents a correlation of experimental data which is useful for the present application, giving an equation that describes the outer boundary of the injectant defined as a 1/2% concentration by volume. Four correlating parameters were used, namely the jet penetration in orifice diameters  $y_p/d^*$ , the distance downstream of the orifice centerline  $x/d^*$ , the orifice exit Mach number, and the jet total pressure divided by the "effective back pressure". The effective back pressure idea was introduced by Orth, et.al.<sup>47</sup> as a way of extending results for injection into a quiescent medium to injection into a supersonic cross-flow. The effective back pressure is taken to be 2/3 of the stagnation pressure behind a normal shock at the freestream Mach number. For sonic orifices the correlation equation reduces to equation 2-27 which will be used herein to describe jet penetration.

$$\frac{y_p}{d^*} = 1.12 \left( \frac{P_{t,f}}{P_{ab}} \right)^{.483} \left( \frac{x}{d^*} + .5 \right)^{.281} \quad [2-27]$$

$$P_{ab} = (2/3) P_{t,N-S}$$

The fuel-air equivalence ratio and the control volume inflow stream height are two key parameters which will now be related to the jet penetration. The amounts of fuel and air involved in the external burning process must be known to arrive at an equivalence ratio. The fuel flowrate through a choked orifice of diameter  $d^*$  is described by equation 2-28:

$$\dot{m}_{H_2} = .1403 C_v \frac{P_{H_2}}{\sqrt{T_{H_2}}} \frac{\pi d^{*2}}{4} \quad [2-28]$$

The total fuel flowrate is then determined by the number of orifices in the row. Estimating the amount of air involved in the unconfined stream is not as straightforward and must be approximated. The central assumption used herein is that the inflow stream height  $y_0$  is equal to the jet penetration  $y_p$ . The air flow is then taken as that which flows at freestream conditions through the inflow plane. Thus each orifice fuels a cross-section of the inflow air which is  $y_p$  high and  $S$  wide where  $S$  is the spacing between the orifices. This airflow is given by equation 2-29.

$$\dot{m}_a = .532 \frac{P_{t,0}}{\sqrt{T_{t,0}}} \left( \frac{A^*}{A} \right)_0 y_p S \quad [2-29]$$

Combining equations 2-28 and 2-29, the fuel-air equivalence ratio based on "penetration times spacing" becomes:

$$\Phi_{pxs} = 5.213 C_v \frac{\left( \frac{P_{H_2}}{P_{t,0}} \right)^{.517} \left( \frac{P_{t,N-S}}{P_{t,0}} \right)^{.483} \left( \frac{A}{A^*} \right)_0}{\sqrt{\frac{T_{H_2}}{T_{t,0}} \left( \frac{S}{d^*} \right) \left( \frac{x}{d^*} + .5 \right)^{.281}}} \quad [2-30]$$

The penetration times spacing equivalence ratio is obviously of a global nature and is most rational if the orifice spacing and the jet penetration are of nearly the same magnitude\*. A parameter which gives a degree of freedom to this calculation is the distance downstream ( $x/d^*$ ) at which the penetration is taken in equation 2-27. The  $1/2\%$  concentration "trajectory" given by equation 2-27 is plotted in figure 2-3, for various values of the jet pressure ratio. For  $x/d^*$  values greater than about 20, the calculated equivalence ratio will not be a strong function of  $x/d^*$  due to its .281 exponent. A value of 30 is used in most subsequent calculations.

The design problem is then one of finding a combination of orifice diameter, spacing, and fuel conditions, which results in the desired equivalence ratio and inflow stream height (jet penetration) at the given flight condition.

#### Fuel Injection Design Example

Equation 2-30 can be rearranged into equation 2-31 where a dimensionless grouping of fuel injection parameters  $F_i$  is written as a function of freestream conditions and the desired fuel-air equivalence ratio.

---

\* In reference 43, the concentration profiles downstream of the orifice are shown to develop into a "kidney shape" of total width roughly equal to the height.

$$F_1 = \frac{\left(\frac{P_{H_2}}{P_{t,0}}\right)^{.517} C_v}{\sqrt{\frac{T_{H_2}}{T_{t,0}} \left(\frac{S}{d^*}\right)}} = \frac{.192 \left(\frac{x}{d^*} + .5\right)^{.281} \phi}{\left(\frac{P_{t,H-S}}{P_{t,0}}\right)^{.483} \left(\frac{A}{A^*}\right)_0} \quad [2-31]$$

Replacing the jet penetration  $y_p$  with the inflow stream height  $y_0$  in equation 2-27 results in a second dimensionless group  $F_2$  which also relates fuel injection parameters to freestream conditions and the desired inflow stream height.

$$F_2 = \left(\frac{d^*}{y_b}\right) \left(\frac{P_f}{P_{t,0}}\right)^{.483} = .734 \left(\frac{y_0}{y_b}\right) \left(\frac{P_{t,H-S}}{P_{t,0}}\right)^{.483} \left(\frac{x}{d^*} + .5\right)^{-.281} \quad [2-32]$$

Now, if a design flight condition and equivalence ratio is chosen, the required inflow stream height from the zero-drag equations (figure 2-2) is known and the fuel pressure, temperature, and orifice geometry can be traded using equations 2-31, and 2-32. For the following example, the Mach 1.4, 1000 psfa dynamic pressure (26700 ft. altitude) flight condition was chosen. An equivalence ratio of one is used since as discussed previously, this provides a good compromise between specific impulse performance and operability in terms of fuel injection and flame stability. This design point results in values for  $F_1$  and  $F_2$  of .4588 and .0239 respectively. Specifying a fuel pressure of 300 psia, results in an orifice diameter of .005824 base heights from equation 2-32. The orifice spacing ratio  $S/d^*$  can now be obtained from equation 2-31 by specifying a fuel temperature and flow coefficient. Using a fuel temperature of 518

degrees Rankine and a flow coefficient of 0.9, the spacing ratio is 9.485. At the Mach 1.4, 26700 ft. flight condition, this orifice design will match the jet penetration and fuel flow such that the inflow stream height and equivalence ratio are the required values for zero drag. Similarly, the specific impulse performance at this condition will be the zero drag value given in figure 2-2c (8679 times  $C_p^0$ ). To match the zero drag fuel flow and jet penetration over the entire trajectory requires a unique schedule of fuel temperature and pressure. For the example design given, this schedule appears in figure 2-4. It is unlikely that this variation of fuel conditions would exist at any one point in the fuel system, where the external burning fuel could be extracted. To follow the variation shown in pressure and temperature would burden the relatively simple external burning system with auxiliary pumps, heat exchangers, etc. making it much less attractive.

#### Performance at Constant Fuel Conditions

Fortunately, the penalty for off-design operation is not substantial as can be seen in figure 2-5 where the example orifice pattern is operated at the design fuel conditions (300 psia, 518 degrees Rankine) over the entire trajectory. Now, the resulting equivalence ratio and stream height will not necessarily result in zero thrust coefficient and the general form of the control volume equations must be used. In figure 2-5a, the inflow stream height which is simply the jet penetration at constant fuel conditions is plotted. The zero drag, stoichiometric design result is

also shown for comparison and obviously intersects the other curve at the Mach 1.4 design point. The jet penetration varies only about 10% over the entire envelope, as expected since the jet momentum is constant and the freestream momentum is nearly so on a constant dynamic pressure trajectory. This results in the continuously increasing equivalence ratio shown in figure 2-5b since the fuel flow is constant, and the airflow decreases along the trajectory.

With the equivalence ratio and inflow stream height known, the control volume equations are solved for the non-zero thrust coefficient. First however, the tangent of the base angle  $y_b/L$  must be specified, and if the three-dimensional expansion assumption is used, the aspect ratio  $w/y_b$  is also needed. The thrust coefficient obtained by assuming a three-dimensional expansion and equilibrium chemistry is plotted in figure 2-5c along with thrust coefficients for a 2-d expansion, and a perfect gas 2-d expansion. To give the plot a sense of scale, it may be noted that the drag coefficient for a 15 degree Prandtl-Meyer expansion is  $-.630$  at Mach 1.1 and  $-.145$  at Mach 2.6. This represents the worst case for the ramp without burning. In reality, three-dimensional effects and boundary layer separation would tend to make these values closer to zero. With respect to the Prandtl-Meyer expansion values, the thrust coefficient with external burning does not vary significantly from zero, which is the reason that the 2-d and 3-d curves are nearly coincident. The perfect gas assumption results in high temperatures and high area ratios causing slightly higher thrust. This is compensated for somewhat by neglecting the fuel mass addition which is included in the real gas calculation.

From the standpoint of thrust, the consequences of simply using constant fuel conditions are negligible for a system designed at an intermediate flight condition along the trajectory.

From figure 2-5b, using constant fuel conditions results in increasing equivalence ratio. For constant thrust, this translates into a continuously decreasing specific impulse as shown in figure 2-5d. The specific impulse as defined by equation 2-24 is plotted for the 3-d thrust coefficient of figure 2-5c assuming a Prandtl-Meyer expansion for the fuel off thrust. The zero thrust curve is also shown for comparison. The  $I_{sp}$  is greater than the zero drag value for negative thrust coefficients and less than the zero drag value for positive thrust coefficients. For example, at Mach 1.2 the zero drag  $I_{sp}$  is 3757 seconds; compared to an  $I_{sp}$  of 4373 seconds at a thrust coefficient of  $-.017$  for the constant fuel conditions case. At Mach 2.0, The zero drag impulse is 2755, as compared to 1992 at a thrust coefficient of  $.014$ . The result of not adhering to a design point fuel schedule is thus slightly less thrust at a higher impulse or slightly more thrust at a reduced impulse. These  $I_{sp}$  numbers are greater than what would be obtained in actual practice since the fuel off thrust coefficient would be somewhat higher. However even at half these impulse values the external burning system is competitive with turbojets given its light weight, simplicity, and the synergistic effect of the normal component of force which is not included in the performance assessment.



### Control Volume Analysis Summary

Application of the conservation equations to a control volume representing the external burning process results in a system of equations which characterizes performance and operability. A subset of these equations in which the thrust coefficient is set to zero provides a zero drag fuel injection orifice sizing criterion. Results indicate that a stoichiometric design strategy provides a good compromise between performance and operability. An inflow stream height on the order of 10% of the base height and a fuel flow of .1 to .2 pounds per second per square foot of base projected area are required to zero the thrust coefficient along a 1000 psfa dynamic pressure trajectory. This results in specific impulse performance competitive with other forms of airbreathing propulsion. A single row of sonic orifices was sized to match the fuel flow and jet penetration for zero drag at a single flight condition. Using constant fuel pressure and temperature, the resulting orifice design worked acceptably over the entire Mach number range indicating that modulation of fuel conditions is unnecessary. These encouraging initial results warranted further analysis and experiment which is the subject of the following chapters.

## CHAPTER III - EULER ANALYSIS

### Background

The control volume analysis ensures conservation of mass, momentum and energy under the stated assumptions, but is a "black box" approach. Internal details of the complex flowfield need not be considered to evaluate the force imparted to the wall surface. An interesting implication of the control volume analysis is that the wall force does not depend on the axial distribution of heat addition, but only on the total energy added. Another feature of the flowfield is the small change in velocity of the external burning stream from inflow to outflow for near-zero thrust coefficients (see equation 2-9). The plume is driven to a subsonic condition by an increase in the speed of sound and not by deceleration. The transonic freestream is in general deflected by the plume, unless the stream expansion caused by heat addition exactly matches the wall geometry\*. Deflection of the outer, transonic stream causes axial pressure gradients which are balanced by the subsonic plume and give rise to an interaction between the hyperbolic outer stream and the elliptic plume.

---

\* In reference 52, Broadbent presents an interesting inverse method for determining the heat addition distribution required for a desired wall pressure distribution and streamline pattern in an inviscid two-dimensional flow. The method is restricted to supersonic flow in which the shape of the streamlines can be estimated readily, and so has limited application to the present case.

The desire to better understand the features and interactions of the inviscid external burning flowfield and to verify in two-dimensions the control volume results, led to the development of an Euler analysis which is the topic of this section. The Euler analysis also proved useful in evaluating the experimental results of chapter IV where the additional interaction of the free-jet boundary was examined. The Euler equations were chosen due to their relative simplicity and as the next step in complexity from the control volume analysis. A representative heat addition distribution is imposed on the flowfield through the energy equation and the equations are solved using a time-marching technique. Assuming the distribution of energy addition a priori may at first seem to be an oversimplification, but the alternative is a viscous model of the complex mixing and chemical processes which are themselves subject to assumptions on turbulence and chemical reaction rates. A much finer grid and orders of magnitude greater run times are other obvious drawbacks to a Navier-Stokes approach. Using the Euler approach, the heat addition is based on available information such as jet penetration and fuel flow and can be varied parametrically. Features of the flowfield and analysis are depicted schematically in figure 3-1. The geometry studied parallels that of the control volume analysis, being a straight ramp adjacent to which heat is added so as to counteract the expansion and reduce the drag force. The heat addition region in general drives the supersonic inflow to a subsonic condition resulting in a mixed supersonic-subsonic outflow. The upper lateral boundary downstream of the ramp is treated in two different ways, as a solid wall parallel to the freestream, and with a second inflow which simulates the flow over the upper surface of the vehicle, generating

a slip line between it and the external burning plume. In comparisons of the two methods to be presented in chapter 4, the plume was quickly deflected by the freestream inflow and the slip line and wall were nearly coincident, resulting in negligible differences in the ramp pressure distributions and drag force. The lower lateral boundary is treated as either a free boundary through which waves may pass, or a free-jet boundary which deflects, reflecting waves of the opposite family back into the flowfield. The heat addition zone is bounded by the wall and a streamline emanating from a specified point at the inflow in the lateral direction, and axially, by specified upstream and downstream locations  $x_1$  and  $x_2$ .

### Development

#### Euler Equations in Conservation Form

The equations of motion for an inviscid, non-conducting gas without body forces were taken from reference 53. For the present case, the term representing the energy addition must be retained in the differential energy equation. The resulting equation set in conservation form and the non-dimensionalization used is as follows:

$$\frac{\partial U}{\partial t} + \frac{\partial E}{\partial x} + \frac{\partial F}{\partial y} = Q \quad [3-1]$$

$$U = \begin{bmatrix} \rho \\ \rho u \\ \rho v \\ E_{tot} \end{bmatrix} \quad E = \begin{bmatrix} \rho u \\ \rho u^2 + P \\ \rho uv \\ (E_{tot} + P) u \end{bmatrix} \quad F = \begin{bmatrix} \rho v \\ \rho uv \\ \rho v^2 + P \\ (E_{tot} + P) v \end{bmatrix} \quad Q = \begin{bmatrix} 0 \\ 0 \\ 0 \\ \dot{Q} \end{bmatrix}$$

$$\begin{aligned} \rho^* &= \frac{\rho}{\rho_0} & P^* &= \frac{P}{\rho_0 (u_0^2 / g_c)} & u^* &= \frac{u}{u_0} & v^* &= \frac{v}{u_0} \\ e^* &= \frac{e}{(u_0^2 / g_c)} & E_t^* &= \frac{E_t}{\rho_0 (u_0^2 / g_c)} & \dot{Q}^* &= \frac{\dot{Q} l}{\rho_0 (u_0^3 / g_c)} \\ t^* &= \frac{t l}{u_0^2} & x^* &= \frac{x}{l} & y^* &= \frac{y}{l} \end{aligned}$$

Following reference 53, a general grid transformation is applied and the equations are put back into conservation form. The resulting equation set in transformed coordinates contains the Jacobian and metrics of the transformation.

$$\frac{\partial \bar{U}}{\partial \bar{t}} + \frac{\partial \bar{E}}{\partial \bar{\xi}} + \frac{\partial \bar{F}}{\partial \bar{\eta}} = \bar{Q} \quad [3-2]$$

$$\bar{U} = \frac{1}{J} U$$

$$\bar{E} = \frac{1}{J} (\xi_x E + \xi_y F)$$

$$\bar{F} = \frac{1}{J} (\eta_x E + \eta_y F)$$

$$\bar{Q} = \frac{1}{J} Q$$

The U, E, F, and Q vectors are as defined in equations 3-1. These equations are then solved on the transformed, uniform, rectangular grid. Algebraic grid generation was used with stretching functions taken from reference 53, used in both the x and y directions.

### Method of Solution

The transformed equations were solved in finite-difference form using MacCormack's explicit, time-marching, predictor-corrector technique as presented in reference 53. A forward predictor, backward corrector differencing scheme was used for internal points, with appropriate switching at boundaries where an initial solution is needed to apply the boundary conditions. The flowfield was initialized to the inflow conditions and then marched in time using a time step determined by the 2-D Courant number:

$$C_{2D} = \frac{(|V|+a) \Delta t}{\sqrt{(\Delta x)^2 + (\Delta y)^2}} \quad [3-3]$$

The flowfield was surveyed at each iteration to determine the maximum allowable time step based on a constant Courant number. For many of the flowfields with heat addition and large density gradients a Courant number of 1/4 was needed to stabilize the solution. To determine convergence, the absolute value of the change in each of the U vector members (obtained

in the corrector step) was summed over the entire flowfield at each time step. These four values which represent the degree to which each of the four conservation equations are satisfied generally decreased by several orders of magnitude, approaching steady-state values which were grid and problem dependent.

### Artificial Damping

Damping was required to stabilize the solution in the vicinity of shock waves as well as near the boundary between heated and unheated regions. Common artificial viscosity models based on velocity gradient are sufficient for adiabatic flow, but for the present case, large gradients in density can occur across the heat addition boundary in the absence of a velocity gradient, rendering the artificial viscosity models ineffective. The method used was a variation on that of Rusanov as presented in reference 54. Terms involving spatial derivatives of the U vector members are added to the members of the E and F vectors in all four equations. This corresponds to adding an artificial viscosity, as well as a mass diffusion, and thermal conductivity. The dissipation terms modify the transformed E and F vectors in equations 3-2 as follows:

$$\begin{aligned}\bar{E} &= \frac{1}{J} [\xi_x (E + C_x U_x) + \xi_y (F + C_y U_y)] \\ \bar{F} &= \frac{1}{J} [\eta_x (E + C_x U_x) + \eta_y (F + C_y U_y)]\end{aligned}\tag{3-4}$$

where  $C_x$  and  $C_y$  are damping coefficients given by:

$$\begin{aligned} C_x &= C_d(|u|+a) \Delta x \\ C_y &= C_d(|v|+a) \Delta y \end{aligned} \quad [3-5]$$

and  $C_d$  is an adjustable damping coefficient. This damping scheme was successful in smoothing oscillations near shocks as well as across heat addition boundaries.  $C_d$  values from .01 to .1 were used with the optimum value being problem dependent.

#### Assignment of Heat Addition Distribution

In defining the heat addition distribution, it is assumed that the inflow stream height and equivalence ratio are known. This determines the total heat added which is then distributed over the heat addition zone. The heat addition zone is bounded laterally by the wall, and the streamline which emanates from a point defined by the height of the external burning stream at the inflow. The total energy input per unit time is obtained from the air flow and fuel-air ratio and is given by equation 3-6.

$$\langle \dot{Q}_{tot} \rangle = 778 \dot{m}_a \left( \frac{\dot{m}_{H_2}}{\dot{m}_a} \right) LHV_{H_2} \left( \frac{ft-lb_f}{sec} \right) \quad [3-6]$$



Where LHV is the lower heating value of hydrogen and is taken to be 52000 BTU/lb<sub>m</sub>. This total energy input must equal the integral of the assumed distribution of heat addition per unit volume over the heat addition zone. After writing the air flow in terms of freestream conditions and the inflow stream height  $y_0$ , this equality written in non-dimensional form becomes:

$$\left( \frac{\dot{m}_{H_2}}{\dot{m}_a} \right) \left( \frac{778 \text{ LHV}_{H_2}}{(u_0^2/g_c)} \right) = \left( \frac{y_b}{y_0} \right) \left( \frac{1}{y_b} \right) \int \int \frac{\dot{Q}(x, y)}{\left( \frac{\rho_0 u_0^3}{1g_c} \right)} d\left( \frac{y}{1} \right) d\left( \frac{x}{1} \right) \quad [3-7]$$

The heat addition zone is defined by the beginning and end points of the expansion surface, and the upper and lower lateral boundaries. The upper boundary is the wall, and the lower boundary is taken as the streamline starting at the inflow stream height  $y_0$  which changes as the solution marches in time. This equation is satisfied at each time step by tracking the bounding streamline and numerically integrating the heat addition distribution. A coefficient which pre-multiplies the distribution function is then adjusted such that equation 3-7 is satisfied at all times as the solution converges and the bounding streamline moves. Note that the left hand side of the equality is equal to the heat addition term in equation 2-20 which facilitates comparison between the Euler and control volume results.

### Boundary Conditions

The inflow is assigned uniform freestream conditions, and the entire flowfield is initialized to these conditions. At the outflow boundary, a zero axial gradient is specified by overwriting the solution at the outflow plane with that from the last interior column for both supersonic and subsonic regions.

The wall boundary is treated using a method suggested in reference 55 which is applicable for both supersonic and subsonic flow. First, the solution at the wall is obtained using backward differences. The velocity vector so obtained is not in general tangent to the wall, i.e. a finite normal velocity exists. This normal velocity is computed and a finite unsteady compression or expansion wave of the proper magnitude is introduced at each wall grid point such that the induced velocity of the wave is equal to and cancels the normal velocity. The conditions downstream of the wave then correspond to the corrected state variables at the wall.

The lower lateral boundary is treated using the method of characteristics extrapolation of reference 54 for supersonic points, and a simple extrapolation from the adjacent interior point if subsonic flow exists downstream of strong shocks passing through the boundary. For the free-jet boundary model, extra grid is added below the free-jet with a separate inflow at the same static pressure, a specified total temperature, and a low subsonic Mach number. The free-jet slip line is thus "captured" as

the solution develops in time. At the lower computational boundary, the velocity components are extrapolated from the adjacent interior points, and the static pressure and total temperature are set to the inflow values.

## Results

Features of a 2-D inviscid external burning flowfield with three different distributions of heat addition imposed on it will be examined first and compared to control volume analysis results. Next, the effects of grid refinement and artificial damping on the solutions are examined. Finally, the 2-D inviscid and control volume results are compared over a range of Mach numbers.

Prior to computing the relatively complex external burning flowfields, a number of test cases were run to verify that the program would properly solve a wedge-compression, a Prandtl-Meyer expansion, and a constant area heat-addition (Rayleigh) flow. These test cases are presented in appendix B.

### Effect of Heat Addition Distribution

A 15° expansion at Mach 1.4 was chosen so that results may be directly

compared to the control volume analysis of section 2. In all three cases to be presented in this section, the 80 by 40 grid shown in figure 3-2 was used with a damping coefficient of .025. The grid density was biased toward the leading edge of the expansion to resolve the relatively small inflow stream height, and the complex interactions in this region. The total heat addition is commensurate with that of the Mach 1.4 example fuel injector design given figure 2-7, i.e. an equivalence ratio of 1.00, and inflow stream height ( $y_0/y_b$ ) of .0865 are used in equation 3-7 to determine the total heat added. The heat addition zone was bounded by the beginning and end points of the expansion ramp in the axial direction, and by the wall and streamline in the transverse direction. The same total energy addition was distributed in three different ways within these boundaries. The first distribution is simply a constant over the entire area as shown in figure 3-3. The streamlines of the converged solution appear in the figure and indicate a delay in the expansion of the external burning plume which results in significant deflections in the freestream. The second distribution employed a Gaussian function in the axial direction to more closely approximate what may be expected in a real mixing and combustion situation. This distribution is depicted in figure 3-4a and causes an initial compression in contrast to the constant heat addition case. The functional form used, shown in figure 3-4b is maximum at the leading edge of the expansion, and decays to zero at the trailing edge. The third distribution shown in figure 3-5a is a variation on the second, where the Gaussian axial distribution is retained, and a parabolic variation in the transverse direction is added. The maximum is placed at the midpoint between the wall and bounding streamline. At the wall and bounding

streamline, half the maximum value is imposed. The resulting streamline pattern is very similar to that of the second case.

Mach number contours for the three cases are shown in figures 3-6 through 3-8 along with the corresponding wall Mach number and pressure coefficient distributions. For case 1 (the constant distribution) the freestream initially expands to a higher Mach number and then recompresses through an oblique shock. Following an initial expansion to Mach 1.7, a quasi-Rayleigh flow region (constant area heat addition) appears in the heated stream up to an axial station of about .2, at which point the wall Mach number is rapidly reduced to a subsonic value of about .4 through what appears to be an extension of the freestream shock. An interesting interaction thus results where the shock pressure jump imposed on the freestream boundary of the heated region accompanies an abrupt transition to subsonic flow and a stream area increase in the plume, which in turn determines the strength of the freestream shock. The pressure coefficient distribution reflects the same phenomena, an initial expansion, a region of gradually increasing pressure, and a rapid recompression. Following the recompression, the now subsonic plume transmits the pressure impressed on it by the deflecting supersonic stream directly to the wall. At the outflow plane, the freestream flow is again parallel to the inflow, and very near the inflow pressure.

The 2-D perfect gas form of the control volume analysis described in chapter II gives a thrust coefficient value (as defined in equation 2-4) of .032, while integration of the 2-D Euler wall pressure distribution

yields a force coefficient of .028. The force increment due to external burning is the appropriate parameter to compare, and for the 2-D inviscid case, a Prandtl-Meyer expansion is used as the baseline. A  $15^\circ$  expansion at Mach 1.4 results in a force coefficient of -.388. The force increment due to heat addition as predicted by the control volume analysis is thus .420 as compared to the 2-D Euler value of .416 which is about 1% lower. A summary of all 2-D Euler runs to be discussed in this section appears in table 3-1.

The Mach number contours for the case 2 heat addition distribution (Gaussian in the axial direction) are shown in figure 3-7a. In contrast to case 1, more heat is added at the corner and the heated stream is immediately driven to a .6 Mach number. The freestream is initially compressed through a shock which again coincides with the location of the supersonic-subsonic transition in the heated stream. The wall pressure then follows that impressed on the plume by the freestream which gradually expands and recompresses, exiting at the inflow pressure. Despite substantial differences in the flowfields and pressure distributions between this case and case 1, integration of the wall pressures gives the same thrust coefficient of .028.

The flowfield generated by the third heat addition distribution appears in figure 3-8. The parabolic transverse heat addition distribution obviously causes transverse Mach number gradients in the plume resulting in a curvature of the sonic line. The freestream flow is essentially identical to that of case 2. The character of the wall Mach number distribution is

also similar, becoming subsonic at about the same location, but with an increase in the overall level. The wall pressure distribution is barely discernable from that of case 2 and results in a thrust coefficient of .030 which is identical to cases 1 and 2 for all practical purposes.

The thrust coefficient is thus independent of the manner in which heat is distributed for the cases examined herein, and matches the value given by the control volume analysis. Good agreement with the control volume analysis is to be expected however, since both methods satisfy the same set of conservation equations. As long as the 2-D Euler flowfield does not severely violate any of the control volume assumptions such as linear theory on the bounding streamline, and parallel, uniform inflow and outflow, the results should be comparable. As discussed in the development of the control volume x-momentum equation (2-8), a variation in the axial distribution of heat would change the shape of the bounding streamline and the associated pressure-area integral term. Since this term was relatively insignificant, the streamline shape was approximated by a straight line, which eliminated all dependence on axial distribution from the control volume results. As evidenced by the 2-D Euler results, the shape of the bounding streamline is affected by changes in the heat addition distributions, but is of little consequence in terms of the thrust coefficient.

Other parameters which can be compared on a less exact basis are the control volume area ratio and outflow velocity. The control volume area ratio given by equation 2-13 is 13.2. From the streamlines in figures 3-3

through 3-5 it is apparent that the heated stream in the Euler solutions expands by about this amount. Equation 2-9 indicates that the outflow velocity will be higher than inflow for positive thrust coefficients. For this particular case, an outflow to inflow velocity ratio of 1.19 is given. Velocity profiles for the Euler solutions at the ramp trailing edge station are plotted in figure 3-9 for all three heat addition distributions along with a line representing the control volume value and exit plane stream height. The profiles are not uniform, but do exhibit velocities higher than the inflow velocity with a mean value near 1.19.

The 2-D Euler results compare well both qualitatively and quantitatively to the control volume analysis despite non-uniform outflow, and non-linear shock waves on the plume boundary. The independence of thrust coefficient to changes in heat addition distribution is primarily an inviscid phenomena. The sharp recompressions seen as the heated stream transitions to subsonic flow may induce boundary layer separation, which would prevent high pressure on the wall surface. The interaction between the heated and unheated streams which caused the sharp recompression in all three cases may be a limiting factor in actual practice.

#### Effect of Artificial Damping

Artificial damping was required to stabilize the solutions, and a question naturally arises as to the effect of the added damping terms which are related to viscous effects on the converged solutions. Only in very few



cases would a solution converge without a non-zero damping coefficient as defined above in equation 3-5. The results of the previous section were all run with a  $C_d$  value of .025. The case 2 heat addition above was chosen as the baseline, and the solution was repeated on an identical grid with the damping coefficient halved, then doubled. The solution would not converge with zero damping. Mach number contours for the three cases are shown in figure 3-10. The most obvious effects are an increase in the thickness of the plume boundary as damping is increased, and an increase in pre-shock oscillations at reduced damping. The wall pressure and Mach number distributions showed little effect of changes in damping. The thrust coefficients were also very similar being .034, and .029 for the minimum and maximum damping cases respectively. Overall, damping coefficients of this magnitude have only a superficial effect on the thrust coefficient.

#### Effect of Grid Refinement

All of the preceeding results were run on the 80 by 40 grid shown in figure 3-2. Increasing the grid density results in longer run times per time step, and requires more time steps to converge. It is of interest therefore to determine the minimum adequate grid density. In the transverse direction, there must be a sufficient number of nodes near the wall to resolve the heat addition distribution and bounding streamline for the heated stream, which for the previous cases is only .087 base heights wide at the inflow plane. Also, the thickness of the plume boundary is a

number of grid spacings wide depending on the amount of damping used. This boundary will appear to be artificially thick on sparse grids although this does not seem to affect the thrust coefficient considerably. In the axial direction, sufficient grid is required near the beginning of the expansion to resolve steep gradients caused by the wall angle and heat addition. The effect of grid density on the computed flowfield is seen in figure 3-11 where Mach number contours are plotted for 50 by 25, 80 by 40, (figure 3-2) and 100 by 50 grids. The damping coefficient of .025, and the grid distribution seen in figure 3-2 were held fixed. The shock wave in the freestream, and the plume boundary both appear to get thinner as grid density increases since they are spread over a fixed number of nodes. Wall pressure distributions shown in figure 3-12 show some differences at the expansion corner. The 50 by 25 grid does not resolve the initial expansion as well as the others, and this is reflected in the slightly higher thrust coefficient value seen in table 3-1. Also note that the 100 by 50 grid yields a .414 change in thrust coefficient which is 1.4% lower than the control volume value. The 80 by 40 grid gives a .416 change in thrust coefficient which is comparable to the fine grid result and is considered adequate for this class of problems.

#### Effect of Freestream Mach Number

Euler results at selected points along a 1000 psfa trajectory were run with the 80 by 40 grid, .025 damping coefficient, and case 2 heat addition distribution. The total heat added is commensurate with the results in

figure 2-7 for the example fuel injector geometry at constant fuel conditions. Figure 3-13 includes Mach number contours at four different freestream Mach numbers along the trajectory. The increase in the number of contour lines as Mach number increases is caused by the contour increment being held constant at .05. The most prominent effects of increasing freestream Mach number are the steepening of wave angles, and the coalescence of waves at the trailing edge of the ramp as the plume is turned back to the axial direction. Wall Mach number and pressure distributions appear in figures 3-14 and 3-15 and show that at Mach 2.4, the plume is actually slightly supersonic just upstream of the corner and a weak shock wave forms. A sharp reduction in Mach number occurs near the leading edge of the expansion in all cases, which is coincident with the recompression seen in the pressure distributions. The peak pressure moves downstream slightly as freestream Mach number increases consistent with the sonic point in the plume. In figure 3-16, the thrust coefficient is plotted versus freestream Mach number along with the control volume results of figure 2-5c. The two methods of analysis agree well over the entire range, demonstrating the validity of the control volume approach which completely disregards the complex flowfield details brought out by the Euler analysis.

#### Euler Analysis Summary

The 2-D Euler equations with an external heat addition term retained in the energy equation were used to model drag reduction by external burning

on an expansion surface. The equations with artificial damping terms added, were solved using MacCormack's time-marching, finite difference technique. Three different spatial distributions of a constant total heat addition were imposed on a Mach 1.4 freestream flowfield. The thrust on the expansion surface determined by numerical integration of the wall pressure distribution was independent of the heat addition distribution and agreed well with the value given by the control volume analysis. Grid refinement and reduced artificial damping had the expected effect of reducing the thickness of the plume boundary and shock waves, but had little effect on the thrust coefficient. A sharp pressure rise in the heated stream at the sonic line was noted for all three distributions of heat addition. This is caused by an interaction of the elliptic region of the plume with the supersonic freestream and may be a limiting factor in external burning performance since viscous effects may cause the plume to separate from the wall surface before the maximum inviscid pressure is reached. Control volume results showed excellent agreement with the Euler analysis over the range of freestream Mach numbers from 1.2 to 2.4, which substantiates some of the simplifying assumptions used in the control volume analysis such as linear theory on the bounding streamline, and uniform outflow.

## CHAPTER IV - EXPERIMENTAL PROGRAM

### Background

The performance potential demonstrated by the control volume and Euler analysis warranted a series of preliminary proof of concept experiments that are the subject of this chapter. One of the objectives of the experimental program was to prove that the external burning of hydrogen would reduce drag on a simple expansion ramp at transonic flight conditions and to provide data for comparison to control volume analysis results. The external burning concept originally envisioned by the author employed the combination spraybar-flameholder pictured in figure 4-1. Recall the control volume analysis result from chapter II that the specific impulse performance was greatest at low equivalence ratio, and high inflow stream height. Use of a spraybar to fuel the inflow instead of relying solely on jet penetration would provide for independent control of the inflow stream height without reliance on jet penetration from the wall, making a lower equivalence ratio, higher performance system more feasible. This arrangement would also provide a more uniform fuel distribution and a flameholding point out in the stream. The spraybar would be deployed transonically, and inject  $2/3$  of the total fuel normal to the freestream in both directions. The remainder of the fuel would be injected from the wall.

An important precursor to an external burning test however is stable

combustion. Further, combustion must be initiated at the proper location, and must be complete within an appropriate length. Heat release far behind the aircraft or test article would be of little value in the reduction of drag. Hydrogen is not widely used as a heating or aviation fuel and does not have as substantial a flame stability database as hydrocarbon fuels. The low pressure and temperature, and high velocity conditions existing in the region where external burning is to be employed led to flame stability concerns. Another objective of the experimental program was thus to study the combustion characteristics of hydrogen and air in the external burning environment.

The experiments were conducted in a 12" diameter, Mach 1.26 free-jet over a range of freestream pressures and temperatures. This particular Mach number was chosen due to the availability of the free-jet nozzle. The preliminary nature of this test program did not warrant fabrication of new nozzles. A complete description of the test facility appears in a subsequent section. Given the 12" exit diameter in which to work, an approximately 1/50 scale expansion ramp model representing the entire aft-end of a single-stage-to-orbit vehicle was constructed complete with the spraybar. This model was to provide results for comparison to the control volume predictions. Preceding tests of this model, a 1/5 scale section of the spraybar only was tested to obtain the flame stability information.

The 1/50 scale expansion ramp model was plagued by problems with silver-soldered joints used to fabricate the tiny spraybar as the gaseous hydrogen fuel did not provide sufficient cooling. The model also caused

unsatisfactory operation of the free-jet due to high blockage. In hindsight, the low equivalence ratio spraybar design philosophy was not practical at least for the small scale models tested. Flame stability considerations also tended toward a stoichiometric design for which jet penetration from the wall is adequate. Given this and other practical problems associated with the spraybar concept such as cooling, drag, and actuation, it was abandoned in favor of a wall injection scheme. Redesigned expansion ramp models were subsequently fabricated and tested successfully. The spraybar geometry used in the flame stability tests was related to the abandoned concept, however it was sufficiently generic that the data obtained was used to verify and extend existing stability correlations to the sub-atmospheric, non pre-mixed, transonic conditions of present interest.

#### Hydrogen-Air Flameholding Previous Work

Flame stability, although not the primary focus of the present work, is crucial to the successful application of external burning. The intent of the following discussion is to review the flameholding process and define the envelope of flight conditions within which external combustion is feasible using the available data and correlations of previous workers. This provides the rationale for the preliminary flame stability tests in the present work.

Flame stability is important in a wide variety of applications as

evidenced by a review of the flameholding literature which reveals a bewildering array of publications covering a wide variety of applications from heating systems to aircraft propulsion. Since the main interest of the present work is the practical application of this technology to the external burning problem, the discussion which follows focuses on appropriate empirical results in lieu of the complex details of flameholding physics. The objective is to understand the important parameters in the combustion stability limits of an unmixed hydrogen-air system at transonic altitude conditions.

A simple observation made in 1955 by Zukoski and Marble<sup>56</sup> provides a basis for the study of the flame stability afforded by a bluff-body or flameholder which generates a recirculating region of hot combustion products in its wake:

"If  $V$  is the free stream velocity and  $L$  the length of the recirculation zone, then the ratio  $L/V$  is a measure of the time which the fresh gas spends in the neighborhood of the hot combustion products. In fact, the critical time  $\tau$  required for ignition of the free stream is given by

$$\tau = L/V_{B.O.} \quad [4-1]$$

where  $V_{B.O.}$  is the measured blowoff velocity."



Experimental data is presented for a stoichiometric mixture of gasoline vapor and a number of different flameholder shapes which supports Zukoski's conclusion that the ignition delay time  $\tau$  is independent of gross fluid dynamic features and depends on the speed at which the chemical reactions takes place.

"The similarity parameter describing the stabilization phenomenon is thus  $V\tau/L$  and in particular the blowoff condition is described by the value

$$\frac{V_{B.O.}\tau}{L} = 1 \quad [4-2]$$

The chemical and fluid dynamic effects are separated into  $\tau$  and  $L$  respectively. The usual dependence of blowoff velocity on the flameholder size follows immediately from the behavior of  $L$  and hence is determined by the fluid dynamics."

The bulk of all data correlations and more sophisticated analytical models are rooted in this simple explanation of the flameholding process. Restricting attention to hydrogen and air, the first comprehensive experimental results found by this author was the work of Dezubay<sup>57</sup> in 1954. Dezubay's experiment consisted of a 1.32" diameter glass tube in which disk flameholders of various diameters were concentrically strut-mounted. A pre-mixed stream of air and gaseous hydrogen flowed through

the glass tube with flame initiated in the wake of the disks. Tests were carried out at static pressures of 2 to 6 psia and ambient total temperature giving a range of subsonic velocities. At a desired test condition, the fuel air ratio was varied to establish both lean and rich stability limits. The stability map so obtained is reproduced in figure 4-2 where the fuel-air ratio at blowout is correlated with velocity, pressure and disk diameter. The ratio of velocity to diameter which appears is consistent with Zukoski's argument except for the .74 exponent on the disk diameter which Dezubay justifies on a theoretical basis. Dezubay's parameter also contains the static pressure which is of interest in relating these results to altitude conditions. As a flight vehicle climbs and accelerates through the transonic flight regime, the conditions for flameholding become more severe due to increasing velocity and decreasing pressure. In figure 4-3, lines of constant  $V_0/P_0^{.61}$  which is the Dezubay correlating parameter for a 1" diameter disk are superimposed on a trajectory map to give a first indication of the operability of external burning. From figure 4-3 a value of 800 is the most severe condition at which flameholding is possible for slightly fuel-rich conditions. For the high altitude 500 psfa trajectory, this limit is reached at about Mach 1.4, and at about Mach 2 for the low altitude 2000 psfa trajectory shown. Obviously these limits are extended by use of a larger flameholder, but a pressure limit of 2 psia (45000 ft.) should also be recognized below which combustion may not be feasible no matter what size flameholder is used. No experimental information on hydrogen-air combustion at pressures less than 2 psia was found except for some high altitude ramjet combustor data at 1.7 psia<sup>58</sup> but very low velocity compared to the present situation.

The preceding extrapolation of Dezubay's results to the present problem is tenuous for a number of reasons. First, the correlation data were all subsonic and the extension to supersonic flow is not obvious. Secondly, the fuel and air will not be pre-mixed at a carefully controlled ratio. The hydrogen will be injected into the air at some distance upstream of the flameholder. Finally, the flameholder used in practice will probably be two-dimensional and of much larger scale requiring a correlation between the recirculation zone lengths of circular and two-dimensional shapes.

The work of Winterfeld<sup>59</sup> provides some information on the issues of supersonic velocity and non pre-mixed flow. Winterfeld's test apparatus consisted of rotationally symmetric flameholders mounted concentrically in a Laval nozzle with the flameholder base coincident with the nozzle exit. Initial tests were in a pre-mixed hydrogen-air stream with a cylindrical flameholder of 6 mm diameter mounted concentrically in a nozzle of variable area ratio from 1.0 to 1.7 giving a range of flow velocities from subsonic to supersonic. Since all tests with this apparatus were conducted at atmospheric pressure and with a constant flameholder diameter, results were presented in terms of the flow velocity and the "air ratio" which is the inverse of fuel-air equivalence ratio. The stability limit determined by Winterfeld is easily put in terms of Dezubay's stability parameter and appears with Dezubay's limit in figure 4-4. Winterfeld's pre-mixed result shows stability to lower fuel-air ratios than that of Dezubay, and to a flow velocity of 1770 feet per second. The maximum flow velocity and rich limits were not obtained due

to facility limitations. Dezubay's results were apparently unknown to Winterfeld at the time and so the reasons for this discrepancy are not discussed. The obvious differences between the two experiments are the higher static pressure and supersonic flow used by Winterfeld, and differences in the flameholder geometry and mounting arrangement. The disks represent a larger effective blockage than a cylinder of equal diameter. Also, the cylindrical flameholder base was coincident with the nozzle exit while the disks were completely enclosed. Despite these differences, Winterfeld's results provide confidence to apply Dezubay's correlation at supersonic speed.

Another series of experiments reported by Winterfeld in reference 59 examined the flameholding characteristics of hydrogen diffusion flames. The apparatus used for these experiments was similar to that discussed previously, only somewhat larger with all of the fuel injected by the flameholder itself. Flameholder diameters of 10, 20 and 30 mm were tested at a Mach number of roughly 2.1 in a Laval nozzle of 115 mm exit diameter (the different diameter flameholders resulted in a slight Mach number variation). Again, all tests were conducted at ambient total temperature, and roughly 1 atmosphere pressure. Hydrogen fuel was introduced near the base through an annular slot. Injection angles of  $90^\circ$  (perpendicular to the freestream),  $45^\circ$ , and  $0^\circ$  (parallel to the freestream injected directly into the base region) were investigated. The recirculation zone gasses were sampled with and without flame to infer the fuel-air ratio at flameout. The ratio of measured recirculation zone length to freestream velocity and the air ratio were used as correlating parameters.

Winterfeld reports that at the lean limit, the  $L/d$  of the recirculation zone for the cylindrical flameholder is 2 for both parallel and normal fuel injection. This allows the results to be cast once again in terms of the DeZubay parameter and included in figure 4-4. The lean stability limit for the diffusion flame is nearly coincident with DeZubay's pre-mixed data.

Winterfeld's results, for pre-mixed and diffusion flames help to reinforce the extrapolation of DeZubay's correlation to the present conditions of figure 4-3. However, no hydrogen-air experimental data could be found to relate the characteristics of two-dimensional flameholders to the axisymmetric shapes discussed above. Some insight can be gained however by recalling the argument of Zukoski and Marble that the important parameter is the length of the recirculation zone, and that this is determined by the fluid dynamics. In reference 56 Zukoski and Marble provide data for a circular cylinder mounted transverse to the flow. The measured wake lengths correlated with the square root of the cylinder diameter for diameters from .19" to 1" and approach flow velocities from 100 to 650 feet per second. For approach flow velocities in excess of about 300 feet per second, the value of  $L/D^{1/2}$  was constant at 6.5. The curious square root dependence was attributed to boundary layer separation upstream of the diametral plane which is Reynolds number dependent, and blockage in the 4" high passage across which the cylinders were mounted. Another series of tests were run on an axisymmetric cone-cylinder and a two-dimensional wedge-plate of thickness equal to the cone-cylinder diameter. These results showed little Reynolds number dependence and

indicated that wake length was proportional to cylinder diameter or plate thickness, and that the measured  $L/D$  of 2.3 was the same for both the axisymmetric cone-cylinder and the transversely mounted plate. These results suggest that a two-dimensional flameholder will have stability characteristics similar to a disk of diameter equal to the two-dimensional flameholder's height.

All of the work discussed in the preceding paragraphs gives confidence that hydrogen-air flame stability will not preclude the successful application of external burning to the transonic drag problem. No one experiment however is directly applicable to the current situation of a two-dimensional, non pre-mixed, supersonic flow at sub-atmospheric pressure. It is for this reason that preliminary flame stability tests were conducted in the present test program.

#### Facility Description

The experimental program was conducted in cell 4 of the Propulsion Systems Laboratory (PSL-4) at the NASA Lewis Research Center. PSL-4 is 25 foot diameter cylindrical altitude chamber used for full-scale direct-connect turbine engine testing. Large continuous flow compressors and exhausters, located in a separate central air equipment building adjacent to PSL, supply high pressure air and altitude exhaust capability to the facility making it ideal for operation of a free-jet. The high pressure air or

"combustion air" system which normally supplies air to the turbine engine test article has recently been modified<sup>60</sup> to provide even higher pressure and temperature conditions representative of a Mach 5 compressor face condition. This was accomplished by augmenting the original heat-exchanger type air heater with a hydrogen-air burner and oxygen make-up. Downstream of the burner, a 4 foot diameter, approximately 8 foot long water-cooled flow conditioning duct is used to reduce distortion upstream of the test article. The free-jet used for the present tests was bolted to the end flange of the flow conditioning duct. Figure 4-5, taken from reference 60 is a cut-away drawing showing the hypersonic modifications. The free-jet was installed in place of the "hot pipe" which was an initial facility calibration test article. Safety considerations dictated that approximately 75 pounds per second of secondary air be admitted into the altitude chamber at the forward bulkhead for the purpose of test cell cooling and dilution of unburned hydrogen. All freejet and secondary air was exhausted from the test cell through a 55" diameter duct, concentric with the free-jet near the aft end of the chamber.

The desired transonic test conditions did not require operation of the hydrogen-air heater, although all of the free-jet air did pass through burners which placed an upper limit on the air flow of about 100 pounds per second. The original heat-exchanger was used during the present tests to elevate the free-jet air total temperature from nominally 540° R to about 1000° R during selected runs. The free-jet used was an existing 12" exit diameter, Mach 1.26, conical nozzle previously calibrated in the NASA Langley Mach 4 engine test facility<sup>61</sup>. It was instrumented with three

static pressure taps equally spaced circumferentially at both the throat and exit. During normal operation, the free-jet supply pressure was set so that the average free-jet exit static pressure matched that of the altitude chamber. Although altitude chamber pressure and free-jet supply pressure were controlled separately, it was possible to maintain the matched condition at the free-jet exit to within .05 psia. The free-jet installation was capable of providing a range of test conditions from 4 to 12 psia.

Hydrogen fuel was supplied by high pressure tube trailers located outside the building. Fuel pressure at the free-jet was controllable from 50 to 400 psia, at a nominal temperature of 520°R. A fuel-rich hydrogen-air preburner was used during initial tests to preheat the fuel to 1500°R at equivalence ratios of approximately 13. Operational problems with this system precluded its use for the most of the test program.

#### Spraybar Test Apparatus and Procedure

The test articles were a 5/8" diameter section of spraybar-flameholder which spanned the entire 12" free-jet exit. Figure 4-6 is a photograph of one of the spraybar models mounted horizontally across the free-jet exit. The 5/8" diameter corresponded to approximately 1/5 scale based on preliminary sizing calculations for a fuel-lean spraybar injection system. Figure 4-7 is a three-view drawing showing details of the spraybar. The cylindrical leading edge and flat trailing edge cross-section was



maintained over the entire 12" but only the center 6" was drilled with fuel injection orifices. The original mechanical design was based on a 5/8" diameter stainless steel pipe to which stainless steel fairings were brazed at the diametral plane extending downstream to form the desired base geometry. This method of construction proved to be unsuitable with the combination of heating and thermal expansion quickly causing failure of the brazed joints. The models were subsequently redesigned, being machined from a solid block of stainless steel to the cross-section shown in figure 4-7 with the two 90° elbows welded on.

#### Equivalence Ratio Estimate

In reducing the flameholding data, a key parameter is the fuel-air equivalence ratio. For situations where known quantities of fuel and air are pre-mixed far upstream of the flameholder, this parameter is easily calculated. For non pre-mixed or diffusion flames, gas sampling of the wake can be used to infer the fuel-air ratio at flameout as was done in reference 59. For the present case, gas sampling equipment was not available so a different approach was taken. From the control volume analysis, the parameters of importance in external burning are the inflow air stream height, and the overall equivalence ratio in the external burning stream. To size fuel injection orifices a method of estimating equivalence ratio based on fuel jet penetration was described in chapter 2. The same method will be used here with the understanding that it is more an estimate of the overall amount of fuel and air involved in the

external burning process, than a measure of the actual fuel-air ratio in the wake of the flameholder. It should therefore be thought of as a correlating parameter for the flame stability results, and not a measured quantity.

The "penetration times spacing" method previously described will be outlined here for convenience. The fuel flow is simply determined for the choked injector at a given fuel pressure, temperature and flow coefficient. For the spraybar with pilots, the appropriate amount of pilot fuel is included. The air flow involved is estimated based on freestream conditions and a flow area defined by the jet penetration times the orifice spacing. The jet penetration is determined by a correlation which gives the height above the injection plane where the hydrogen concentration is 1/2% by volume in terms of the fuel pressure, freestream conditions and the distance downstream of the orifice. The distance downstream of the orifice at which to calculate the jet penetration is somewhat subjective, but again does not diminish the methods usefulness as a correlating technique.

#### Fuel Injector Sizing

A total of 6, .10" diameter main orifices injected fuel normal to the freestream in both directions. Note the offset between the three upper and three lower orifices in figure 4-7. The orifice size and spacing were designed to give fuel-air equivalence ratios in the fuel-lean range based

on the penetration times spacing estimate. The spraybar pictured in figure 4-7 had 15, .020" diameter pilot orifices which injected approximately 10% of the fuel directly into the wake. A spraybar without these pilot orifices was also tested. Given a range of freestream pressures from 4 to 12 psia, and fuel pressures from 50 to 400 psia, operating envelopes can be constructed in terms of the estimated equivalence ratio and the DeZubay stability parameter. These operating envelopes are pictured in figure 4-8 for different values of  $x/d^*$  which is a free parameter in the jet penetration correlation, and free-jet total temperatures of 540° and 960° Rankine. Ambient temperature fuel, and an orifice flow coefficient of .8 was assumed in all cases. Within a given envelope, increasing fuel pressure increases the equivalence ratio along a vertical line. Increasing altitude (reducing static pressure), increases the value of the DeZubay stability parameter. The effect of increasing the assumed  $x/d^*$  is to increase the value of jet penetration used to define the air flow in the equivalence ratio estimate (see equation 2-27). This increase in air flow at constant fuel flow reduces the equivalence ratio proportionately. Fortunately, the jet penetration depends on  $x/d^*$  to approximately the 1/4 power, so that a large variation in the assumed  $x/d^*$  has relatively little effect on the estimated equivalence ratio. This is demonstrated in figure 4-8 where  $x/d^*$  is increased by a factor of 4, and the maximum equivalence ratio is reduced by 47%. For the spraybar with no pilot injectors, the calculated equivalence ratios are reduced by 10%.

### Instrumentation

To define flame stability limits, only the freestream and fuel conditions need be known, along with some way of determining when the barely visible hydrogen-air flame extinguishes. The freejet nozzle throat and exit were instrumented with three static pressure taps each, equally spaced circumferentially. Total pressure and temperature were measured at three points on the large flange visible in figure 4-6 to which the freejet was attached. An open 1/16" stainless steel tube was strapped to the spraybar base to measure base pressure.

An infra-red video camera, mounted inside the altitude chamber had been used previously to monitor the surface temperatures of turbojet engine components. For the present investigation, the camera was mounted so as to look through the external burning plume. The field of view obtained with the wide angle lens used is depicted in figure 4-9. The 2.0 to 5.6 micron indium-antimonide detector in the camera provided a good image of the 2.6 micron water vapor emission in the external burning plume. This was the primary method used to determine flame-out.

A schlieren system was set up inside the altitude chamber in close proximity to the free-jet providing the 6" by 12" field of view also shown in figure 4-9. Vibration, test cell cooling air flow, and altitude conditions resulted in a rather severe environment for the sensitive schlieren optics and xenon light source. In spite of numerous difficulties, useful information was obtained from the system during much

of the test program.

A water-cooled probe was used to obtain total temperature profiles 18" downstream of the free-jet exit. The probe had a single iridium-40% rhodium vs. iridium thermocouple of bare wire in crossflow construction. An electric screw-type actuator provided 10" of travel allowing measurement from 8 inches below the free-jet axis to 2" above as shown in figure 4-9. The data reduction scheme for this measurement is included as appendix c.

A color video camera with remote pan, tilt, and zoom provided a good overall view of the experiment looking upstream from above the free-jet.

#### Ignition System

Ignition was accomplished during initial tests by strapping a ceramic insulated electrode to the flat base of the flameholder. This electrode was connected to a 10,000 volt continuous transformer arcing directly to the spraybar. The insulated electrode often burned away following ignition prompting the installation of a translating spark plug arrangement. Both ignition systems are visible in Figure 4-6. The long vertical tube is the translating ignitor shown in the extended position. The tube itself acted as the ground electrode, and contained the high voltage electrode which arced against it at the tube end. Following ignition the tube was withdrawn completely out of the free-jet flow by a

pneumatic cylinder. The .060" spark gap was positioned approximately 1/8" downstream of the spraybar base at the elevation of the upper surface.

### Test Procedure

The test cell pressure was set first to the desired level, then free-jet supply pressure was increased to the calculated value of stagnation pressure for an isentropic Mach 1.26 flow. The stagnation pressure was then adjusted slightly so as to match the measured average free-jet exit static pressure to the test cell pressure. With the free-jet on-design, the fuel-rich hydrogen-air preburner was ignited producing fuel conditions of approximately 1500° Rankine and 350 psia. Model ignition was then attempted with the spark ignitor. Following ignition the air supply to the fuel preburner was shut off and the fuel temperature quickly dropped to ambient. Ignition of the model in this manner was only possible at a free-jet exit static pressure of 10 psia or greater, and even then was not assured. Tactics such as varying the preburner air supply pressure thus varying the unburned fuel fraction and temperature, and cycling the ignitor actuator to change the spark location were often used to achieve ignition. A catastrophic failure in the preburner fuel-air valving system during the spraybar tests prevented its use for the rest of the program. Without hot fuel, an alternate method of ignition was adopted in which the free-jet stagnation pressure was reduced until the free-jet exit Mach number based on the exit static pressures was about 0.8. Ignition of ambient temperature fuel at the subsonic Mach number was much more

consistent and was used for the remainder of the program.

Following ignition of the spraybar, the free-jet supply and test cell pressure were adjusted simultaneously to the desired altitude condition with fuel pressure at or near the maximum available. This corresponds to moving along the maximum fuel pressure line on the operating maps of figure 4-8. As stated earlier, the free-jet supply and test cell pressures were controlled independently by separate personnel. During the altitude change process the free-jet did stray off-design, sometimes causing instabilities and flame-out. In general, once the desired altitude condition was set with the free-jet on-design, fuel pressure was reduced slowly, reducing the equivalence ratio at a constant value of the DeZubay parameter until flame-out occurred.

## Results

### Spraybar Base Pressure Measurements

During initial runs with the spraybar installed in the free-jet, a terminal shock appeared in the schlieren image downstream of the spraybar. This was not unexpected at the Mach 1.26 freestream condition, however the shock position did change as the free-jet strayed off-design, prompting interest in the sensitivity of the spraybar base pressure to the free-jet exit pressure ratio, since pressure affects flame stability. Figure 4-10 shows schlieren images of the free-jet operating slightly overexpanded,

on-design, and slightly underexpanded. The terminal shock is seen clearly on either side of the spraybar wake. The schlieren knife edge was oriented horizontally resulting in the apparent lack of symmetry from top to bottom. In figure 4-11, the effect of shock movement on the spraybar base pressure is shown. The base pressure is three-tenths of the free-jet exit pressure and is insensitive to shock movement for on-design and underexpanded conditions. The base pressure rises sharply however as the free-jet becomes overexpanded and the shock moves upstream. As a result, a rather tight tolerance was put on the acceptable operating condition for the free-jet. Except for cases where the free-jet was deliberately operated off-design, and during altitude changes, all of the spraybar and expansion ramp tests were run at free-jet exit pressure ratios of between .99 and 1.01. The back pressure for the terminal shock then is the same as the free-jet exit pressure, and this was deemed to be most representative of a flight condition.

The effect of combustion on the base pressure is shown in figure 4-12. External burning increases the pressure ratio to about .7 regardless of altitude or fuel pressure. Although not the purpose of the spraybar tests, this represents a significant reduction in the drag of the spraybar or any other two-dimensional step flameholder which may be employed.

### Flame Stability

Conditions at which the flame extinguished appear in figure 4-13 for the



piloted spraybar, in terms of the penetration times spacing equivalence ratio and the DeZubay stability parameter. An  $x/d^*$  of ten was used to calculate the equivalence ratio, and the corresponding operating envelope is also shown. No flame-outs occurred at 12 psia at the minimum fuel pressure. Filled symbols denote flame-outs that occurred at high fuel pressure during an altitude change. Since the free-jet design condition could not be maintained during this operation, these points are somewhat anomalous but are included for completeness. The flame-out points fall in a band somewhat outside the DeZubay pre-mixed stability boundary. This is not unexpected since as discussed earlier the penetration times spacing equivalence ratio may not accurately represent the local fuel-air ratio in the base which controls flame stability.

Even without detailed knowledge of the local equivalence ratio, this result provides confidence in the DeZubay correlation for external burning conditions. A non pre-mixed, two-dimensional system can be expected to work at altitude to values of the DeZubay parameter in excess of 800 at stoichiometric or slightly fuel-rich conditions. For a fuel-lean system, operation would be limited to lower values of the DeZubay parameter. In the design of a flight system, the extra stability margin afforded by stoichiometric operation must be weighed against the performance benefit of fuel-lean operation shown by the control volume analysis. For small-scale drag reduction experiments where the flameholder dimension is disproportionately large to begin with, a stoichiometric system is desirable.

The spraybar without pilot orifices was tested in the same manner with ignition at subsonic speed and ambient temperature fuel. Despite repeated attempts, flame-out always occurred near Mach one as the free-jet supply pressure was increased toward the supersonic design value.

#### Effect of Elevated Free-Jet Temperature

A flame-out that occurred at elevated freestream temperature at 6 psia is also shown on figure 4-13. For static pressures of 8 psia and greater the flame was stable down to the minimum fuel pressure with no flame-outs. Curiously, repeated attempts to set a 4 psia condition at maximum fuel pressure resulted in flame-out. The 4 psia condition at 960° R represents the lowest Reynolds number tested being about 2.7 million per foot as well as the lowest free-jet mass flow. Control of the free-jet during altitude changes near these minimum flow conditions was difficult. Off-design excursions and reduced fuel-air mixing rates probably both contributed to these high fuel pressure flame-outs. Note that the operating envelope shown in figure 4-13 applies only to the 540°R points; refer to figure 4-8 for the 960°R envelope..

The DeZubay parameter contains no explicit temperature dependence, so one would not expect it to correlate data with varying temperature. The effect of higher temperature is to increase the rate at which the chemical reactions take place thereby reducing the ignition delay time. Based on the arguments presented earlier this translates into a higher freestream

velocity at flame-out for the same size flameholder. Thus, the stability limit at elevated temperature should occur at greater values of the DeZubay parameter. Since the total temperature in flight during an acceleration through the transonic regime will increase with increasing velocity, a limit based on data at ambient total temperature is conservative. The DeZubay parameter is therefore still considered acceptable for the external burning situation.

#### Scaling of Small-Scale Test Results

In anticipation of the smaller scale drag reduction experiments which were conducted following the spraybar flame stability tests, an attempt was made to determine whether or not sub-scale experimental results would be adversely affected by the finite rate at which hydrogen and air react. Knowledge of "chemical kinetics" as it affects ignition and reaction delay is important in assessing any small-scale external burning test result since these characteristic times depend on fuel type, fuel-air ratio, pressure and temperature but do not vary with model scale. A one millisecond ignition delay at the freestream velocity will correspond to a greater fraction of the model length at small-scale than at full-scale. This could lead to unrealistically poor performance and flame stability problems at the model scale. For the present case of non pre-mixed hydrogen and air streams, the rate of fuel-air mixing also plays an important role in the combustion process and is properly modeled by matching the Reynolds number. If the delay caused by the reaction

kinetics is insignificant compared to that resulting from fuel-air mixing, the process is said to be "mixing limited". For a mixing limited situation, sub-scale results would be similar to full-scale at the same Reynolds number. A common practice in combustor testing is to use full scale hardware (at least in the axial direction) thus making scaling or correction for chemical kinetics effects unnecessary. Full scale testing of the entire aft end of a flight vehicle is impractical however, especially in the 12" diameter free-jet available. In the interest of determining whether or not the spraybar tests were mixing limited, infrared images of the plume at elevated free-jet temperature and pressure can be compared to images at the same Reynolds number, but reduced temperature and pressure. The fuel-air mixing process should be similar for the two conditions, so a difference in the plume characteristics can be attributed to non-equilibrium reaction effects. If the images show comparable axial distributions of hot water vapor, the process can be considered mixing limited as long as the difference in freestream pressure and temperature was sufficient to appreciably alter the reaction rates.

A free-jet exit static pressure of 12 psia at a total temperature of 960°R results in a unit Reynolds number of 4.9 million per foot. The same Reynolds number occurs at a static pressure of 6 psia and total temperature of 540° R. To confirm that the difference in reaction rates between the two test conditions is adequate to alter the plume if the process is not mixing limited, reference is made to the work of Bahn<sup>62</sup> who studied the effects of pressure, temperature and fuel-air ratio on hydrogen-air kinetics. Bahn's analytical approach involved 25 reactions

and was used to compute ignition delay and time to complete reaction. The ignition delay was defined as the time to maximization of  $\text{HO}_2$  which was found to play an important role in the ignition process. The time to complete reaction was defined arbitrarily as the time it takes for the reaction to proceed to a temperature of  $2200^\circ\text{K}$ . The lack of a strict definition is of little consequence however since the complete reaction occurs almost instantaneously following ignition. The calculations were carried out at constant pressure for given initial temperatures and fuel-air ratios.

For the present purpose of estimating the difference in reaction time between two test conditions, the pressures are relatively well defined as 6 and 12 psia, but the appropriate initial temperature and fuel-air ratio are not. Fortunately, the effect of fuel-air ratio was found to be small for equivalence ratios from  $1/4$  to 4. If the free-jet total temperature is assumed for the initial mixture temperature, an unrealistically long ignition delay would be predicted. In fact the lowest initial temperature reported by Bahn was  $650^\circ\text{K}$  ( $1170^\circ\text{R}$ ) for which the computed ignition delay is over eight minutes. The appropriate initial temperature must obviously be nearer that of the flameholder recirculation zone since ignition and reaction did occur just downstream of the spraybar. Using an average free-jet velocity and a distance of one foot gives a time increment of about .8 millisecond for which an appropriate initial temperature according to Bahn's charts would be about  $1000^\circ\text{K}$ .

In the pressure and temperature regime of present interest, the effect of

pressure is not clear. A "double reversal" occurs near one atmosphere where increasing pressure causes a sharp rise in the ignition delay time. At higher or lower pressure the usual trend of reduced ignition delay with increased pressure applies. The doubling of freestream pressure from 6 to 12 psia therefore cannot be relied on to reduce the ignition delay. The effect of temperature however exhibits no such reversal, and a 100°K increase in initial temperature, results in roughly an order of magnitude reduction in ignition delay time. The reaction length should be significantly shorter than at the elevated free-jet temperature. If the combustion process is not mixing limited, i.e. if the reaction length is significant compared to the distance required for mixing, combustion will appear further upstream.

Before examining the infra-red images, a brief explanation of the calibration method will be given. The infra-red signal generated by hydrogen-air combustion products in the 2 to 5.6 micron detector range is largely due to hot water vapor which emits at a wavelength of 2.6 microns. The amplitude of the signal depends on the molar density, temperature, and emittance of the water vapor as well as the path length or thickness of the plume. The infra-red imaging system which consisted of the video camera and a processor records and displays temperature contours over the entire field of view based on a single emittance input by the user. This is an adequate approach for mapping the surface temperature of a gray body but is not suitable for measuring gas temperatures. The emittance of the plume at 2.6 microns varies with temperature so a single representative emittance which would properly convert the radiation signal into

temperature does not exist. The approach taken was to record the images with the emittance set to one, then calibrate the temperatures using total temperature data from the water-cooled probe. Measured temperature profiles were compared to temperatures reported by the camera at the same locations. The minimum and maximum temperatures reported by the camera were assigned the measured minimum and maximum temperatures resulting in a linear mapping between camera temperature and actual gas temperature. This mapping was then applied throughout the entire field of view. This approximate approach implies a one to one correspondence between the radiation signal and gas temperature which may not be strictly valid, but is adequate for the present purpose of making a qualitative comparison.

Calibrated infra-red images of the plume at the nominal free-jet total temperature of  $540^{\circ}$  R appear in figure 4-14 for two different fuel pressures. The total temperature profiles used to calibrate the images are shown in figure 4-14c. The infra-red images are somewhat coarse, consisting of a 256 by 60 array, and exhibit a horizontal feature which is a characteristic of the imaging system and not of the plume. Combustion is more vigorous at 350 psia as evidenced by the images as well as the temperature profiles. The 250 psia condition is near the stability limit. Some asymmetry from top to bottom is noted and the reason for this is not known. Most importantly though, a delay in the onset of combustion is seen at both fuel pressures. Infra-red images at the same Reynolds number, but at the elevated free-jet temperature and pressure are presented in figure 4-15 along with the temperature profiles used for the calibration. Again, combustion is more vigorous at the higher fuel

pressure, although neither case is near the stability limit, and again a slight asymmetry is apparent. The most prominent difference between the hot and cold cases is the reduced distance from the spraybar to the onset of combustion for the hot case. In making a qualitative comparison of the hot and cold images, the unavoidable slight differences in estimated equivalence ratio and jet penetration should be noted. The jet penetration being of somewhat more significance since the ignition delay is relatively insensitive to equivalence ratio.

The overall impression given by the infra-red images and temperature profiles is that the increased freestream pressure and temperature did cause a reduction in the ignition delay distance at the same Reynolds number. The spraybar combustion process at this Reynolds number then is not mixing limited, being affected to a degree by a change in the reaction kinetics. This result implies that model scale would have an affect on the performance of external burning. Sub-scale test results however would be conservative, since flameholding would be more difficult, and any heat release occuring downstream of the test article probably serves no useful purpose. Although detailed small-scale experimental results may not directly apply to a larger scale flight vehicle, successful application of the external burning concept at small-scale leads to a high confidence in full-scale success.

#### Expansion Ramp Tests Apparatus and Procedure



The objectives of the expansion ramp tests were to verify drag reduction, and provide data for comparison to analysis results. Figure 4-16 serves to illustrate that although the expansion ramp tests were preliminary and generic in nature, the model geometry used is related to the aft end of a representative vehicle. The upstream flat surface from which fuel was injected represents the engine cowl. The downstream surface which is deflected  $12^\circ$  represents the deflected cowl and exhaust shear layer. The  $12^\circ$  turn generates a Prandtl-Meyer expansion and corresponding low pressure which external burning is to eliminate.

A 3-view drawing of one of the expansion ramp models appears in figure 4-17. Two models were constructed, identical except for the spacing and diameter of the fuel injection orifices. Each model was machined from a single slab of  $3/4$ " thick stainless steel. The expansion surface downstream of the  $12^\circ$  corner was flame-sprayed with a zirconium-oxide coating which provided the only thermal protection other than the freestream air which impinged on the unfueled side of the ramp. The models were instrumented with two rows static pressure taps, 18 on centerline, and 12 off-centerline as well as two static pressures on the  $3/4$ " high base. A row of 5 thermocouples were imbedded in the expansion surface to monitor surface temperature. The "baseline" flameholder shown is a  $1/8$ " high by  $1/4$ " wide piece of stainless steel bar stock mounted such that the trailing edge was coincident with the  $12^\circ$  corner. The expansion ramp models were installed in the free-jet in much the same way as the spraybars. A photograph of the expansion ramp installation appears in figure 4-18. The sidewalls extending beneath the model were installed

to prevent the higher pressure air under the expansion ramp from spilling around and affecting the external burning process. Gaseous hydrogen fuel was supplied through the right (looking upstream) 90° elbow visible in the photo.

The infra-red camera, Schlieren system, and water-cooled total temperature probe as depicted in figure 4-9 were also used during the expansion ramp tests.

#### Fuel Injector Sizing

The fuel injectors on the two models were sized for zero drag using the design procedure outlined in chapter II (see equations 2-30 and 2-31). An  $x/d^*$  of 10 was used in the jet penetration correlation. The fuel-lean design had 8, .044" diameter orifices for zero drag at an equivalence ratio of 1/2. The other model was designed for zero drag at stoichiometric conditions with 26, .025" diameter orifices. All orifices were equally spaced and drilled normal to the surface 1/2" upstream of the 12° expansion corner. Total temperature profiles just downstream of the model trailing edge obtained in initial tests of the 26 injector model, suggested that the equivalence ratios actually obtained were somewhat lower than predicted and that an  $x/d^*$  of 30 in the jet penetration correlation would be more appropriate. This lowers the estimated equivalence ratios by about 26%. An  $x/d^*$  of 30 is thus implicit in any subsequent mention of estimated equivalence ratio for the expansion ramps.

No results are reported for the low equivalence ratio, 8 injector model as it was unsuccessful in sustaining combustion in the Mach 1.26 flow. It was subsequently redrilled with 56, .018" diameter injectors for zero drag at stoichiometric conditions using an  $x/d^*$  of 30. This design exhibited good flame stability.

### Flameholder Sizing

During the initial design of the expansion ramp models, it was unknown exactly what size flameholder would be appropriate. Given the relatively small model scale, a disproportionately large flameholder with respect to the fueled stream height would be required to remain within the DeZubay pre-mixed stability limit for all test conditions. During initial tests of the 26 injector configuration, an attempt was made to stabilize combustion without a flameholder, using only the disturbance created by the fuel injection process. While stable combustion was maintained, the flameholding site as evidenced by the infra-red video monitor was coincident with a boundary layer separation halfway down the ramp surface and had little effect on the ramp surface pressures. The need for a flameholder to initiate combustion further upstream was apparent, and the 1/8" height of the "baseline" flameholder was determined to be the minimum conceivable in the following manner. Figure 4-19 depicts operating envelopes for the 26 injector design in terms of the DeZubay parameter and estimated equivalence ratio for 1/8" and 1/4" high steps. The dimension used in the DeZubay parameter is twice the step height due to symmetry; a

step actually represents one-half of a spraybar type flameholder. The 1/4" step falls within the stability limit over much of the altitude range at high fuel pressure, but is disproportionately large. The minimum value of the DeZubay parameter for the 1/8" step is lower than 800, but outside the stability loop due to the low estimated equivalence ratio. The equivalence ratio is a global value though, and it was thought that the mixture in the flameholding region would vary enough that stoichiometric regions would exist. Also, the disturbance due to fuel injection should afford additional stability. Finally, the stability limit shown is obviously not exact, being only a guideline based on limited data at these conditions. It was thus decided to begin with a 1/8" step as the baseline flameholder.

#### Test Procedure

The fuel pre-heater was not used during the expansion ramp tests. Fuel temperature as measured near both 90° elbows was nominally 520° R. Unless otherwise noted, all tests were run at a free-jet total temperature of 540°R. As with the spraybar tests, ignition was accomplished using the translating spark ignitor at a subsonic free-jet condition. The .060" spark gap was positioned approximately 1/16" downstream of the trailing edge of the flameholder, with the ground electrode 1/16" off of the model surface with the ignitor fully extended. The inability of the spark to ignite the model at the Mach 1.26 condition is considered a result of incorrect spark positioning. Adjusting the spark position involved a

relatively lengthy facility shutdown and hydrogen purge procedure and so an optimum position which may have made supersonic ignition possible was not pursued. Following ignition, the free-jet supply pressure was increased to the design value and the altitude condition was set in the same manner as in the spraybar tests. Once on condition, data was generally taken at various fuel pressures from maximum to flame-out, with fuel off, and with fuel on at the maximum fuel pressure but not burning.

### Expansion Ramp Test Results

The baseline configuration consists of the 26, .025" diameter fuel injection geometry with the 1/8" high by 1/4" wide flameholder. Results for this configuration will be presented in detail first, with comparisons to the control volume analysis. This is followed by results of model and test cell modifications done to study facility interference, and reconcile the experimental data with the control volume analysis. Next, the effect on performance of a number of perturbations on the baseline fuel injection and flameholding geometry is given. Finally, flame stability data for all of the model configurations is presented. A summary of expansion ramp configurations tested is given in table 4-1, and details of the various flameholders are contained in appendix D.

### Baseline Performance

The aerodynamics of the expansion ramp with fuel off is somewhat more complex than was originally desired. Figure 4-20 shows centerline and off-centerline pressure distributions over the range of ambient pressures tested. A dotted line representing a  $12^\circ$  Prandtl-Meyer expansion is also shown for reference. At the leading edge, a pressure coefficient of  $-.3$  exists, followed by a rapid compression. The expansion at the leading edge is attributed to an upwash caused by a detached bow shock. The model leading edge was sharp with the upper surface parallel to the freestream, but the lower surface was at a  $14^\circ$  angle. The  $5^\circ$  required for an attached shock at Mach 1.26 was impractical given the length available. Since the bow shock at Mach 1.26 is nearly isentropic, the flow is again supersonic following expansion around the knife edge. Another bow shock caused by the flameholder then causes the compression to a pressure coefficient of roughly  $.25$ . The expansion around the flameholder base and  $12^\circ$  turn is evident at model station 3. The centerline pressure distributions show an initial overexpansion followed by a recompression to a region of constant pressure at roughly the Prandtl-Meyer value. At model station 6, a "hump" in the distributions is seen with pressure rising to greater than ambient, then reducing to near the sub-ambient base pressure at the trailing edge. This is characteristic of a shock-boundary layer interaction which is not unexpected at transonic conditions. The magnitude of the hump however is influenced by wave reflections from the free-jet boundary. This will be discussed in a subsequent section on facility interactions. The off-centerline distributions do not exhibit the region of constant pressure at model station 6, and only rise to ambient pressure at about model station 10, but are in general similar to the centerline distributions which

indicates little potential for transverse flow on the ramp surface. Both centerline and off-centerline distributions with fuel off show little variation with altitude.

The result of simply injecting fuel with no subsequent combustion on the centerline pressure distributions is shown in figure 4-21 where the fuel off and fuel on distributions are plotted together. The effects are most pronounced at 4 psia where the jet penetration and estimated equivalence ratio are maximum, and Reynolds number is minimum. The influence of fuel injection is felt upstream, all the way to the leading edge for the 4 and 8 psia conditions. Downstream of the expansion, the effects are slight at 8 and 12 psia, but at the 4 psia condition, the pressure force on the ramp is clearly reduced by fuel injection.

Following the subsonic ignition procedure, combustion was sustained at Mach 1.26 to a minimum estimated equivalence ratio of 0.5. A visual observation of the flame indicated that it was attached at the 1/8" high flameholder. Pressure distributions during external burning at various fuel pressures and altitudes appear in figure 4-22. External burning eliminates the overexpansion at model station 3, and results in a relatively constant pressure along the entire ramp length. The base pressure measured on the 3/4" model trailing edge more closely matches the ramp surface pressures with combustion. The effects of fuel pressure and altitude are almost negligible despite large changes in the jet penetration and estimated equivalence ratio. The flat nature of the pressure distributions and the fact that the base pressure is not

significantly different are indications of the elliptic nature of the flow on the ramp. Unfortunately, it is difficult to distinguish between a separated flow, and an attached flow driven subsonic by combustion as both may result in the observed pressure distributions. The 2-D Euler results of chapter III indicated that a sharp pressure gradient may accompany the transition to subsonic flow within the plume, which substantiates the separation argument, but without detailed off-surface measurements, it is difficult to distinguish between the two.

The 35mm camera system used to take still Schlieren photos was unavailable during runs with the baseline configuration, but was installed for subsequent tests with other model configurations. Features of the Schlieren images changed little however for all configurations tested as evidenced by a video monitor in the control room. Typical Schlieren images with fuel off, and with external burning appear in figure 4-23. The profile of the model upper surface is clearly visible to a point near the trailing edge. The sharp leading edge of the model is at the intersection of the upper surface with the sidewall profile but is obscured by the 5/8" diameter elbows used for support and fuel supply. The bow shock standing off of these tubes is evident in all of the images, and is nearly coincident with the fuel injection and flameholding disturbances. The fuel off image shows much more shock structure, and a separation point roughly halfway down the ramp surface. With external burning, the most prominent feature is the density gradient at the plume boundary. Much less structure is evident in the freestream apparently as



a result of reduced turning as the plume fills the void left by the model. Within the plume, the absence of any structure indicates subsonic flow, but from these images alone it is impossible to distinguish between an attached flow driven subsonic by combustion and a separated flow.

Total temperature profiles obtained 4" downstream of the expansion ramp trailing edge and 1" off the centerline are shown in figure 4-24. The effect of increasing fuel pressure and altitude is clearly seen as both the temperature and vertical extent of the plume increase. Fuel pressure and altitude increases result in higher jet penetration and estimated equivalence ratio. Temperatures approaching hydrogen-air stoichiometric are seen at the highest altitude, 4 psia condition. The marked variation in plume characteristics is in sharp contrast to the pressure distributions of figure 4-22 which showed little or no variation with fuel pressure or altitude. The profiles exhibit a definite peak near the free-jet centerline at the boundary between the external burning plume and the freestream. The lower boundary of the plume is less definite, extending below the elevation of the model base. No inference can be drawn regarding the state of the boundary layer from these profiles.

Infra-red images corresponding to three of the temperature profiles of figure 4-24 appear in figure 4-25. The images were calibrated using the same procedure outlined previously for the spraybar tests. The same temperature scale was used for all three of the images so a direct comparison can be made. Hot model surfaces appear as saturated regions since the calibration used is only valid in the plume. Dramatic increases

in the size and intensity of the external burning plume are apparent as the estimated equivalence ratio increases. At the highest equivalence ratio, a cooler region near the ramp surface is visible, and a delay in the onset of combustion is apparent with the maximum temperature occurring near the trailing edge of the model.

#### Comparison to Control Volume Analysis

The control volume equations presented in chapter II predict the axial thrust coefficient given the model geometry, freestream conditions, and the inflow stream height and equivalence ratio. Since it is more practical to specify as input the fuel conditions and fuel injector geometry, the inflow stream height and equivalence ratio were estimated using the jet penetration and the penetration times spacing method. In attempting to match an experimental result, it is of interest to insure that the inflow stream height and equivalence ratio estimates are not seriously in error. To this end, the total temperature profiles measured approximately 4" downstream of the model trailing edge are taken to represent the outflow temperature, and are compared to the equilibrium temperature at the estimated equivalence ratio used in the control volume analysis. The penetration times spacing method yields this equation for the equivalence ratio:

$$\Phi_{pxs} = 5.213 C_v \frac{\left(\frac{P_{H_2}}{P_{t,0}}\right)^{.517} \left(\frac{P_{t,N-S}}{P_{t,0}}\right)^{.483} \left(\frac{A}{A^*}\right)_0}{\sqrt{\frac{T_{H_2}}{T_{t,0}} \left(\frac{S}{d^*}\right) \left(\frac{x}{d^*} + .5\right)^{.281}}} \quad [4-3]$$

One of the assumptions in the control volume analysis is that the inflow and outflow conditions are uniform. To obtain a representative value of total temperature from the measured profiles, all temperatures within 20% of the peak were averaged. These average plume temperatures for the baseline and all of the other configurations tested at ambient free-jet total temperature are plotted in figure 4-26a versus the estimated equivalence ratio obtained from equation 4-3 using an  $x/d^*$  value of 30. These data encompass all of the different flameholder geometries, and two different spacing ratios (the 26 and 56 injector models) as well as various other variations including upper sidewalls, fairings, etc. A degree of correlation is provided by equation 4-3 but the data seems to stratify into two separate groups representing the two different orifice spacing ratios, and falls below the equilibrium curve for low equivalence ratios. Since the control volume analysis uses the equilibrium curve, this would result in an optimistic performance prediction. The penetration times spacing method, which seems to provide the appropriate functional form, can be revised to provide a better degree of correlation based on the present data. First, the exponent on spacing ratio is changed to 1/2 to collapse the data into a single curve. A better fit with the equilibrium values results from changing the fuel pressure

dependence from an exponent of .517 to 1.0, and adjusting the constant from 5.304 to .336. The  $x/d^*$  term is also lumped into the constant and the revised equation for estimating equivalence ratio is as follows:

$$\Phi_{corr} = .129 C_v \frac{\left(\frac{P_{H_2}}{P_{t,0}}\right) \left(\frac{P_{t,N-S}}{P_{t,0}}\right)^{.483} \left(\frac{A}{A^*}\right)_0}{\sqrt{\frac{T_{H_2}}{T_{t,0}}} \sqrt{\frac{S}{d^*}}} \quad [4-4]$$

The average plume temperatures are replotted using the new estimate in figure 4-26b. Equation 4-4 gives a good estimate of the "effective" equivalence ratio based on the experimental outflow temperatures. It reflects any reduction in combustion efficiency caused by incomplete mixing and ignition delay. Since these factors may depend on scale and model geometry, the validity of equation 4-4 outside the range of parameters in the present experiment cannot be guaranteed. It is now simply a correlation with it's functional form suggested by physical reasoning, and exponents adjusted intuitively to match the present data. The equivalence ratio so defined will be referred to as the correlated equivalence ratio in all subsequent discussion.

Given the correlated equivalence ratio, and measured fuel flow, the corresponding amount of air involved can be determined, which is in general different than that given by the penetration times spacing method. Assuming that the inflow stream height is still equal to the jet penetration, the inflow conditions could be adjusted so as to give the

proper massflow. This would lead to an iterative process though, since an adjustment in the inflow conditions would affect the jet penetration. Alternatively, freestream conditions can be assumed for the inflow, and a stream height consistent with the airflow can be calculated independent of the jet penetration correlation. Taking this approach, the effective height of the air stream is given by the following:

$$\frac{y_0}{y_b} = 56.18 \frac{(d^*/y_b)\sqrt{d^*/S}}{(P_{t,N-S}/P_{t,0})^{.483}} \quad [4-5]$$

Note that the inflow stream height calculated in this manner is only a function of the orifice geometry, and the freestream Mach number, and is independent of fuel and freestream conditions. The equivalence ratio and inflow stream height given by equations 4-4 and 4-5 can now be used in the control volume analysis as better approximations than those given by the original penetration times spacing method.

The experimental thrust coefficient was determined based on area-averaging the static pressure distributions. Separate thrust values were computed based on the centerline and off-centerline rows, then the two values were averaged using a 2/3 weighting on the centerline value, and 1/3 on the outboard. This somewhat arbitrary weighting between the centerline and outboard rows is of little consequence since the pressure distributions are so similar. The predicted and measured drag coefficients are compared in figure 4-27. Equilibrium hydrogen-air combustion and three-dimensional expansion assumptions were used in the control volume analysis. In figure

4-27a, the penetration times spacing method was used with an  $x/d^*$  of 30 to estimate the equivalence ratio for both the experimental data and the control volume results, thus the inflow stream height used in the control volume estimate equals the jet penetration. As stated earlier, the model was originally designed for zero thrust at stoichiometric conditions. The control volume prediction curve passes through zero thrust at an equivalence ratio different than one because an  $x/d^*$  value of 10 was used originally in the design, and also the experimentally determined orifice flow coefficient of .83 is now taken into account. The equivalence ratio and inflow stream height based on the data correlation is used in figure 4-27b and results in a broader range of equivalence ratios, with the predicted zero drag point at an even lower equivalence ratio. The measured thrust coefficient shows little variation with equivalence ratio and is below the control volume prediction regardless of the method used.

The performance of external burning in terms of a drag reduction per unit fuel flow is difficult to assess since as stated above, the fuel off results are susceptible to interference from the free-jet boundary above the model. To provide some sense of scale however it should be noted that the thrust coefficient resulting from a  $12^\circ$  Prandtl-Meyer expansion is -.4. The actual fuel off thrust coefficient would be closer to zero however due to the beneficial effects of boundary layer separation and three-dimensional effects.

#### Facility Interaction Studies

The disparity between measured thrust coefficients and the control volume prediction may at first seem completely attributable to boundary layer separation. However, characteristics peculiar to the external burning flowfield must be considered before this conclusion can be drawn. The control volume analysis (equation 2-9) indicates that the plume velocity is weakly proportional to the thrust coefficient. For the slightly negative thrust coefficients obtained experimentally therefore, the plume velocity should be nearly equal to freestream. In contrast to a classical wake flow which reaccelerates to the freestream velocity due to large transverse velocity gradients, the subsonic external burning plume may persist for a considerably longer distance downstream of the model in the absence of velocity shear. The only mechanism tending to increase the plume Mach number is the reduction in sound speed caused by heat transfer across the plume boundaries. Pressure distributions on the ramp are thus susceptible to upstream communication of disturbances which may occur well downstream of the model such as in the facility exhaust collector. This and other possible sources of facility interference which were studied are depicted schematically in figure 4-28.

In close proximity to the model, is a sub-ambient pressure region at the 3/4" high model base (see figure 4-22). The blunt base and the airflow which is channeled beneath the ramp by the sidewalls does not exactly represent the generic external burning outflow conditions considered thus far, i.e. a simple turn back to the freestream direction. The fact that the pressures on the ramp during burning were nearly equal to this base pressure gives rise to a concern that the model base region may have

influenced the results.

The free-jet boundary also provides a possible source of interference, since disturbances generated by the model would be reflected back and impinge on the plume as waves of the opposite family. This would tend to have an equalizing effect on thrust, since a compression wave generating high pressure on the ramp would be reflected back as an expansion, tending to depressurize the plume.

#### Effect of Exhaust Collector Modification

Any experiment involving combustion within the PSL-4 test cell requires an amount of cooling and dilution airflow consistent with safety guidelines. This auxiliary air is admitted into the test cell at the forward bulkhead and flows around the flow conditioning duct and free-jet at about 80 fps keeping the test cell walls and electronic equipment cool as well as providing enough dilution so that if the hydrogen fuel is not burned in the experiment, the mixture which flows out of the test cell is still inert. The free-jet air and auxiliary air exit through an exhaust collector at the rear of the cell which is simply a round duct 55" in diameter. The leading edge of the exhaust collector was located 51" downstream of the model trailing edge, and did not have any type of bellmouth contour. The relationship of the exhaust collector and model is depicted in figure 4-29. Since the leading edge of the duct was relatively sharp, the possibility existed of a sharp-lip separation and



vena-contracta which would cause a low pressure region through which the external burning plume would flow. The exhaust collector was subsequently instrumented with a row of 11 static pressure taps shown in figure 4-29. Pressure distributions at ambient pressures of 12, 8, and 4 psia are shown in figure 4-30 for the 75 pps of auxiliary air nominally used. The 4 psia condition where the velocity is highest at the inlet due to the constant auxiliary air mass flow, shows a definite sharp-lip separation and low pressure throughout the duct. The possibility of this low pressure feeding forward to the model prompted a re-installation of the exhaust collector such that the leading edge was 105" downstream of the model. Following this, a study of the effect of auxiliary air flowrate on the duct pressure distribution was done at the 4 psia test cell condition. The results of this study appear in figure 4-31 and indicate that by reducing the auxiliary air flow to 40 pps, the separation and low pressure is eliminated. It was concluded that 40 pps of auxiliary air was still within safety limits and all subsequent testing was done at this flowrate. The effect of reducing the auxiliary air flowrate and moving the exhaust collector entrance downstream on external burning performance is shown in figure 4-32 to be negligible however. It can be concluded therefore that the low pressure region located about 5 feet downstream of the model did not feed forward through the subsonic plume and reduce performance.

#### Effect of Plume Boundary Simulator

The trailing edge of the model does not exactly represent the intended

geometry depicted in figure 4-16. The external burning plume should turn back to the flight direction immediately downstream of the vehicle. The finite model base height, and air flow beneath the model combine to create an area of low pressure in the base region as evidenced by the pressure distributions in figures 4-20 through 4-22. To provide a definite boundary for the external burning plume, thereby more closely modeling the intended situation, a flat plate was installed downstream of the model, parallel to the freestream. The 12" square "plume boundary simulator" installed behind the model is shown in figure 4-33. It was constructed in the same manner as the expansion ramp models using a 3/4" thick slab of stainless steel, with a zirconium-oxide coating on the upper surface. The plate had a row of 11 static pressure taps on the centerline spaced at 1" intervals, and a transverse row of 5 taps at the midpoint. The outboard leading edges of the plate were machined to a 10° knife edge to reduce blockage. The total temperature probe actuator was moved 1" off centerline and a 3/4" diameter hole was drilled in the plate, to allow the water-cooled total temperature probe to pass through. A test was run with the hole plugged to insure that the centerline pressure measurements were not affected by the hole.

The Euler analysis described in section 3 was used to demonstrate the equivalence between a solid boundary parallel to the freestream, and the actual situation where freestream flow deflects the plume. The Euler analysis assumes a perfect gas, so heat addition based on the fuel heating value and fuel-air ratio would tend to result in too much heat being added. So that a more representative heat addition was used in modeling

the experiment, 2-D perfect gas, and 2-D real gas control volume calculations were compared over the range of equivalence ratios tested to determine the equivalence ratios to be used in the perfect gas calculations which result in the real gas thrust coefficient values. These reduced equivalence ratios appear in table 4-3 along with the corresponding experimental conditions. The heat addition distribution used was Gaussian in the axial direction and constant in the transverse direction, as this gave pressure distributions having characteristics similar to the experiment. The Gaussian distribution used was slightly different than that used in section 3 and is depicted in figure 4-34. Although additional numerical experimentation could have been undertaken to more closely match experimental pressure distributions, this was not the objective of the Euler analysis. The purpose of these calculations was simply to validate the use of a plume boundary simulator.

The 12° expansion ramp profile was modeled with both types of downstream plume boundaries. A 100 by 50 grid shown in figure 4-35a was used for the solid boundary case. To model the freestream inflow boundary, 20 points were added in the transverse direction as shown in figure 4-35b. The heat addition corresponding to a correlated equivalence ratio of .452 was used for this comparison (see table 4-2). Streamlines and heat addition contours for both cases appear in figure 4-36. The momentum of the subsonic plume is small compared to that of the freestream, due to the large reduction in density at about constant velocity. The plume is therefore quickly turned back to the axial direction by the upper freestream flow as evidenced in figure 4-36b where deflection of this

auxiliary freestream is negligible. Mach number contours for both cases which appear in figure 4-37 are very similar as well, with the only difference being the large transverse gradient between the upper freestream and the plume. The expansion surface pressure distributions compared in figure 4-38 are nearly coincident over the entire ramp surface and result in a negligible difference in thrust coefficient. The solid wall is thus a valid representation of the true lateral plume boundary, at least for the 2-D inviscid case. The equivalence of these two boundaries may not be as clear if the plume is separated, since the solid boundary hinders reverse flow into the separated region. Despite this, the plume boundary simulator provides a known boundary and a better experimental simulation of the intended external burning geometry than the basic expansion ramp model.

Centerline pressure distributions with and without the plume boundary simulator are shown in figure 4-39a with fuel off along with the 2-D shock-expansion theory result for reference. Upstream of 8" the distributions are similar. Downstream of this point the baseline distribution falls off to the low base pressure while the distribution with the plume boundary simulator peaks at the  $12^\circ$  corner. The pressure then quickly decays to a zero pressure coefficient. There was little effect of ambient pressure on the fuel off distributions, the 8 psia cases shown are representative of all altitudes. The transverse row of static pressure taps on the plume boundary simulator at the 20" station showed no transverse variation in pressure at all conditions and so are not

presented. The plume boundary simulator thus eliminates the troublesome region of low pressure immediately downstream of the expansion ramp and provides a definite lateral boundary for the plume. A comparison of centerline pressure distributions with external burning appears in figures 4-39b through 4-39d for high, low, and intermediate correlated equivalence ratios. Pressures upstream of the expansion are comparable, but a definite increase in expansion ramp pressure is induced by the plume boundary simulator at all equivalence ratios. The pressure is still independent of equivalence ratio however, and does not rise above ambient to a level consistent with control volume predictions.

Total temperature profiles appearing in figure 4-40 at the same three conditions show comparable levels of temperature but a more symmetric shape than those of the baseline configuration in figure 4-24. An increase in thrust coefficient is seen in figure 4-41 over the entire range of equivalence ratios tested. Even less variation with equivalence ratio is evident with the plume boundary simulator installed. The test arrangement is now considered free of interference from flow beneath the model and a low base pressure region. Thrust coefficients remain below predicted values however and do not exhibit the expected variation with equivalence ratio.

#### Effect of Free-Jet Boundary

The model size was obviously large with respect to the free-jet exit.

Ideally, the model would have been sized to fit completely within the conical area formed by Mach lines emanating from the nozzle lip, commonly referred to as the "test rhombus" of the free-jet. In external burning tests where an accurate thrust measurement is to be made, it would be advisable to size the installation even more conservatively, including a sizable portion of the subsonic plume within the test rhombus since disturbances impinging on the subsonic plume near the model trailing edge may feed forward. In the present tests, the free-jet size was determined by availability of the existing Mach 1.26 nozzle. Also, facility air flow capability would have precluded use of an appreciably larger free-jet. Considerations in sizing the expansion ramp models included ease of machining the small fuel injection orifices, as well as instrumentation, flame stability, and scaling. The models could not be made small enough to fit within the test rhombus, however it was decided that this situation was acceptable due to the preliminary nature of the experiments. To increase confidence in the data obtained, the magnitude of the free-jet boundary effect on thrust was estimated using the Euler analysis. Solutions in which a "flight" boundary condition was imposed on the lower computational boundary, (as in figures 4-37) were compared to cases where a free-jet boundary was used. The free-jet boundary was captured in the solution by extending the lower boundary of the grid shown in figure 4-35a beyond the 6" free-jet exit radius and imposing a low speed inflow to this region. The static pressure and total temperature match that of the free-jet. The solution would not converge if a zero velocity was imposed, so a .3 Mach number inflow was used. This is still a good representation of the actual case since the velocity adjacent to the nozzle was not zero due

to the auxiliary air flow and ejector pumping of the free-jet. The 100 by 80 grid used, pictured in figure 4-42 had the same grid density in the heat addition region as the 100 by 50 grid so that differences in thrust were not artificially induced by grid refinement effects. A .025 damping coefficient was used in all cases.

A case with no heat addition was run first to simulate the fuel off situation for which the experimental pressure distributions showed a curious recompression to above ambient pressure. Shock-expansion theory can be used in lieu of Euler analysis for the flight boundary case since the flowfield is made up of simple regions. The thrust coefficient so obtained is equal to the pressure coefficient following a  $12^\circ$  Prandtl-Meyer turn which is  $-.4$ . Mach number contours and the wall pressure distribution for the free-jet case appear in figure 4-43. The centered expansion turns the free-jet boundary toward the wall, and is reflected back as a strong shock, resulting in a  $-.2$  thrust coefficient. This shock is evident in the fuel off schlieren image of figure 4-23 along with a large separated zone. Although viscous and three-dimensional effects would alter the flowfield somewhat, the 2-D inviscid result suggests that the high ramp pressure with fuel off is induced by the free-jet boundary.

The effect of the free-jet boundary on the inviscid external burning flowfield is summarized in figure 4-44 where the thrust coefficient for both flight and free-jet boundaries are plotted versus equivalence ratio along with control volume analysis results. The heat addition schedule of table 4-2 was used in the Euler calculations, so as expected the 2-D real

gas control volume curve lies near that of the Euler "flight boundary" analysis. The 3-D real gas control volume result is also shown to depict the magnitude of three-dimensional effects which are small for thrust coefficients near zero. The free-jet boundary cases always remain nearer to zero than the corresponding flight boundary cases. For cases where the flight thrust coefficient is less than zero, the free-jet boundary causes an increase in thrust. Conversely, the free-jet boundary tends to reduce thrust coefficients greater than zero. The curves cross at approximately zero thrust so the effect of the free-jet boundary is always to reduce the absolute value of non-zero thrust coefficients, and the magnitude of the effect is proportional to the thrust level. This is an intuitive result since for zero thrust coefficient the streamline deflection and hence reflected disturbances are minimal. The reflected wave interactions are seen in figures 4-45 through 4-47 where Mach number contours for flight and free-jet cases are compared at three equivalence ratios. The minimum equivalence ratio case in figure 4-45 has a flight thrust coefficient of  $-0.075$  with an expansion propagating into the freestream. In the free-jet case, this expansion turns the free-jet boundary inward slightly and is reflected back as a compression which impinges on the subsonic plume. The interaction between the plume and free-jet boundary continues downstream resulting in a net increase in thrust. At the higher equivalence ratios, an initial compression is generated by burning, and the resulting reflected expansion wave reduces the thrust. In the maximum equivalence ratio case of figure 4-47, a pocket of subsonic flow appears downstream of the strong shock generated by burning. The resulting reflected expansion and subsequent interaction reduce the thrust coefficient from  $.223$  to



.078. The rather pronounced effects shown above apply to a two-dimensional flowfield. In the present experiment, three-dimensionality will reduce the magnitude of this effect somewhat but not alter its nature.

The free-jet boundary reduces the sensitivity of ramp forces to equivalence ratio but does not prevent thrust coefficients greater than zero. Therefore, while the free-jet boundary interaction may contribute to the insensitivity of experimental results to equivalence ratio, it is not the sole cause of persistent sub-zero thrust coefficients. The most serious effect noted is the wave interaction with fuel off which causes artificially high force levels, making an assessment of the force increment due to external burning in the experiment difficult.

The experimental arrangement including the plume boundary simulator is thus considered to be free of serious facility interactions during external burning runs since the thrust coefficients are near zero and free-jet boundary interactions are minimal. The discrepancy between the predicted and measured thrust coefficient is not completely attributable to any of the postulated facility interference effects. Another explanation for lower than predicted performance is that following initial expansion at the flameholder and 12° turn, the pressure rise due to combustion separates the boundary layer, precluding the recompression seen in the Euler analysis at the sonic point. In an attempt to determine whether or not the plume was indeed separated, a crude pitot tube was attached to the water-cooled temperature probe. The small platinum tube

did not survive the extreme environment though, and provided no useful data. Time limitations made construction of a more sophisticated probe impossible.

Subsequent efforts were focused on initiating combustion further upstream to reduce the initial expansion at the flameholder and 12° corner. To this end, a number of different fuel injection and flameholding configurations were tested. Results of these tests are presented in the following sections.

#### Alternate Fuel Injection and Flameholding Configurations

In the subsequent discussion of alternate configurations, the plume boundary simulator is always present. The "baseline" configuration to which comparisons will be made is now configuration 2 which includes the plume boundary simulator. Performance of this configuration was shown in figures 4-39 through 4-41.

The second expansion ramp model had a row of 56, .018" diameter fuel injectors designed for zero drag at stoichiometric conditions based on the control volume method with an  $x/d^*$  of 30 used in equation 4-3 for the jet penetration. The design actually called for 58 evenly spaced injectors, but the two outboard holes locations were very close to the edge of the model and were not drilled. Except for the new fuel injection pattern, this model was identical to the first. With the smaller orifices, the

distance from the injection plane to the trailing edge of the flameholder was 27.8 diameters as compared to 20 for the baseline configuration. Ramp centerline pressure distributions for this configuration appear in figure 4-48a with fuel off, and with external burning at low, intermediate and high equivalence ratios. Although the plume boundary simulator was installed for this as well as all subsequent configurations, the plots terminate at the trailing edge of the ramp in order to accentuate the flameholder and initial expansion region. Pressure on the plume boundary simulator itself quickly decayed to freestream static for all conditions and configurations. As expected, the fuel off distribution is identical to that of the baseline configuration with the plume boundary simulator installed (figure 4-39a) since the ramp and flameholder geometries are identical. The effect of the plume boundary simulator is obvious with fuel off, causing a slight pressurization at the trailing edge. With burning, the 56 injector configuration does not generate an appreciably higher thrust than the baseline, in spite of the increased length available for mixing upstream of the flameholder. Total temperature profiles corresponding to the three external burning pressure distributions appear in figure 4-48b. Compared to the baseline profiles of figure 4-40, the 56 injector configuration profiles are slightly more symmetric in shape. Note that the equivalence ratios are different for the 56 injector model, so a direct comparison of temperature level should not be made.

The next variation tried was to move both the fuel injection and flameholding upstream  $1/2$ ". This was accomplished by welding closed the

existing 26 orifices on the baseline model, and re-drilling the identical 26 hole pattern, 1/2" upstream. The original, 1/8" by 1/4" rectangular cross-section baseline flameholder could not be mounted 1/2" upstream due to interference of the attachment screws with the hydrogen plenum just beneath the surface. An alternate flameholder was constructed which used smaller screws located further upstream, and provided the desired 1/8" high step, 1/2" upstream of the 12° expansion. A photograph of this configuration appears in figure 4-49. The new flameholder was constructed of a 1/16" thick stainless steel plate, 3/8" wide with it's trailing edge bent up to 1/8" above the model surface. It should be noted that this geometry probably results in different recirculation zone length than the square baseline flameholder cross-section. Centerline pressure distributions for this configuration are shown in figure 4-50a. A more severe compression is apparent at the leading edge since the fuel injection plane is now 1/2" further upstream at 2". With fuel off, the overexpansion at the corner is less severe than with the baseline flameholder. During external burning however, the overexpansion is slightly more severe, but quickly recompresses to freestream pressure, resulting in slightly higher thrust than the baseline. Thrust coefficients for all of the alternate configurations are compared in a subsequent figure (4-55). A low equivalence ratio case was not obtained since flame stability for this configuration was not as good as the baseline, where the trailing edge of the flameholder was coincident with the 12° expansion.

The persistence of sub-ambient pressure at the model knee during burning,

and the meager increase in thrust level indicates that heat release is not being initiated at the flameholder, but further downstream nearer the  $12^\circ$  turn similar to the baseline case. The reduced flame stability of this configuration suggests that the recirculation zone length generated by the  $1/8$ " high flameholder alone is probably only marginally sufficient to initiate ignition, without a lengthening caused by the  $12^\circ$  expansion. The flameholder and initial portion of the  $12^\circ$  corner provide a larger effective flameholding region than the  $1/8$ " high step itself. Total temperature profiles for this configuration, shown in figure 4-50b are somewhat flatter than those of the baseline configuration, exhibiting higher temperatures nearer the wall.

The effect of simply moving the fuel injection plane and flameholder upstream  $1/2$ " thus has little effect on performance since the initiation of heat release was probably not moved forward with respect to the expansion. Before proceeding with a more sophisticated flameholder scheme, an attempt was made to alleviate the expansion at the sharp model leading edge caused by the detached shock, thereby reducing uncertainty in the local conditions in the fuel injection and flameholding region. To accomplish this, a 1" extension pictured in figure 4-51 was added to the leading edge of the 26 injector model (the model is shown without a flameholder). The  $5^\circ$  sharp leading edge on this extension was to allow an attached wave on the lower surface, resulting in clean Mach 1.26 flow on the upper surface. The extension extends 1" into the free-jet, and was instrumented with two static pressure taps on the centerline. The extension into the free-jet is inconsequential given that the 1.26 exit

plane Mach number exists further than 1" into the free-jet on the free-jet axis.

The effect of this extension on the centerline pressure distributions downstream of the flameholder is seen to be almost negligible in figure 4-52a where a direct comparison with the baseline configuration is made with fuel off. The expansion near station 0 (the baseline model leading edge) is reduced somewhat, but apparently the model blockage still causes a detached wave and resultant upwash. Limited external burning data at 8 psia static pressure was taken with this configuration and the baseline flameholder. Since the leading edge extension has little effect, this data may be compared to baseline configuration data in figure 4-52b and c to show the effect of moving the injection plane forward from 20 to 40 orifice diameters upstream of the 12° corner. As was the case with the 56 injector model at 27.8 orifice diameters, negligible differences in performance are noted.

The final configuration to be presented is pictured in figure 4-53, and consisted of a 1/4" high "serrated" flameholder mounted in the upstream position with its trailing edge 1/2" upstream of the 12° expansion. This flameholder was intended to promote fuel-air mixing, and create a longer recirculation zone. To accommodate a longer recirculation zone, The 1/16" thick plate seen in the photograph was added to the model, extending 3/4" downstream of the 12° corner, to provide more distance between the flameholder and expansion in which to initiate ignition and heat release.

The distance from the injection plane to the trailing edge of the plate is 70 orifice diameters. This configuration departs slightly from the previous in that the extension plate covers the  $12^\circ$  expansion and forms a short blunt base. Centerline pressure distributions for this configuration appear in figure 4-54a. With fuel off, a low base pressure in the region covered by the extension plate is apparent followed by the recompression to slightly greater than freestream pressure. Combustion increases the pressure in the separated region beneath the plate to slightly less than ambient, and this pressure persists to the end of the ramp. Again, it seems that heat release was initiated not at the serrated flameholder, but in the recirculation region formed by the extension plate. Total temperature profiles for this configuration appear in figure 4-54b and are similar in shape to those of the baseline configuration. Again, the indication is that the flame was held in the recirculation region downstream of the plate and not upstream at the serrated flameholder. A number of other different combinations of the flameholders, extensions, etc. discussed above were tried, but none resulted in higher performance, and some exhibited very poor flame stability.

Thrust coefficients for all four of the variations discussed above along with the baseline are shown in figure 4-55. Only the 26 orifice upstream injection with the upstream  $1/8"$  flameholder seems to show a discernable improvement in ramp surface force, but all are still below the control volume predictions. Only a slight difference in predicted performance is evident between the 26 and 56 injector configurations. This is to be

expected, since the inflow stream height ratios ( $y_o/y_b$ ) given by equation 4-5 are similar (.197 and .182 for the 26 and 56 injector models respectively), and for a given equivalence ratio, this is the only parameter in the control volume analysis which would affect thrust. The 56 injector model does however operate over a wider range of equivalence ratios. The final configuration discussed (26 upstream injectors, 1/4" serrated flameholder) was subsequently run at elevated freestream temperature, and also with upper sidewalls. Although neither of these two variations resulted in an increase in thrust they are included for completeness.

#### Results with Heated Freestream

Increasing the freestream total temperature has a number of effects. The most desirable is the increase in hydrogen-air reaction rate which may allow ignition and heat release to occur further upstream. This reduction in ignition delay comes at the expense of a lower Reynold's number, and a higher freestream velocity, but these effects are small compared to the exponential dependence of ignition delay on temperature (see the section on scaling of small-scale test results and reference 62). Figure 4-56a presents centerline pressure distributions at a free-jet total temperature of 960°R with fuel off, and with external burning at low, intermediate, and high equivalence ratios. The distributions are nearly identical to the corresponding results at 540° in figure 4-54, which are at somewhat lower equivalence ratios. Total temperature profiles appear in figure 4-56b and



exhibit a higher maximum temperature as expected, but are similar in shape to the cold results. Figure 4-56c shows the negligible effect of the heated freestream on thrust coefficient. The control volume results show a marked effect however since at increased freestream temperature, the temperature ratio and thus the stream area ratio are reduced.

#### Effect of Upper Sidewalls

The control volume analysis, which has provided the impetus for attempting to improve performance, has been done with a three-dimensional expansion approximation. Even so, the possibility existed that lateral spillage was preventing higher thrust coefficients. Thusfar, in all of the configurations tested, the external burning plume has been confined on only one surface. To approximate a more two-dimensional flow, upper sidewalls pictured in figure 4-57 were used which extended 2" above the ramp at the leading edge. The upper surface of the sidewalls was parallel to the freestream, and the leading edges were ground to a  $10^\circ$  knife edge. In the photograph, the original baseline configuration appears without the plume boundary simulator. The effect of these sidewalls with fuel off, as shown in figure 4-58a is to prevent lateral inflow to the low pressure regions, resulting in lower pressure over more of the ramp surface. The fuel-off recompression, which as discussed previously is strengthened by free-jet boundary interference, occurs further downstream. With external burning at the maximum equivalence ratio (figure 4-58b), the effect of the sidewalls is very slight, resulting in a small increase in pressure. The

effect is seen upstream to near the leading edge as the sidewalls contain the injection disturbance. A comparison of total temperature profiles with and without the upper sidewalls appears in figure 4-58c. The upper sidewalls prevent transverse inflow of cooler air, resulting in a slightly fuller profile near the wall. The effect of upper sidewalls on thrust coefficient is negligible as shown in figure 4-58d.

#### Expansion Ramp Flameholding

Flame stability data was taken during the expansion ramp tests in the same manner as in the spraybar tests described previously. Combustion was stabilized at a given altitude condition, which results in a specific value of the DeZubay parameter, then fuel pressure was reduced, lowering the equivalence ratio until a flame-out occurred. Points at which flame-outs occurred are plotted in figure 4-59 along with the DeZubay pre-mixed stability limit. The data appear to fall well outside the pre-mixed limit in contrast to the spraybar results. The characteristic dimension used to calculate the DeZubay parameter is subject to interpretation however, given the more complex geometry of the expansion ramp flameholding region. For figure 4-59, twice the overall geometric height of aft-facing flameholder area (denoted by  $H$  in appendix D) was used in the DeZubay parameter. Recall from the discussion on flameholder sizing that a step is equivalent to one-half of an unconfined two-dimensional flameholder. There is no inherent reason that the expansion ramp flameholders should

allow stable combustion at more severe conditions than the pre-mixed limit. This is another indication that the  $12^\circ$  corner downstream of the flameholders caused a lengthening of the recirculation region. The longer recirculation zone corresponds to a larger effective flameholder height, which would reduce the DeZubay parameter to more reasonable values near the pre-mixed limit. The preceding argument is consistent with the premise that combustion was not initiated near the flameholders, but further downstream allowing some initial overexpansion to occur.

#### Expansion Ramp Performance Assessment

The control volume analysis of chapter II indicated that the performance of external burning had the potential to be competitive with other forms of airbreathing propulsion. The specific impulse measured experimentally will now be compared to that predicted. The specific impulse in terms of the change in axial force per unit fuel flow is difficult to assess however, because of the aforementioned free-jet boundary interference with fuel off. The free-jet boundary causes the thrust coefficient with fuel off to be too high, which reduces the change in thrust coefficient due to external burning. Nonetheless, the thrust coefficient and specific impulse as defined by equation 2-24 are shown in figure 4-60 for configuration 10. Configuration 10 is representative of all others since the results showed little dependence on geometry. In figure 4-60a, The thrust coefficient is plotted vs. the correlated equivalence ratio to show the change in axial force used to compute the specific impulse. The

thrust coefficient predicted by the control volume analysis is also shown for comparison. Two different fuel off force values will be considered. First, as labelled in the figure, is the actual fuel off thrust coefficient of  $-.097$  obtained experimentally in the same manner as the burning values, by pressure-area summation. This value is known to be affected by interference from the free-jet boundary, and is too high. The other value to be considered is that of a Prandtl-Meyer expansion about the  $12^\circ$  turn at Mach  $1.26$  which is  $-.4$ . This value is too low since in actuality, transverse flow and boundary layer separation would tend to relieve this low pressure. The "deltas" between these two fuel off values and the thrust during external burning (which is considered to be less affected by free-jet boundary interference), represent the extremes between which the proper answer lies. In figure 4-60b, the specific impulse corresponding to these two extremes is shown along with the control volume prediction which is based on the control volume thrust coefficient values and the Prandtl-Meyer expansion. The experimental impulse based on the Prandtl-Meyer expansion falls short of the control volume prediction because of the lower than predicted thrust coefficients. The impulse computed in this manner which represents the upper limit, peaks at about  $4000$ . The other curve based on the measured fuel off thrust shows much lower performance. This curve is the actual experimentally determined impulse with no allowance for the free-jet boundary interference, and represents the lower limit, peaking at  $400$  sec. No means were available to determine the proper fuel off drag coefficient. Even at the experimentally demonstrated lower limit of  $400$  seconds though, the simple external burning system exhibits performance competitive with

rocket propulsion. Other factors which must also be considered when comparing external burning to other propulsion augmentation options, are it's light weight and simplicity, as well as the beneficial normal or lift force which would reduce wing loading and vehicle trim drag.

## CHAPTER V - SUMMARY AND CONCLUSIONS

This work represents the first comprehensive study of the application of hydrogen external burning to transonic drag reduction. A control volume technique and a two-dimensional Euler analysis were developed specifically for the transonic conditions of interest. The Euler analysis revealed an interaction between the burned and unburned streams which is peculiar to the transonic inflow conditions. Experiments conducted in a Mach 1.26 free-jet advanced the understanding of transonic external burning in two areas. First, the operational envelope of the concept was characterized by extending the validity of an existing flame stability correlation to non pre-mixed, transonic altitude conditions. Secondly, drag reduction experiments on simple expansion ramp models provided external burning data which was relatively free of facility interference.

An initial assessment of the performance potential of external burning was made using the control volume approach. The analysis indicates that transonic drag can be eliminated for a hydrogen fuel expenditure of .1 to .2 pounds per second per square foot of aft-facing base area on a 1000 psfa trajectory. This fuel must be distributed, preferably in stoichiometric proportions in an air stream of height equal to roughly 10% of the base height. The jet penetration afforded by normal, sonic injection from the wall is sufficient to accomplish this, and an injector size and spacing rationale was developed. Specific impulse performance competitive with conventional airbreathing propulsion systems such as

turbojets is indicated. The ratio of control volume outflow to inflow velocity was shown to be nearly one at zero thrust (drag eliminated), and was weakly proportional to thrust coefficient for non-zero thrust. The increase in sound speed caused by combustion thus drives the external burning plume subsonic for all transonic conditions of interest.

The control volume study was supplemented by the two-dimensional Euler analysis. Energy representative of hydrogen-air combustion was added in various distributions, demonstrating that although wall pressure distributions varied considerably, the thrust force generated was independent of the heat addition distribution and depended only on the total heat added. Good agreement between the control volume and Euler analysis was obtained. An interesting feature of the external burning flowfield revealed by the Euler analysis, was a sharp compression in the plume at the sonic line caused by the interaction of the subsonic, elliptic region with the unheated still supersonic outer flow. This compression, which may separate the plume boundary layer is viewed as a possible limiting factor in external burning performance.

Hydrogen-air flame stability was studied experimentally in a Mach 1.26 free-jet using a combination spraybar-flameholder to determine the operational flight envelope of external burning. An existing combustion stability correlating parameter developed for a pre-mixed, subsonic hydrogen-air stream adequately correlated the non pre-mixed, supersonic data. The maximum Mach number and altitude to which stable combustion can be maintained depends on many variables including the flameholder size,

and vehicle trajectory, but it can be concluded that combustion stability will not prevent the successful application of external burning to transonic drag reduction. Operation to Mach 2 on a 1000 psfa trajectory appears feasible.

Infra-red images of combustion during spraybar tests with differing freestream temperature and pressure, but comparable Reynold's number indicate that the combustion process is not completely mixing limited, and is influenced by the finite-rate reaction process. This result makes scaling of small-scale test results tenuous, but it is reasoned that results at reduced scale are conservative.

External burning expansion ramp tests were run in the same free-jet facility to demonstrate drag reduction and provide data for comparison to the analysis results. The expansion ramp models were related geometrically to a single-stage-to-orbit vehicle base. Initial results demonstrated a reduction in drag due to external burning, raising the ramp thrust coefficient to nearly zero, but not to the level predicted by the control volume analysis. The experimental thrust coefficient also showed very little sensitivity to the estimated equivalence ratio in contrast to the control volume results. Ramp pressure distributions showed an initial overexpansion to somewhat less than freestream pressure, followed by a flat distribution to the trailing edge. The disparity between measured and predicted performance prompted an investigation into various facility interference issues related to the subsonic external burning plume. No interference mechanism was identified as being of sufficient magnitude to



account for the discrepancy. With fuel off however, wave reflections from the free-jet boundary above the model result in an artificially high thrust coefficient. This makes an assessment of the actual performance of external burning in terms of the change in axial force due to burning difficult.

Euler results in two dimensions indicate that the performance predicted by the control volume analysis is accompanied by a sharp recompression in the heated stream at the sonic line. The lower than expected, and constant nature of the thrust coefficient obtained experimentally is attributed to this effect. It is surmised that the initial overexpansion to less than freestream pressure was followed by boundary layer separation, precluding a strong recompression and limiting performance to the level repeatedly demonstrated.

Further experiments in which flameholding and fuel injection schemes were varied in an attempt to reduce initial overexpansion by initiating combustion further upstream resulted in no significant improvement in performance. It is concluded that combustion could not be initiated in close proximity to the relatively small flameholders used because the recirculation zone of the flameholders alone was of insufficient length. A lengthening of the recirculation zone caused by the the  $12^\circ$  expansion is what allowed stable combustion, but also resulted in the initial overexpansion. The use of larger flameholders was not explored as the height of the ones used was already a significant fraction of the fueled

stream height. A further increase would lead to inconsistency with the full scale system where the flameholder height necessary would be a smaller fraction of the fueled stream height.

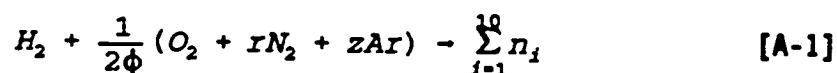
The specific impulse in terms of the change in axial force per unit fuel flow actually demonstrated in the experiment was computed despite the fact that the fuel off thrust coefficient was known to be too high due to free-jet boundary interference. As a result the impulse values obtained are conservative, and peaked at 400 sec which is competitive with a chemical rocket. The impulse was also computed assuming a Prandtl-Meyer expansion around the  $12^\circ$  corner with fuel off, resulting in a peak value of 4000 sec which represents an upper limit.

Larger scale tests would alleviate many of the flameholding issues, and should allow somewhat higher performance, since combustion could be initiated at the flameholding site and not downstream following an initial overexpansion. However a factor which may limit the performance of external burning in transonic flow is boundary layer separation due to the compression at the sonic line observed in the Euler analysis.

# APPENDIX A - HYDROGEN-AIR EQUILIBRIUM CALCULATION

In the control volume analysis of chapter II, the gas at the outflow station is assumed to be the products of hydrogen-air combustion in equilibrium. The calculation procedure used to determine the composition and adiabatic flame temperature is outlined below.

The hydrogen air system considered is described by equation A-1. The combustion products are assumed to consist of ten species.



<u>i</u>	<u>species</u>
1	H <sub>2</sub>
2	O <sub>2</sub>
3	N <sub>2</sub>
4	H <sub>2</sub> O
5	H
6	O
7	N
8	OH
9	NO
10	Ar

$\phi$  is the fuel-air equivalence ratio (the fuel-air ratio normalized by the stoichiometric fuel-air ratio). The coefficients  $z$  and  $r$  are determined by the composition of air which for the present study is assumed to be the following:

78.12% N<sub>2</sub>  
20.95% O<sub>2</sub>  
0.93% Ar

This results in  $z=0.044391$ , and  $r=3.7289$ . At a given temperature and pressure, ten equations are needed to solve for the ten unknown species concentrations. Four equations result from atomic conservation. Written in terms of species partial pressures, they are:

$$\frac{n_H}{n_O} = \frac{2P_{H_2} + 2P_{H_2O} + P_H + P_{OH}}{2P_{O_2} + P_{H_2O} + P_O + P_{NO} + P_{OH}} = 2\phi \quad [A-2]$$

$$\frac{n_O}{n_N} = \frac{2P_{O_2} + P_{H_2O} + P_O + P_{NO} + P_{OH}}{2P_{N_2} + P_N + P_{NO}} = \frac{1}{r} \quad [A-3]$$

$$\frac{n_{Ar}}{n_N} = \frac{P_{Ar}}{2P_{N_2} + P_N + P_{NO}} = \frac{z}{2r} \quad [A-4]$$

$$P = \sum_{i=1}^{10} P_i \quad [A-5]$$

Six additional equations are obtained using equilibrium constants for the following six dissociation reactions:

$$P_{H_2} = 2P_H \quad [A-6]$$

$$P_{O_2} = 2P_O \quad [A-7]$$

$$P_{N_2} = 2P_N \quad [A-8]$$

$$P_{H_2O} = 2P_H + P_O \quad [A-9]$$

$$P_{OH} = P_H + P_O \quad [A-10]$$

$$2P_{NO} = P_{O_2} + P_{N_2} \quad [A-11]$$

Equilibrium constants which are functions of temperature relate the partial pressures of reactants and products at equilibrium for these reactions, and furnish the remaining six equations needed to close the ten species calculation:

$$K_{P_1} = \frac{P_{H_2}}{P_H^2} \quad [A-12]$$

$$K_{P_2} = \frac{P_{O_2}}{P_O^2} \quad [A-13]$$

$$K_{P_3} = \frac{P_{N_2}}{P_N^2} \quad [A-14]$$

$$K_{P_4} = \frac{P_{H_2O}}{P_H^2 P_O} \quad [A-15]$$

$$K_{P_5} = \frac{P_{OH}}{P_O P_H} \quad [A-16]$$

$$K_{P_6} = \frac{P_{NO}^2}{P_{O_2} P_{N_2}} \quad [A-17]$$

The equilibrium constants are determined using the method given by Prothero<sup>1</sup>, who provides sixth-order curvefits for entropy (S) and enthalpy (H). The free energy of a single chemical species is given by:

$$F_1 = H_1 - T S_1 \quad [\text{A-18}]$$

The free energy of reaction for each of the dissociation reactions given by equations A-6 through A-11 is then:

$$\Delta F_r = \sum_{i=1}^R x_i F_i \quad [\text{A-19}]$$

Where the  $x_i$ 's are the coefficients of the dissociation reactions and are negative for reactants and positive for products. Finally, the equilibrium constant for a given reaction is given by:

$$\ln K_p = -\frac{\Delta F_r}{RT} \quad [\text{A-20}]$$

Equations A-2 through A-5 and A-12 through A-17 are ten non-linear equations in ten unknowns, the solution of which is not trivial. The method used is briefly outlined below.

An equation involving only the partial pressure of  $\text{H}_2$  and  $\text{O}_2$  is obtained in the following manner. First, equation A-5 is subtracted from A-3. The

resulting equation is written in terms of the partial pressures of  $H_2$ ,  $O_2$ , and  $N_2$  using the equilibrium constant relations and equation A-4.

$$\begin{aligned}
 & p_{H_2} + \frac{1}{\sqrt{K_{P_1}}} \sqrt{p_{H_2}} - p_{O_2} + \left( \frac{2}{r} + \frac{z}{r} + 1 \right) p_{N_2} \\
 & + \frac{\left( \frac{1}{r} + \frac{z}{2r} + 1 \right)}{\sqrt{K_{P_2}}} \sqrt{p_{N_2}} + \left( \frac{1}{r} + \frac{z}{2r} \right) \sqrt{K_{P_2}} \sqrt{p_{O_2}} \sqrt{p_{N_2}} - P = 0
 \end{aligned}
 \tag{A-21}$$

Equation A-2 is written in terms of the  $H_2$ ,  $O_2$ , and  $N_2$  partial pressures in a similar manner, and then solved for the square root of the nitrogen partial pressure.

$$\begin{aligned}
 \sqrt{p_{N_2}} = & \frac{1}{2\phi \sqrt{K_{P_1}} \sqrt{p_{O_2}}} (2p_{H_2} - 4\phi p_{O_2} + \frac{1}{\sqrt{K_{P_1}}} \sqrt{p_{H_2}} \\
 & - \frac{2\phi}{\sqrt{K_{P_2}}} \sqrt{p_{O_2}} + \frac{(1-2\phi)K_{P_2}}{\sqrt{K_{P_1}} K_{P_2}} \sqrt{p_{O_2}} \sqrt{p_{H_2}} + \frac{(2-2\phi)K_{P_1}}{K_{P_1} \sqrt{K_{P_2}}} \sqrt{p_{O_2}} \sqrt{p_{H_2}})
 \end{aligned}
 \tag{A-22}$$

These two equations are then combined into a single relation involving only the  $H_2$  and  $O_2$  partial pressures. An initial guess is made for the  $H_2$  partial pressure which results in two values for the  $O_2$  partial pressure from equation A-21. One of these values results in negative partial pressures upon back-substitution and is discarded. The sum of the partial pressures is then checked against the specified total pressure and a new value for the  $H_2$  partial pressure is determined based on the error. The iteration continues until equation A-5 is satisfied to within a given tolerance.

The preceding method determines the equilibrium composition given the temperature and pressure of the combustion products, and the fuel-air ratio of the reactants. This routine is nested within the adiabatic flame temperature procedure which balances the enthalpy of the equilibrium products with the known enthalpy of the reactants by iterating the temperature of the products.

To validate the preceding methodology, results were checked against those of Wear<sup>2</sup> et. al. for hydrogen gas fuel and dry air. Figure A-1 is a sample comparison of the adiabatic flame temperature computed using the present method with Wear's results for a reactant temperature of 300° K, and a pressure of one atmosphere. Good agreement was obtained over the entire range of pressures and fuel-air ratios of interest for the external burning problem.



### References

1. Prothero, A., "Computing with Thermochemical Data," Combustion and Flame, Vol. 13, No. 4, 1969.
2. Wear, J.D., Jones, R.E., McBride, B.J., and Beyerle, R.A., "Combustion Gas Properties III - Hydrogen Gas Fuel and Dry Air," NASA TP 2477, June, 1985.

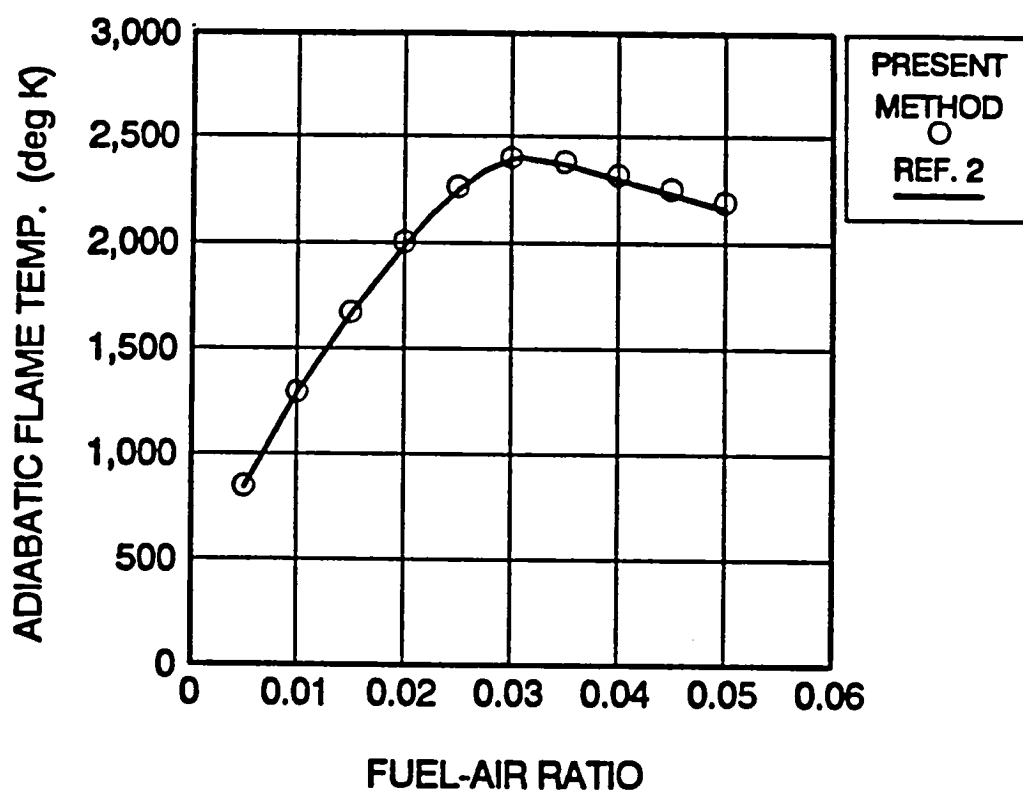


Figure A-1. Comparison of calculated adiabatic flame temperatures with results of reference 2.

## APPENDIX B - EULER ANALYSIS TEST CASES

The following 2-D Euler test cases were run to verify that the program would properly solve simple compressible flows prior to applying the analysis to the more complex problem of external burning. All of the test cases were run on  $21 \times 11$  grids with uniform grid spacing. A 2-D Courant number of  $1/4$  was used throughout. The absolute value of the change in each of the U vector members (determined by the corrector step in the MacCormack solver) was summed over the entire grid at each time step to determine convergence.

### 10° Compression

Figure B-1 depicts the 10° compression test case along with the exact solution. The grid used appears in figure B-2. Mach number contours at three levels of artificial damping are presented in figure B-3. The case with no damping ( $C_d=0$ ) exhibits strong pre-shock oscillations. As expected, these oscillations are reduced by increased damping. Wall pressure distributions for all three damping values appear in figure B-4 and are nearly coincident, all approaching the exact value.

### 10° Expansion

The 10° expansion test case and exact solution are outlined in figure B-5, and the grid used is shown in figure B-6. Mach number contours appearing in figure B-7 show only slight variation with damping. The effect of damping on the wall pressure distributions is almost negligible as shown in figure B-8. The downstream wall pressure is very close to but slightly

under the exact value.

### Rayleigh flow

The constant-area heat addition or Rayleigh flow test case is depicted in figure B-9 along with the exact solution. A heat added per unit mass (normalized by the square of freestream velocity) of .328 reduces the Mach 2.4 inflow to Mach 1.2. The grid, and the region of heat addition used are shown in figure B-10. The heat was added uniformly over the shaded region. Mach number contours for this case exhibited no transverse gradients whatsoever, and so give no more information than the wall Mach number distributions shown in figure B-11. The exit Mach number is slightly under the exact value. This is consistent with the small errors in total temperature and pressure at the outflow seen in figures B-12 and 13.

Agreement with exact solutions for all three types of problems is adequate for the intended use of the analysis, which is to examine the features of the external burning flowfield, and overall performance trends. A damping coefficient of .025 is sufficient to damp non-physical oscillations, and does not adversely affect the accuracy of the solution.

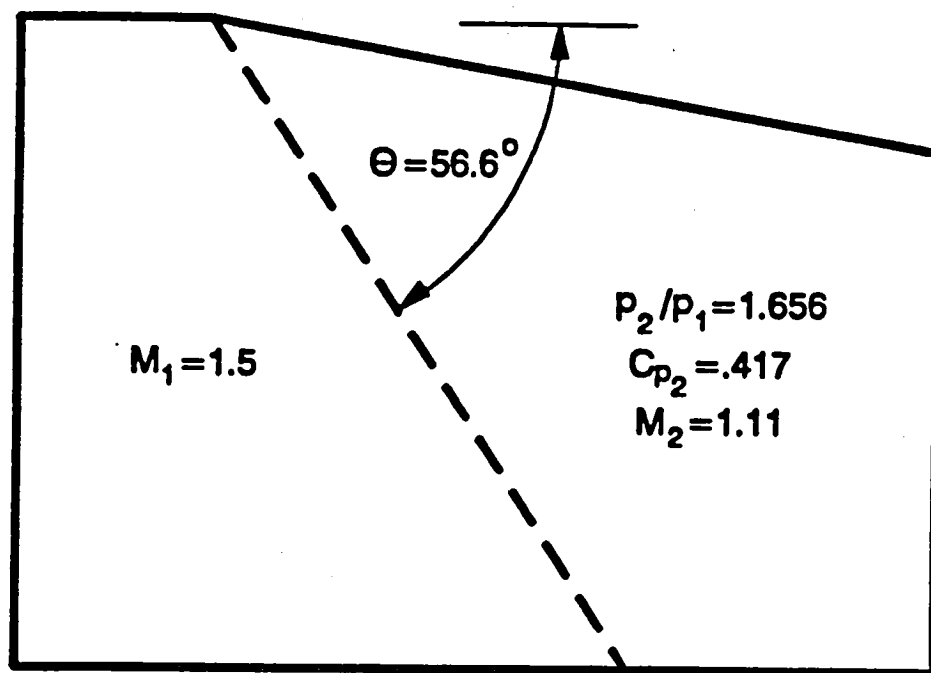


Figure B-1. 10° Compression test case

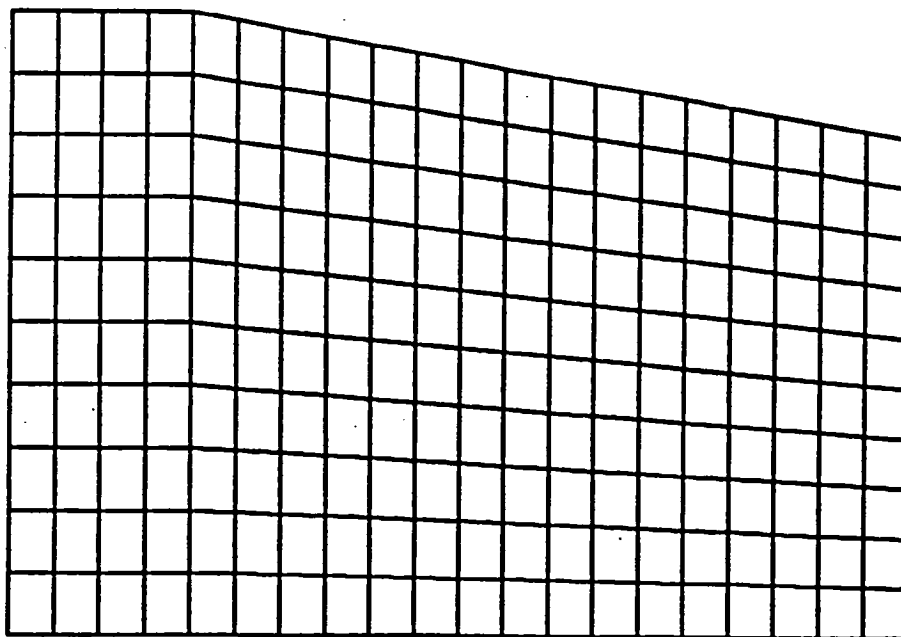


Figure B-2. Compression test case grid; 21 x 11 nodes.

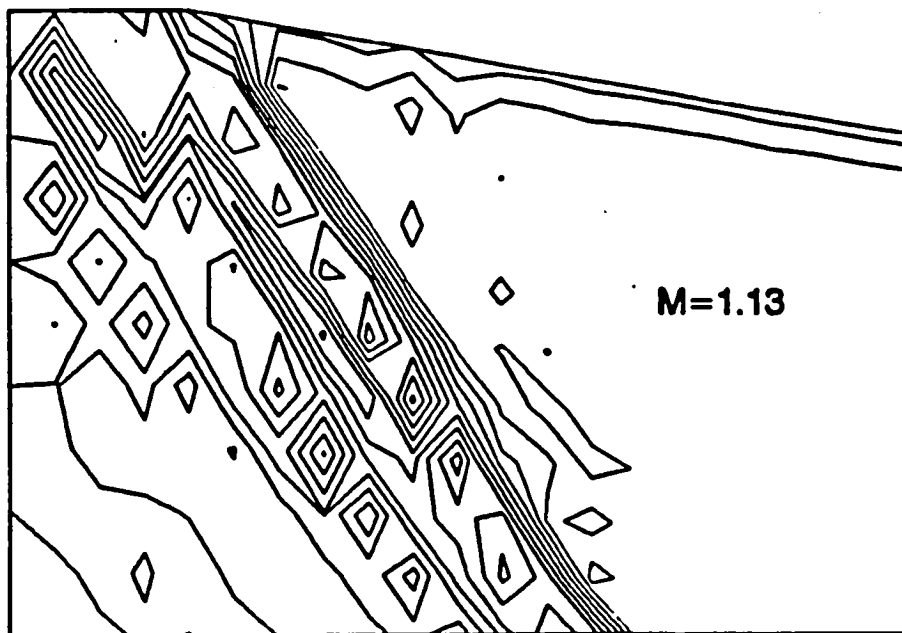
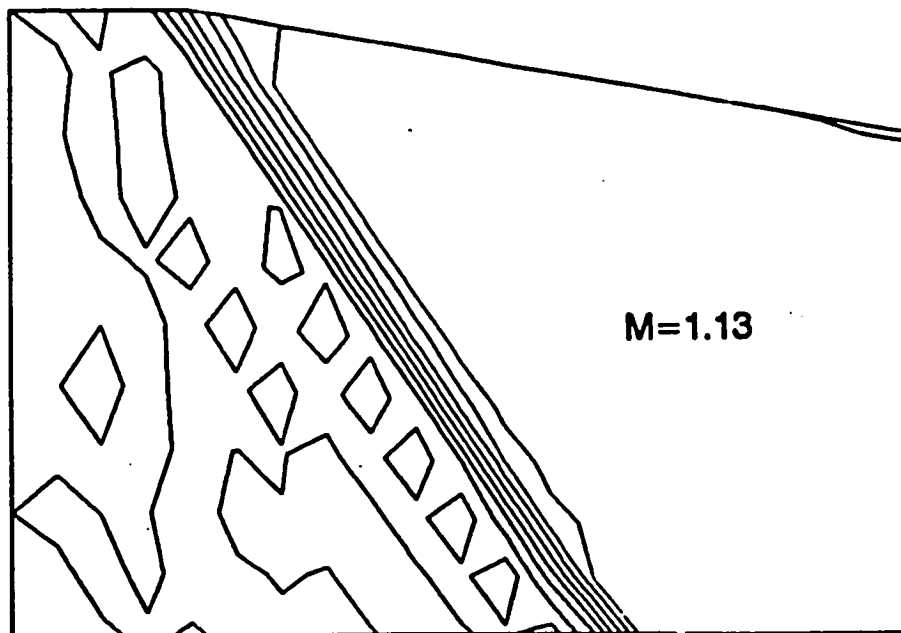
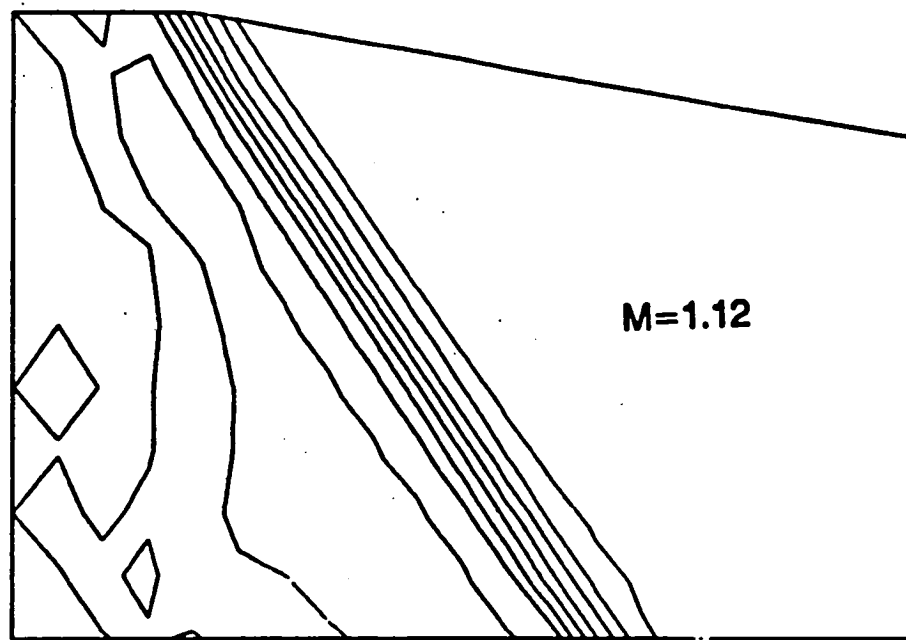
a)  $C_d=0$ .b)  $C_d=0.025$ .

Figure B-3. 10° Compression test case results at various levels of damping. Mach number contours (.05 contour increments).



c)  $C_d=.05$ .

Figure B-3. Concluded

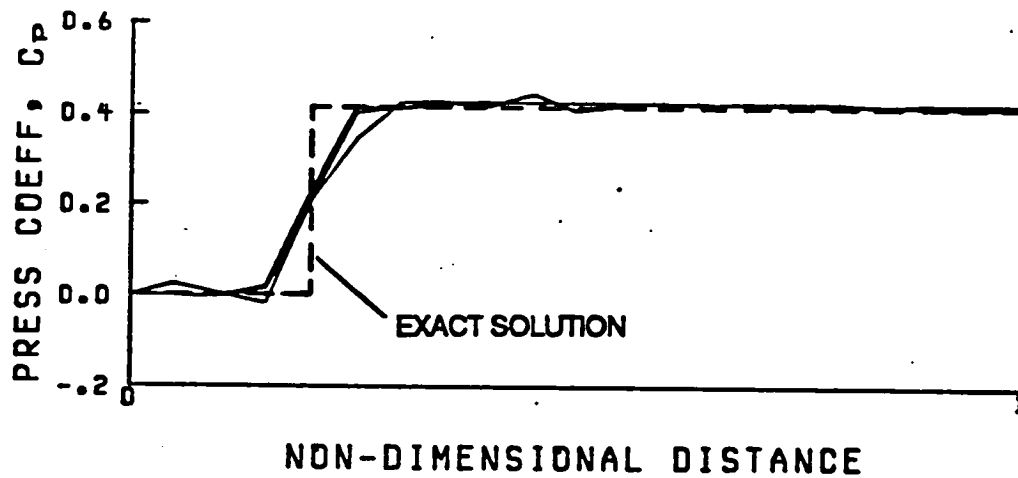


Figure B-4. Wall pressure distributions for  $10^\circ$  compression test case at various levels of damping.

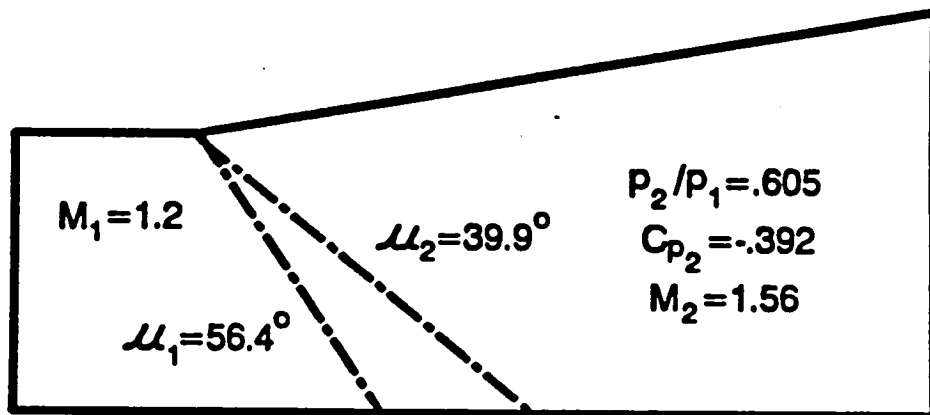


Figure B-5.  $10^\circ$  Expansion test case

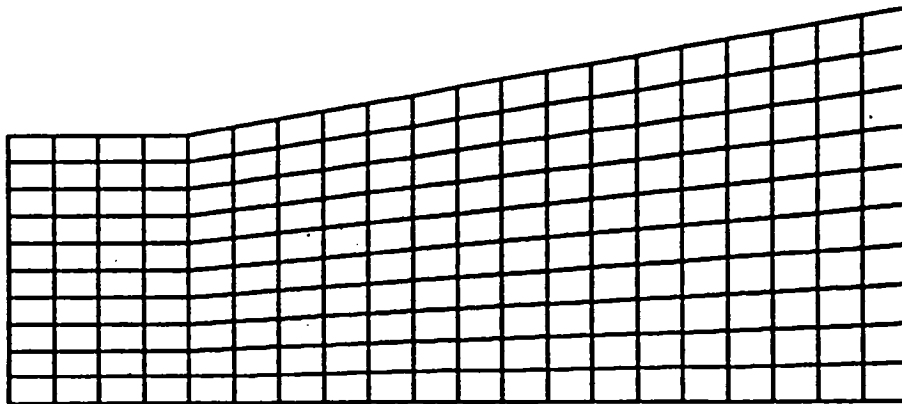
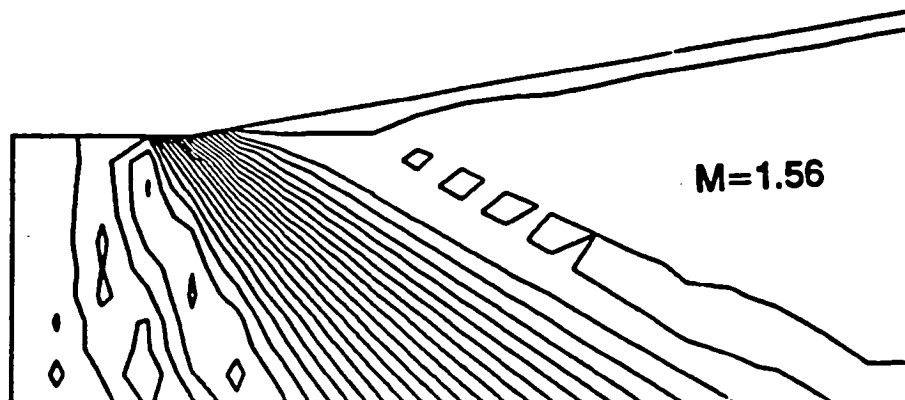
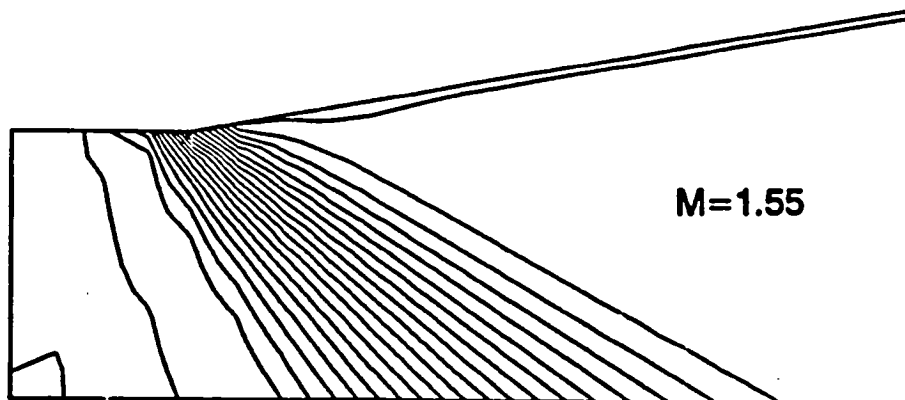


Figure B-6. Expansion test case grid; 21 x 11 nodes.



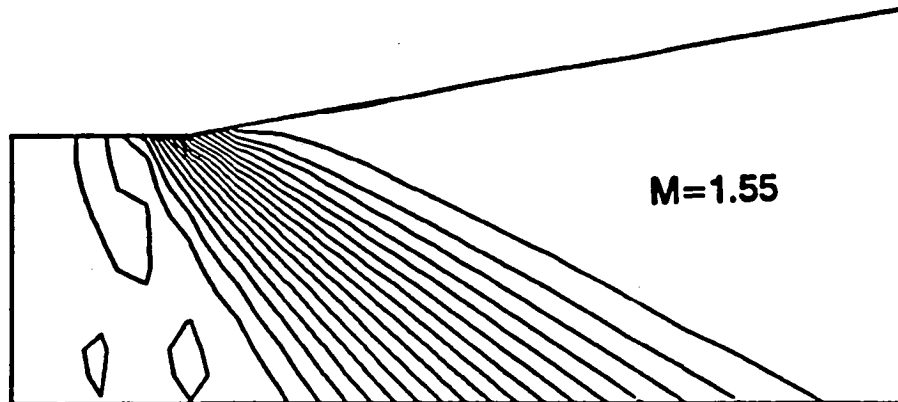
a)  $C_d = 0$ .



b)  $C_d = 0.025$ .

Figure B-7. 10° Expansion test case results at various levels of damping. Mach number contours (.02 contour increments).





c)  $C_d = .05$ .

Figure B-7. Concluded

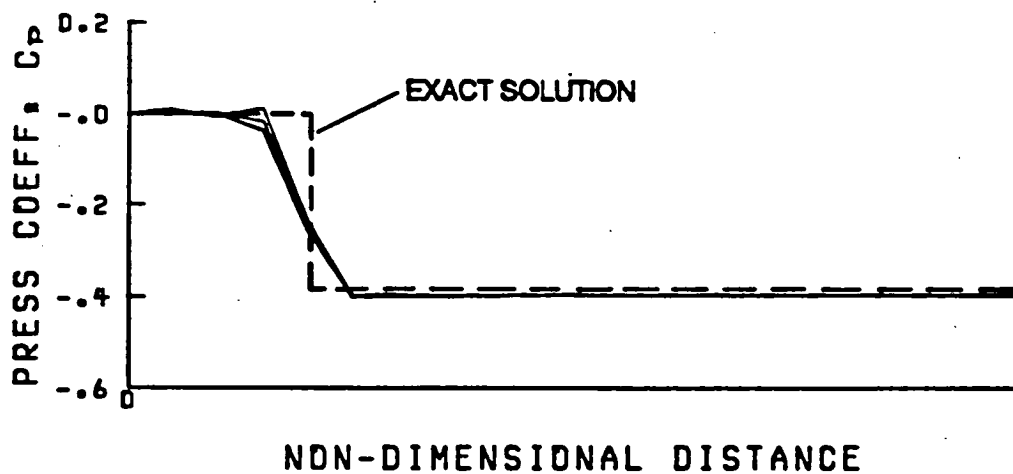


Figure B-8. Wall pressure distributions for  $10^\circ$  expansion test case at various levels of damping.

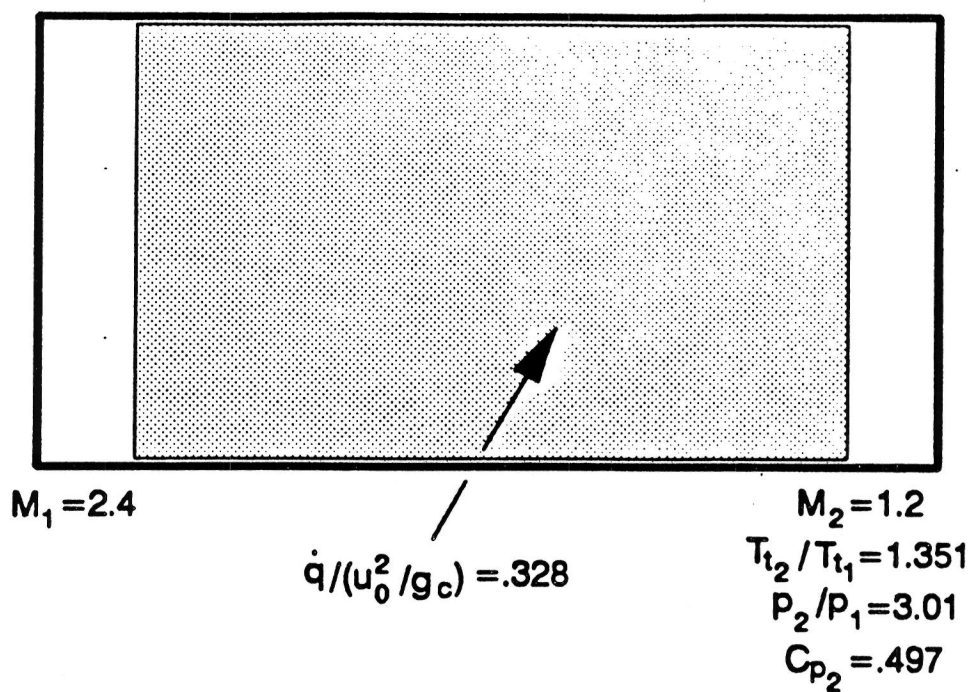


Figure B-9. Rayleigh flow test case;  $\dot{q} / (u_0^2 / g_c) = .328$ .

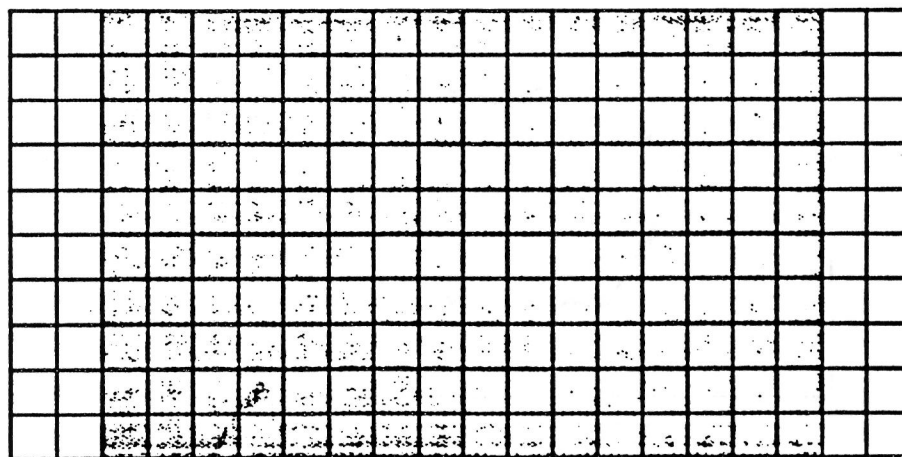


Figure B-10. Rayleigh flow test case grid and heat addition region; 21 x 11 nodes.

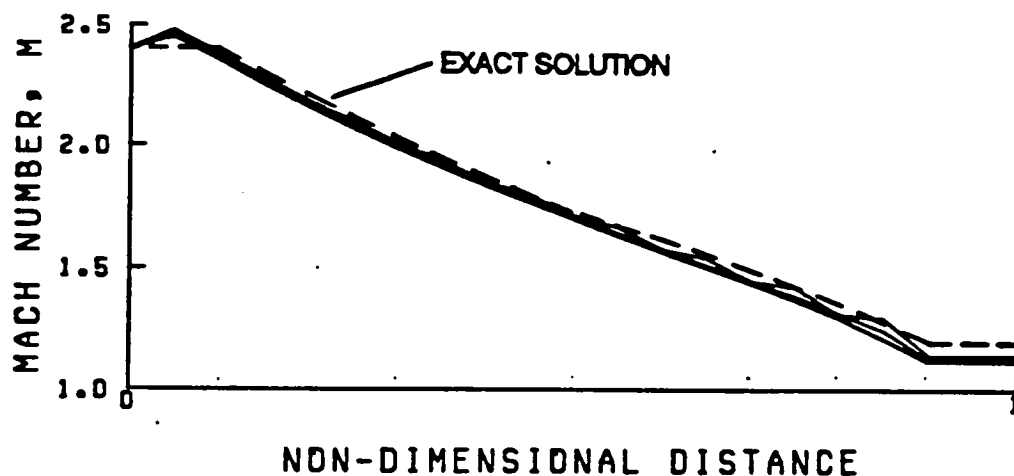


Figure B-11. Mach number distributions for Rayleigh flow test case at various levels of artificial damping.

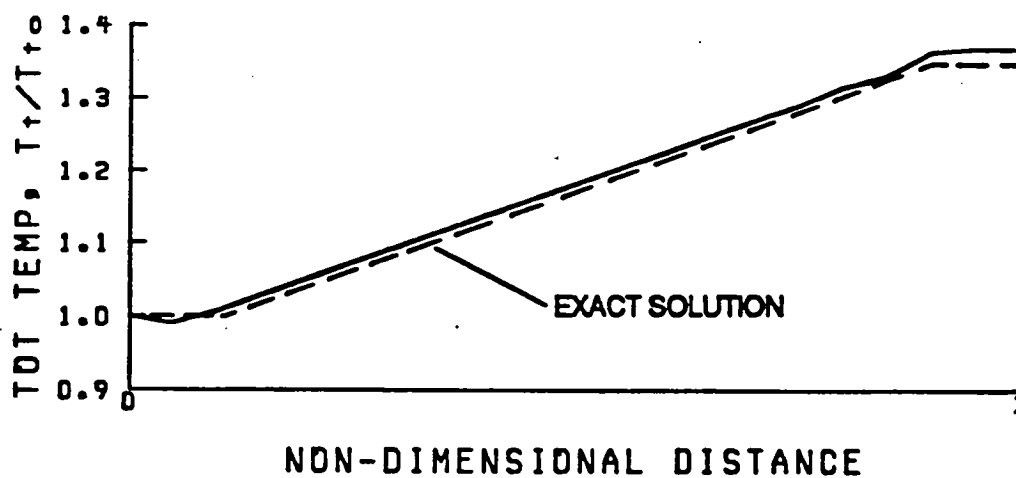


Figure B-12. Total temperature distributions for Rayleigh flow test case at various levels of artificial damping.

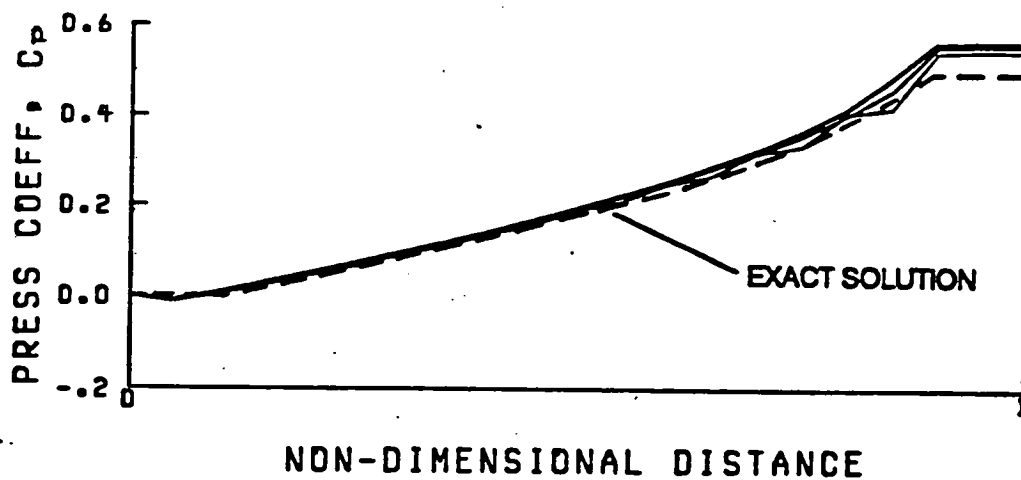


Figure B-13. Pressure distributions for Rayleigh flow test case at various levels of artificial damping.

## APPENDIX C - WATER-COOLED TOTAL TEMPERATURE PROBE DATA REDUCTION

The water-cooled total temperature probe used was based on an existing "bare wire in crossflow" design<sup>1</sup>. To withstand expected temperatures greater than 4000° Rankine, an iridium-40% rhodium vs. iridium thermocouple pair was used. The cost of these precious metals made it necessary to splice the wires with copper wire a short distance away from the sensor within the water jacket. This splice creates a variable temperature reference junction which must be independently measured. The temperature of this reference junction was measured with a standard Type T" (copper-constantan) thermocouple. Figure C-1 depicts schematically the thermocouple circuit. Tables of voltage (electromotive force or emf) from the wire manufacturer were based on a 0°C reference junction, and so the following procedure was required to infer the indicated gas total temperature from the measured emf. The emf measured is the emf induced at the Ir40%Rh vs. Ir pair minus the emf induced at the reference junction due to the copper splice:

$$emf_{meas} = emf_{T_g} - emf_{T_{ref}} \quad [C-1]$$

Adding and subtracting the emf for a 0° reference junction results in the following equation:

$$emf_{meas} = (emf_{T_g} - emf_{0^\circ C}) - (emf_{T_{ref}} - emf_{0^\circ C}) \quad [C-2]$$

The last term in equation C-2 represents the emf generated by an Ir40%Rh

vs. Ir pair with a 0°C reference, so the tables can be entered at the measured reference temperature to obtain this value. This emf is then added to that measured to obtain the emf based on a 0°C reference:

$$emf_{T_r} - emf_{0^\circ C} = emf_{meas} + (emf_{T_{ref}} - emf_{0^\circ C}) \quad [C-3]$$

This then is the emf used to obtain the indicated gas temperature from the tables. The indicated temperature must then be corrected for conduction, recovery, and radiation losses. The bare-wire in crossflow design afforded a wire length to diameter ratio of approximately 15 which makes a conduction correction unnecessary.

#### Recovery correction

The recovery correction is a function of Mach number, and compensates for the fact that the entire thermocouple junction is not immersed in the total temperature of the flow. The recovery correction used is a function of Mach number and pressure and was taken directly from reference 1. The correction is small, being a maximum of about 3% for subsonic Mach numbers. The effect of pressure on this factor is negligible for the bare-wire in crossflow design. The Mach number at the probe was not measured, and so was estimated in the following manner, using the fact that the external burning process occurs at nearly constant velocity.

The gas composition at the probe was inferred by assuming that the indicated probe temperature was equal to the adiabatic flame temperature

of a fuel-lean hydrogen-air mixture at one atmosphere. The composition of these combustion products along with the indicated temperature was used to compute a sound speed. The ratio of freestream velocity to this sound speed was then used as the estimated Mach number at the probe. For low probe temperatures where the estimated probe Mach number was supersonic, the recovery correction curve was extrapolated.

The preceeding methodology accounts for the variation of recovery correction with Mach number only approximately, but is sufficient given the magnitude of the correction, and the preliminary nature of the experiments.

#### Radiation correction

The radiation correction used is that presented by Glawe<sup>2</sup> et. al. For unshielded probes, the equation used reduces to the following:

$$\Delta T_{rad} = T_i \frac{K_{rad}}{\sqrt{M p/p_0}} \left( \frac{T_i}{T_0} \right)^{3.82} \quad [C-4]$$

Where	$\Delta T_{rad}$	correction in deg. K
	$K_{rad}$	radiation correction coefficient
	$M$	stream Mach number
	$p$	stream static pressure in atmospheres
	$p_0$	reference pressure of 1 atmosphere
	$T_i$	probe indicated temperature in deg. K
	$T_0$	reference temperature (555°K)

The stream Mach number computed for the recovery correction was used, and

the pressure was taken as the free-jet exit pressure. An experimentally determined relation for  $K_{rad}$  in terms of wire diameter is given for unshielded probes, and yields a value of 2 for the .032" dia. wire used. This value of  $K_{rad}$  resulted in corrected temperatures which were in excess of that theoretically possible for hydrogen and air. The  $K_{rad}$  relation was based on data which for a number of reasons may not be strictly applicable to the present situation. First, it was obtained in natural gas combustion products at a maximum temperature of 2550°R. Also, type "K" thermocouples were used which would have a different emittance than the Iridium-Rhodium wire. For these reasons, it was deemed appropriate to adjust the value of  $K_{rad}$  to .4 such that the theoretical maximum equilibrium temperature for hydrogen and air at one atmosphere would not be exceeded.

The maximum radiation corrections resulting were only 6% of the corrected temperature, so again the approximations used would not lead to large error in the final measurement. Obviously, more accurate measurements could have been obtained by calibrating the probe at the conditions of interest, but the nature of the test objectives did not warrant this extra effort.



### References

1. Glawe, G.E., Simmons, F.S., and Stickney, T.M., "Radiation and Recovery Corrections and Time Constants of Several Chromel-Alumel Thermocouple Probes in High-Temperature, High-Velocity Gas Streams," NACA TN 3766, Oct. 1956.
2. Glawe, G.E., Holanda, R., and Krause, L.N., "Radiation and Recovery Corrections and Time Constants of Several Sizes of Shielded and Unshielded Thermocouple Probes for Measuring Gas Temperature," NASA TP 1099, Jan. 1978.

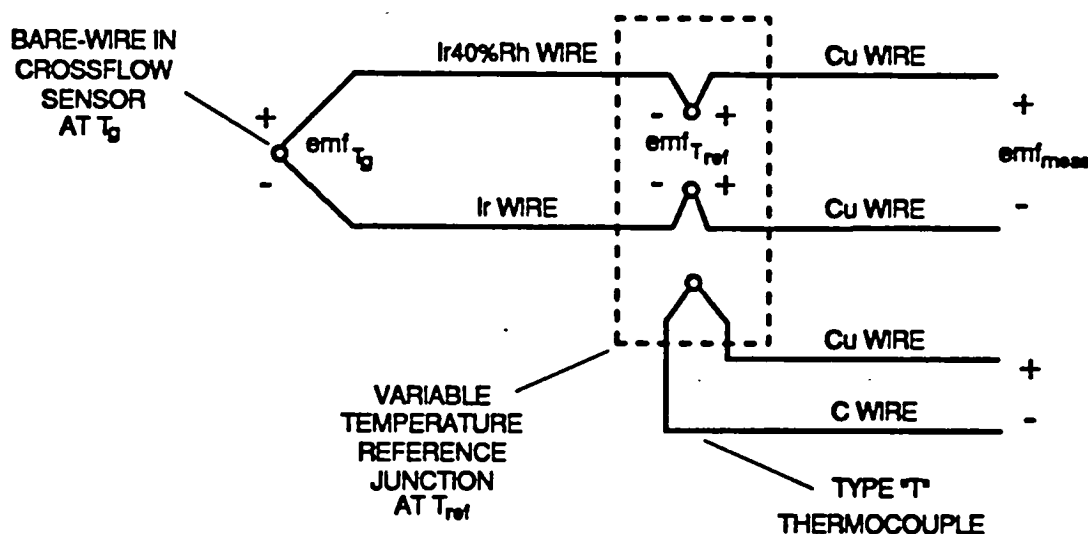


Figure C-1. Schematic of Ir40%Rh vs. Ir thermocouple with variable temperature reference junction.

**APPENDIX D - EXPANSION RAMP FUEL INJECTOR AND FLAMEHOLDER CONFIGURATIONS**

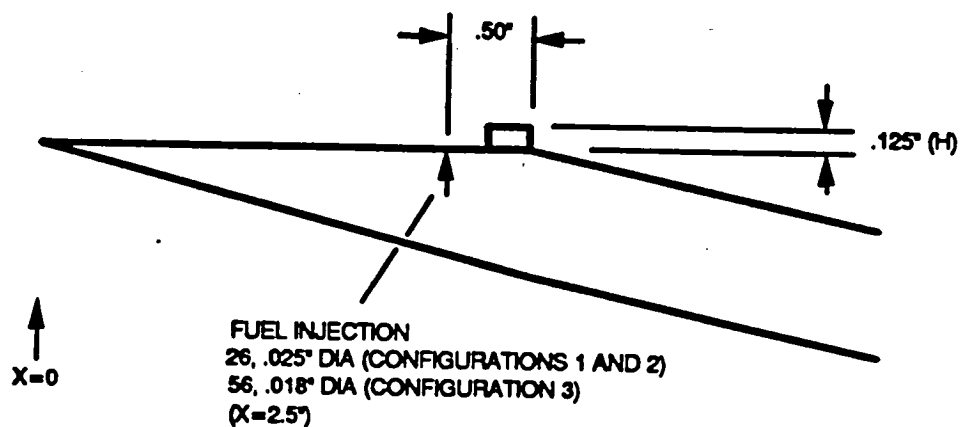


Figure D-1. Configurations 1,2 and 3 (flameholder "A").

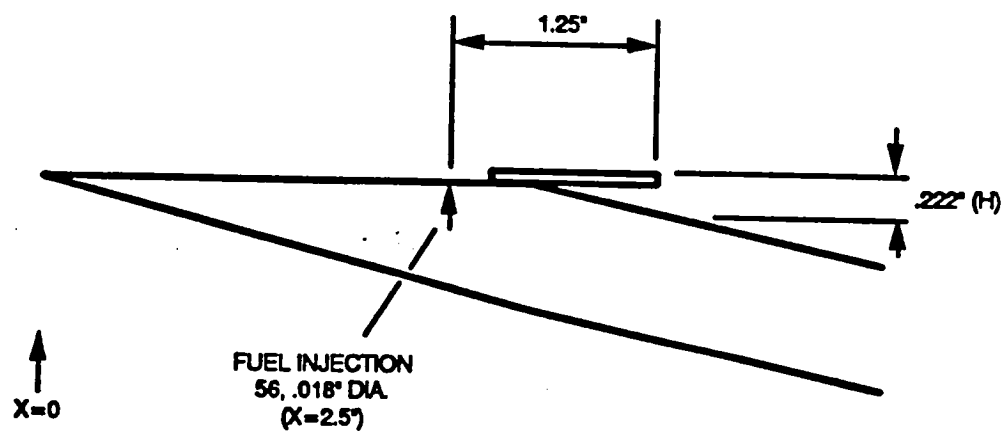


Figure D-2. Configuration 4 (flameholder "B").

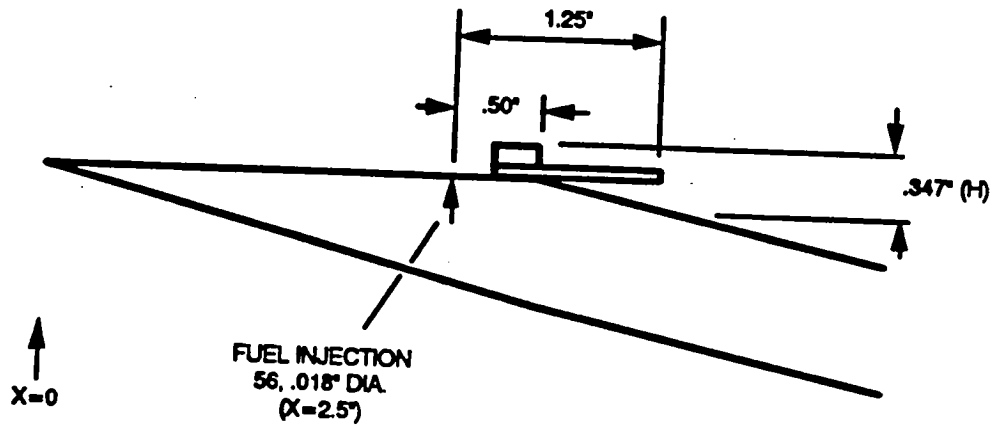


Figure D-3. Configuration 5 (flameholder "C").

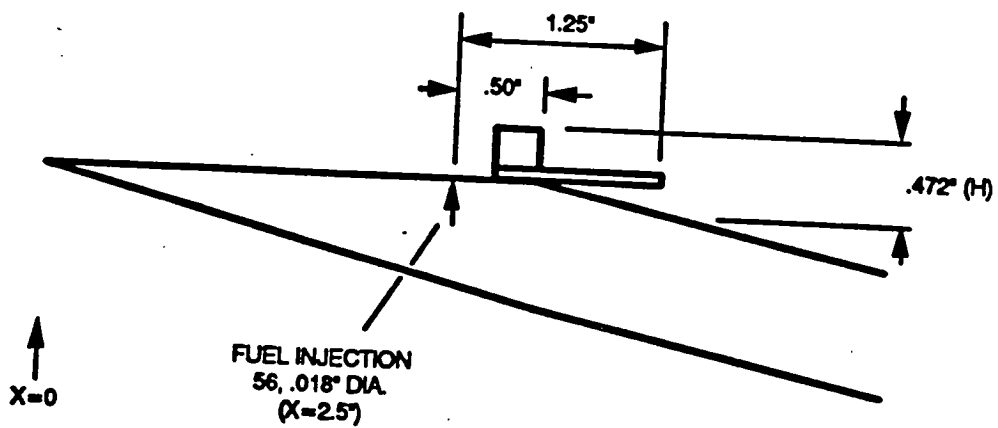


Figure D-4. Configuration 6 (flameholder "D").

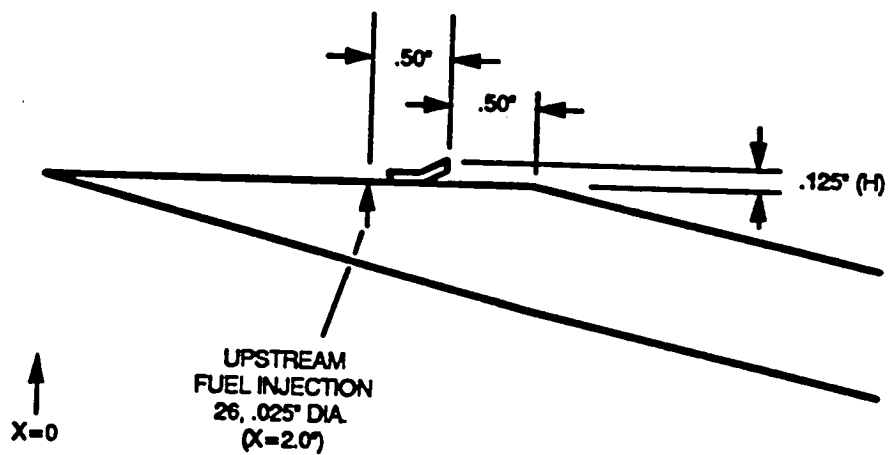


Figure D-5. Configuration 7 (flameholder "E").

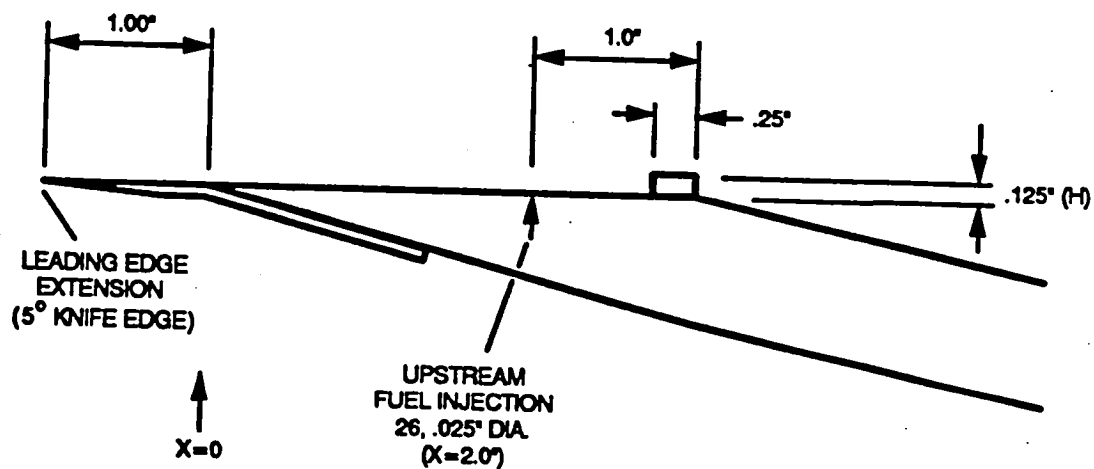


Figure D-6. Configuration 8 (flameholder "A").

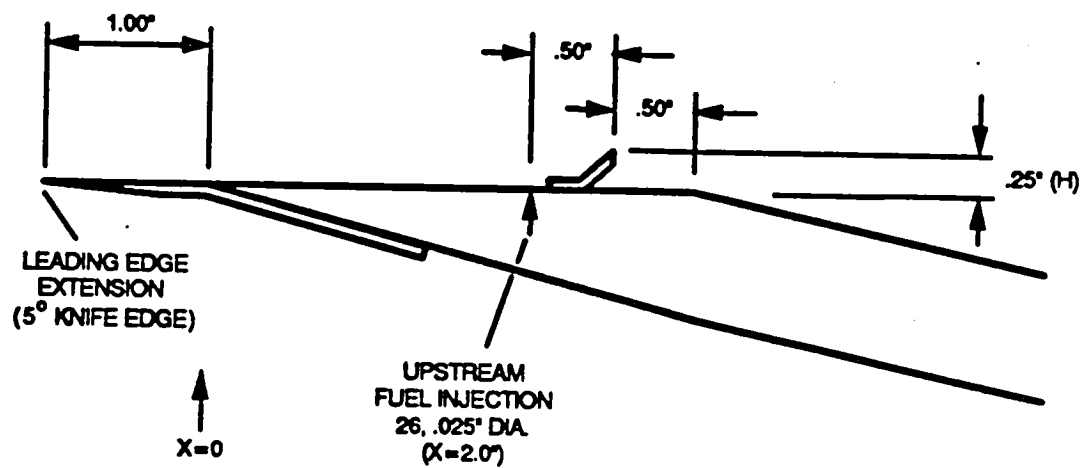


Figure D-7. Configuration 9 (flameholder "F").

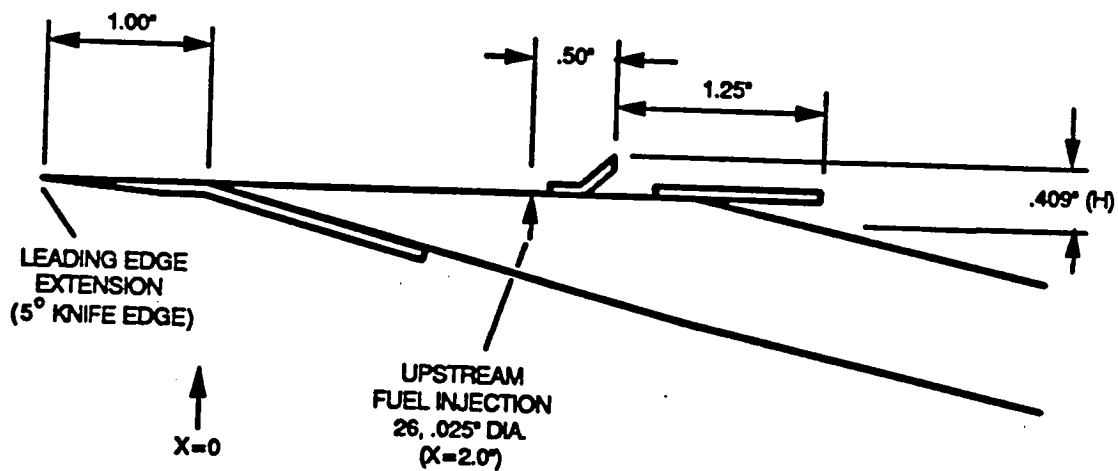


Figure D-8. Configurations 10 and 11 (Flameholder "G").

## REFERENCES

1. Aerodynamics of Base Combustion, ed. S. N. B. Murthy, et al., MIT Press, Cambridge, 1976, pp. 143-210.
2. Billig, F.S., "External Burning in Supersonic Streams," APL TG-912, May 1967, (JHU-APL).
3. Davis, T., Forney, H.B., Smith E. H., Tyson, T. L., and Wolf, R. L., "Two Dimensional External Combustion Airfoil," Experiment, Inc., TM-704, July 26, 1955.
4. Fletcher, E.A., Dorsch, R.G., and Gerstein, M., "Combustion of Aluminum Borohydride in a Supersonic Wind Tunnel," NACA RM E55D07a, 1955.
5. Dorsch, R.G., Serafini, J.S., and Fletcher, E.A., "A Preliminary Investigation of Static-Pressure Changes Associated With Combustion of Aluminum Borohydride in a Supersonic Wind Tunnel," NACA RM E55F07, 1955.
6. Dorsch, R.G., Serafini, J.S., and Fletcher, E.A., "Exploratory Investigation of Aerodynamic Effects of External Combustion of Aluminum Borohydride in Airstream Adjacent to Flat Plate in Mach 2.46 Tunnel," NACA RM E57E16, 1957.
7. Serafini, John S., Dorsch, Robert G., and Fletcher, Edward A., "Exploratory Investigation of Static and Base-Pressure Increases Resulting from Combustion of Aluminum Borohydride Adjacent to Body of Revolution in Supersonic Wind Tunnel," NACA RM E57E15, 1957.
8. Dorsch, R.G., Serafini, J.S., Fletcher, E.A., and Pinkel, I.I., "Experimental Investigation of Aerodynamic Effects of External Combustion in Airstream Below Two-Dimensional Supersonic Wing at Mach 2.5 and 3.0," NASA Memo 1-11-59E.
9. Dorsch, R.G., Harrison, A., and Dryer, M., "Investigation of Aerodynamic Effects of External Combustion Below Flat Plate Model in 10-by 10-foot Wind Tunnel at Mach 2.4," NASA TN D-282, April, 1960.
10. Billig, F.S. "A Study of Combustion in Supersonic Streams," Bumblebee Series Report No. 321, The Johns Hopkins University, Applied Physics Lab, July 1964.
11. Dugger, G.L., Deklau, B., Billig, F.S., and Matthews, S.E., "Summary Report on External Ramjet Program," JHU/APL, TG-419, Oct., 1961.
12. Townend, L.H., and Reid, J., "Some Effects of Stable Combustion in

- Wakes Formed in a Supersonic Stream," in Supersonic Flows, Chemical Processes, and Radiative Transfer, Edited by D. B. Olfe and V. Zakkay, Pergamon Press, New York, 1964.
13. Strahle, W.C., "Theoretical Consideration of Combustion Effects on Base Pressure in Supersonic Flight," Twelfth Symposium (International) on Combustion, July 14-20, 1968 pp. 1163-1173, The Combustion Institute, 1969.
  14. Strahle, W.C., "Some Outer Limits in the Theory of Transonic Flow with External Burning," Combustion Science and Technology, Vol. 1, 1970, pp. 357-363.
  15. Fuhs, A.E., "Quasi Area Rule for Heat Addition in Transonic and Supersonic Flight Regimes," Naval Postgraduate School, Technical Report AFAPL-TR-72-10, Aug. 1972.
  16. Smithey, W., "Projectile Thrust-Drag Optimization With External Burning," Ph.D. Thesis, Naval Postgraduate School, Monterey, CA, AD-784764, June 1974.
  17. Caswell, G.J., "Base Drag Reduction by External Burning in the Inviscid Stream," M.S. Thesis, Naval Postgraduate School, Monterey, CA, Sept. 1973.
  18. Naber, M. E., "Investigation of External Burning Assisted Projectile-Reduction of Base Drag of Supersonic Projectile by Increasing Base Pressure," M. S. Thesis, Naval Postgraduate School, Monterey, California, September 1973.
  19. Smithey, W., Naber, M., Caswell, G., and Fuhs, A.E., "External Burning Assisted Projectile - Theory and Experiment," 9th Joint Propulsion Conference, Las Vegas, Nev., Nov. 5-7, 1973, AIAA Paper 73-1193.
  20. Neal, D.H., Hubbartt, J.E., Strahle, W.C., and Wilson, W.W., "Effects of External Compression on an axisymmetric Turbulent Near Wake," AIAA Journal, Vol. 16, No. 9, September, 1978, pp. 940-947.
  21. Neal, D.H., Hubbartt, J.E., Strahle, W.C., and Wilson, W.W., "Experiments and Analysis Related to External Burning for Propulsion," Air Force Office of Scientific Research, Wash., D.C., AFSOR-TR-77-0602, March, 1977.
  22. Strahle, W.C., Hubbartt, J.E., Neale, D.H., and Huval, D.J., "Experiments Related to External Burning for Propulsion," Air Force Office of Scientific Research, Wash., D.C., AFOSR-77-1291, Oct, 1977.
  23. Neal, D.H., Hubbartt, J.E., and Strahle, W.C., "Mach 3 Hydrogen External/Base Burning," 18th Aerospace Sciences Mtg., Pasadena, CA., Jan. 14-16, 1980, AIAA Paper 80-0280.



24. Strahle, W.C., Hubbartt, J.E., and Waltrick, R., "Base Burning Performance at Mach 3," AIAA Paper 81-1469, 17th Joint Propulsion Conference, Colorado Springs, CO., 1981.
25. Hubbartt, J.E., Strahle, W.C., "External/Base Burning for Base Drag Reduction at Mach 3," AIAA Journal, Vol. 19, p. 1502-1504, Nov. 1981.
26. Schadow, K.C., and Chieze, D.J., "Experimental Study on Base Drag Reduction With Combined Lateral and Axial Injection, AIAA Journal, Vol. 16, No. 10, October, 1978, pp. 1084-1089.
27. Schadow, K.C., "Base Drag Reduction By External Burning," Combustion and Detonation Processes; Annual International Mtg., 10th, Karlsruhe, W. Germany, June 27-29, 1979, Proceedings, pp. 243-260.
28. Schadow, K.C., "Experimental Investigation of Combined External Burning/Base Burning," AIAA, SAE, ASME 16th Joint Propulsion Conference, Hartford, CT, 1980, AIAA Paper 80-1257.
29. Cavalleri, R.J., "Experimental Evaluation of the External Burning Rocket Concept," 12th Joint Propulsion Conference, Palo Alto, CA., July 26-29, 1976, AIAA Paper 76-641.
30. Director, M. N., "Evaluation of an External Burning Experiment," 13th Joint Propulsion Conference, Orlando, Fl., July 11-13, 1977, AIAA Paper No. 77-926.
31. Pinkel, I.I., and Serafini, J. S., "Graphical Method for Obtaining Flow Field in Two-Dimensional Supersonic Stream to Which Heat is Added," NACA Technical Note 2206, Nov., 1950.
32. Pinkel, I.I., Serafini, J. S., and Gregg, J. L., "Pressure Distribution and Aerodynamic Coefficients Associated with Heat addition to Supersonic Air Stream Adjacent to Two-Dimensional Supersonic Wing," NACA RM E51K26, 1952.
33. Tsien, H.S., and Beilock, M., "Heat Source in a Uniform Flow," Journal of Aeronautical Science, Dec. 1949, p. 756.
34. Schetz, J.A., Favin, S., and Billig, F.S., "Analytical Comparison of the Performance of Different Base-Burning Modes," AIAA Journal, Vol. 14, Sept., 1976, pp.1337-1338.
35. Schetz, J.A., Billig, F.S., Favin, S., "Approximate Analysis of Base Drag Reduction by Base and/or External Burning for Axisymmetric, Supersonic Bodies," AIAA Paper 80-1258, 16th Joint Propulsion Conf., Hartford, Connecticut, 1980.
36. Shapiro, A.H. The Dynamics and Thermodynamics of Compressible Fluid Flow, The Ronald Press Co., New York, 1953.

37. Vaughan, J.C., "A Two-Dimensional Study of The Jet Interaction and Downstream External Burning Resulting From a Gaseous Sidejet Expanding Into a Supersonic Stream," Ph.D. Thesis, Purdue Univ., West Lafayette, Ind. 1972.
38. Callens, E.E., Miller, J.T., and Potter, J.L., "An Investigation of an Upper Stage Rocket Plane With External Burning Thrust Augmentation," ARO Inc., Arnold Air Force Station, Tenn., ARO-VKF-TR-72-94 AEDC-TR-72-181.
39. Marino, A., "Theoretical Performance with External Burning on Surface," General Applied Science Labs, Inc., Westbury, New York, Feb. 1965, GASL TR-506.
40. Harvey, D.W., and Catton, I., "A Model of External Burning Propulsion," 17th Aerospace Sciences Mtg., New Orleans, LA., Jan 15-17, 1979, AIAA Paper 79-0358.
41. Harvey, D.W., Davis, J.C., "External Burning Propulsion Analysis," 17th Joint Propulsion Conference, July 27-29, Colorado Springs, CO, AIAA Paper 81-1477.
42. Adamson T.C., Jr., and Nicholls, J.A., "On the Structure of Jets From Highly Underexpanded Nozzles Into Still Air," Journal of the Aero/Space Sciences, Jan. 1959, pp. 16-24.
43. Zukoski, E.E., and Spaid, F.W., "Secondary Injection of Gases into a Supersonic Flow," AIAA Journal, Vol. 2, No. 10, Oct. 1964, pp. 1689-1696.
44. Crist, S., Sherman, P.M., and Glass, D.R., "Study of the Highly Underexpanded Sonic Jet," AIAA Journal, Vol. 4, No. 1, Jan. 1966, pp. 68-71.
45. Schetz, J.A., and Billig, F.S., "Penetration of Gaseous Jets Injected into a Supersonic Stream," J. Spacecraft, Vol. 3, No. 11, Nov. 1966, pp. 1658-1665.
46. Schetz, J.A., Hawkins, P.F., and Lehman, H., "Structure of Highly Underexpanded Transverse Jets in a Supersonic Stream," AIAA Journal, Vol. 5, No. 5, May 1967, 882-884.
47. Orth, R.C., Schetz, J.A., and Billig, F.S., "The Interaction and Penetration of Gaseous Jets in Supersonic Flow, NASA CR-1386, 1969.
48. Chrans, L.J., and Collins, D.J., "Stagnation Temperature and Molecular Weight Effects in Jet Interaction," AIAA Journal, Vol, 8, No. 2, Feb. 1970, pp. 287-293.
49. Hersch, M., Povinelli, L.A., and Povinelli, F.P., "Optical Study of Sonic and Supersonic Jet Penetration From A Flat Plate Into A

Mach 2 Airstream, NASA TN D-5717, Mar. 1970.

50. Povinelli, F.P., and Povinelli, L.A., "Correlation of Secondary Sonic and Supersonic Gaseous Jet Penetration Into Supersonic Crossflows," NASA TN D-6370, June 1971.
51. Billig, F. S., Orth, R. C., and Lasky, M., "A Unified Analysis of Gaseous Jet Penetration," AIAA Journal, Vol. 9 No. 6, June 1971, pp. 1048-1058.
52. Broadbent, E.G., "Flows With Heat Addition and Associated Pressure Fields," Fluid Dynamic Transactions, Vol.6, Pt.I, 1972.
53. Anderson, D.A., Tannehill, J.C. and Pletcher, R.H., Computational Fluid Mechanics and Heat Transfer, McGraw-Hill, New York, 1984.
54. Roache, P.J., Computational Fluid Mechanics, Hermosa Publishers, Albuquerque, N.M., 1982.
55. Anderson, J.D. Jr., Hypersonic and High Temperature Gas Dynamics, McGraw-Hill, New York, 1989.
56. Zukoski, E.E, and Marble, F.E., "Experiments Concerning the Mechanism of Flame Blowoff From Bluff Bodies," Proceedings of the Gas Dynamics Symposium on Aerothermochemistry, Northwestern University, Evanston, Il, August, 1955.
57. Dezubay, E. A., "A Study of Flame Stability Based on Reaction Rate Theory," A.S.M.E. Paper 54-SA-27, May 5, 1954.
58. Jonash, E.R., Smith, A.L., and Hlavin, V.F., "Low-Pressure Performance of a Tubular Combustor with Gaseous Hydrogen," NACA RM E54L30a, May 9, 1955.
59. Winterfeld, G., "On the Stabilization of Hydrogen Diffusion Flames by Flame-Holders in Supersonic Flow at Low Stagnation Temperatures," Combustion in Advanced Gas Turbine Systems. Proceedings of an International Propulsion Symposium held at the College of Aeronautics, Cranfield, April 1967.
60. Haas, J.E., Chamberlin, R., and Dicus, J.E., "New Hypersonic Facility Capability at NASA Lewis Research Center," AIAA Paper 89-2534, 25th Joint Propulsion Conference, Monterey, CA, July, 1989.
61. Andrews, E.A. Jr., "A Subsonic to Mach 5.5 Subscale Engine Test Facility," AIAA-87-2052, 23rd Joint Propulsion Conference, San Diego, CA, June, 1987.
62. Bahn G.S., "Calculations on the Autoignition of Mixtures of Hydrogen and Air," NASA CR 112067, April 1972.

CASE	$M_0$	HEAT ADDITION DISTRIBUTION AXIAL/TRANSVERSE	GRID	DAMPING COEFF $C_d$	THRUST COEFF $C_T$	DELTA THRUST COEFF $\Delta C_T$	CONTROL VOLUME RESULT $\Delta C_{T,cv}$
1	1.4	CONST/CONST	80 x 40	.025	.028	.416	.420
2	"	GAUSS/CONST	"	"	.028	.416	"
3	"	GAUSS/PARBL	"	"	.030	.418	"
4	"	GAUSS/CONST	"	.0125	.034	.422	"
2	"	" "	"	.025	.028	.416	"
5	"	" "	"	.05	.029	.417	"
6	"	" "	50 x 25	.025	.036	.424	"
2	"	" "	80 x 40	"	.028	.416	"
7	"	" "	100 x 50	"	.026	.414	"
8	1.2	" "	80 x 40	"	.008	.519	.537
2	1.4	" "	"	"	.028	.416	.420
9	1.6	" "	"	"	.031	.342	.349
10	2.0	" "	"	"	.027	.244	.257
11	2.4	" "	"	"	.025	.189	.201

Table 3-1. Summary of Euler Analysis Runs.

CONFIG NO	NUMBER OF ORIFICES	ORIFICE DIA (IN)	INJECTION PLANE STA (IN)	FLAME HOLDER	PLUME BOUNDARY SIM	LEADING EDGE EXTENSION	UPPER SIDES
1	26	.025	2.5	A	NO	NO	NO
2	26	.025	2.5	A	YES	NO	NO
3	56	.018	2.5	A	YES	NO	NO
4	56	.018	2.5	B	YES	NO	NO
5	56	.018	2.5	C	YES	NO	NO
6	56	.018	2.5	D	YES	NO	NO
7	26	.025	2.0	E	YES	NO	NO
8	26	.025	2.0	A	YES	YES	NO
9	26	.025	2.0	F	YES	YES	NO
10	26	.025	2.0	G	YES	YES	NO
11	26	.025	2.0	G	YES	YES	YES

Table 4-1. Expansion ramp configuration summary.

CORR EQUIV RATIO,	REDUCED EQUIV RATIO,	NORM HEAT ADDED,	INFLOW STREAM HEIGHT,	CONTROL VOLUME THRUST COEFF, $C_{T,CV}$		EULER THRUST COEFF, $C_{T,Euler}$	
$\phi_{corr}$	$\phi_{Euler}$	$Q_{tot}$	$y_o/y_b$	(3-D)	(2-D)	(FLIGHT)	(FREEJET)
0	0	0	0	NA	NA	-.401	-.195
.248	.230	5.42	.197	-.055	-.070	-.075	-.034
.452	.400	9.42	.197	.023	.033	.035	.004
.662	.560	13.19	.197	.071	.101	.111	.033
.941	.740	17.43	.197	.110	.164	.190	.063
1.379	.840	19.78	.197	.127	.192	.223	.078

Table 4-2. Results of freejet and flight boundary Euler calculations with comparison to control volume results.

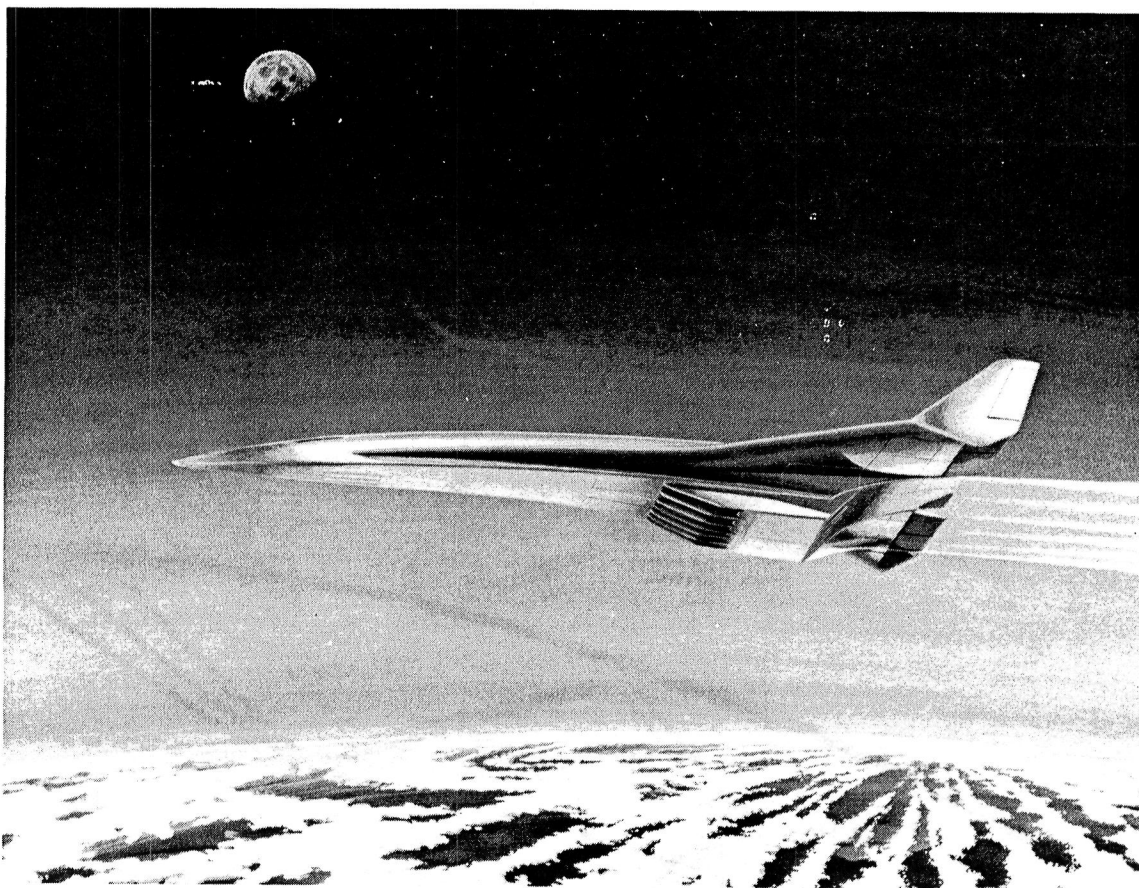
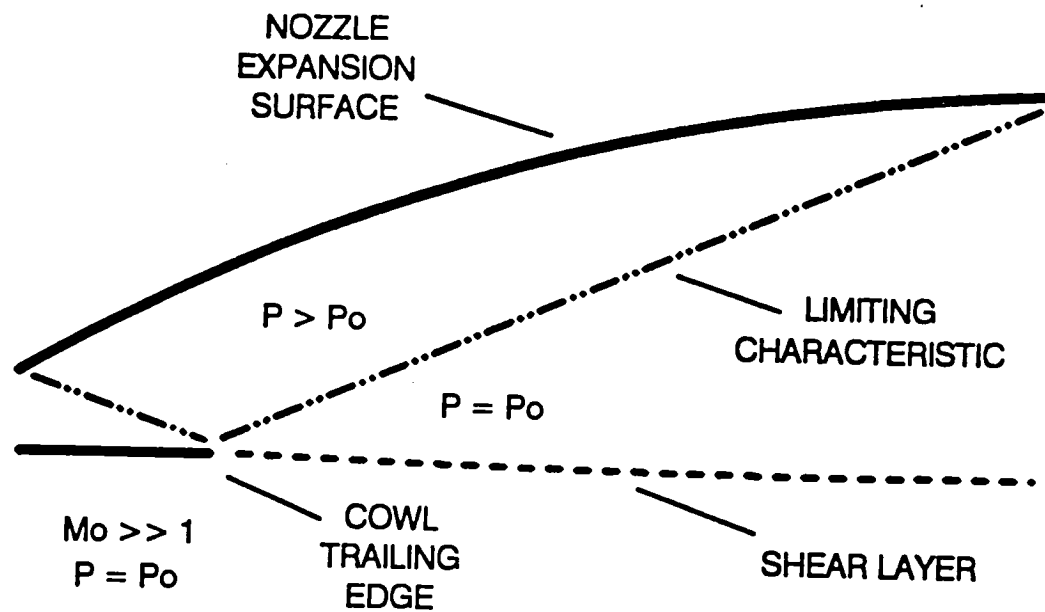
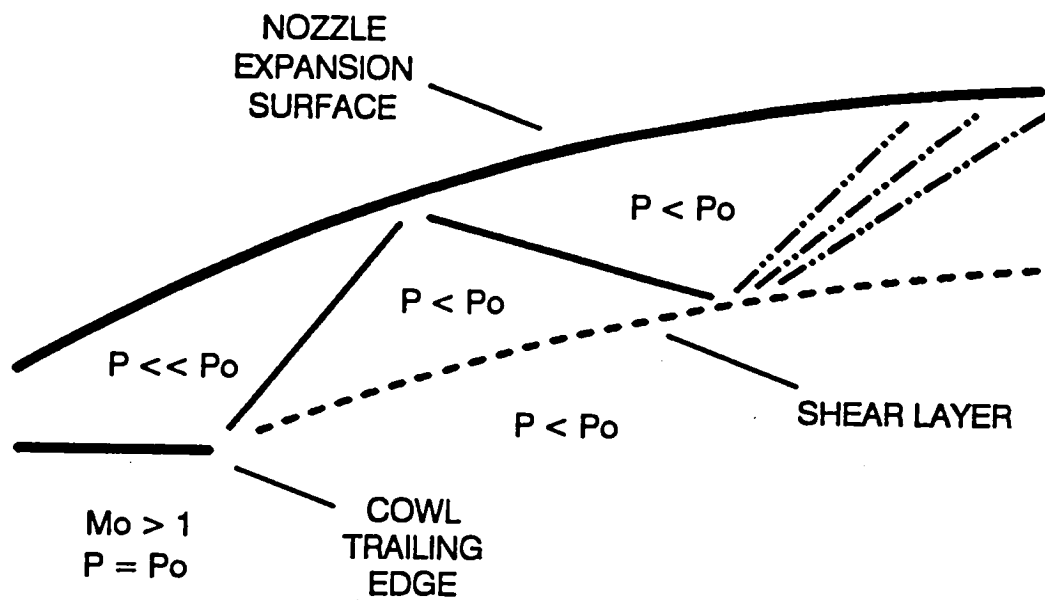


Figure 1-1. Artists conception of a single-stage-to-orbit vehicle.



a) On-design at high speed.



b) Over-expanded at transonic conditions.

Figure 1-2. Single expansion ramp nozzle design and operation.



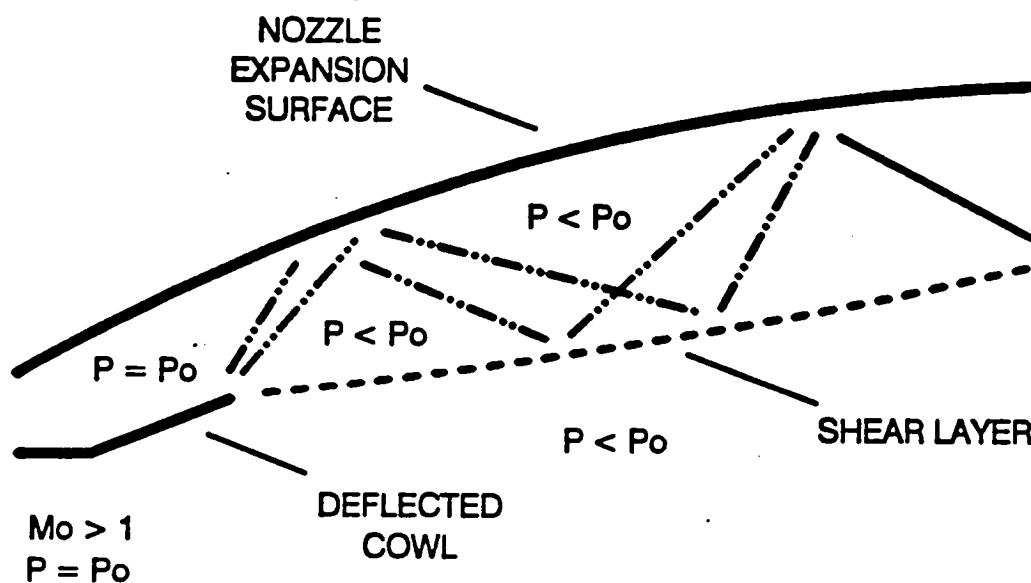


Figure 1-3. Cowl flap deflection to prevent internal over-expansion.

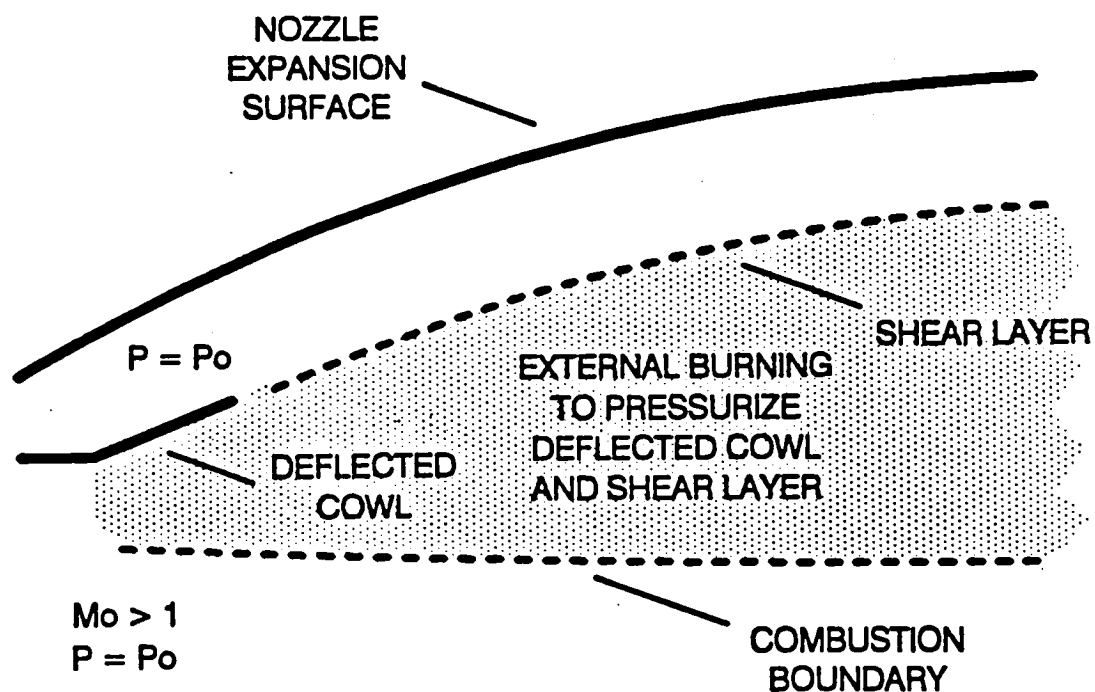


Figure 1-4. External burning concept applied to single expansion ramp nozzle.

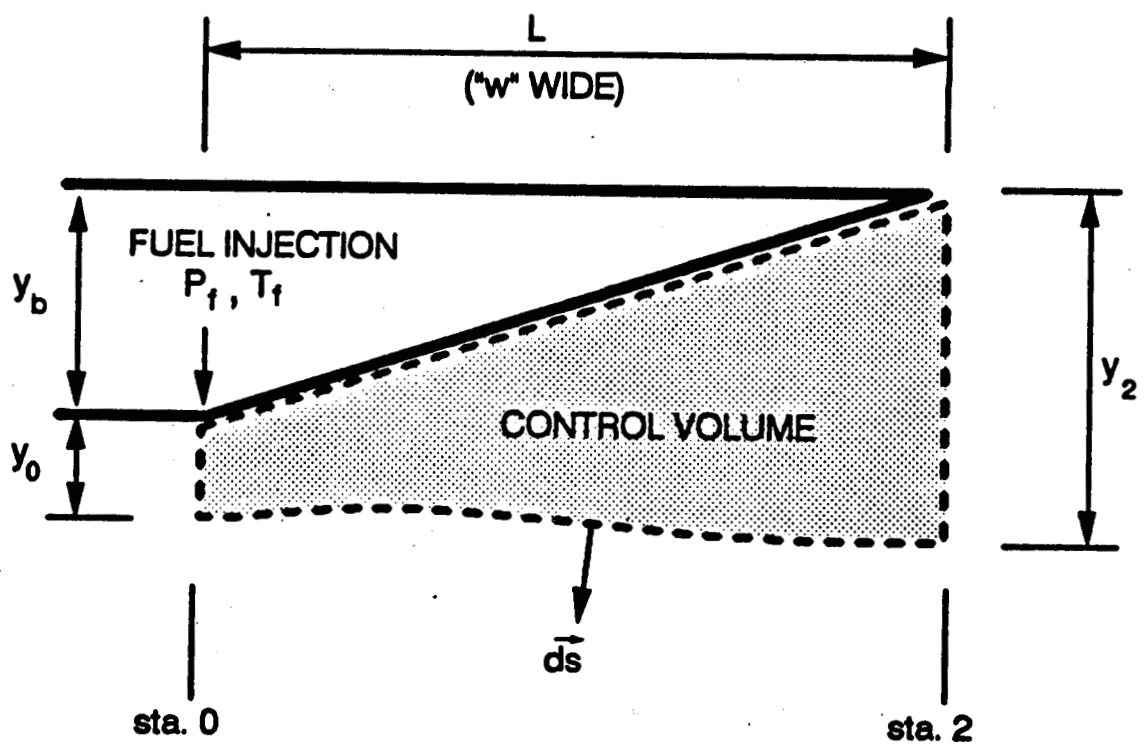
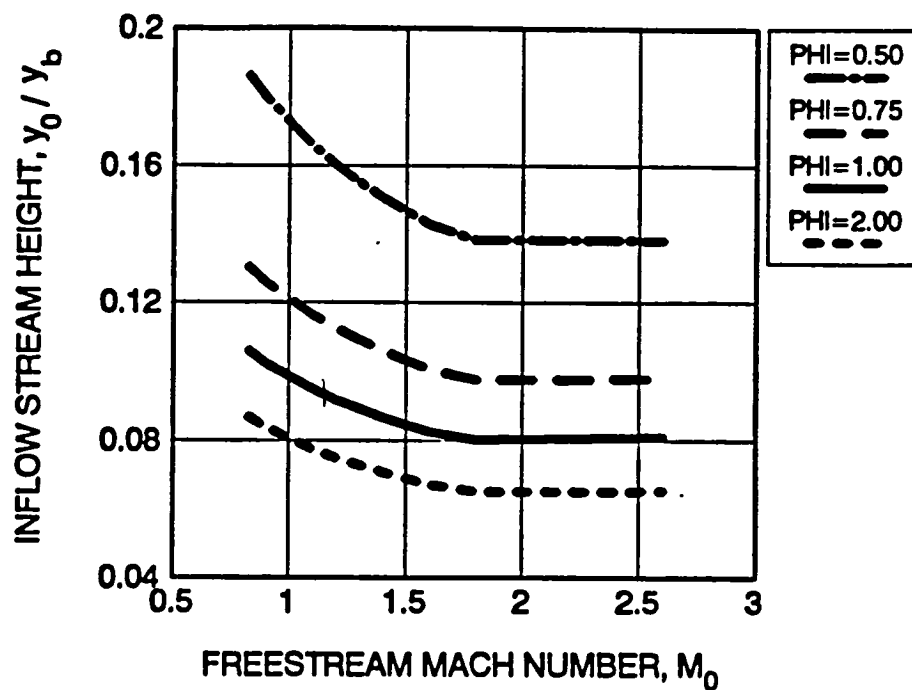
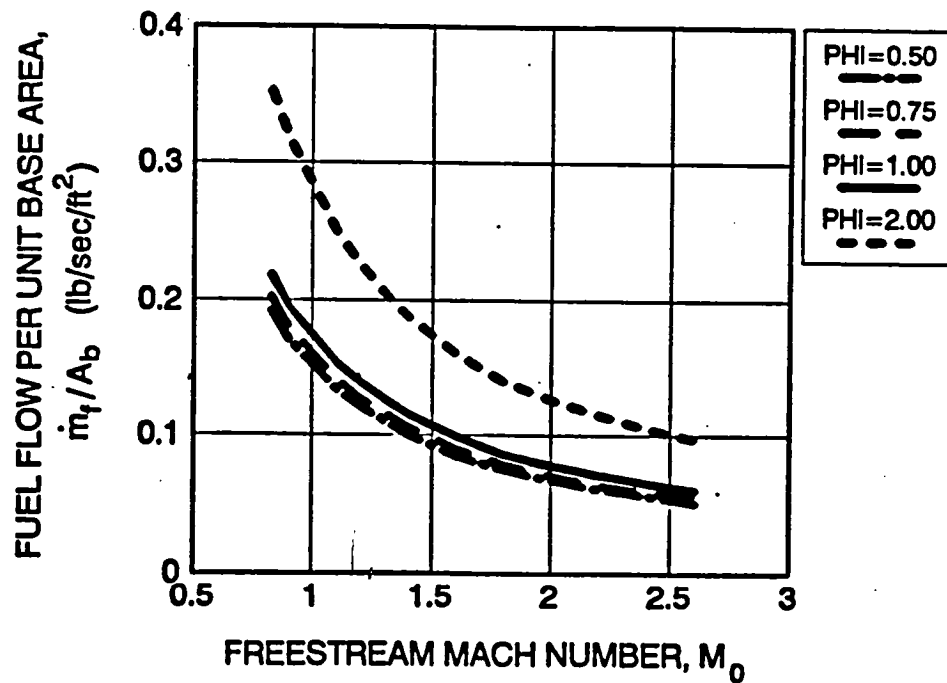


Figure 2-1. Control volume nomenclature.

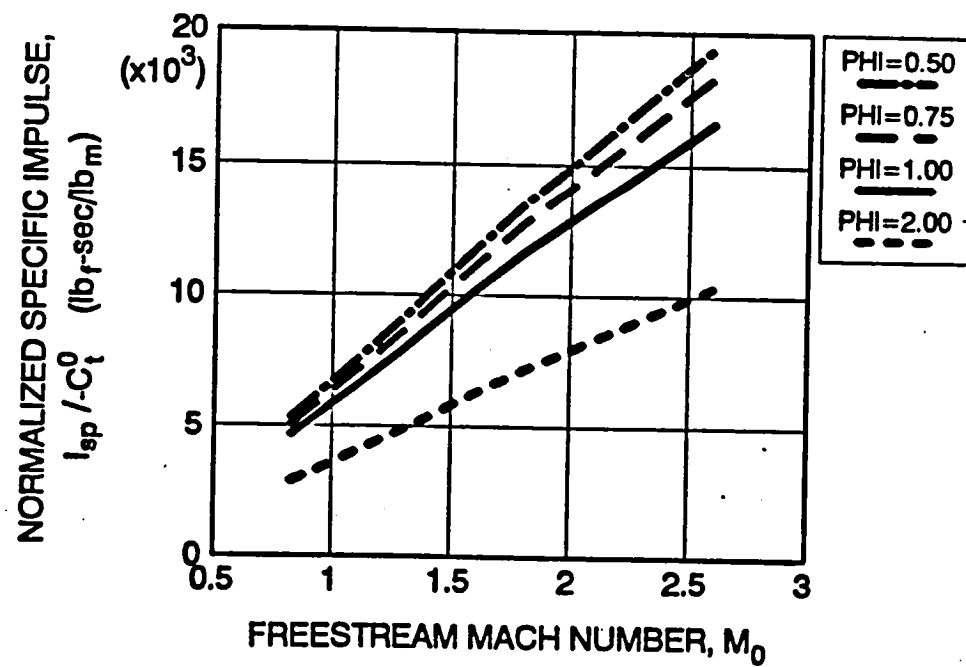


a) Ratio of inflow stream height to base height.



b) Fuel flow per unit base area.

Figure 2-2. Results at zero drag along a  $Q_0=1000$  psfa trajectory.



c) Normalized specific impulse.

Figure 2-2. Concluded.

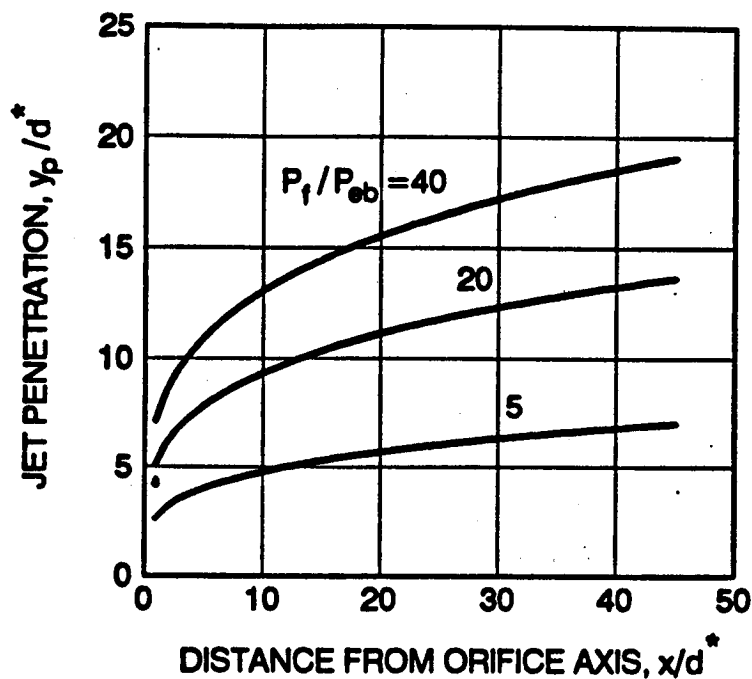


Figure 2-3. Trajectory of 1/2% fuel volume concentration from correlation of reference 50 for various fuel pressure ratios.

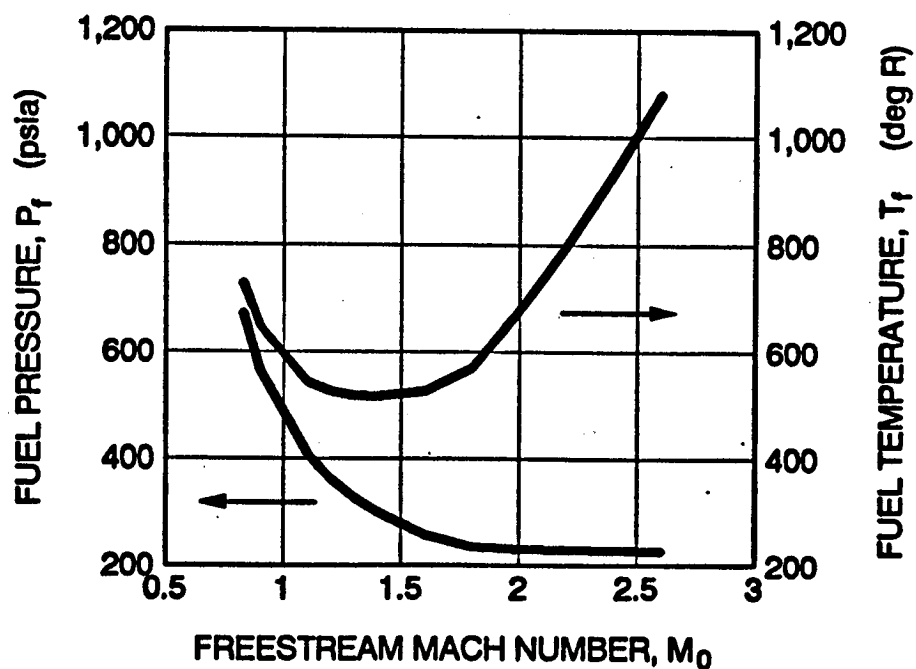
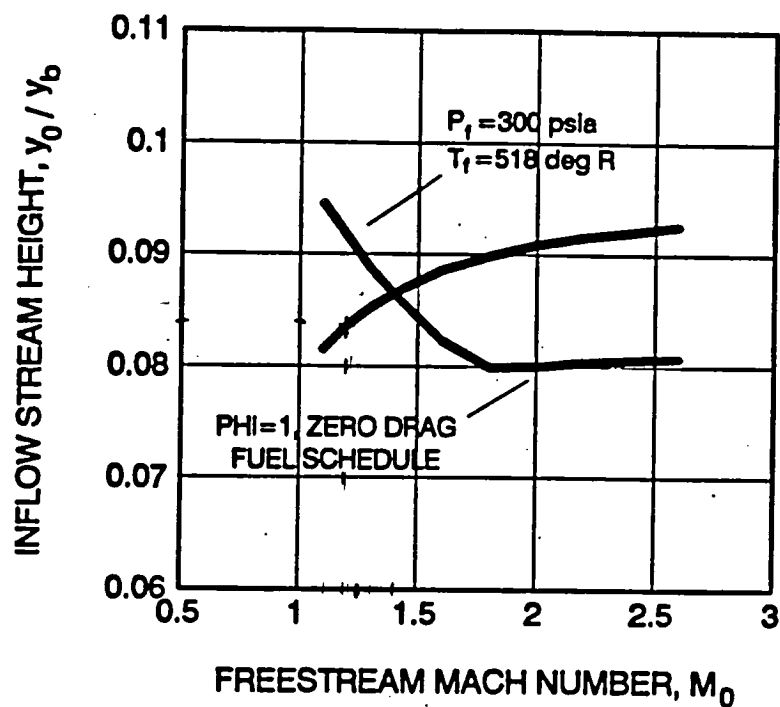
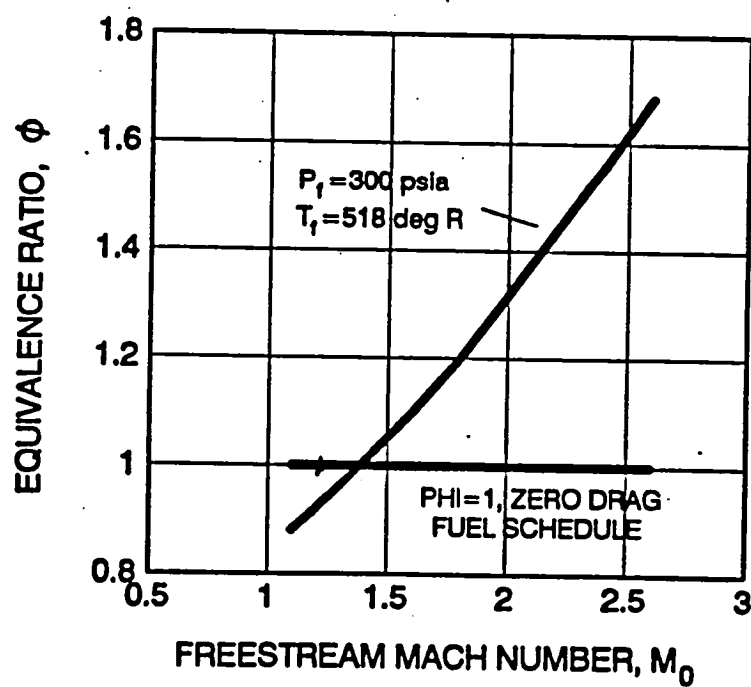


Figure 2-4. Fuel schedule required to maintain zero thrust at stoichiometric conditions with a fixed orifice geometry;  $Q_0=1000$  psfa,  $d^*/w=.005824$ ,  $S/d^*=9.485$ ,  $C_v=.9$ ,  $T_f=518^\circ\text{R}$ .

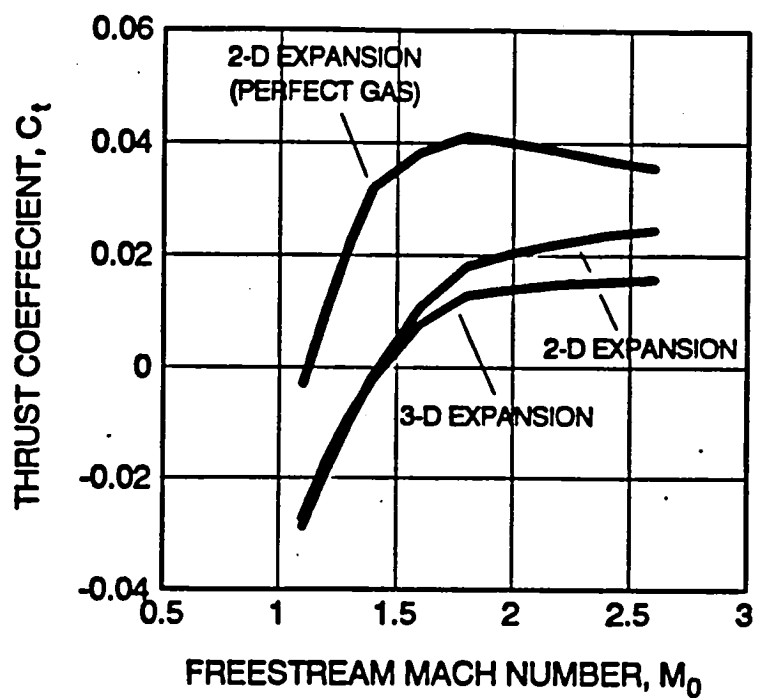


a) Ratio of inflow stream height to base height.

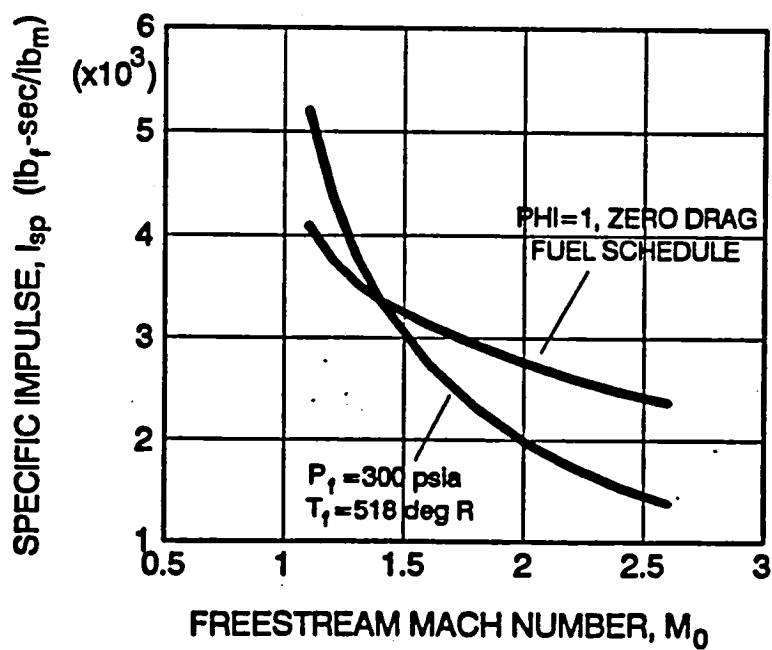


b) Equivalence ratio.

Figure 2-5. Results at constant fuel conditions for a fixed orifice geometry;  $Q_0 = 1000$  psfa,  $d^*/w = .005824$ ,  $S/d^* = 9.485$ ,  $C_v = .9$ ,  $T_t = 518^\circ\text{R}$ .



c) Thrust coefficient for various expansion assumptions;  $y_b/L=3.732$ ,  $w/y_b=2.5$ .



d) Specific impulse.

Figure 2-5. concluded.

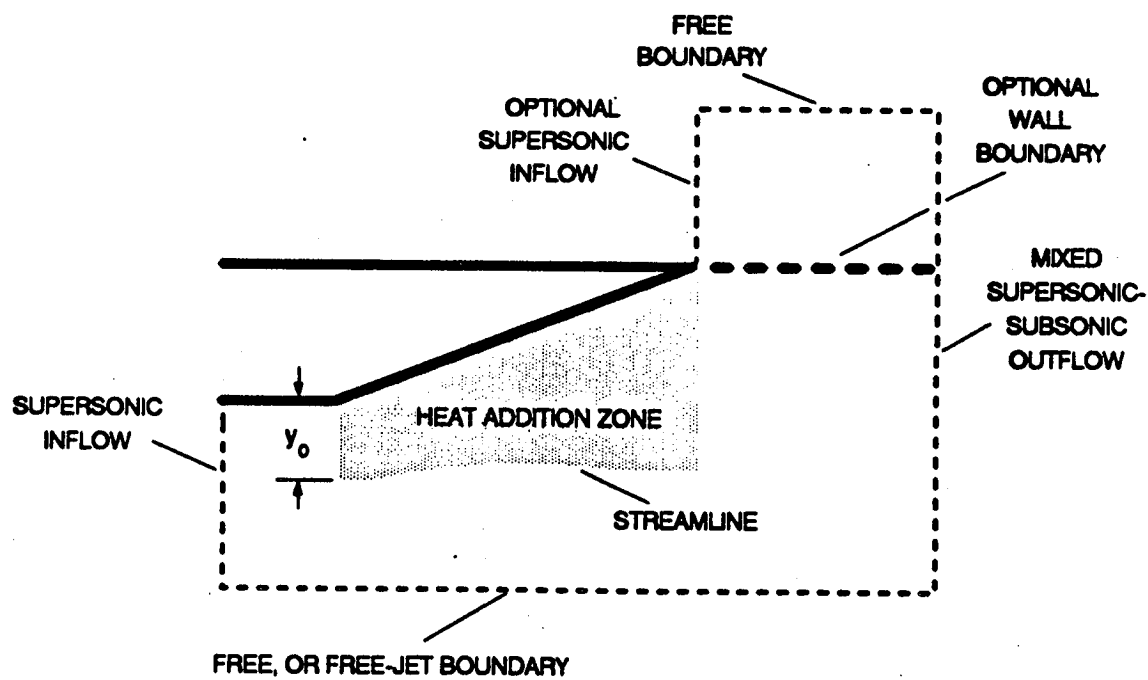


Figure 3-1. Euler analysis schematic.



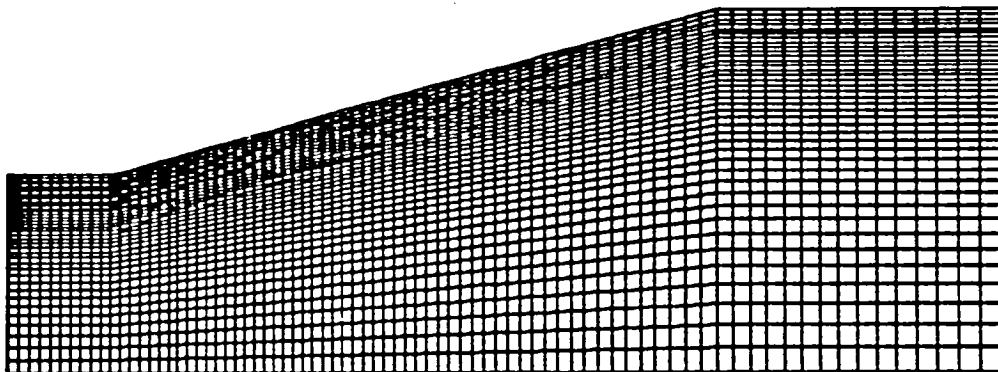


Figure 3-2. 80 x 40 grid.

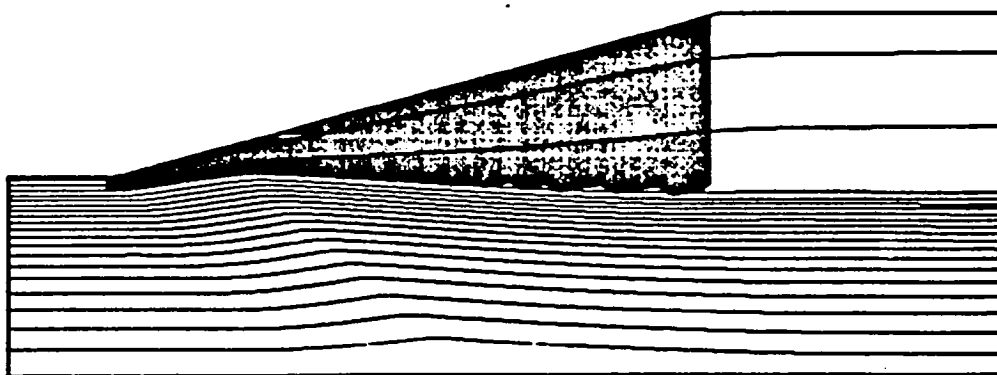
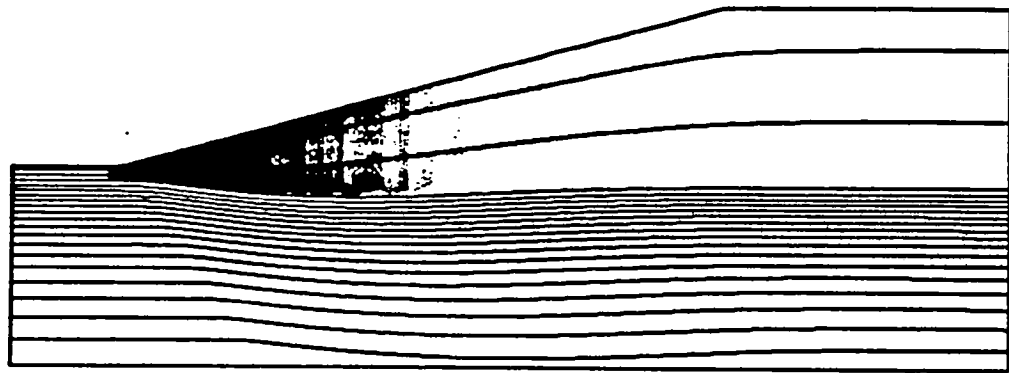
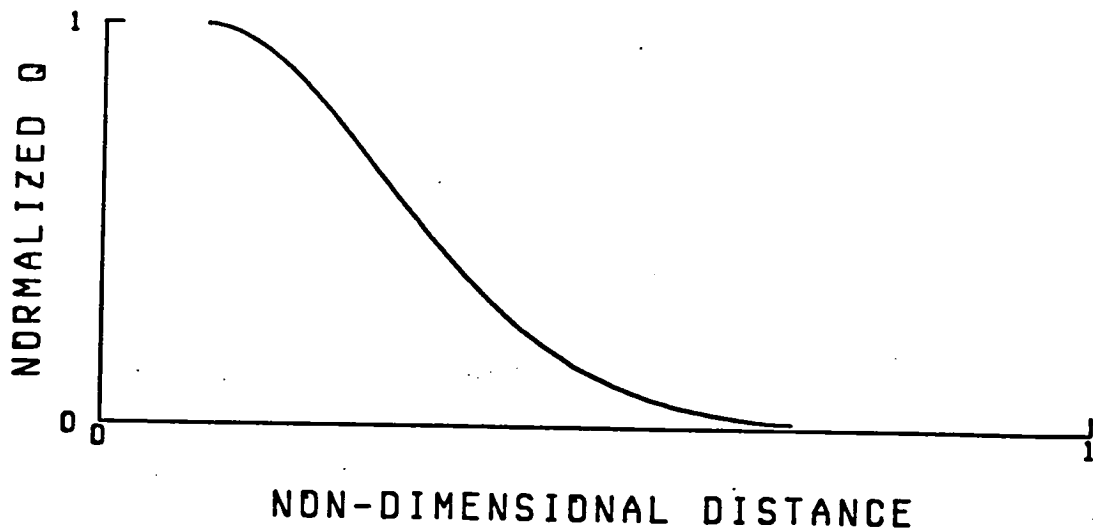


Figure 3-3. Case 1 heat addition distribution and streamlines.

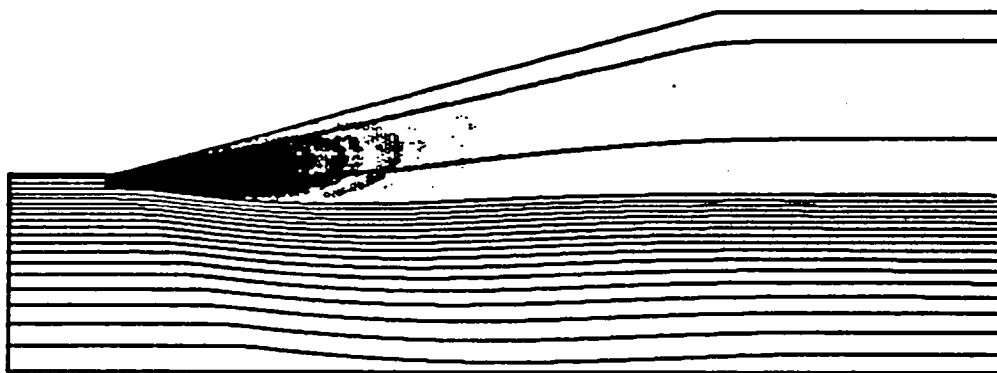


a) Heat addition contours and streamlines.

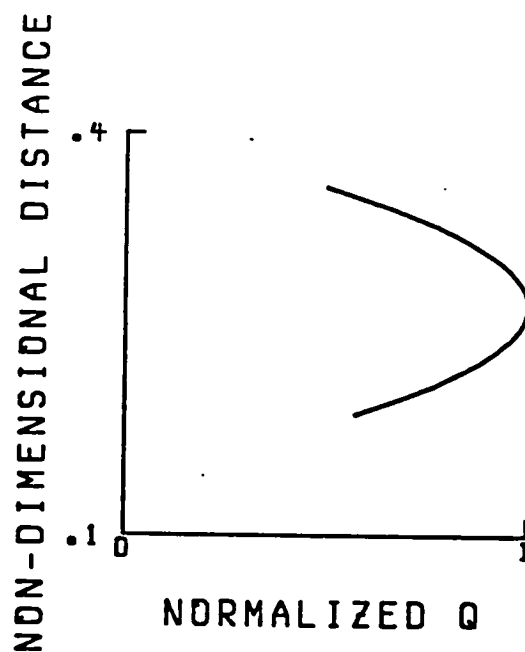


b) Gaussian axial heat addition distribution function.

Figure 3-4. Case 2 heat addition distribution, Gaussian in axial direction, constant in transverse.



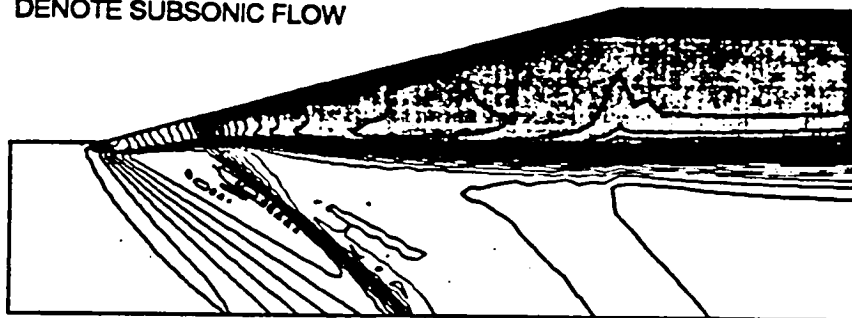
a) Heat addition contours and streamlines.



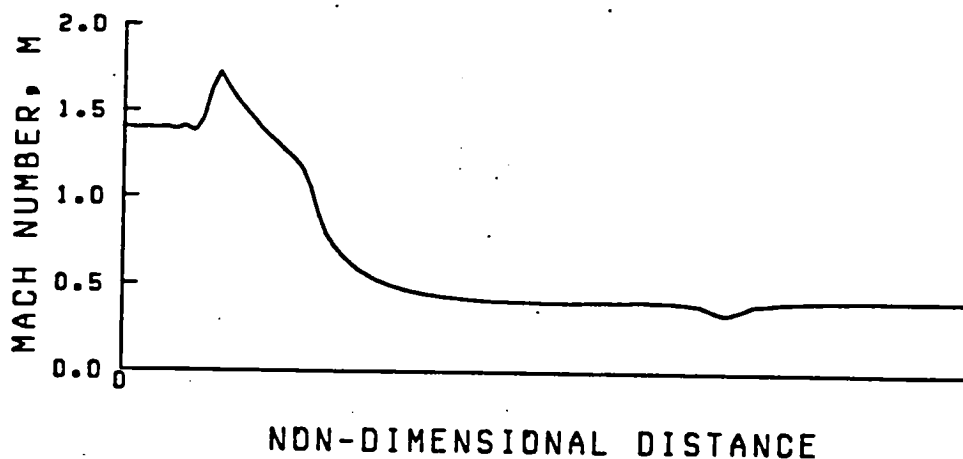
b) Parabolic transverse distribution function.

Figure 3-5. Case 3 heat addition distribution, Gaussian in axial direction, parabolic in transverse.

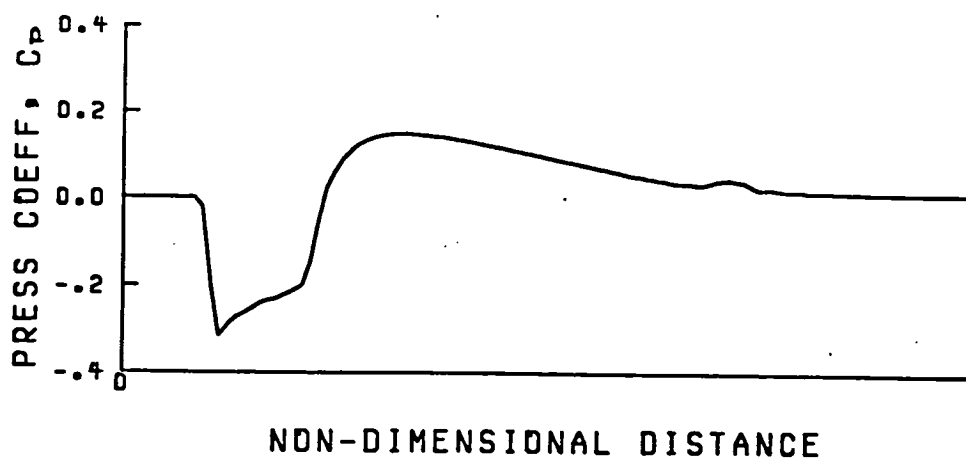
SHADED REGIONS  
DENOTE SUBSONIC FLOW



a) Mach number contours (.05 contour intervals).



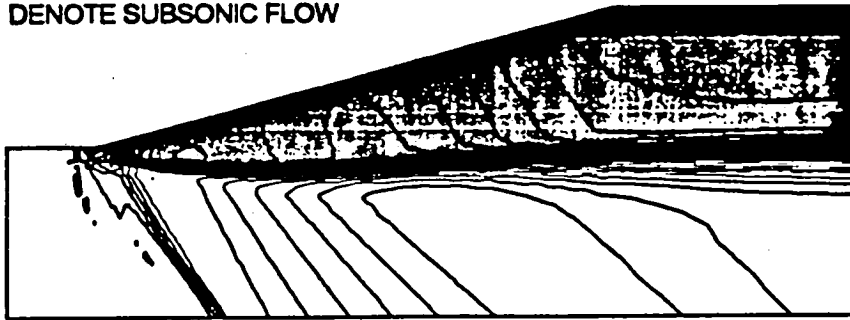
b) Wall Mach number distribution.



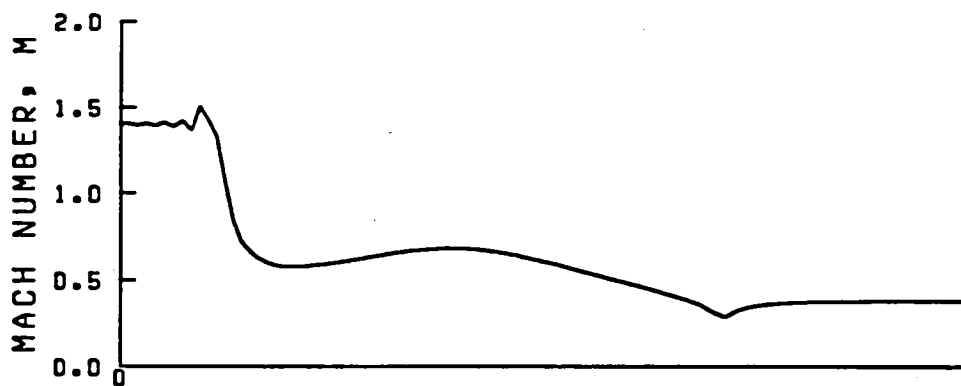
c) Wall pressure distribution.

Figure 3-6. Euler results for case 1 heat addition;  $M_0=1.4$

SHADED REGIONS  
DENOTE SUBSONIC FLOW

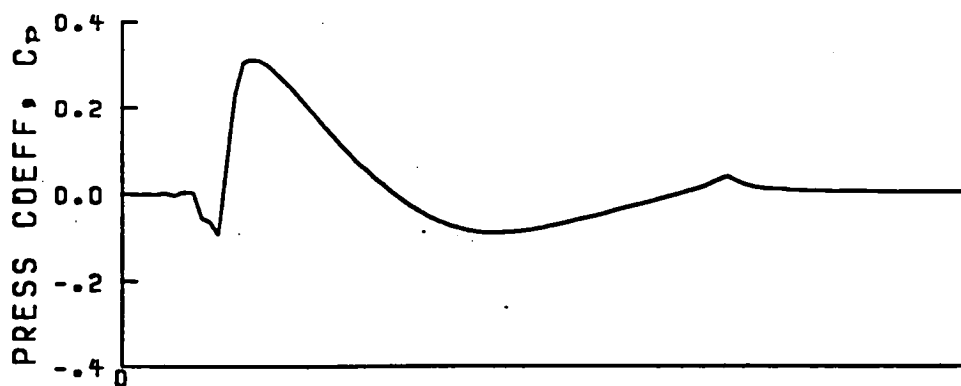


a) Mach number contours (.05 contour intervals).



NON-DIMENSIONAL DISTANCE

b) Wall Mach number distribution.

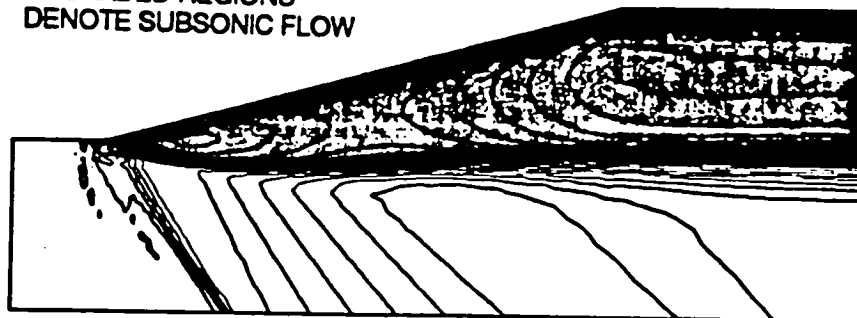


NON-DIMENSIONAL DISTANCE

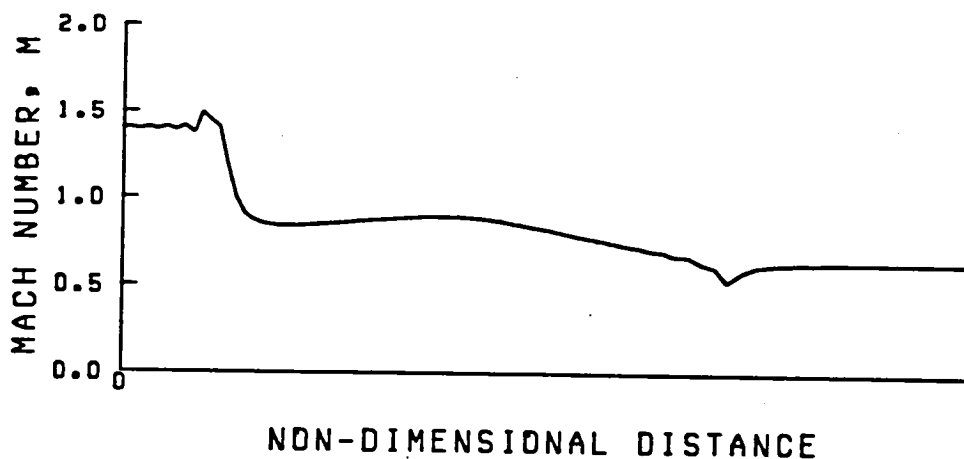
c) Wall pressure distribution.

Figure 3-7. Euler results for case 2 heat addition;  $M_0=1.4$

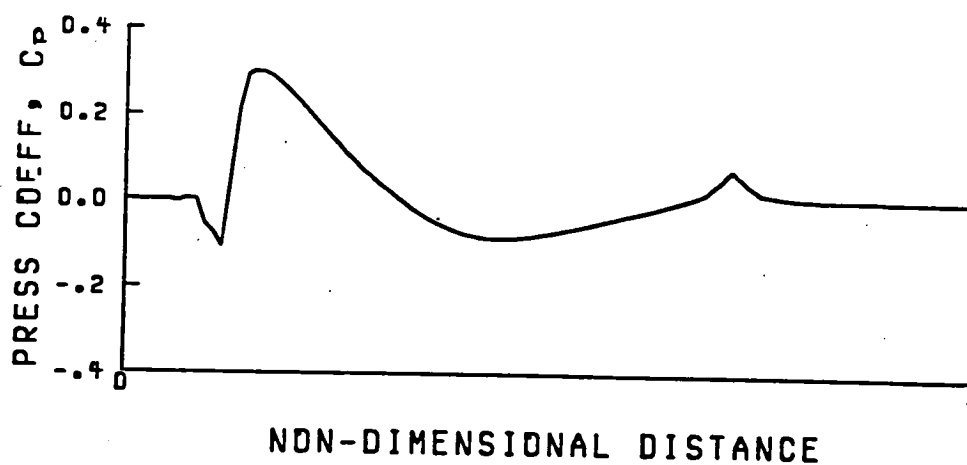
SHADED REGIONS  
DENOTE SUBSONIC FLOW



a) Mach number contours (.05 contour intervals).



b) Wall Mach number distribution.



c) Wall pressure distribution.

Figure 3-8. Euler results for case 3 heat addition;  $M_0=1.4$

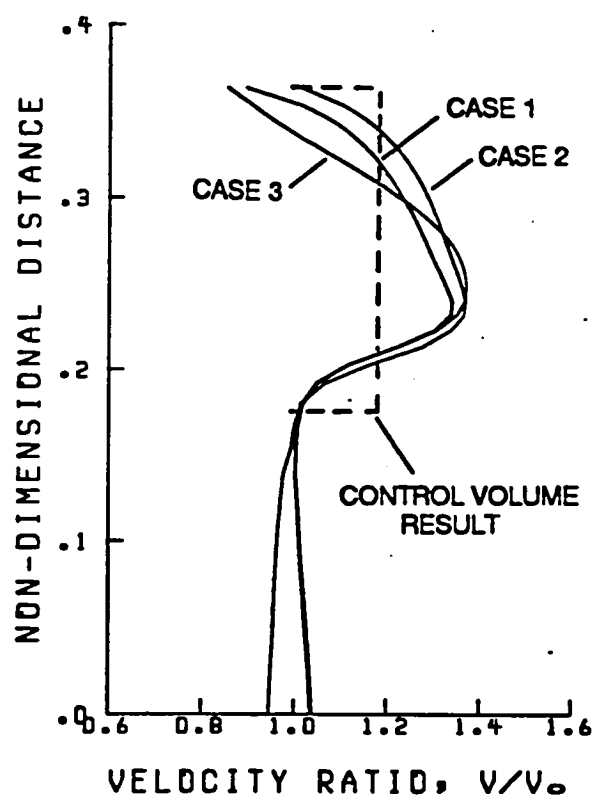
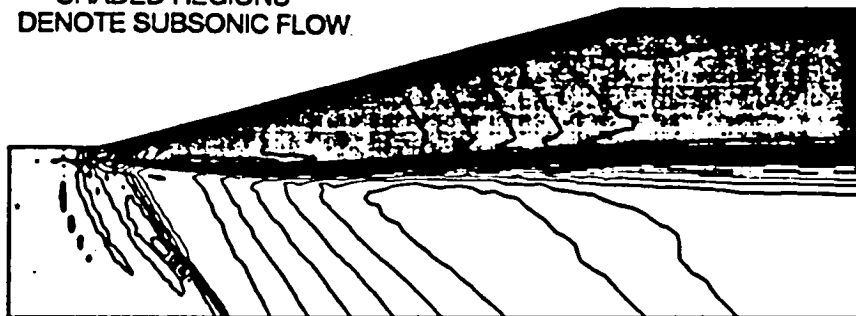


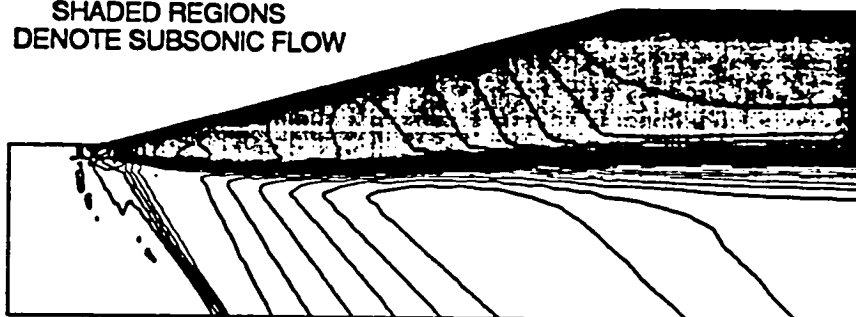
Figure 3-9. Velocity profiles at ramp trailing edge.

SHADED REGIONS  
DENOTE SUBSONIC FLOW



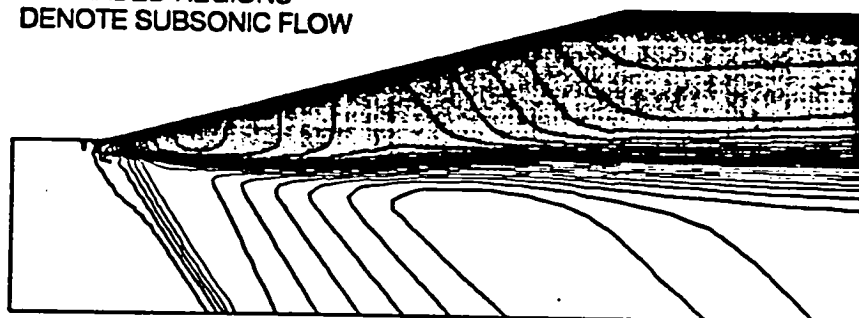
a)  $C_d = .0125$ .

SHADED REGIONS  
DENOTE SUBSONIC FLOW



b)  $C_d = .025$ .

SHADED REGIONS  
DENOTE SUBSONIC FLOW

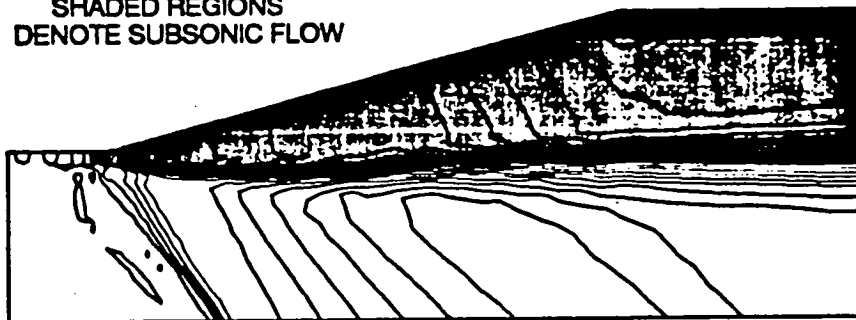


c)  $C_d = .05$ .

Figure 3-10. Effect of artificial damping on Euler results. Mach number contours (.05 contour increment);  $M_0 = 1.4$ ,  $80 \times 40$  grid, case 2 heat addition.

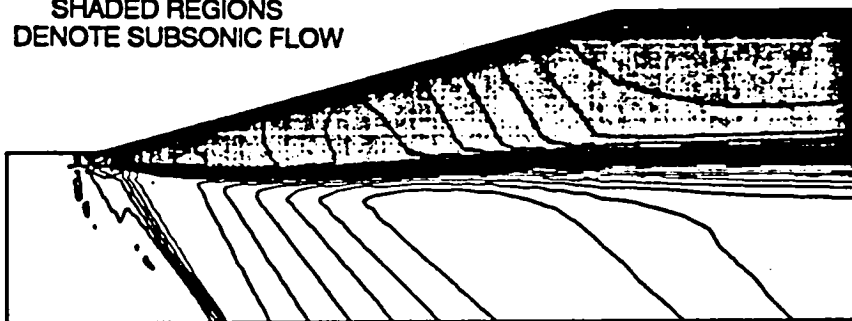


SHADED REGIONS  
DENOTE SUBSONIC FLOW



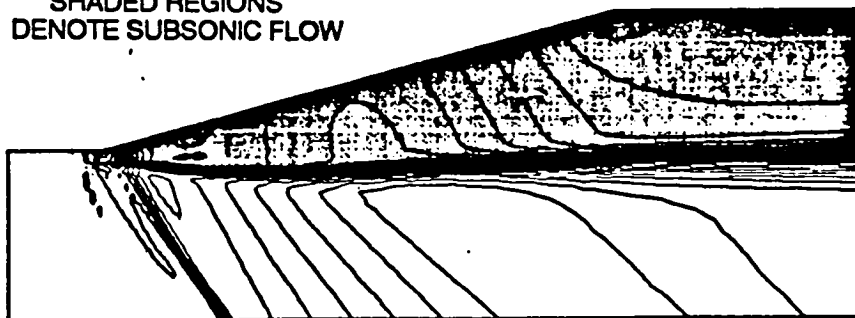
a) 50 x 25 grid.

SHADED REGIONS  
DENOTE SUBSONIC FLOW



b) 80 x 40 grid.

SHADED REGIONS  
DENOTE SUBSONIC FLOW



c) 100 x 50 grid.

Figure 3-11. Effect of grid refinement on Euler results. Mach number contours (.05 contour increment);  $M_0=1.4$ ,  $C_d=.025$ , case 2 heat addition.

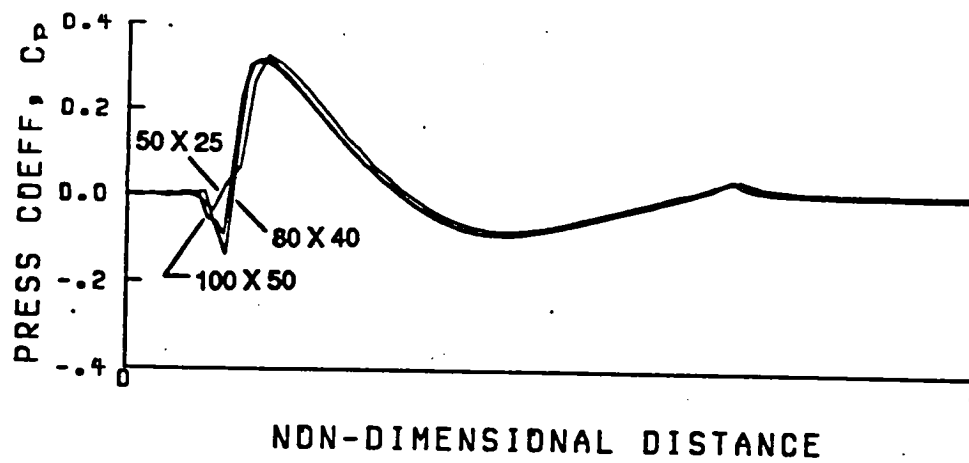
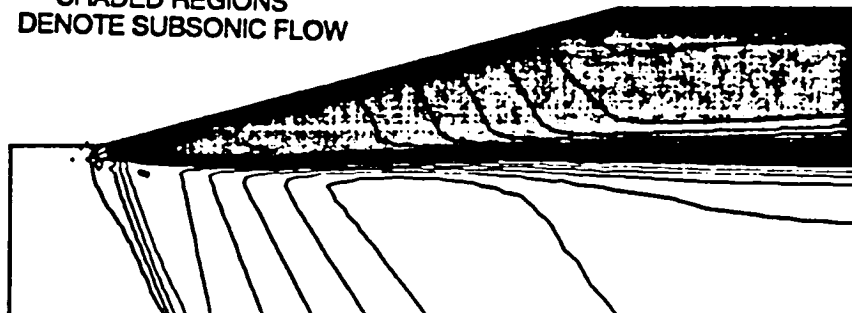


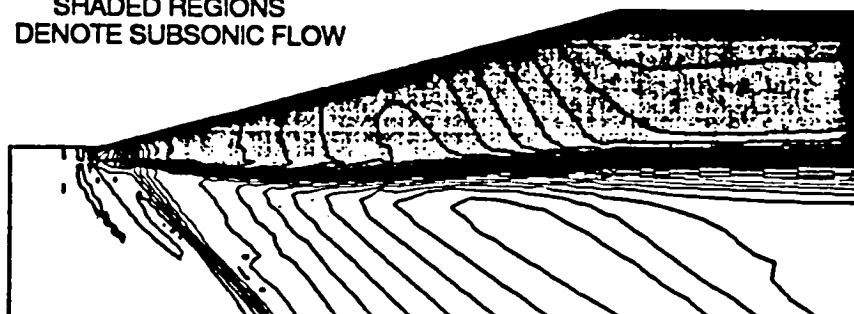
Figure 3-12. Effect of grid density on wall pressure distributions.

SHADED REGIONS  
DENOTE SUBSONIC FLOW



a)  $M_0=1.2$ .

SHADED REGIONS  
DENOTE SUBSONIC FLOW



b)  $M_0=1.6$

Figure 3-13. Mach number contours at various freestream Mach numbers (.05 contour increment); 80 x 40 grid,  $C_d=.025$ , case 2 heat addition.

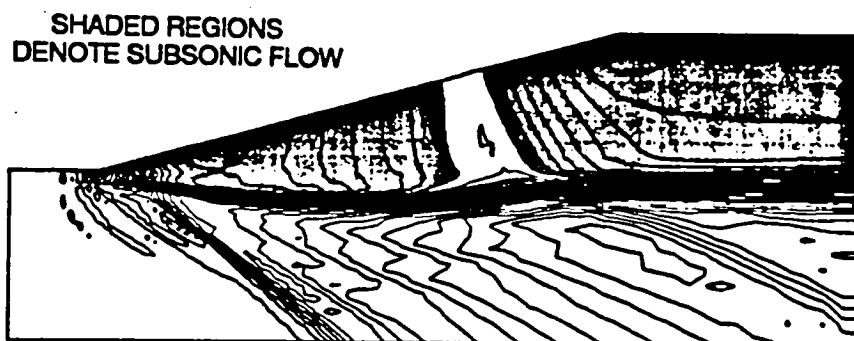
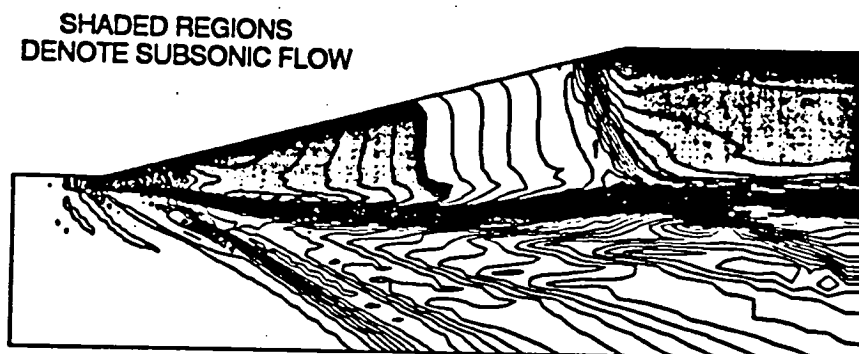
c)  $M_0 = 2.0$ .d)  $M_0 = 2.4$ .

Figure 3-13. Concluded.

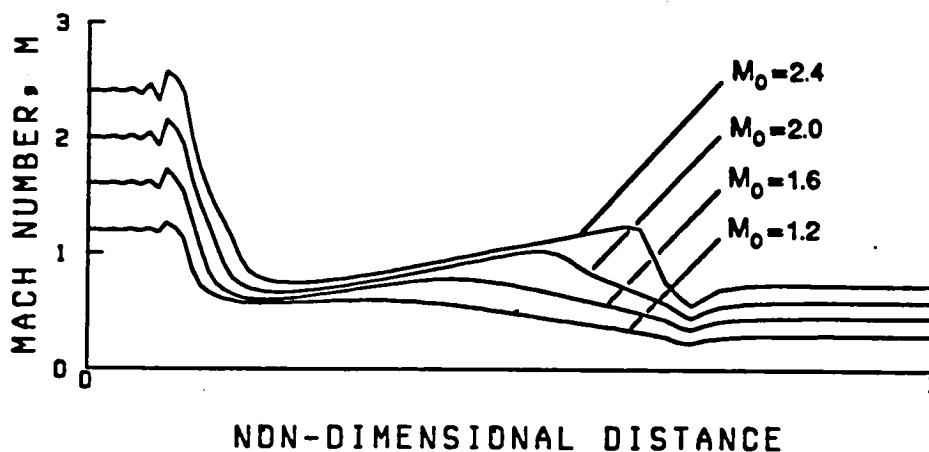


Figure 3-14. Wall Mach number distributions at various freestream Mach numbers; 80 x 40 grid,  $C_d = .025$ , case 2 heat addition.

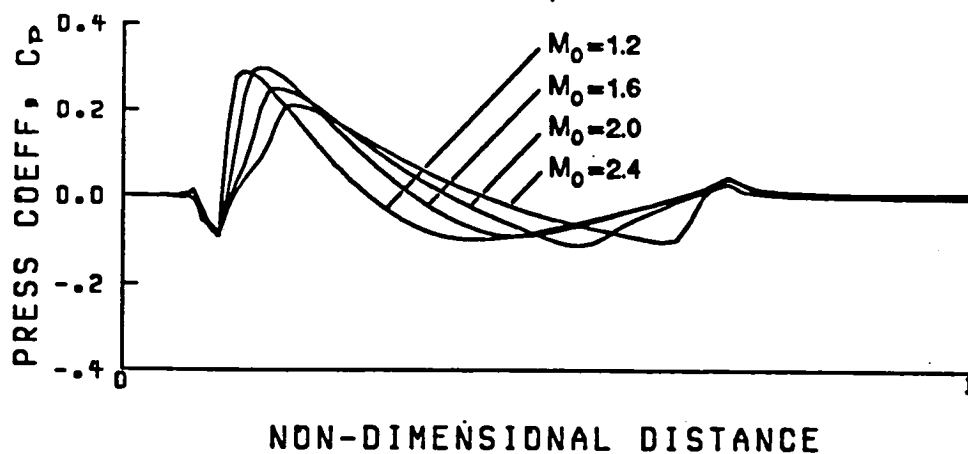


Figure 3-15. Wall pressure distributions at various freestream Mach numbers; 80 x 40 grid,  $C_d = .025$ , case 2 heat addition.

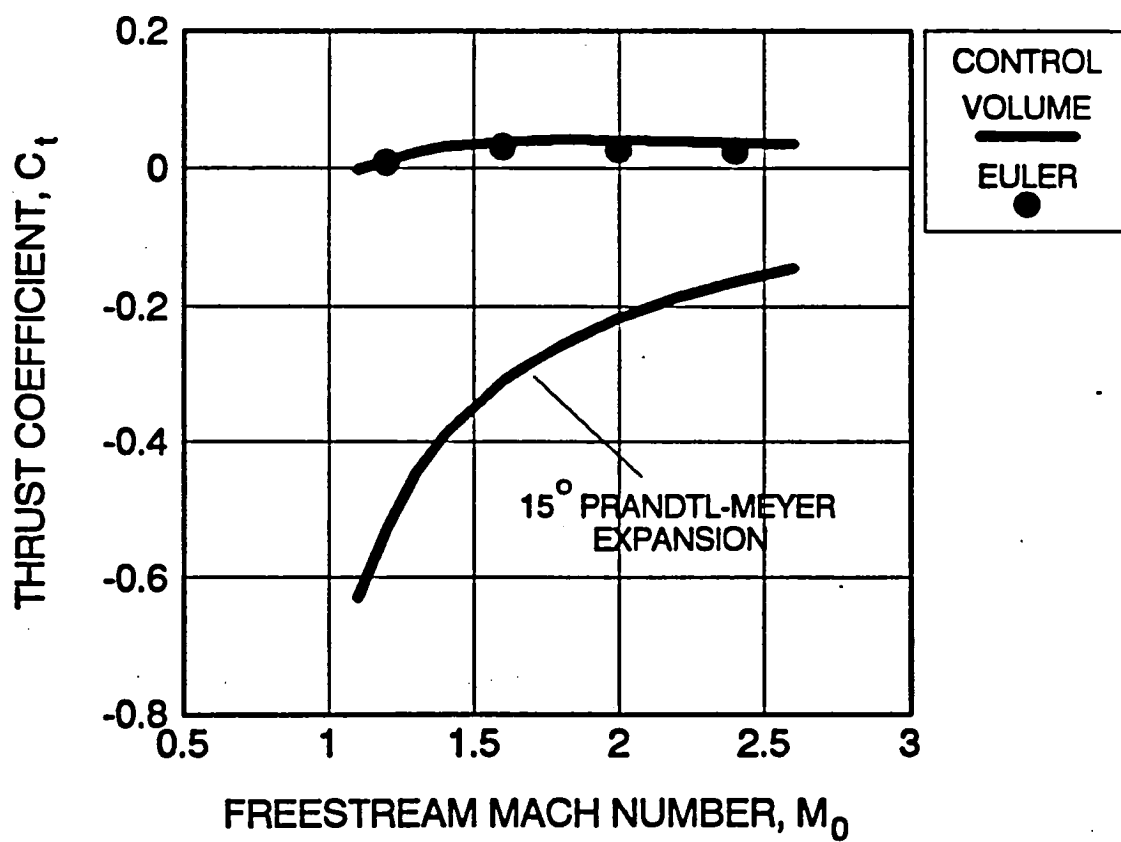


Figure 3-16. Comparison of Euler and control volume analysis thrust coefficient predictions.

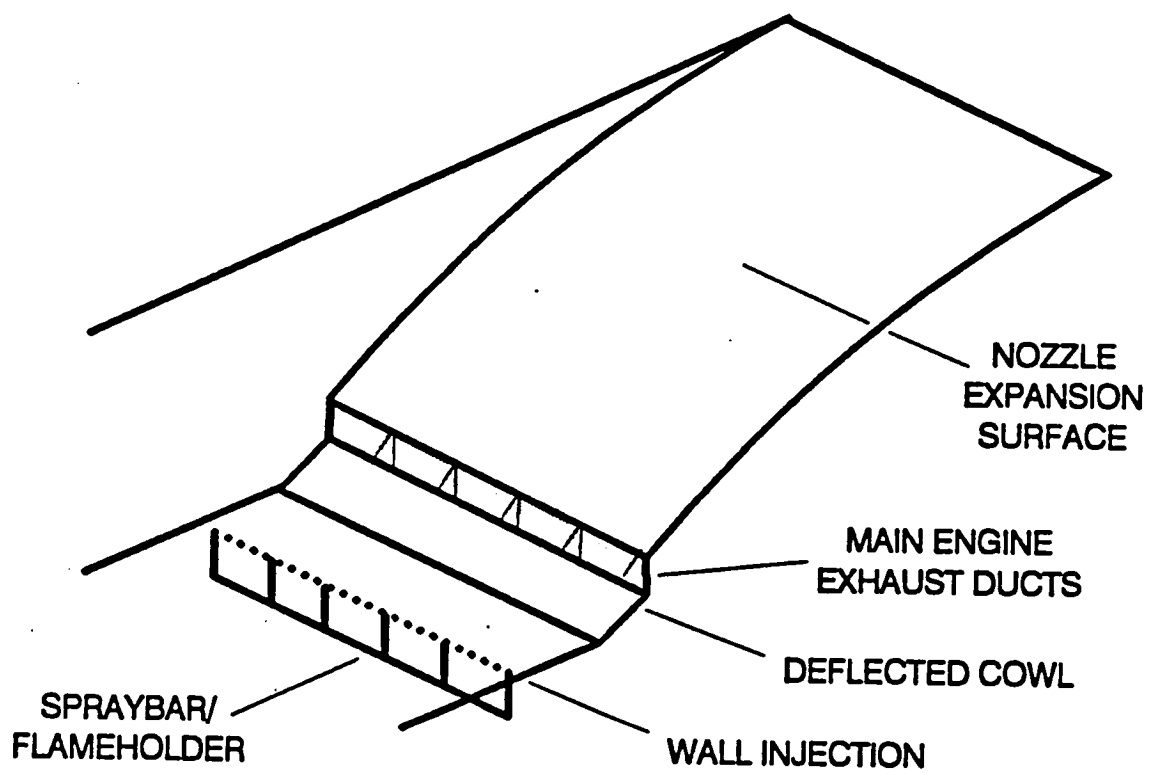


Figure 4-1. Combination spraybar-flameholder concept.

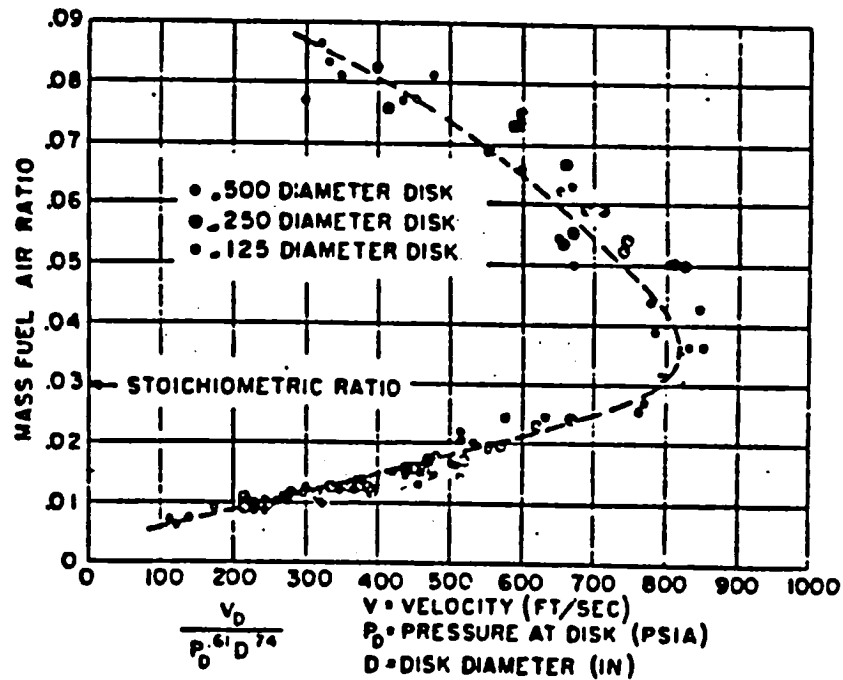


Figure 4-2. Flame stability for a pre-mixed, subsonic hydrogen-air stream (reproduced from reference 57).

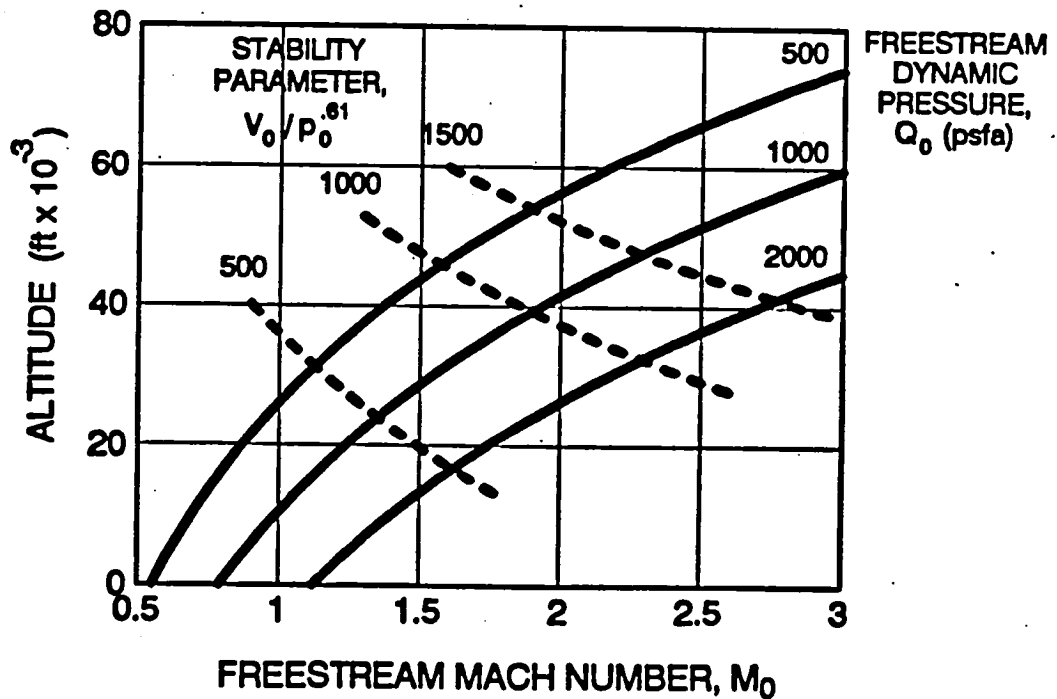


Figure 4-3. Flame stability along flight trajectories for a 1" dia. disk.



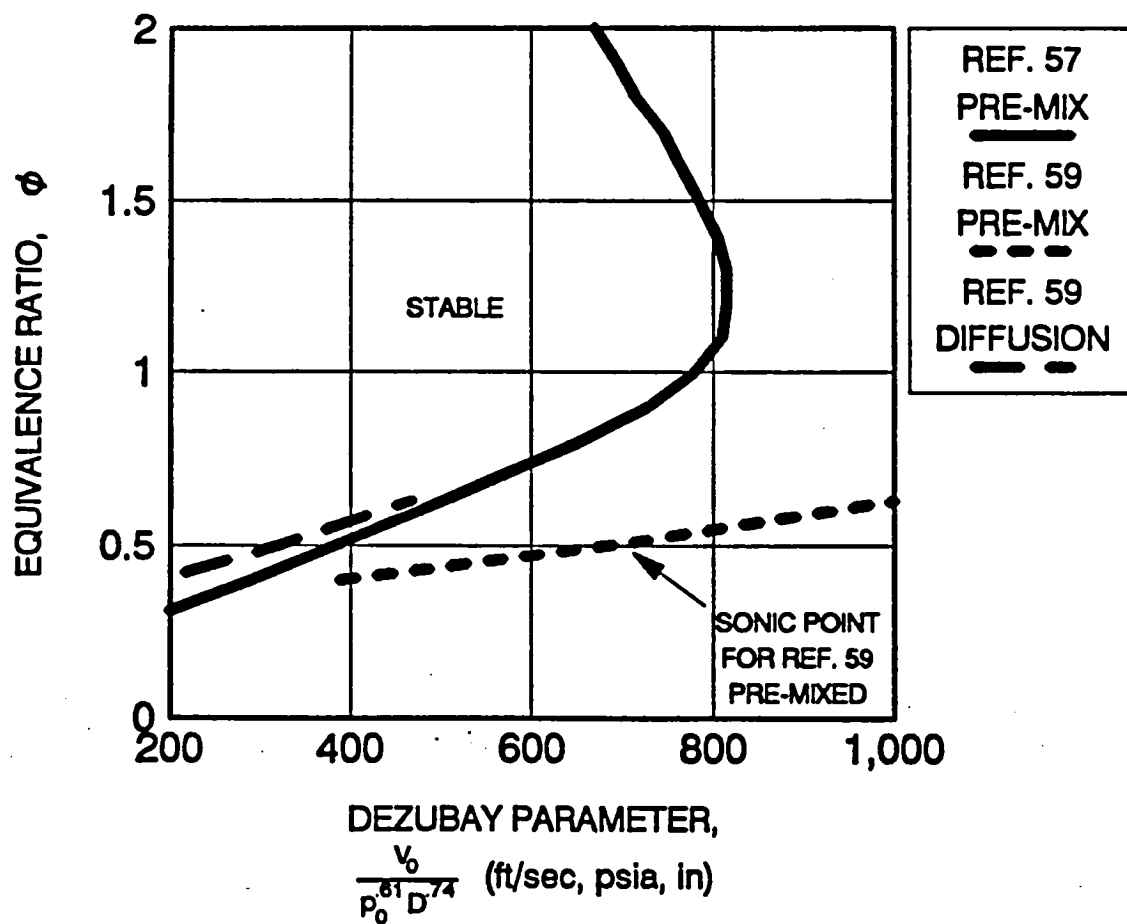
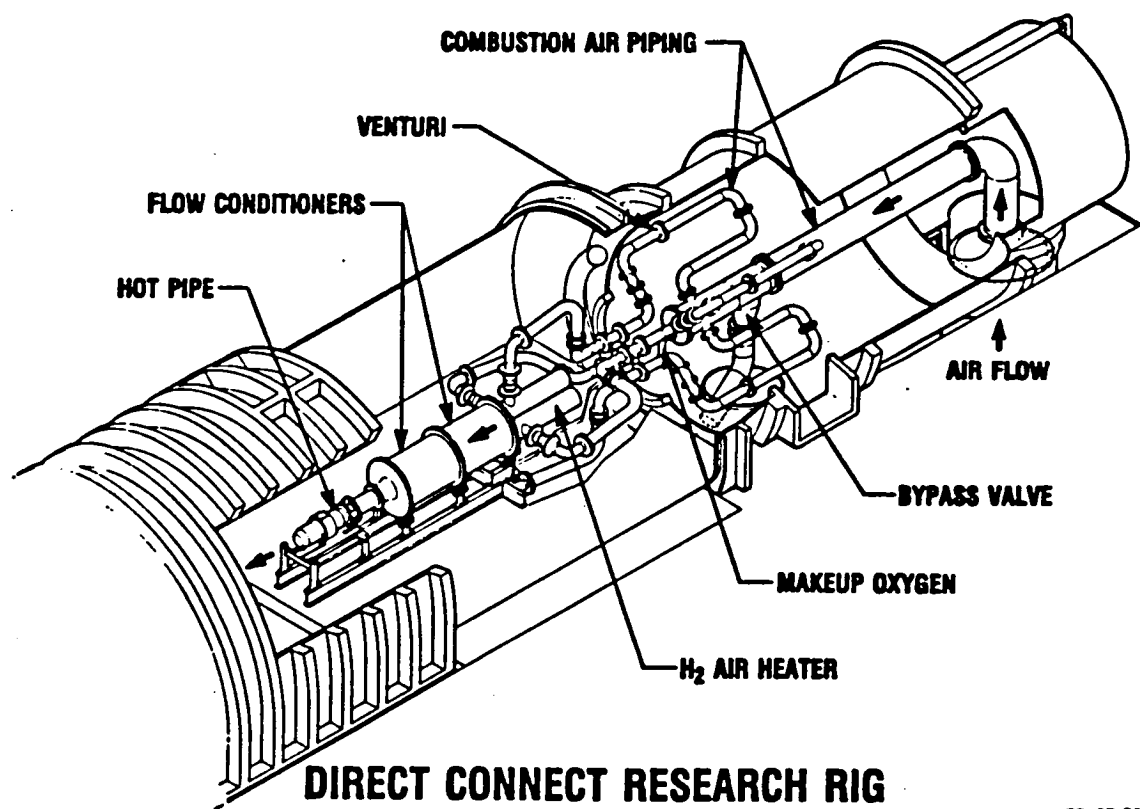


Figure 4-4. Non pre-mixed, and supersonic stability limits from reference 59 in terms of DeZubay parameter.

## PSL-4 HYPERSONIC MODIFICATION



CD-67-28112

Figure 4-5. Propulsion Systems Lab Cell 4 after hypersonic modifications (reproduced from reference 60).

ORIGINAL PAGE  
BLACK AND WHITE PHOTOGRAPH

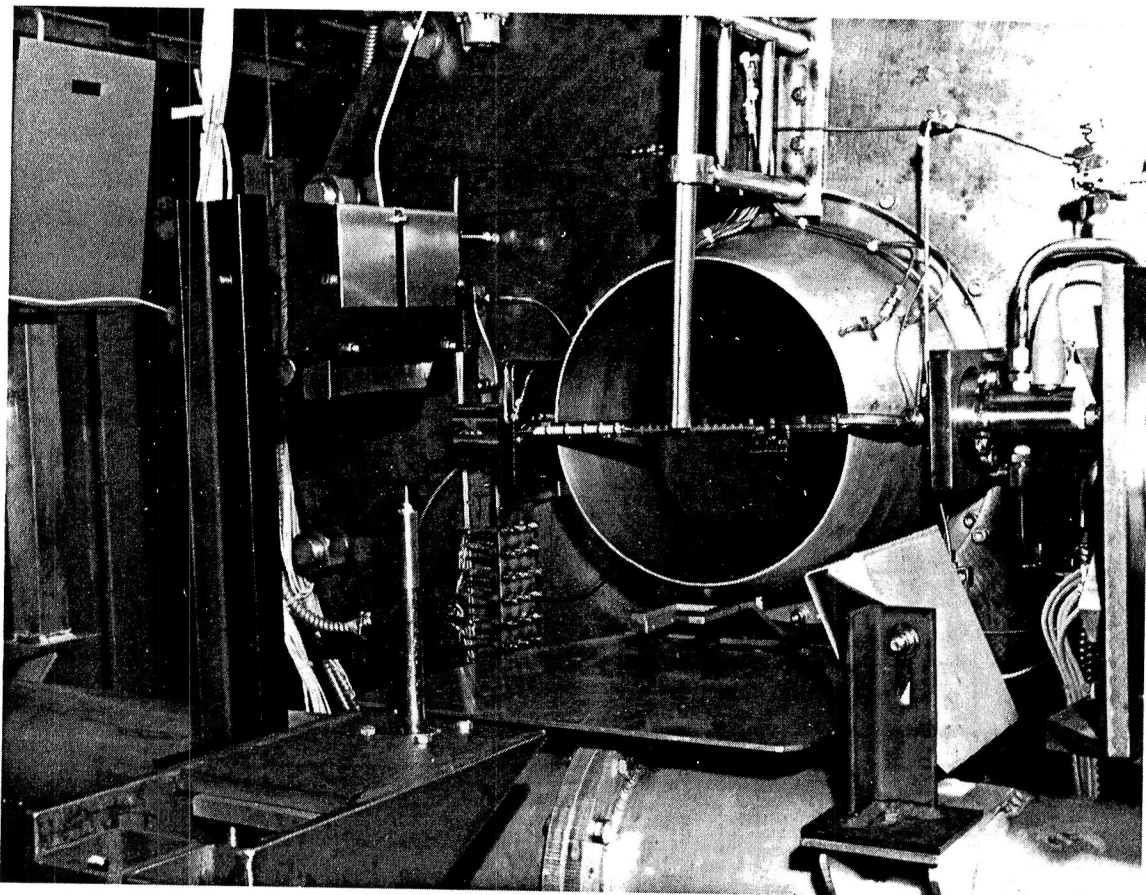


Figure 4-6. Spraybar mounted in free-jet with spark ignitor and water-cooled probe in extended positions.

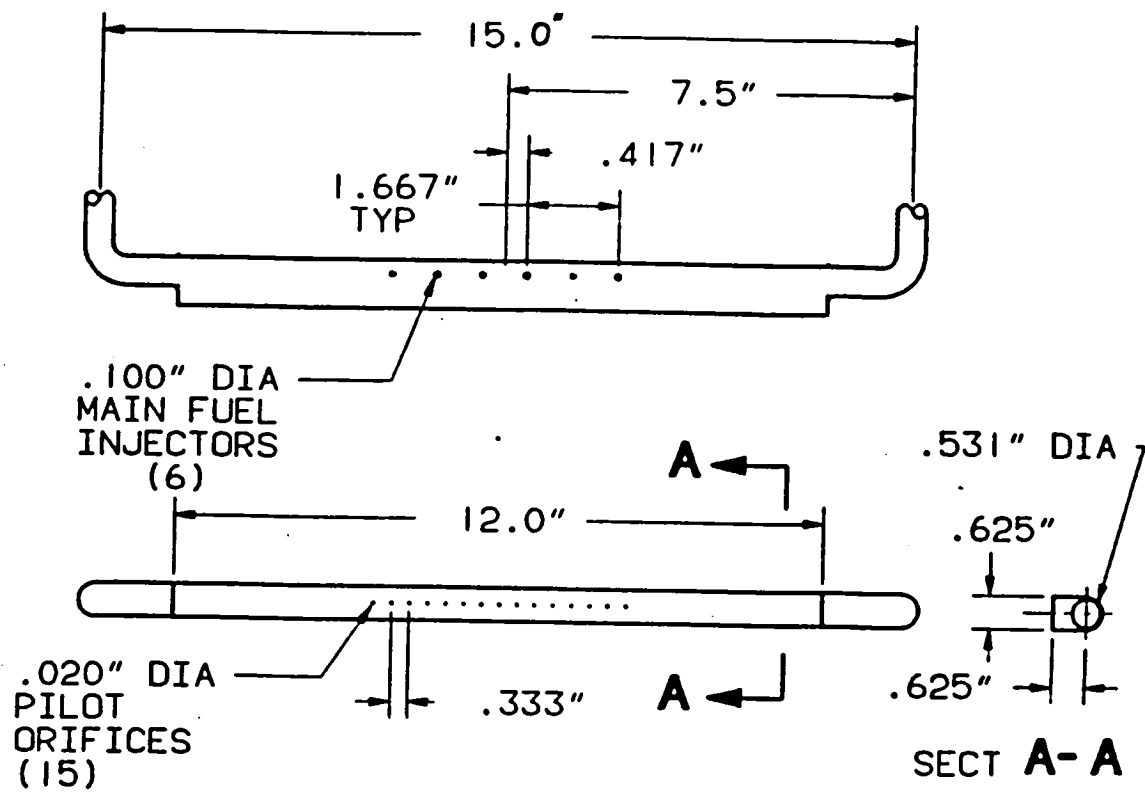


Figure 4-7. Details of piloted spraybar.

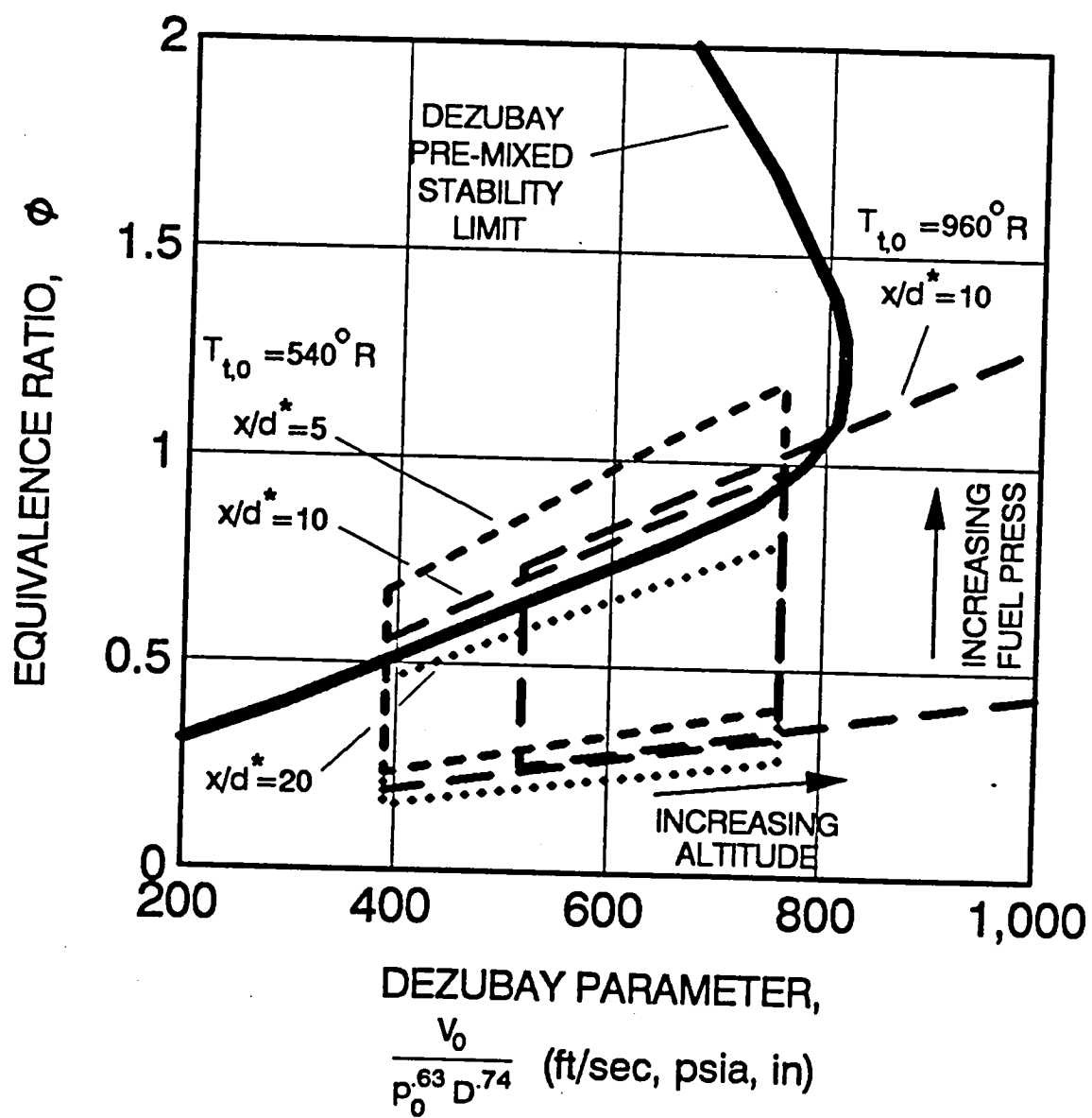


Figure 4-8. Piloted spraybar operating envelopes at Mach 1.26.

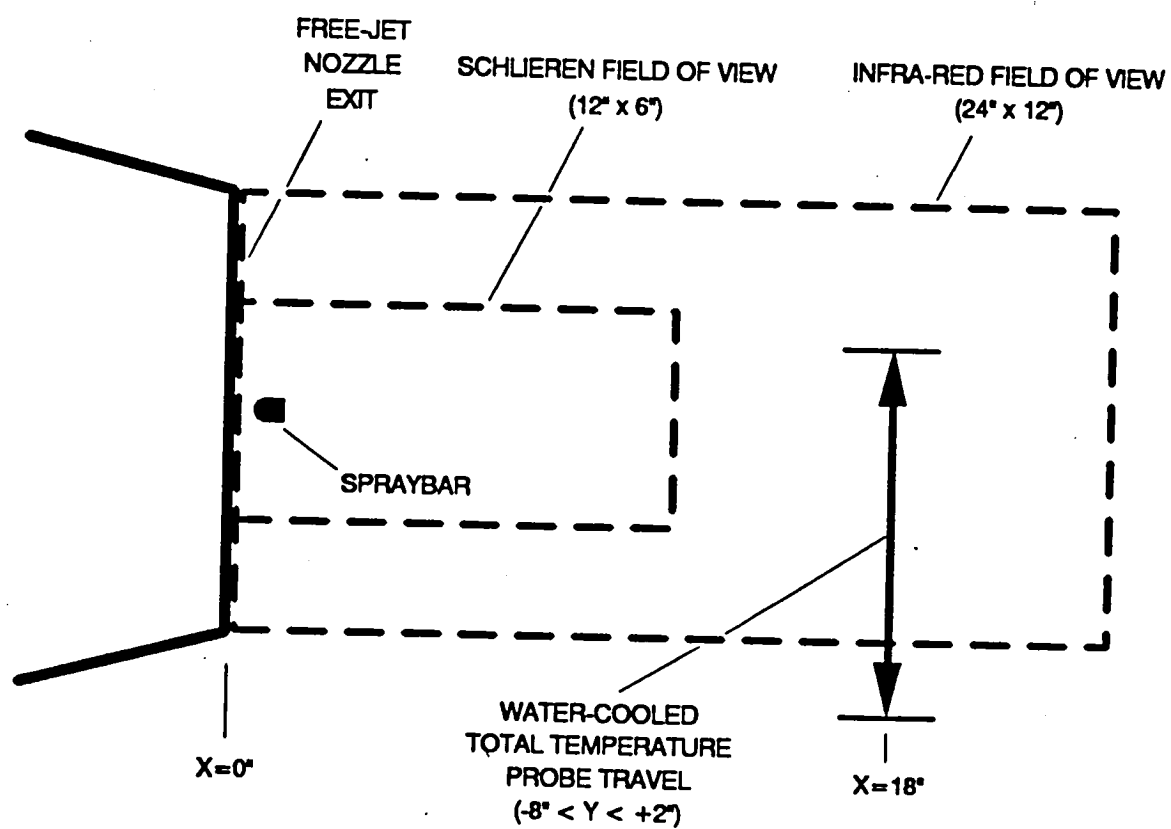
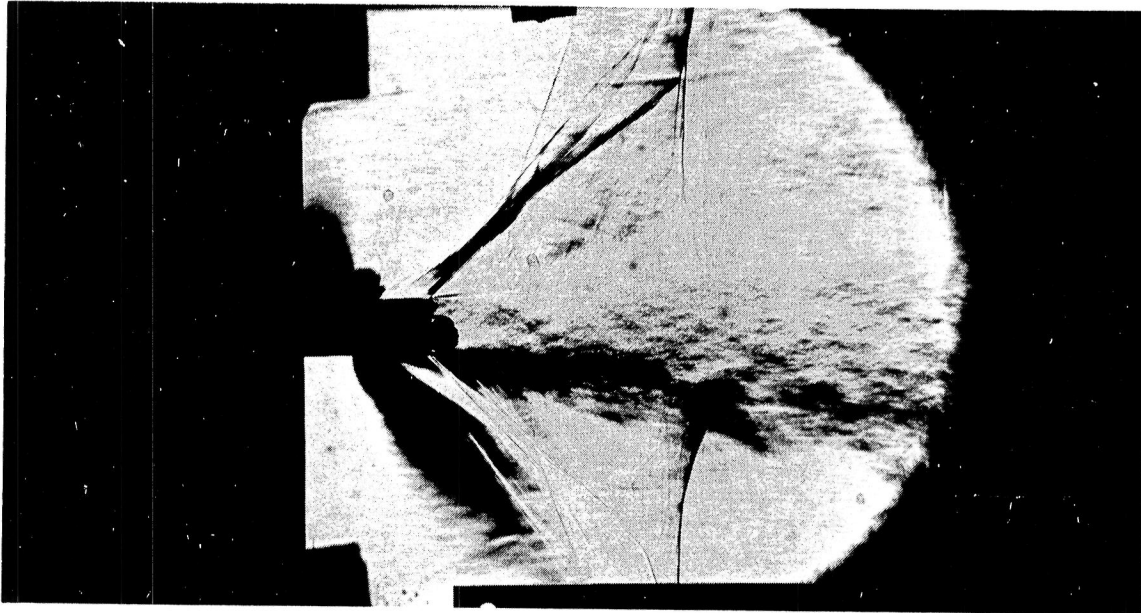
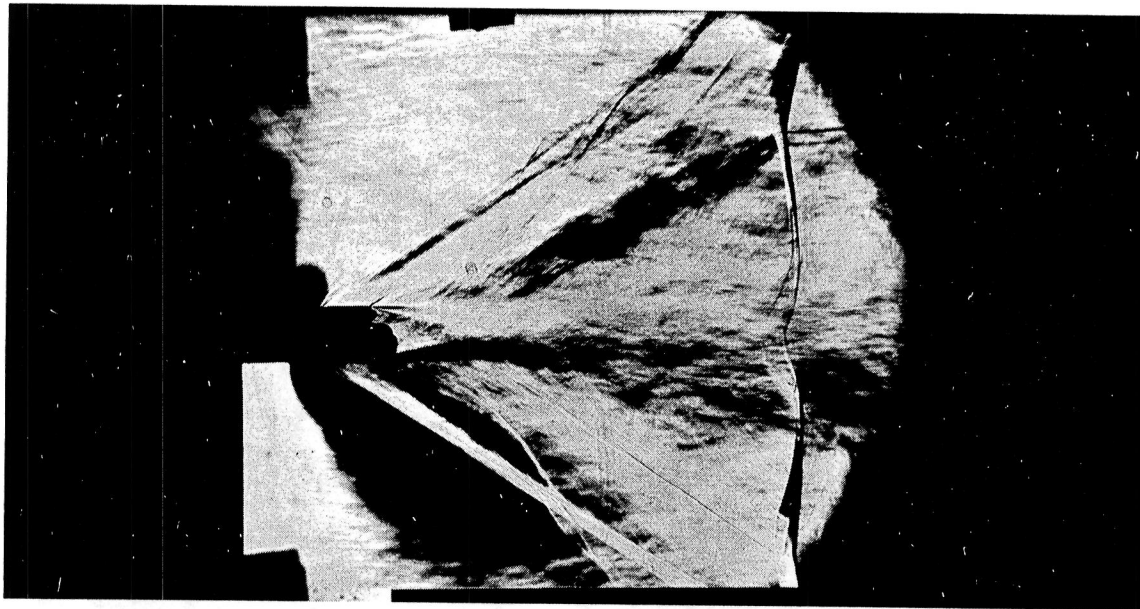


Figure 4-9. Field of view for optical instrumentation and location of translating water-cooled total temperature probe.



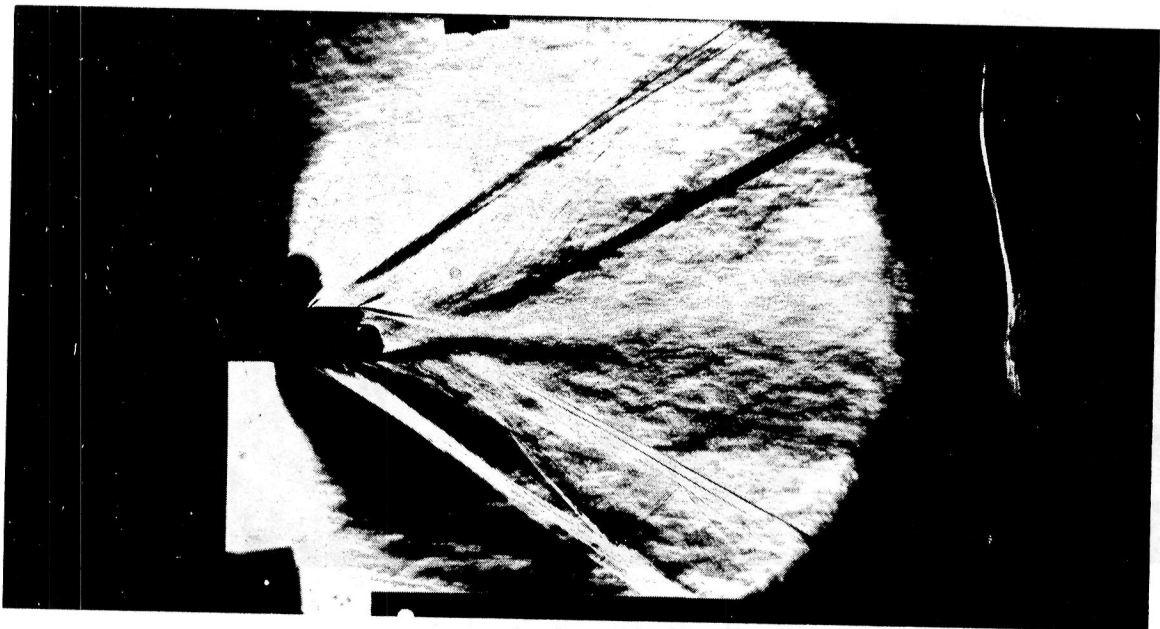
a) Over-expanded,  $p_0/p_a = .8$ .



b) On design,  $p_0/p_a = 1.0$ .

Figure 4-10. Schlieren images at various free-jet exit pressure ratios;  $p_0$  (free-jet exit pressure) held constant at 8 psia.

ORIGINAL PAGE  
BLACK AND WHITE PHOTOGRAPH



c) Under-expanded,  $p_o/p_a=1.2$ .

Figure 4-10. Concluded.



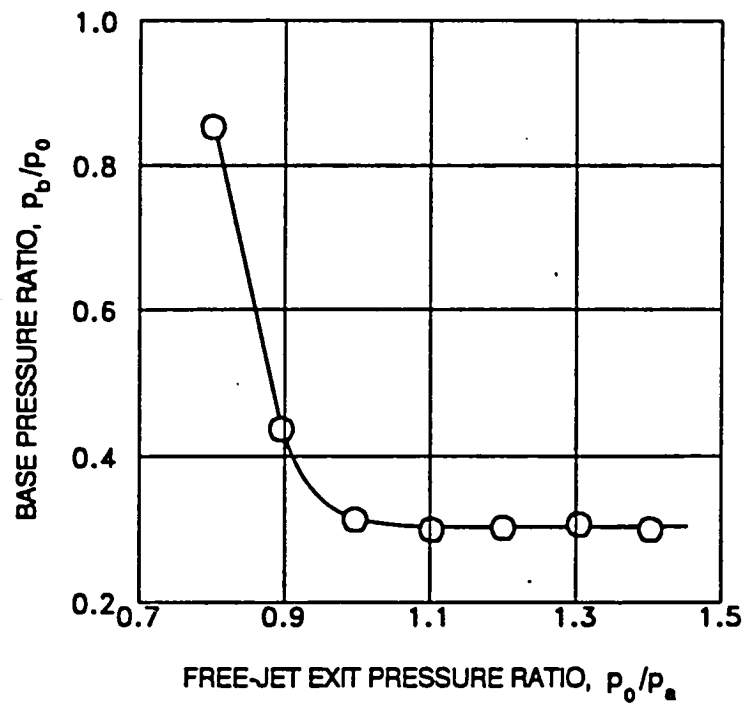


Figure 4-11. Effect of free-jet exit pressure on spraybar base pressure;  $p_0$  (free-jet exit pressure) held constant at 8 psia.

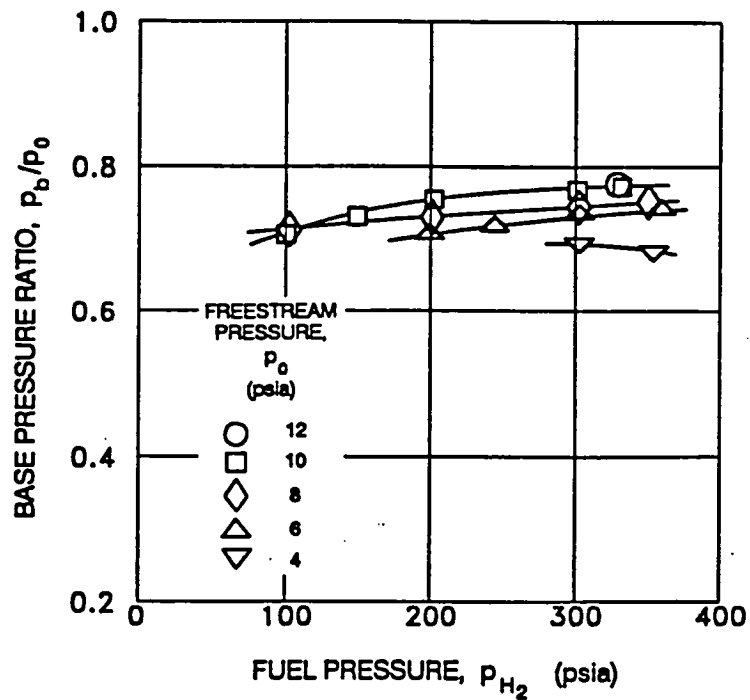


Figure 4-12. Spraybar base pressure with external burning.

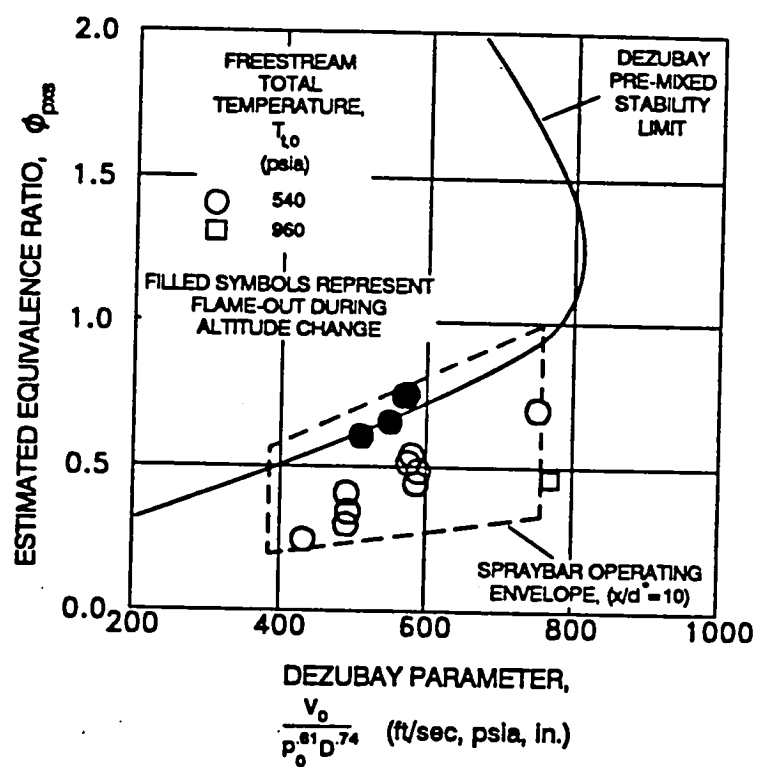
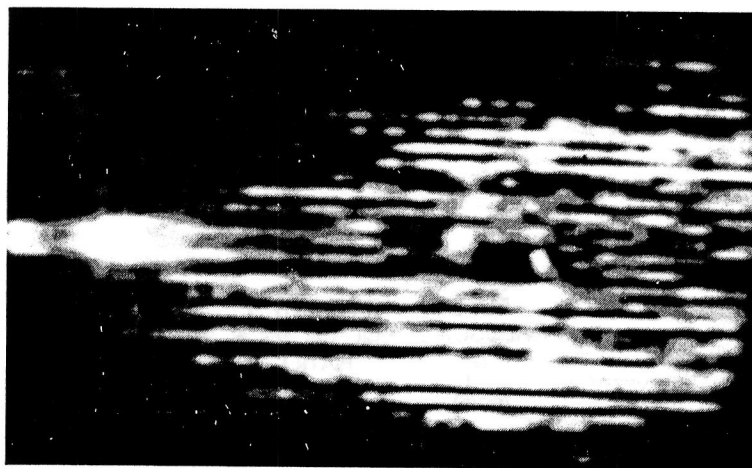


Figure 4-13. Flame stability for piloted spraybar.

ORIGINAL PAGE  
BLACK AND WHITE PHOTOGRAPH

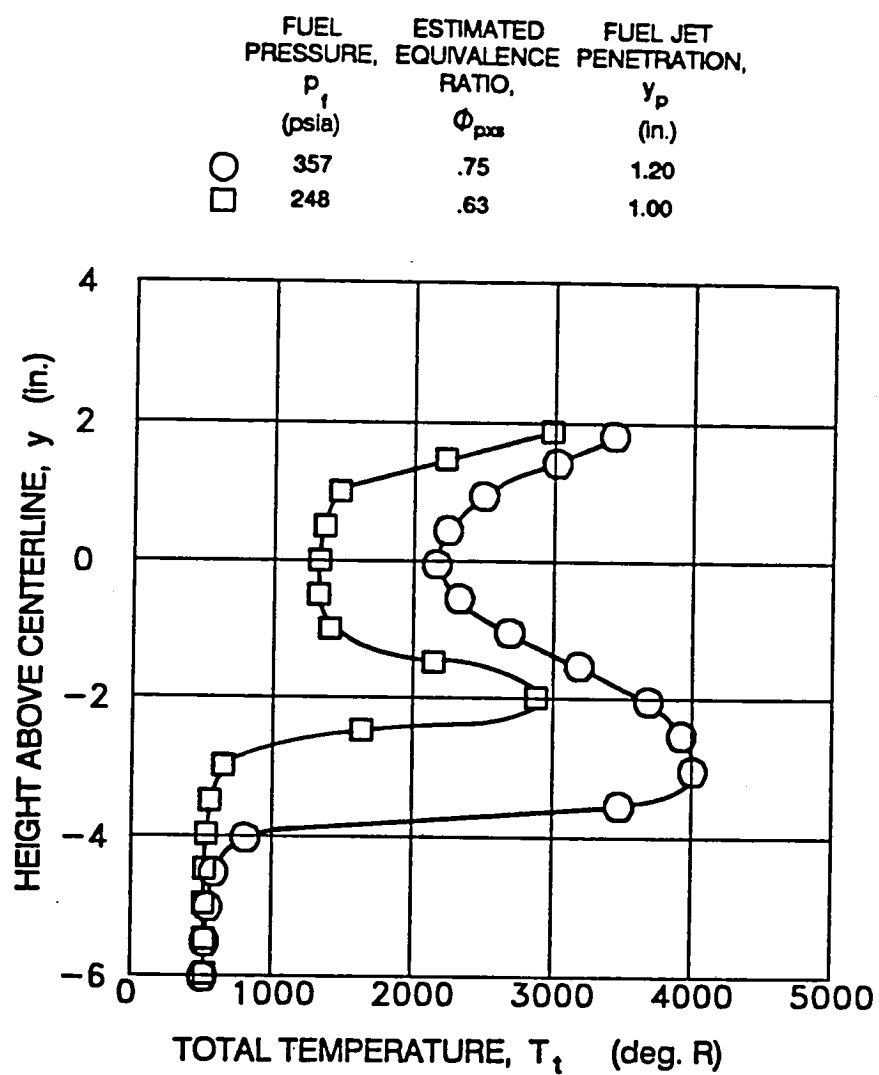


a) Infra-red image;  $p_f=250$  psia,  $y_p=1.0"$ ,  $\phi_{pxs}=.63$ .



b) Infra-red image;  $p_f=350$  psia,  $y_p=1.2"$ ,  $\phi_{pxs}=.75$ .

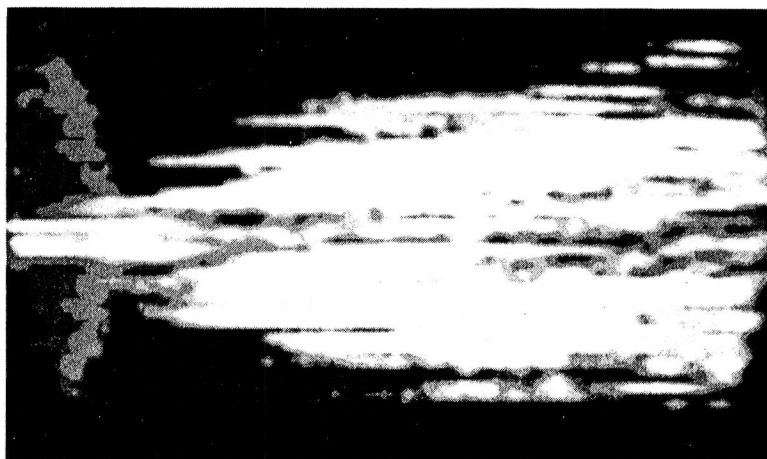
Figure 4-14. Plume characteristics at nominal temperature and pressure;  
 $T_{t,0}=540^\circ\text{R}$ ,  $p_0=6$  psia,  $Re=4.9 \times 10^6/\text{ft}$ .



c) Total temperature profiles.

Figure 4-14. Concluded.

ORIGINAL PAGE  
BLACK AND WHITE PHOTOGRAPH

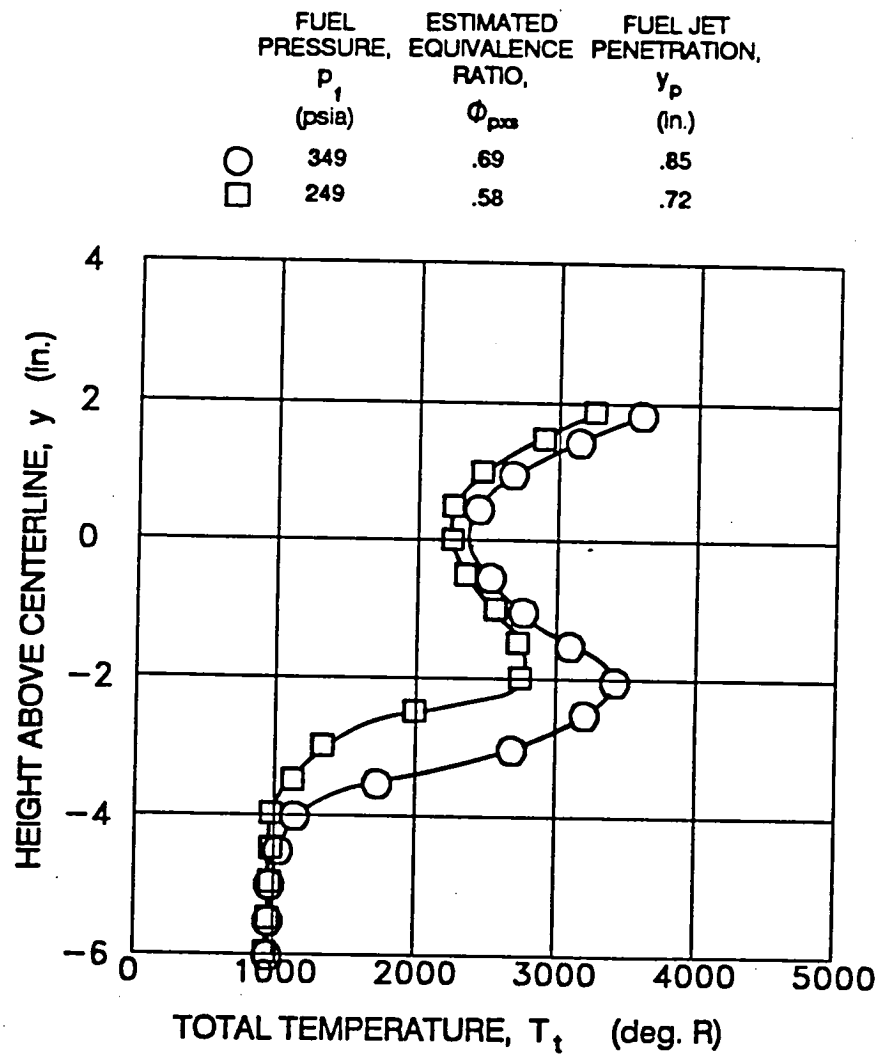


a) Infra-red image;  $p_f=250$  psia,  $y_p=.72''$ ,  $\phi_{pxs}=.58$ .



b) Infra-red image;  $p_f=350$  psia,  $y_p=.85''$ ,  $\phi_{pxs}=.69$ .

Figure 4-15. Plume characteristics at increased temperature and pressure;  $T_{t,0}=960^\circ\text{R}$ ,  $p_0=12$  psia,  $Re=4.9 \times 10^6/\text{ft}$ .



c) Total temperature profiles.

Figure 4-15. Concluded.

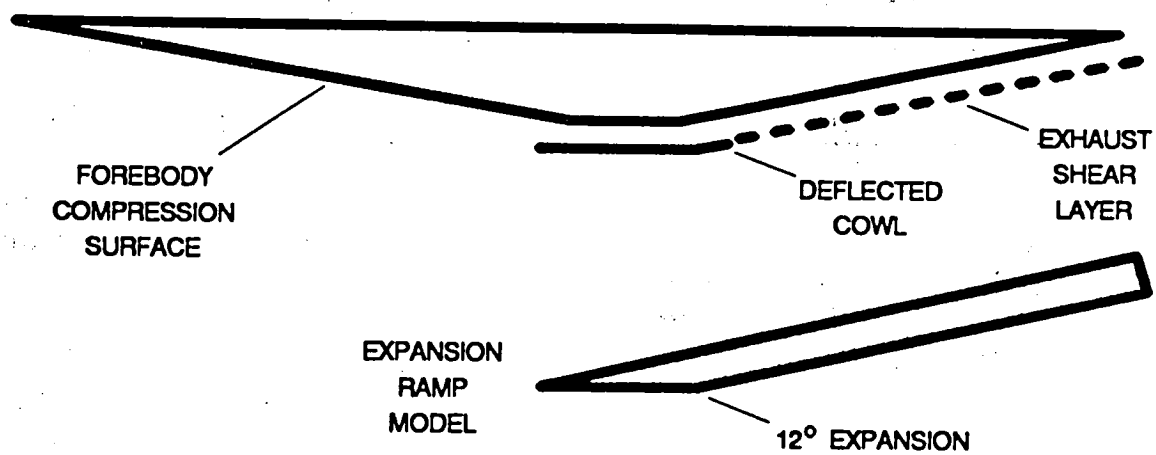


Figure 4-16. Relation of expansion ramp models to vehicle base.

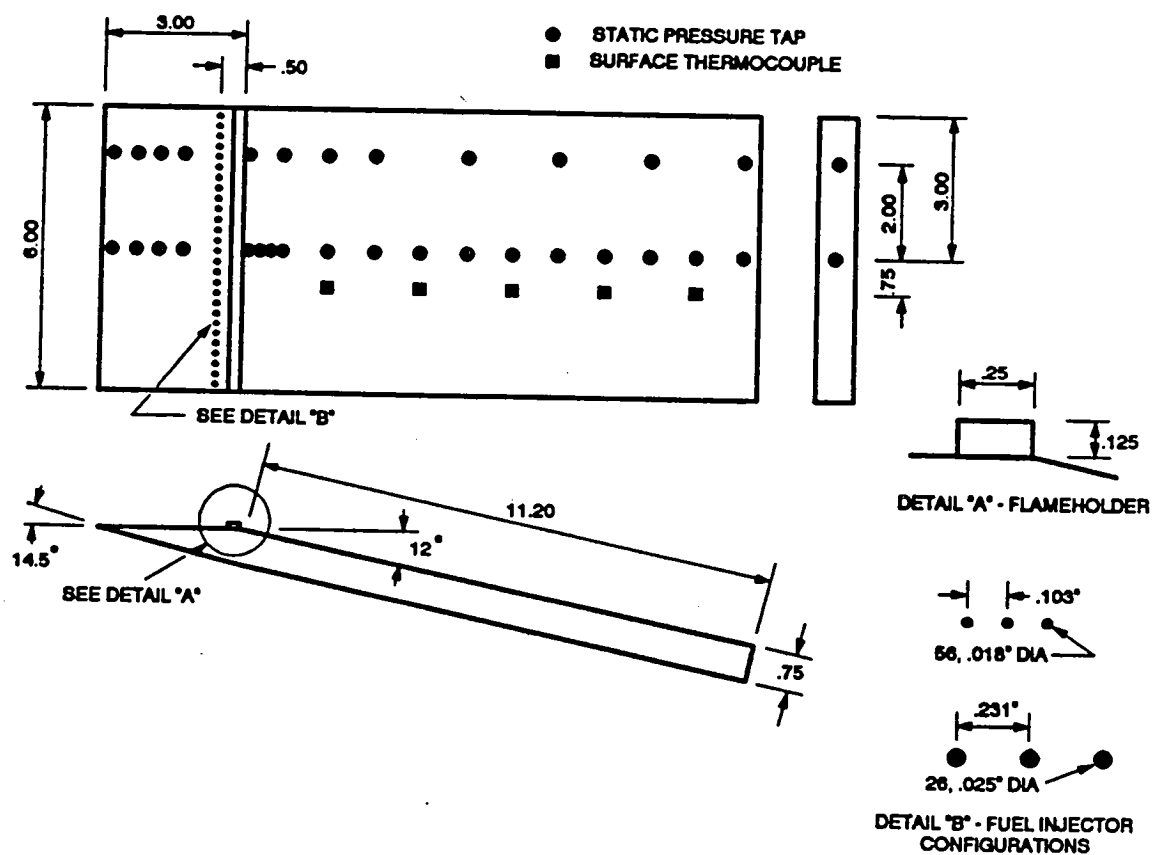


Figure 4-17. Expansion ramp model details.



ORIGINAL PAGE  
BLACK AND WHITE PHOTOGRAPH

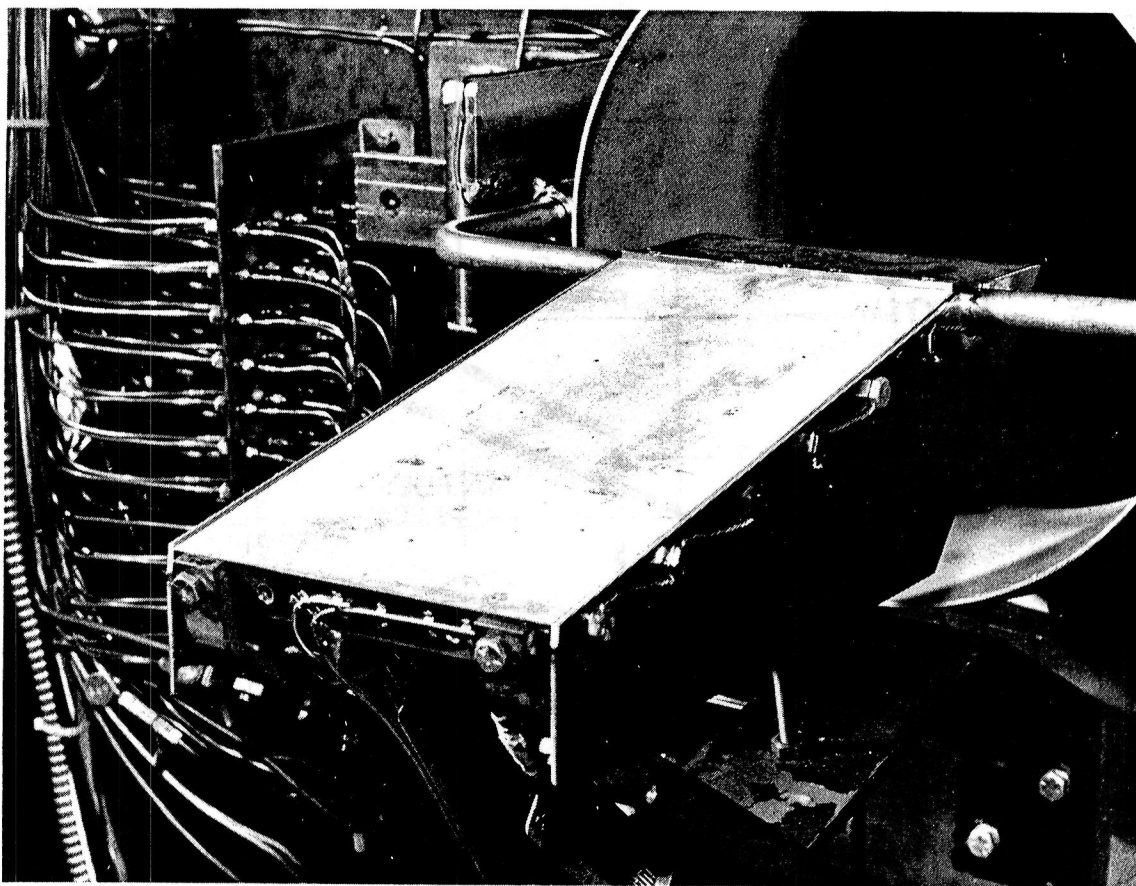


Figure 4-18. Expansion ramp mounted in free-jet.

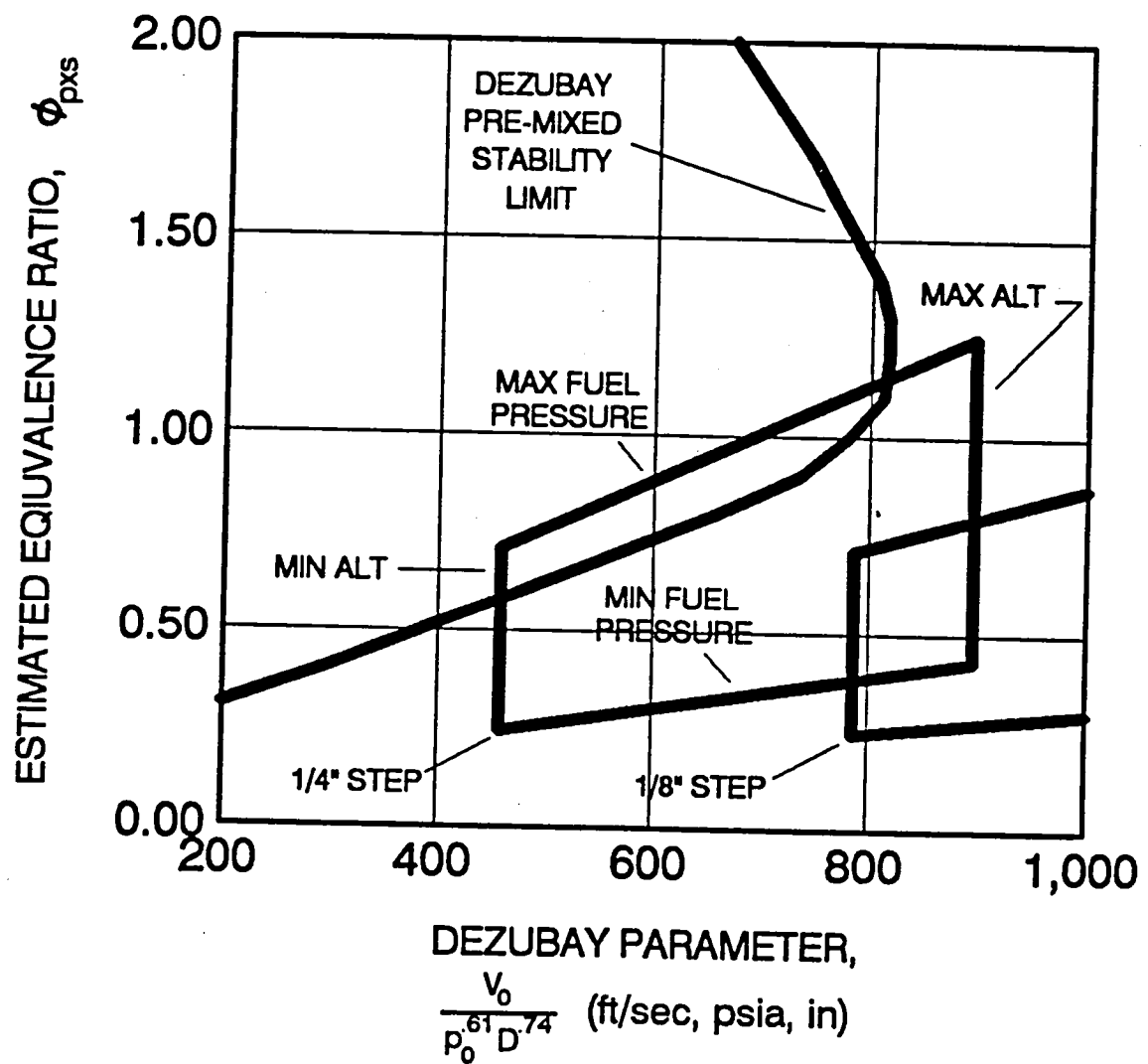
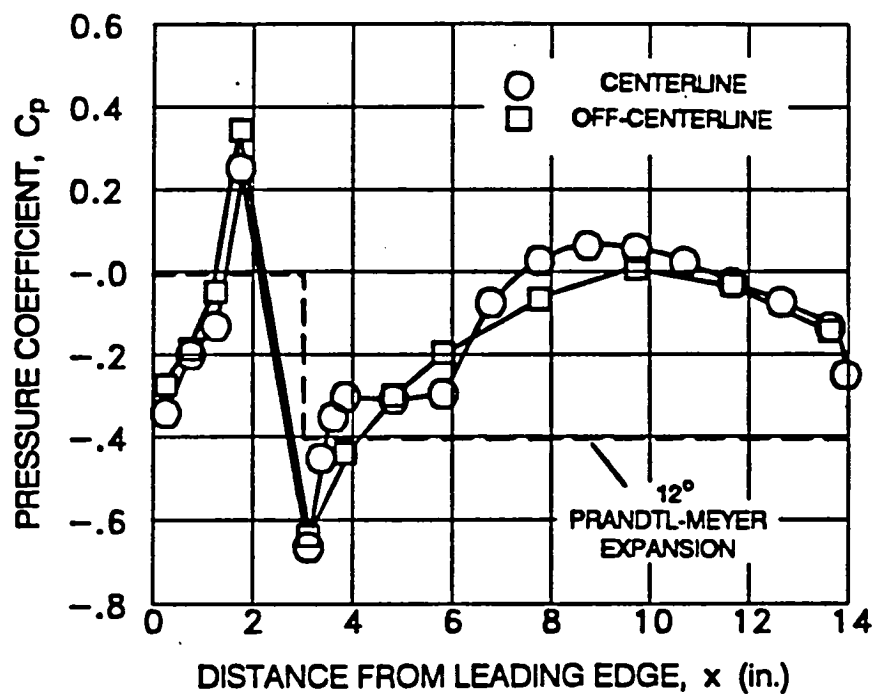
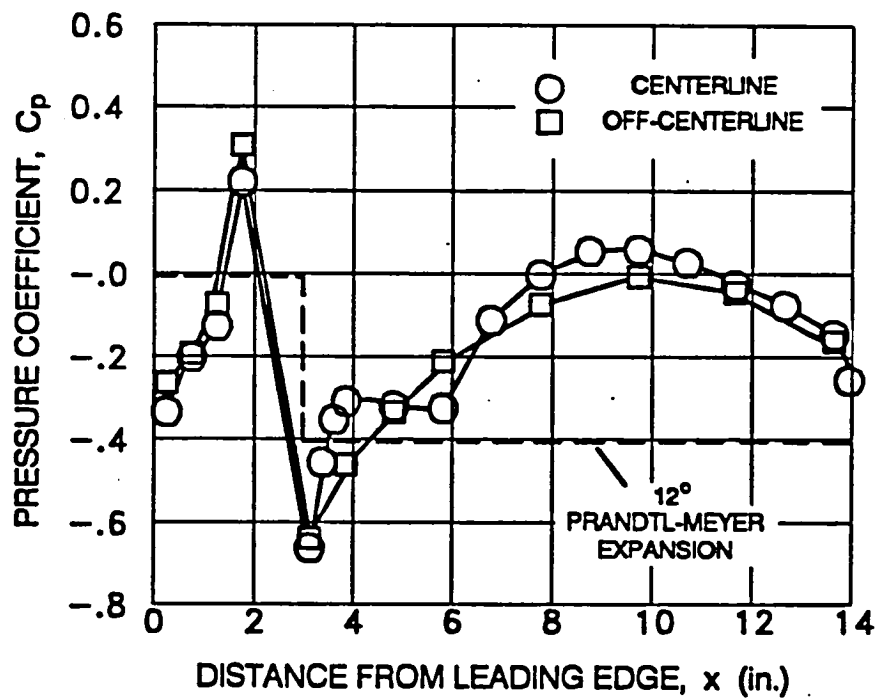


Figure 4-19. Flame stability envelopes for 26 injector model;  
 $4 < p_0 < 12$  psia,  $50 < p_f < 375$  psia.

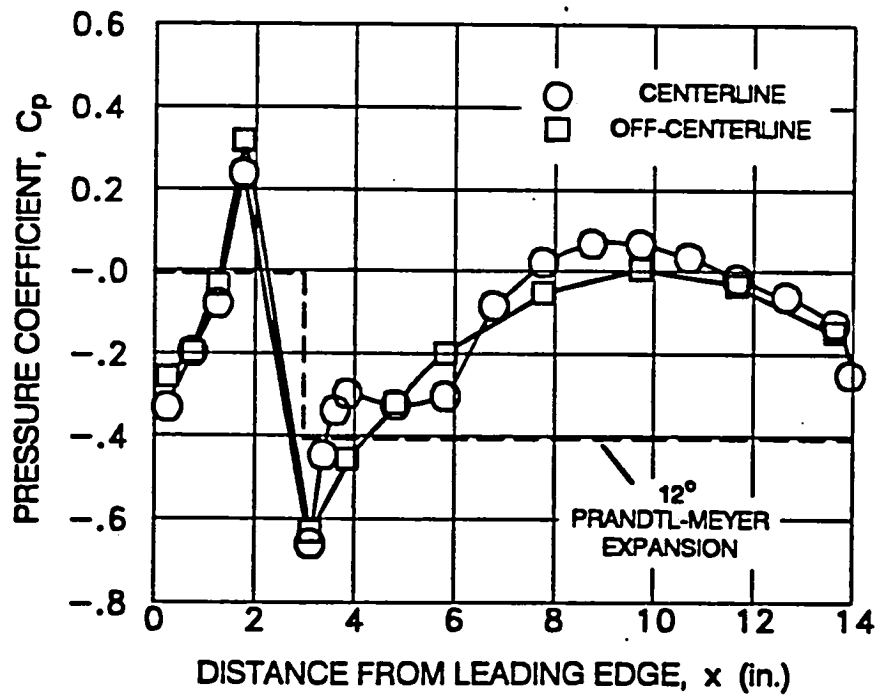


a)  $p_0 = 12$  psia.



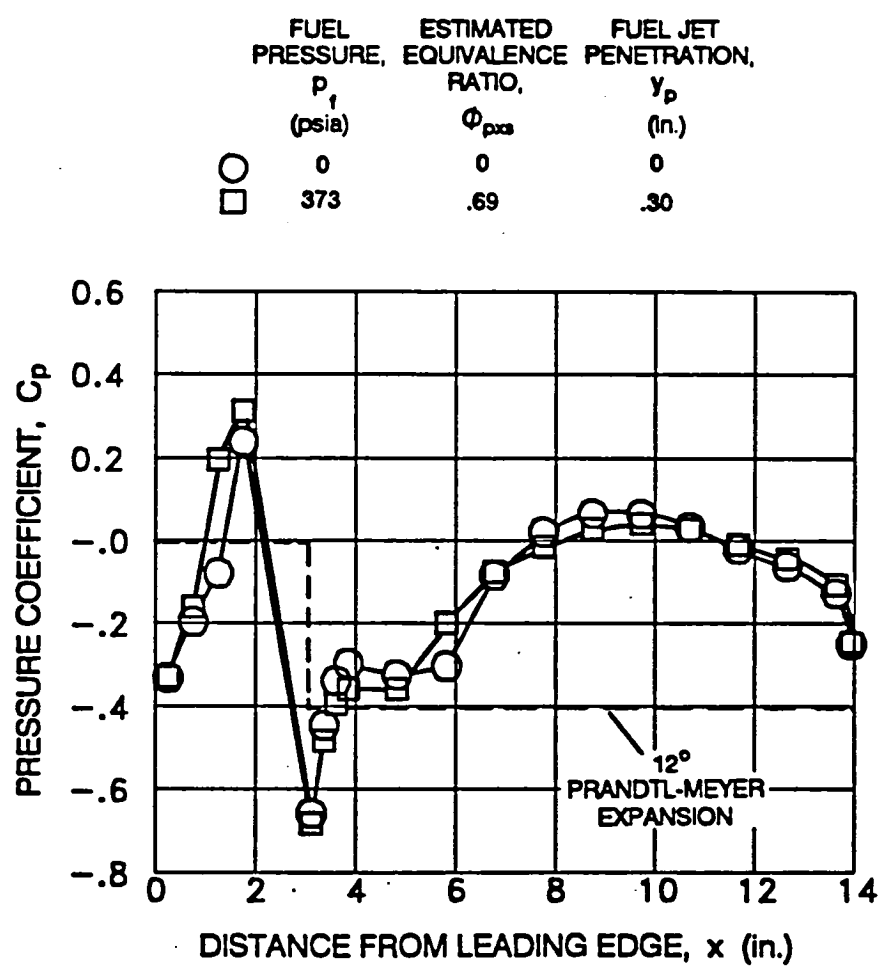
b)  $p_0 = 8$  psia.

Figure 4-20. Fuel-off static pressure distributions; configuration 1.



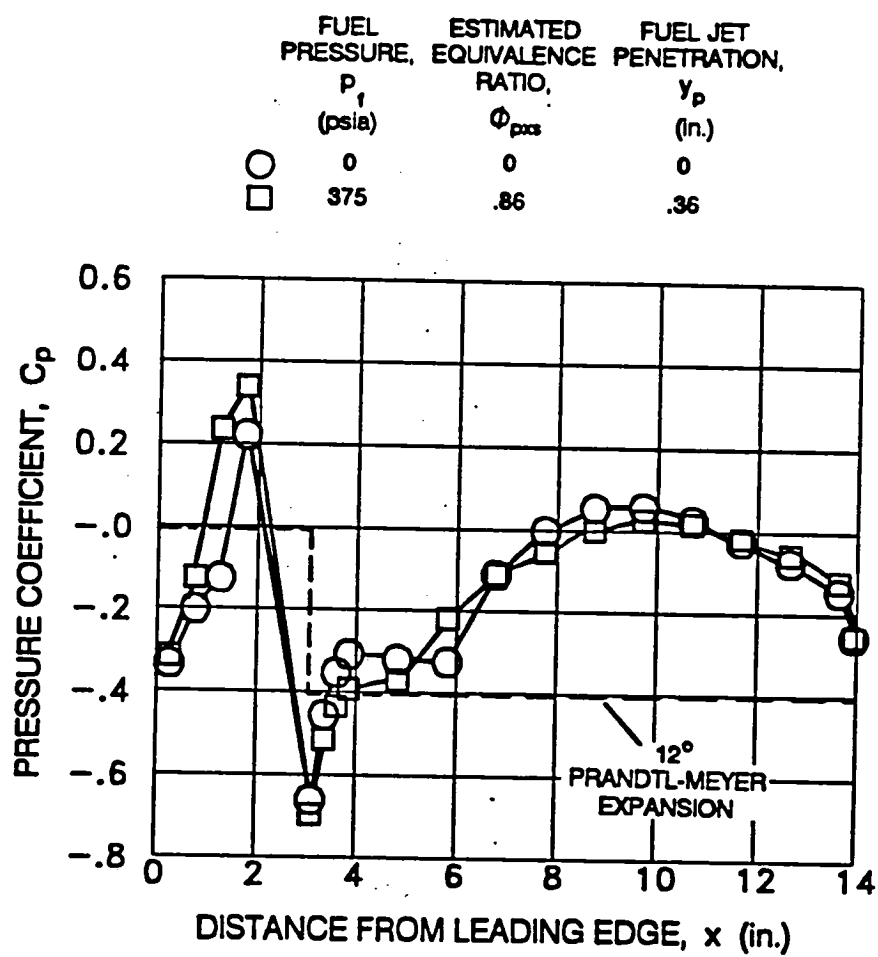
c)  $p_0 = 4$  psia.

Figure 4-20. Concluded.



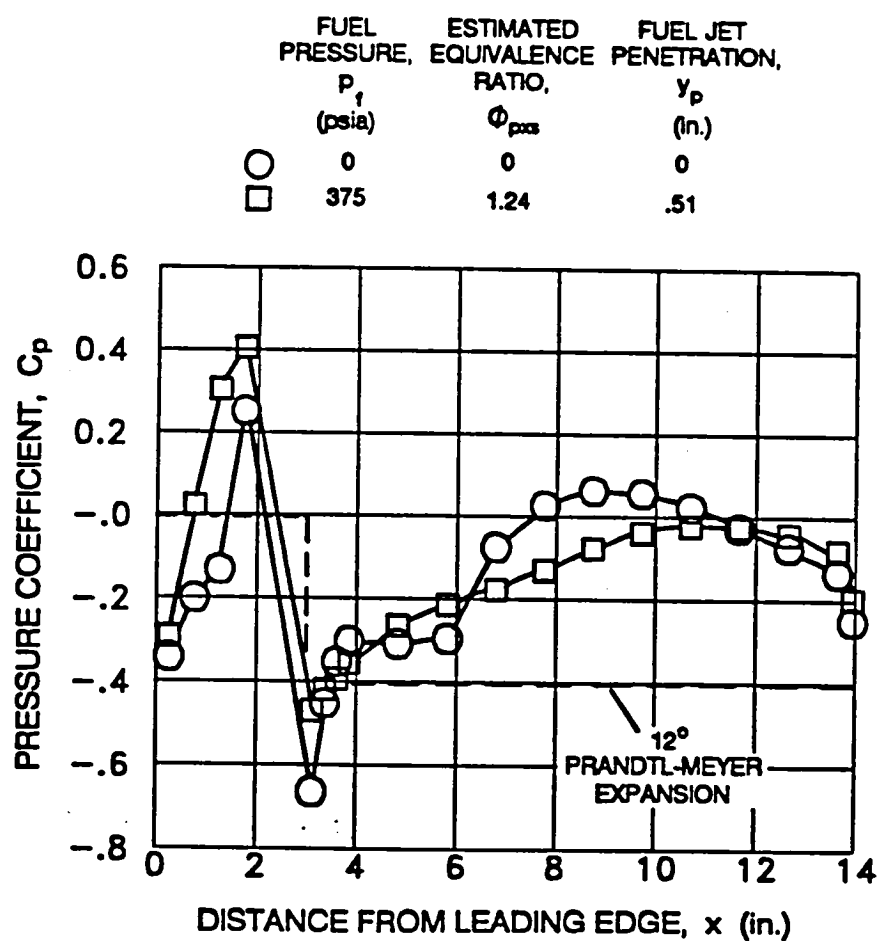
a)  $p_0 = 12$  psia.

Figure 4-21. Effect of fuel mass addition on centerline static pressure distributions; configuration 1.



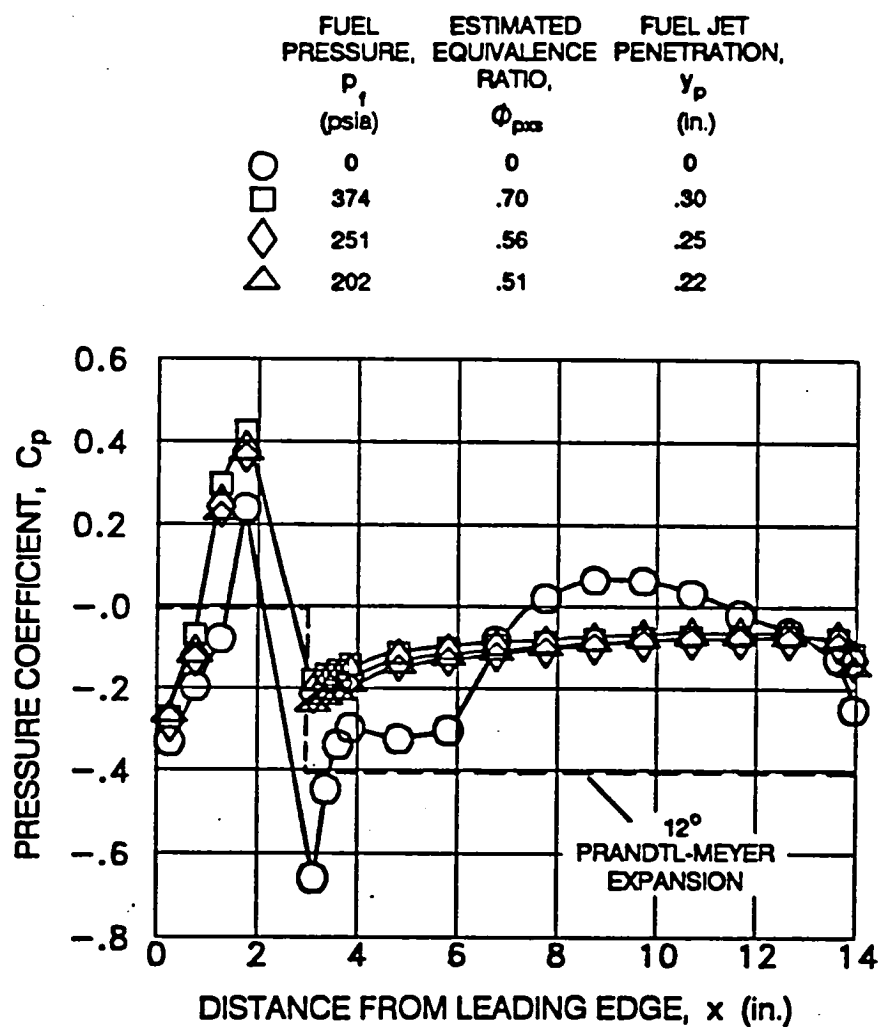
b)  $p_0 = 8$  psia.

Figure 4-21. Continued.



c)  $p_0 = 4$  psia.

Figure 4-21. Concluded.

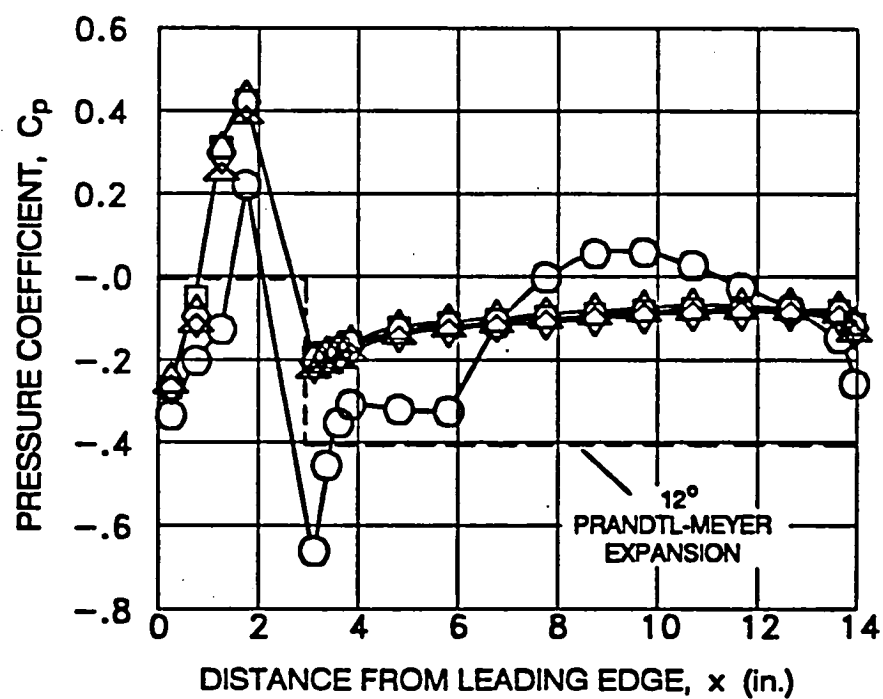


a)  $p_0=12$  psia.

Figure 4-22. Effect of external burning on centerline static pressure distributions; configuration 1.

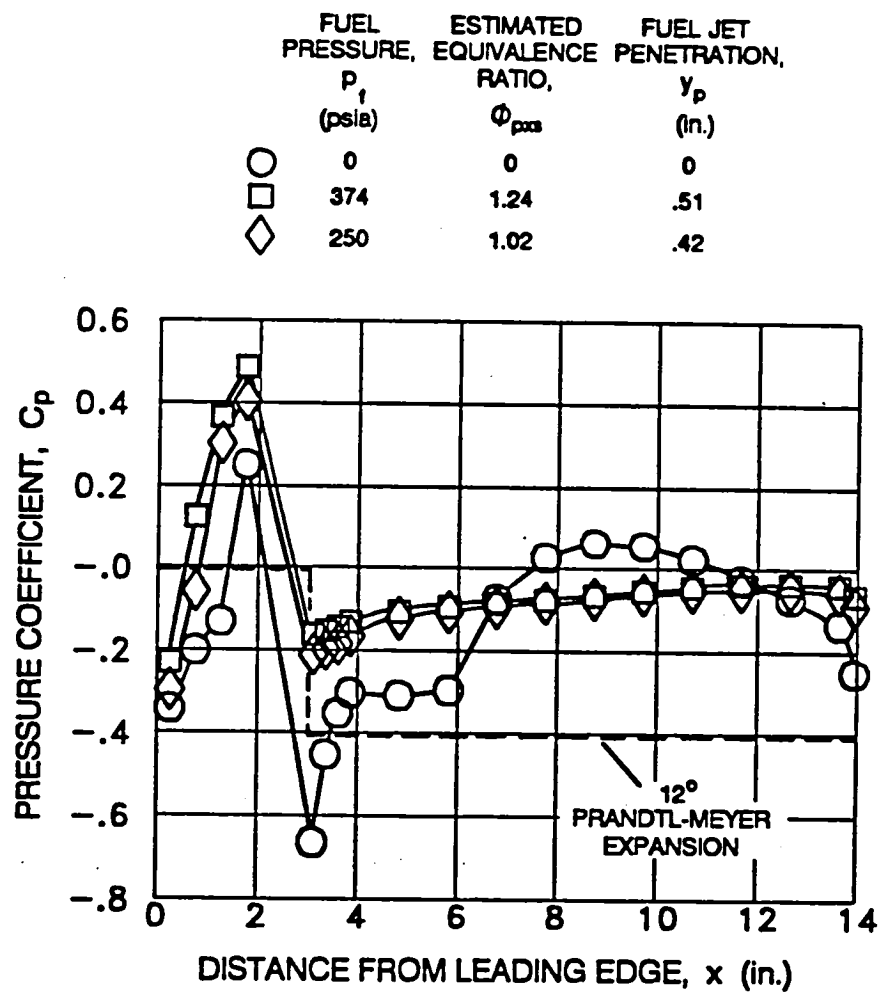


	FUEL PRESSURE, $p_f$ (psia)	ESTIMATED EQUIVALENCE RATIO, $\phi_{pm}$	FUEL JET PENETRATION, $y_p$ (in.)
○	0	0	0
□	373	.84	.36
◇	251	.70	.30
△	201	.61	.27



b)  $p_0 = 8$  psia.

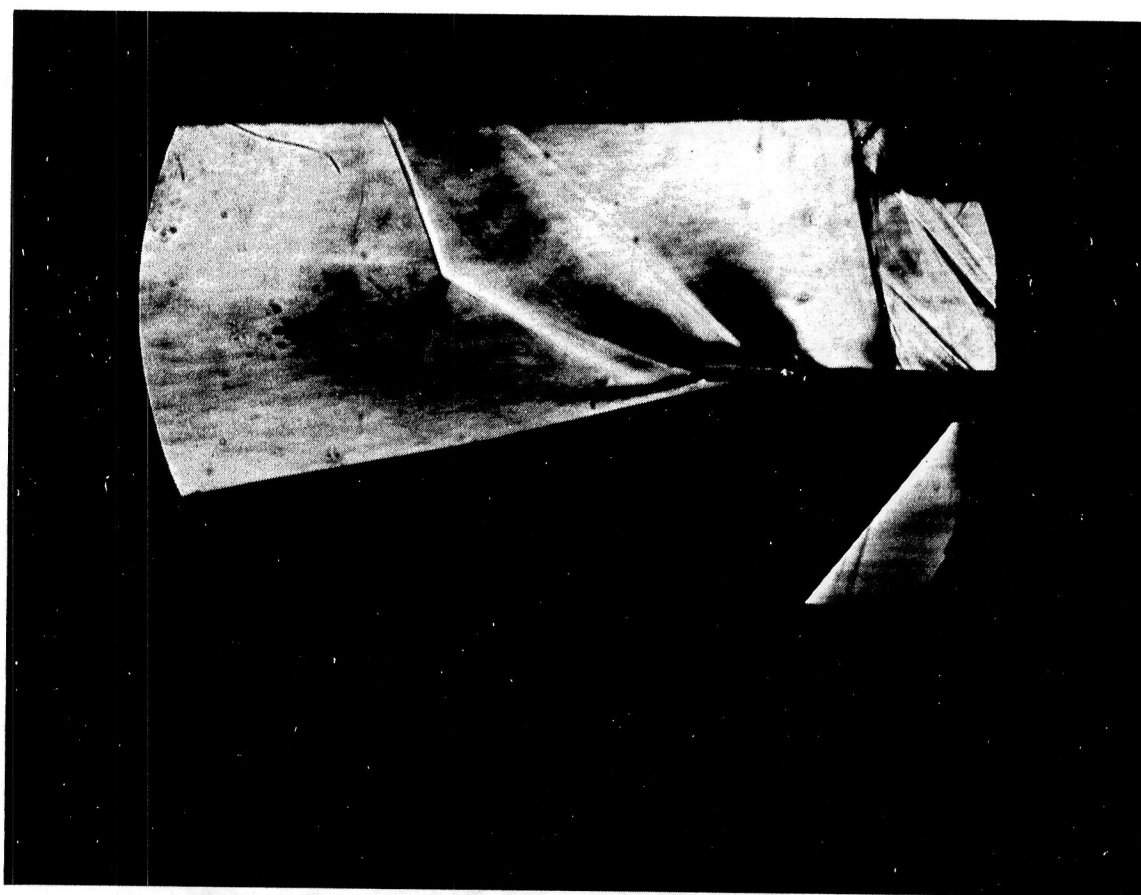
Figure 4-22. Continued.



c)  $p_0 = 4$  psia.

Figure 4-22. Concluded.

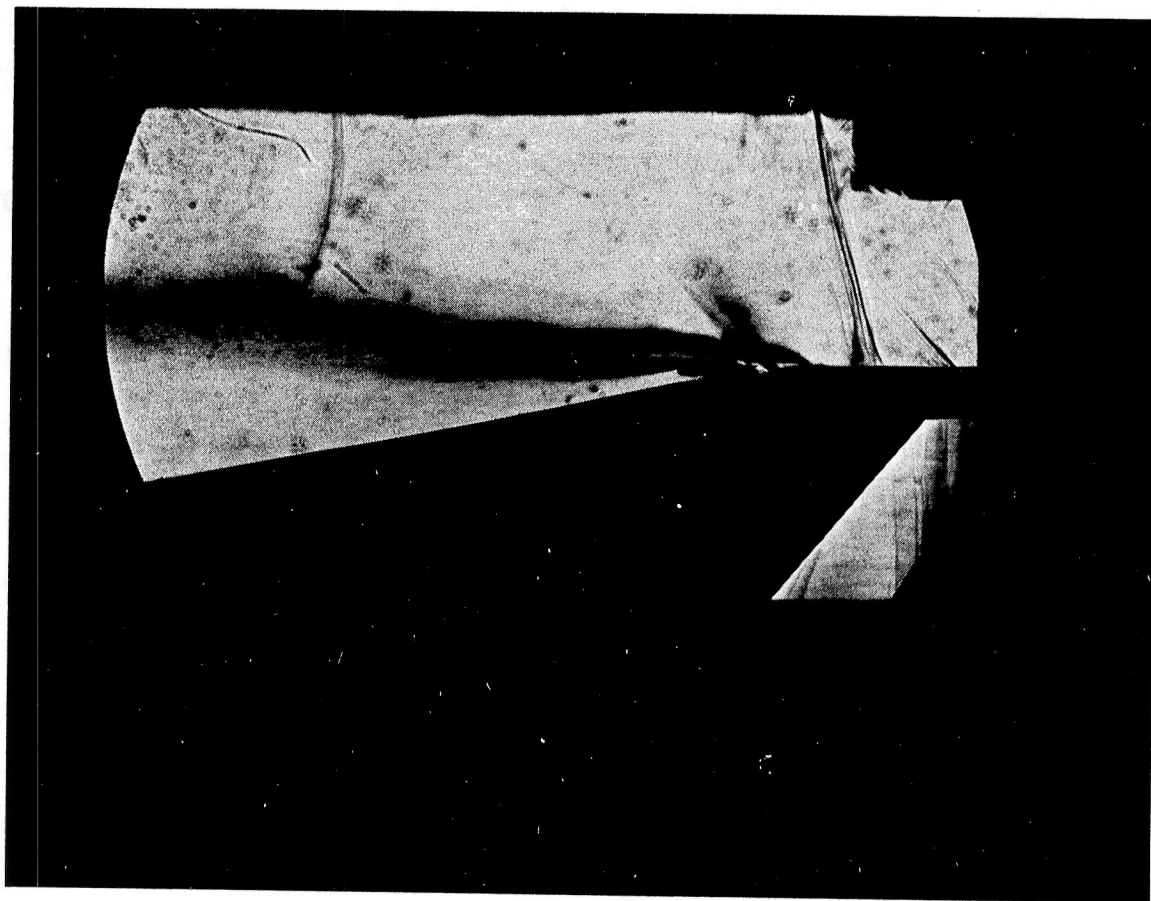
ORIGINAL PAGE  
BLACK AND WHITE PHOTOGRAPH



a) Fuel-off.

Figure 4-23. Schlieren images of external burning (configuration 10).

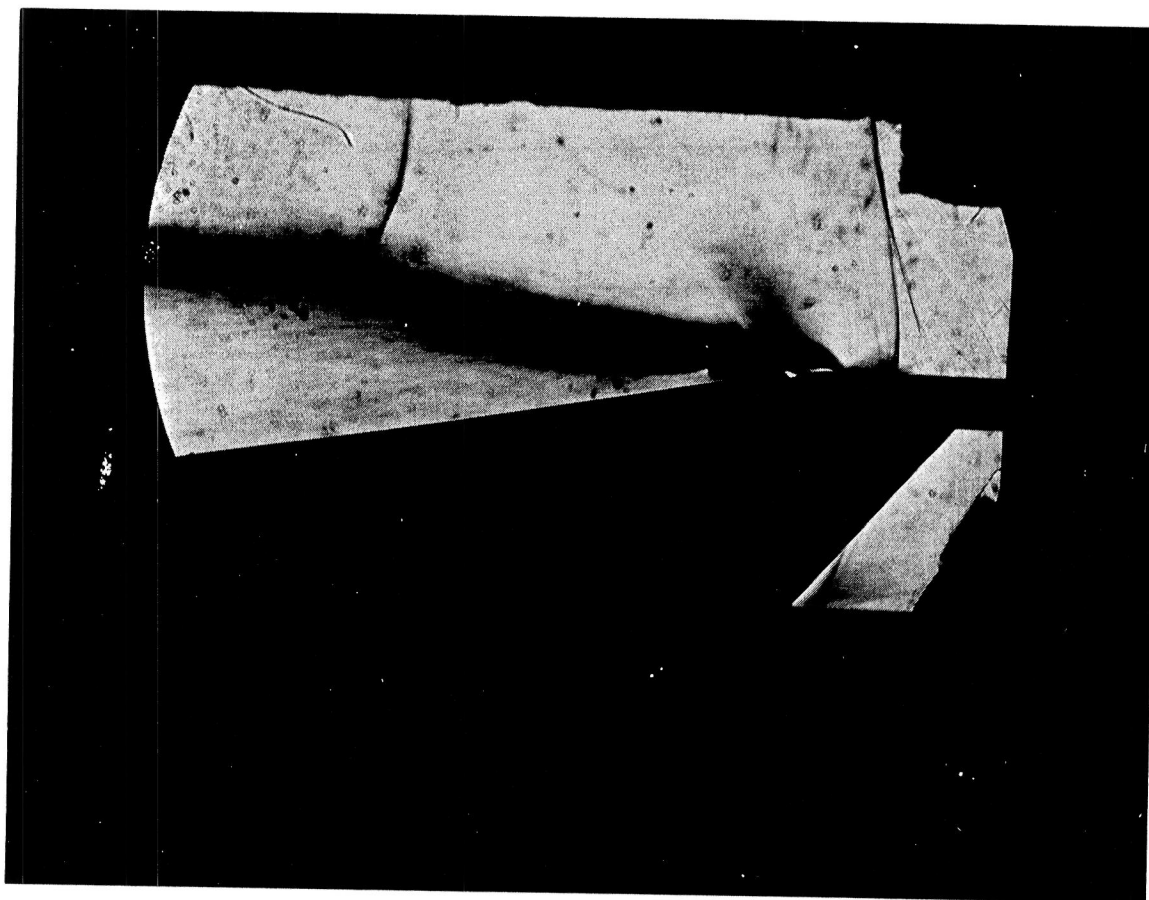
ORIGINAL PAGE  
BLACK AND WHITE PHOTOGRAPH



b) Low equivalence ratio;  $p_f=250$  psia,  $p_0=12$  psia ( $\phi_{pxs}=.56$ ,  $y_p=.25''$ ).

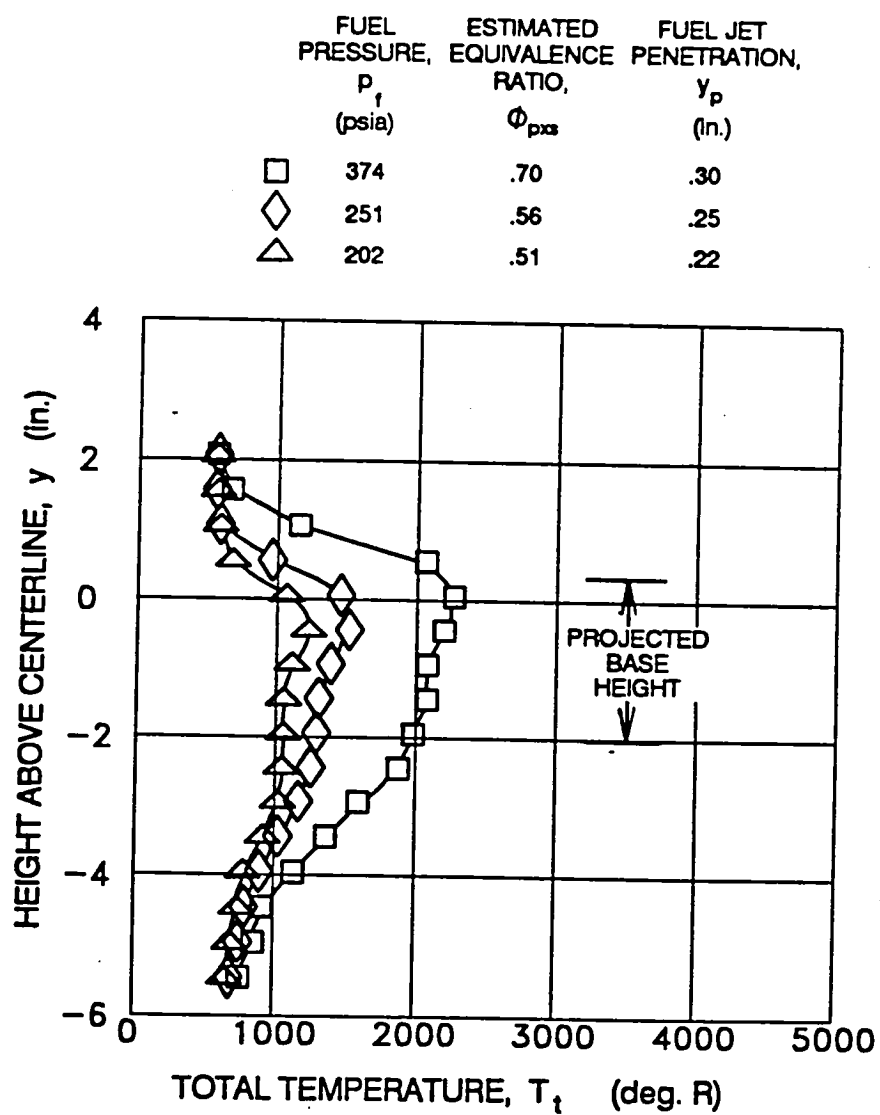
Figure 4-23. Continued.

ORIGINAL PAGE  
BLACK AND WHITE PHOTOGRAPH



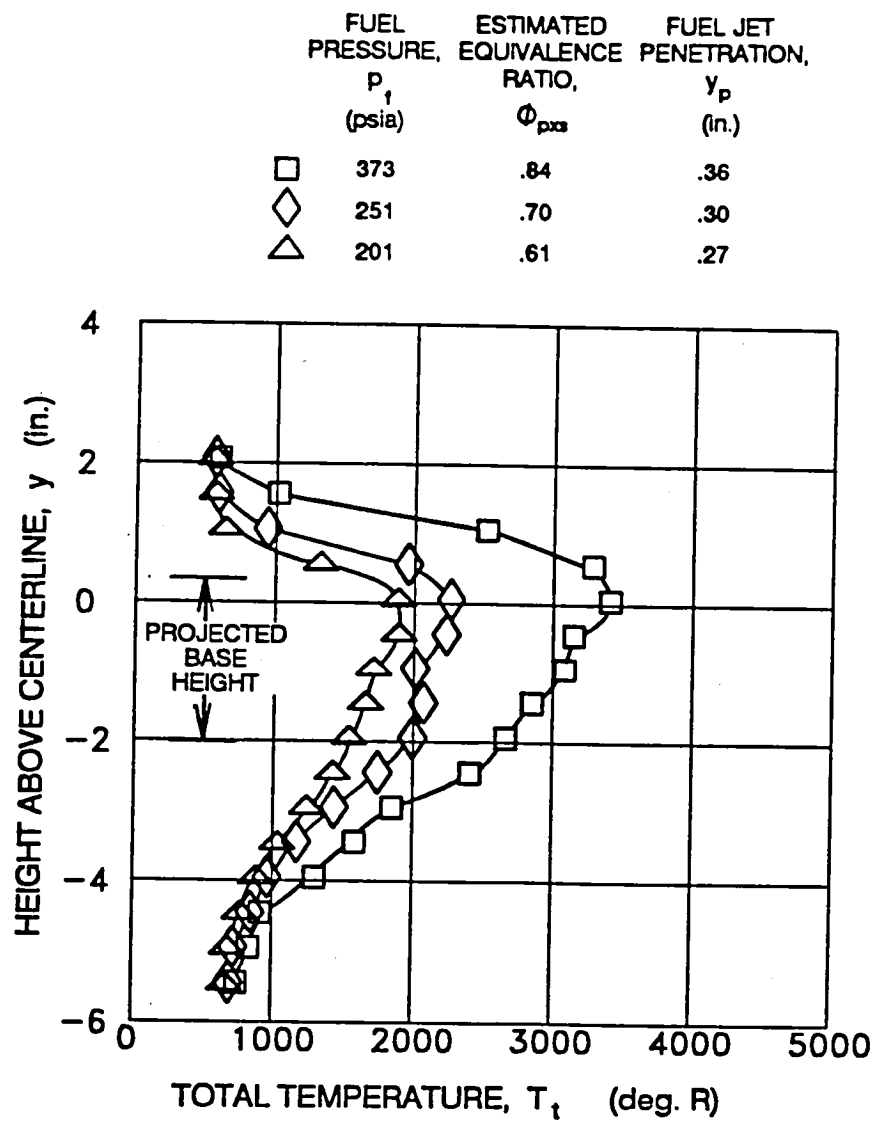
c) High equivalence ratio;  $p_f=375$  psia,  $p_0=4$  psia ( $\phi_{pxs}=1.24$ ,  $y_p=.51''$ ).

Figure 4-23. Concluded.



a)  $p_0=12$  psia.

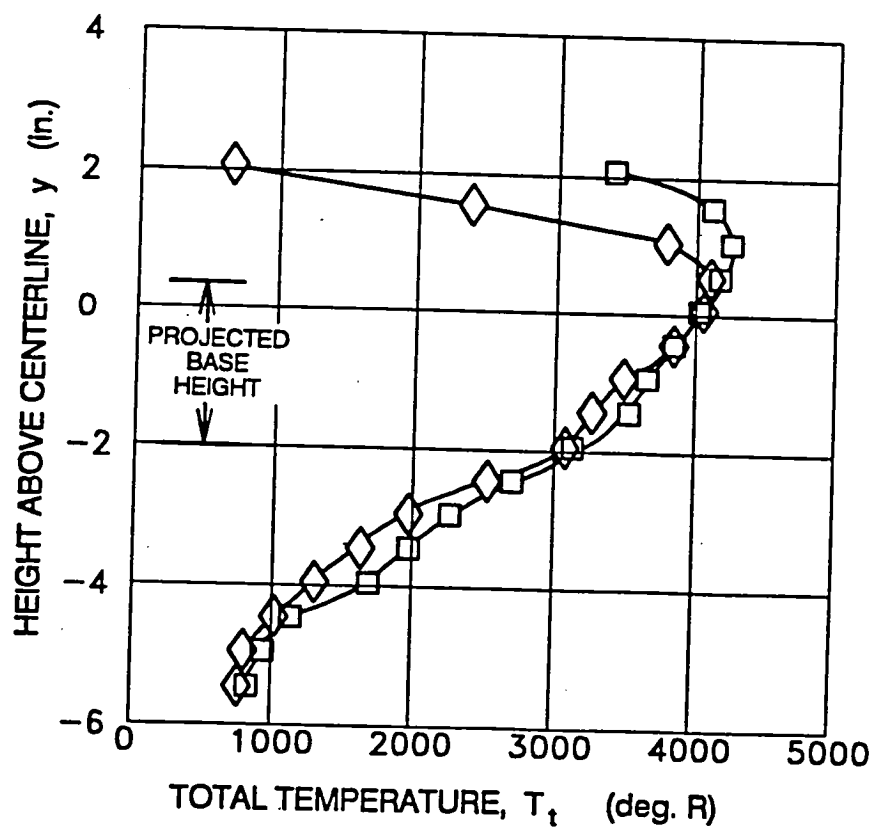
Figure 4-24. Total temperature profiles; configuration 1.



b)  $p_0=8$  psia.

Figure 4-24. Continued.

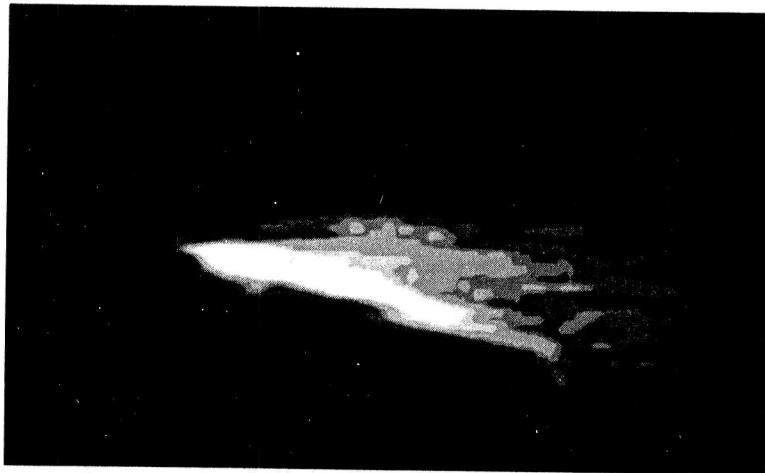
	FUEL PRESSURE, $P_f$ (psia)	ESTIMATED EQUIVALENCE RATIO, $\Phi_{pzs}$	FUEL JET PENETRATION, $y_p$ (in.)
□	374	1.24	.51
◇	250	1.02	.42



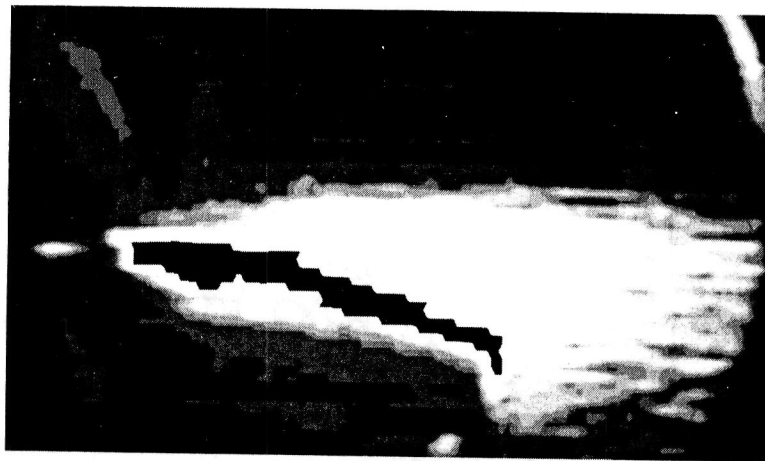
c)  $p_0 = 4$  psia.

Figure 4-24. Concluded.





a) Low equivalence ratio;  $p_f=200$  psia,  $p_0=12$  psia ( $\phi_{pxs}=.51$ ,  $y_p=.22''$ ).

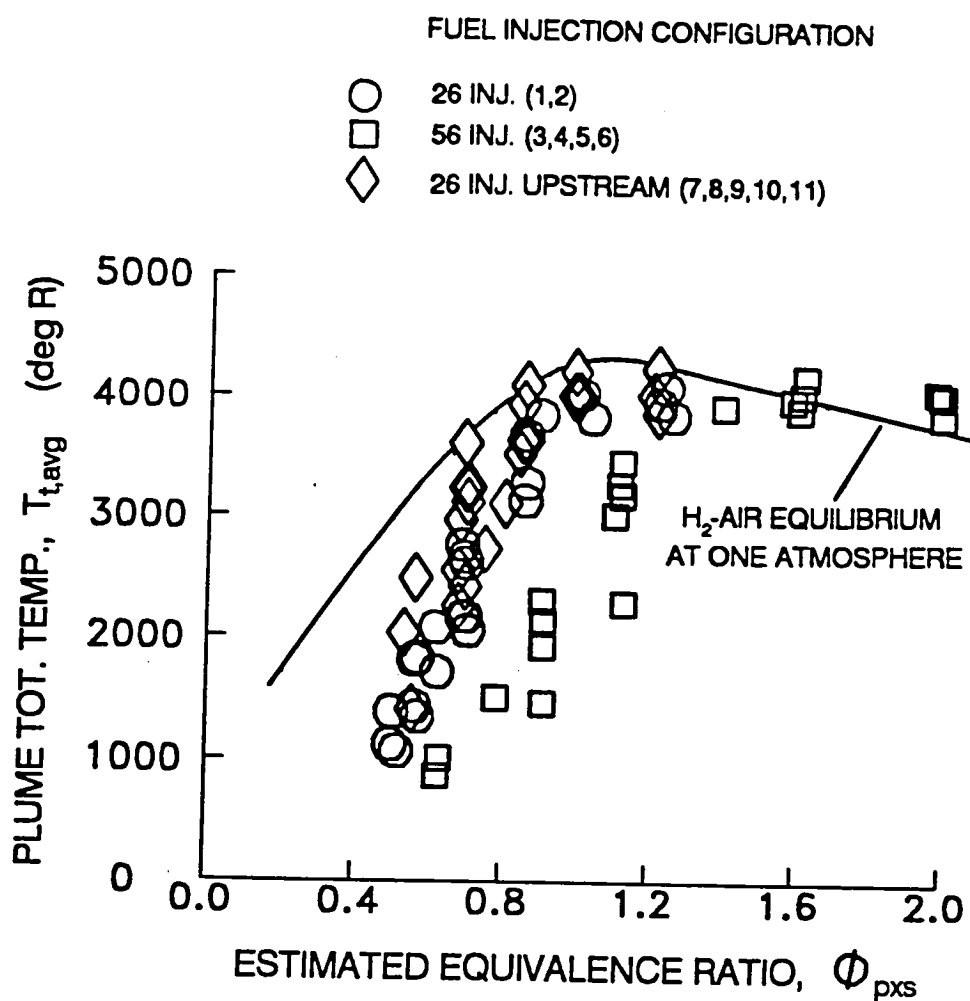


b) Medium equivalence ratio;  $p_f=250$  psia,  $p_0=8$  psia ( $\phi_{pxs}=.70$ ,  $y_p=.30''$ ).



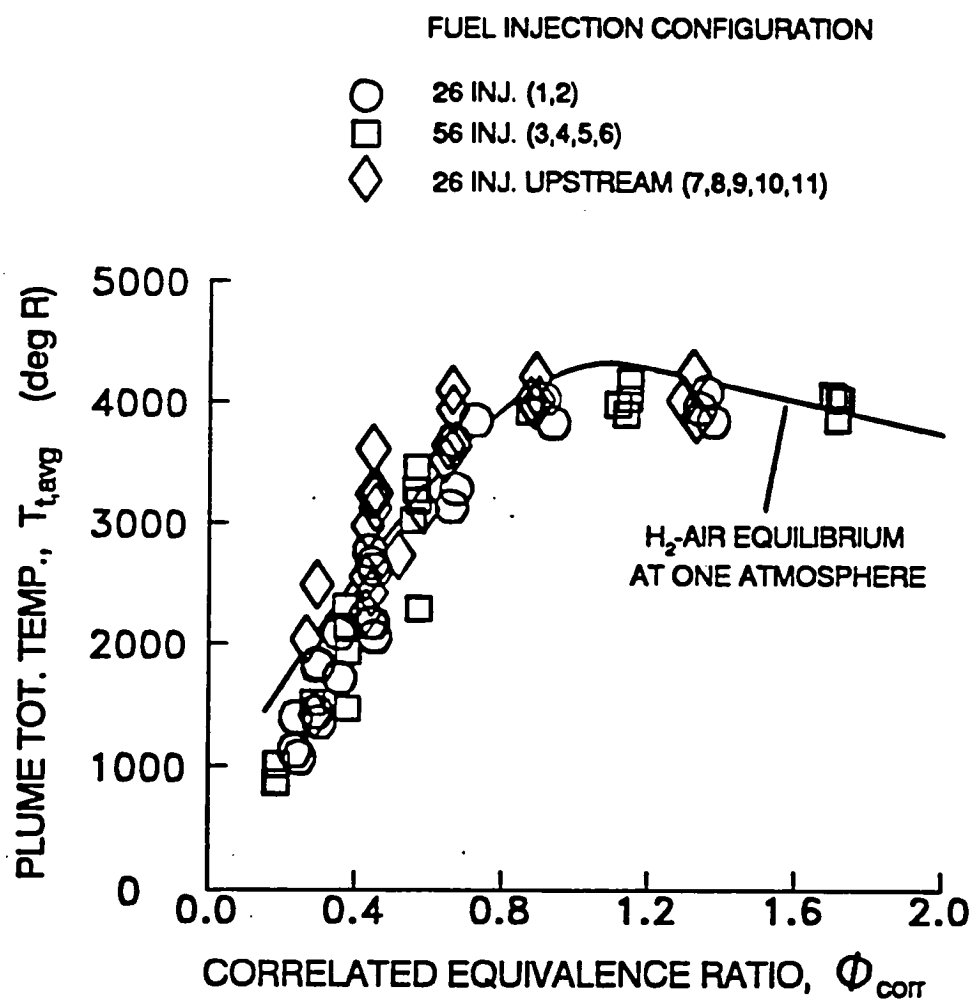
c) High equivalence ratio,  $p_f=375$  psia,  $p_0=4$  psia ( $\phi_{pxs}=1.24$ ,  $y_p=.51''$ ).

Figure 4-25. Infra-red images of external burning; configuration 1.



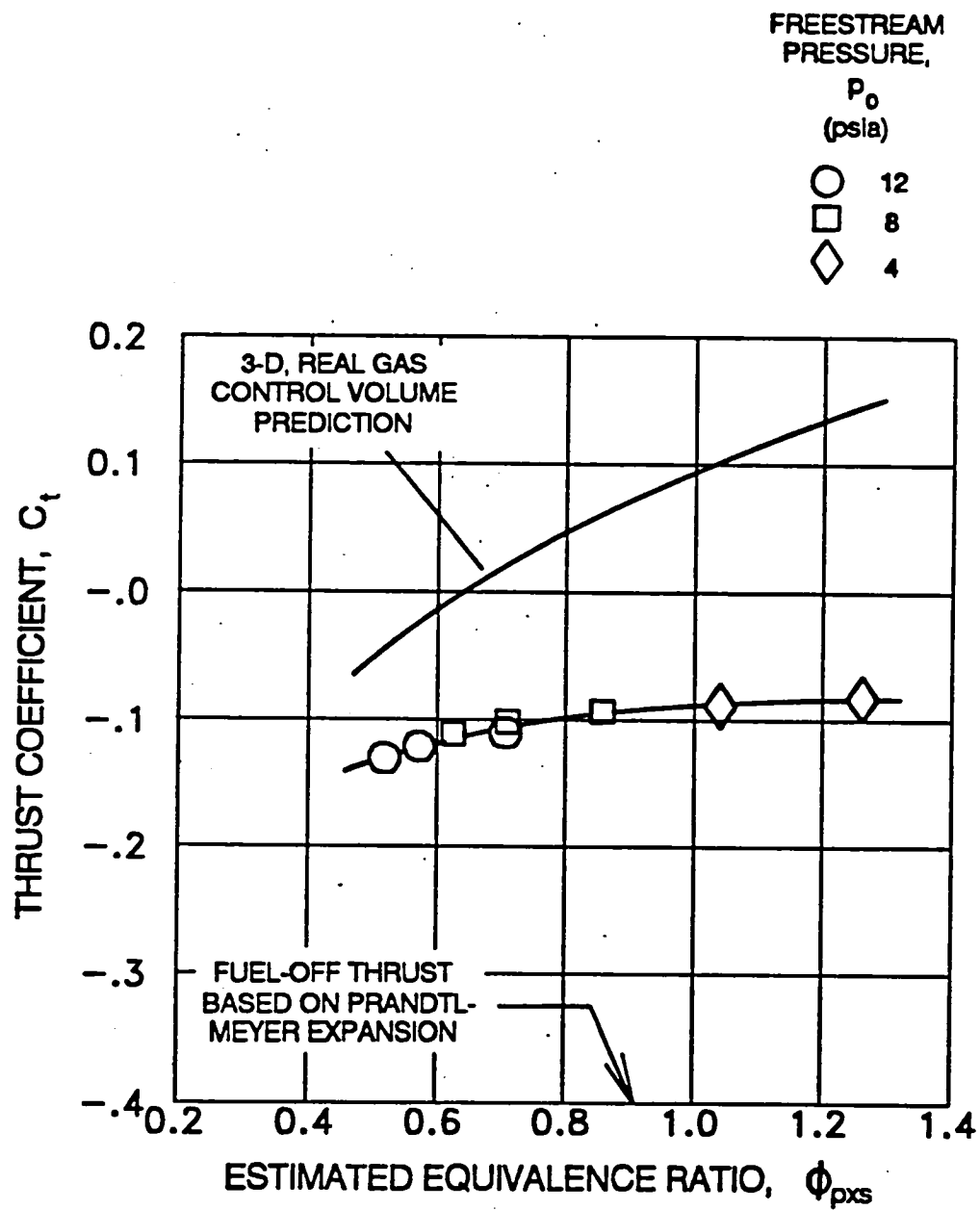
a) Equivalence ratio based on penetration times spacing method with  $x/d^* = 30$ .

Figure 4-26. Average plume temperature correlation.



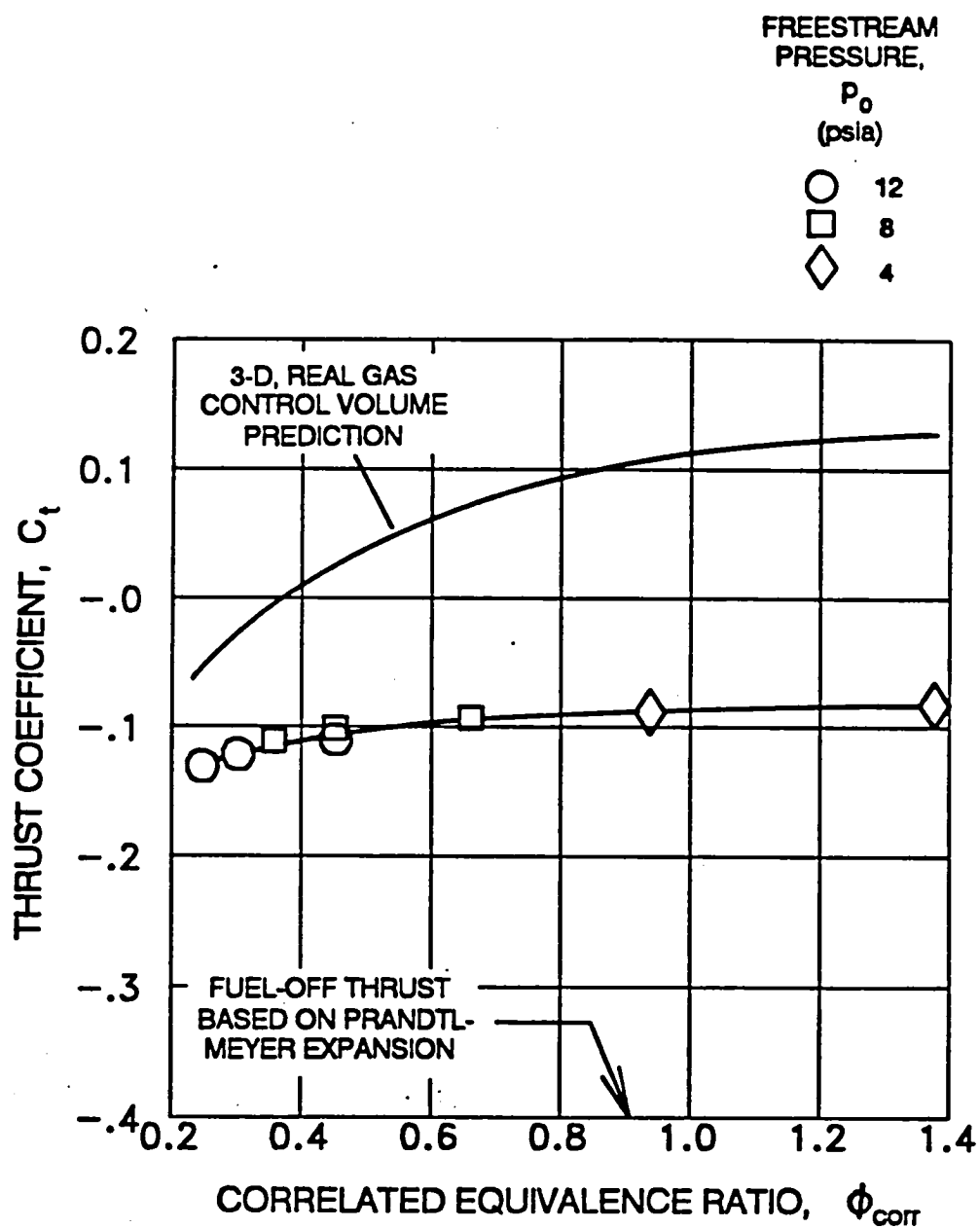
b) Equivalence ratio and inflow stream height based on correlation of average measured plume temperature.

Figure 4-26. Concluded.



a) Equivalence ratio based on penetration times spacing method with  $x/d^* = 30$ .

Figure 4-27. Thrust coefficient; configuration 1.



b) Equivalence ratio and inflow stream height based on correlation of average measured plume temperature.

Figure 4-27. Concluded.

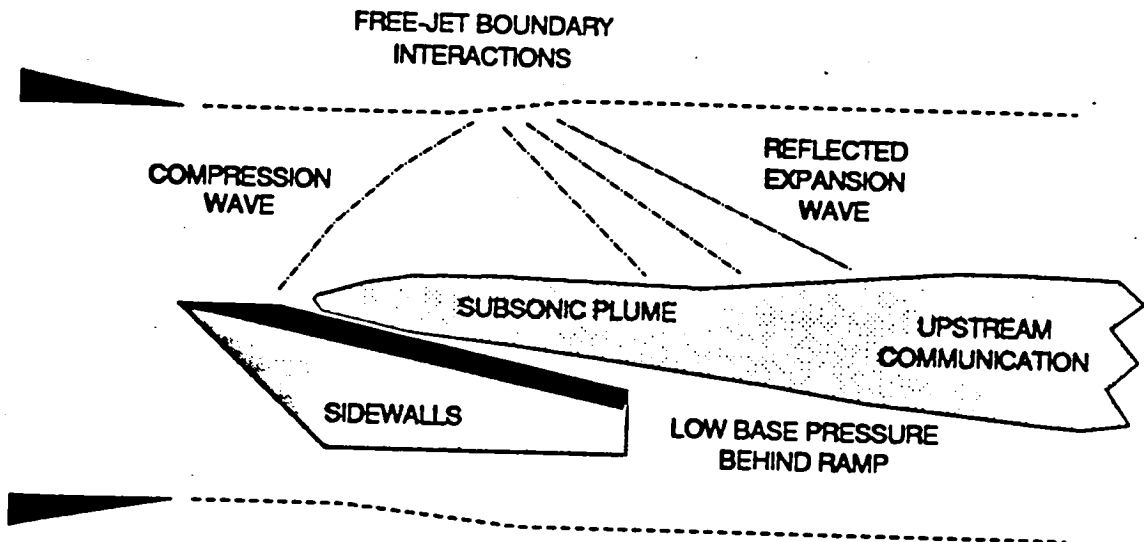


Figure 4-28. Facility interactions suspected of causing low performance.

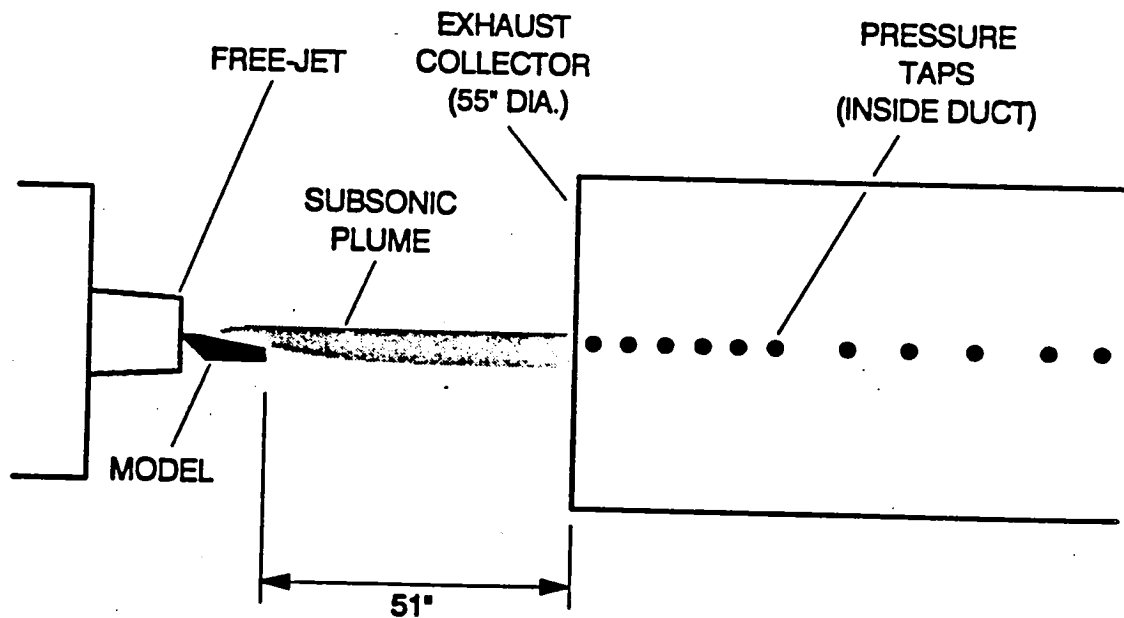


Figure 4-29. PSL-4 Facility exhaust collector layout.

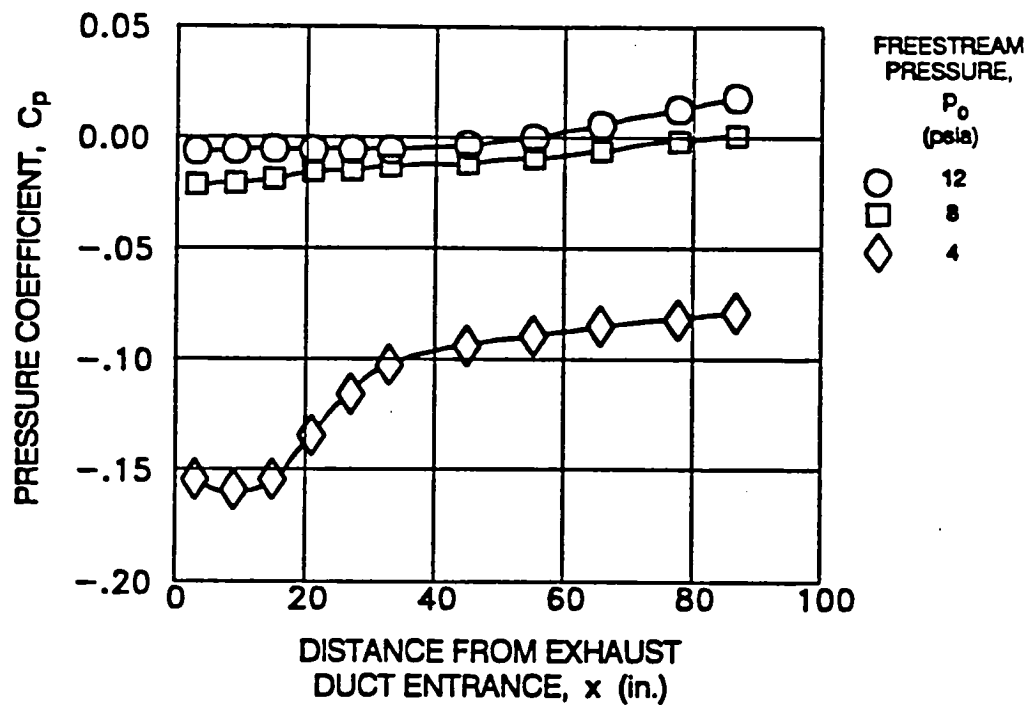


Figure 4-30. Effect of altitude on exhaust collector pressure distributions during external burning;  $p_f = 375$  psia.

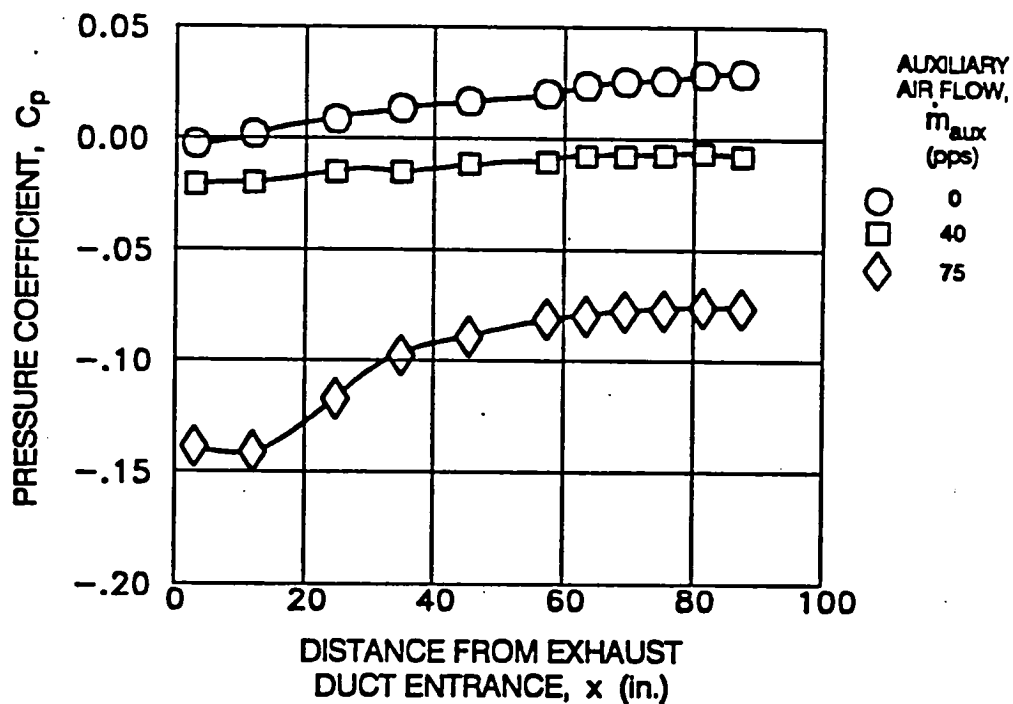


Figure 4-31. Effect of auxiliary air flow on exhaust collector pressure distributions;  $p_0 = 4$  psia, fuel-off.

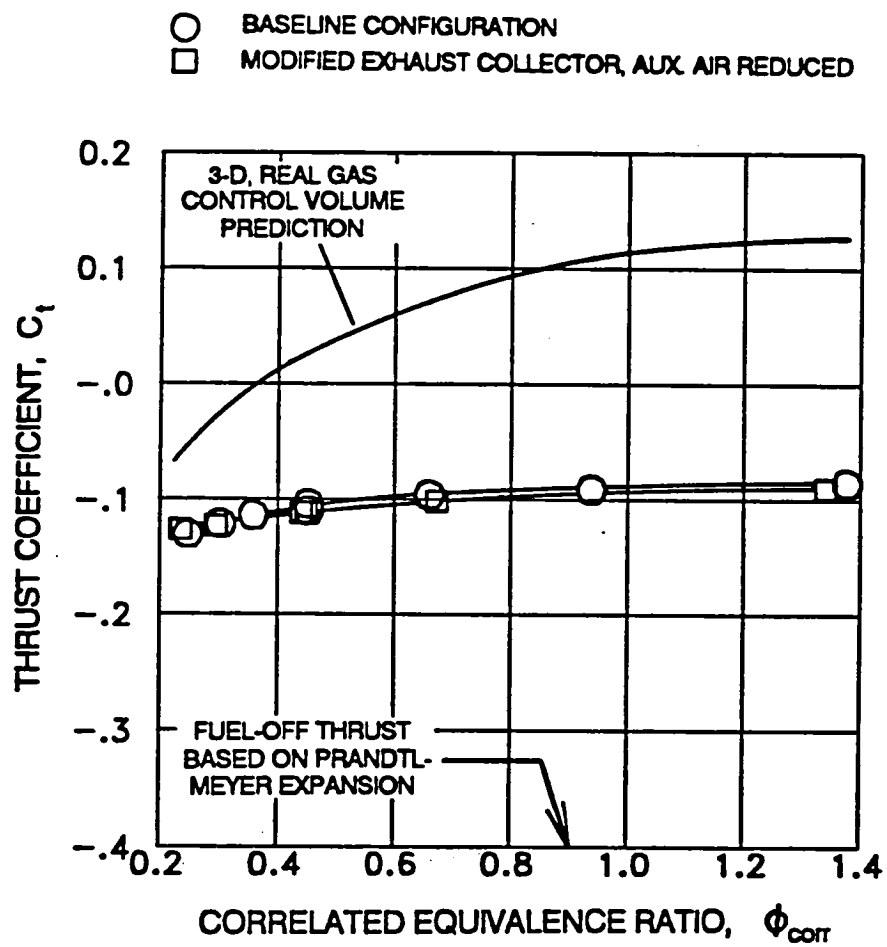


Figure 4-32. Effect of exhaust collector modification on thrust coefficient; configuration 1.



ORIGINAL PAGE  
BLACK AND WHITE PHOTOGRAPH

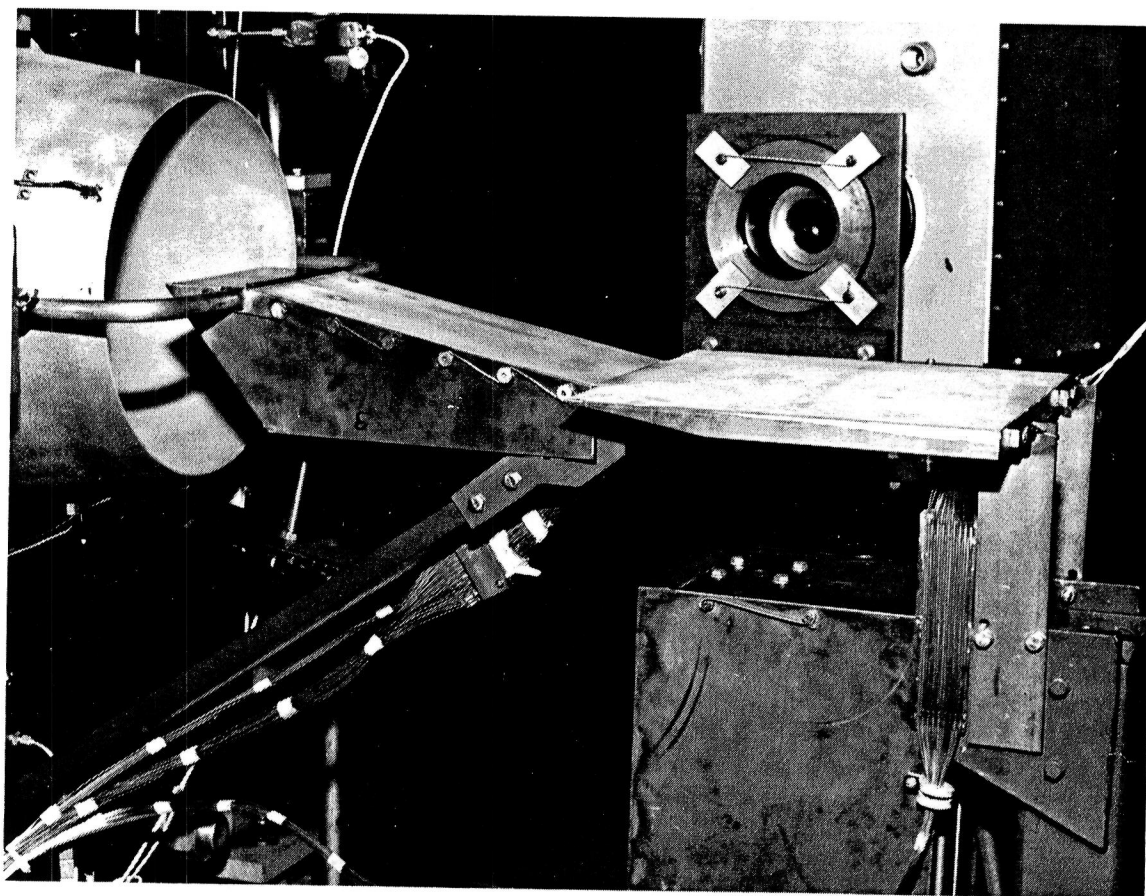


Figure 4-33. Plume boundary simulator installation; configuration 2.

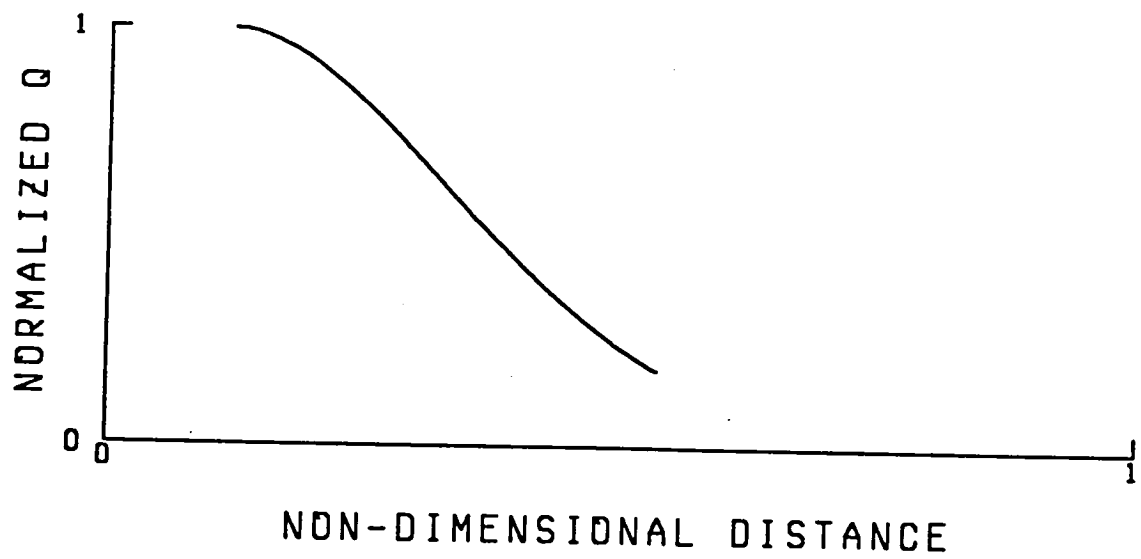
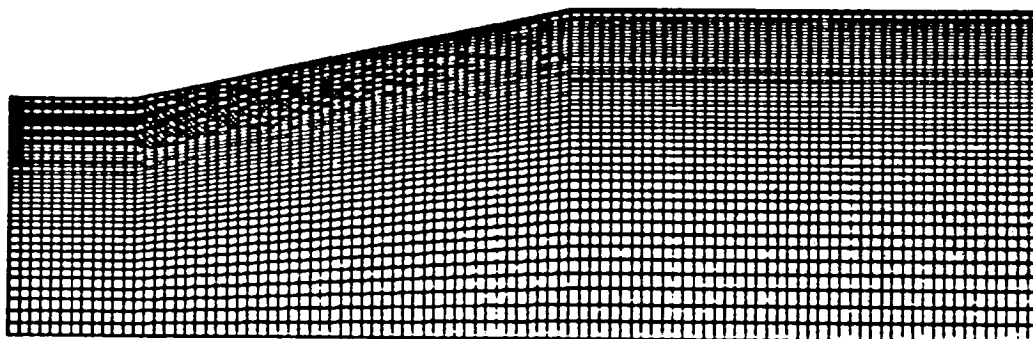
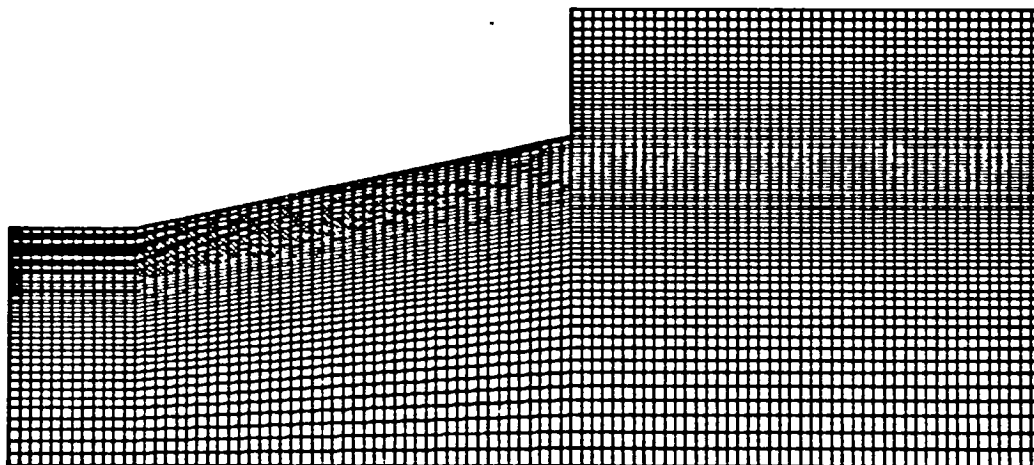


Figure 4-34. Gaussian axial heat addition distribution function.

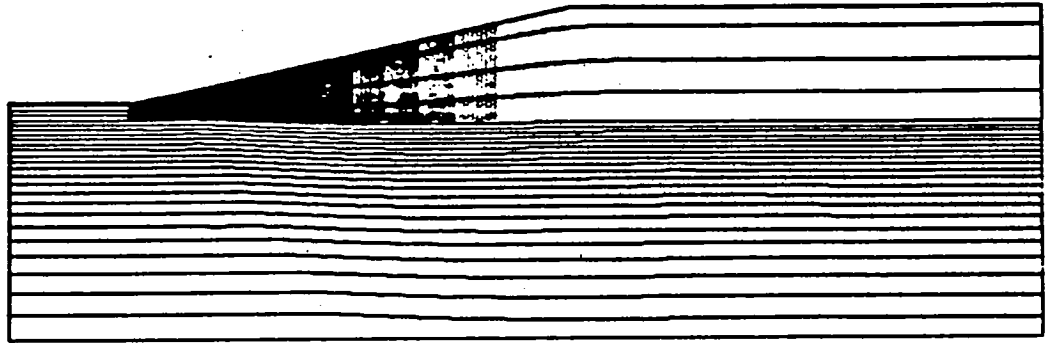


a) Solid wall boundary, 100 x 50 nodes.

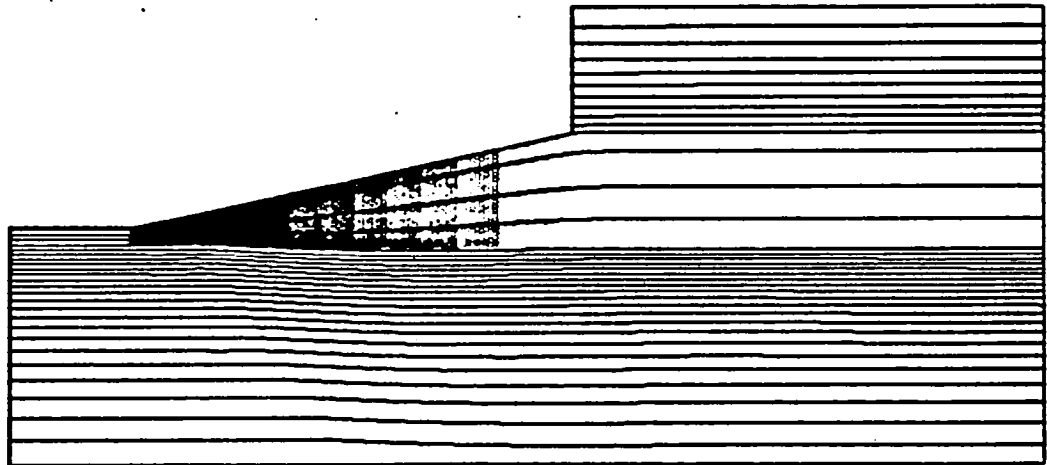


b) Freestream boundary, 100 x 70 nodes.

Figure 4-35. 2-D Euler grids used to validate use of plume boundary simulator.



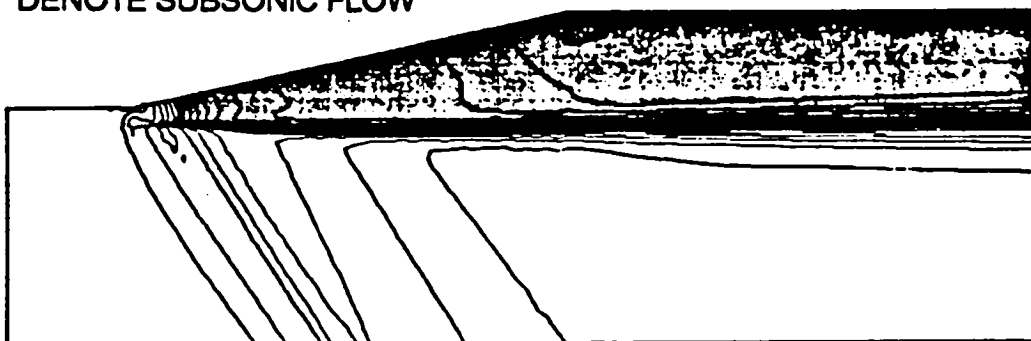
a) Solid wall boundary.



b) Freestream boundary.

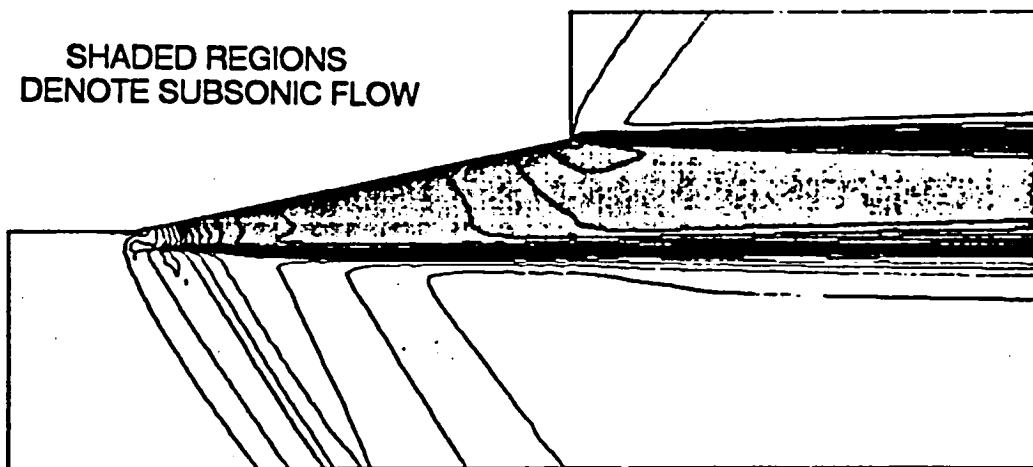
Figure 4-36. Comparison of streamlines, total heat added corresponds to  $\phi_{\text{corr}} = .45$ ,  $y_0/y_b = .20$ .

SHADED REGIONS  
DENOTE SUBSONIC FLOW



a) Solid wall boundary.

SHADED REGIONS  
DENOTE SUBSONIC FLOW



b) Freestream boundary.

Figure 4-37. Comparison of Mach number contours (.05 contour increment). Total heat added corresponds to  $\phi_{\text{corr}} = .45$ ,  $y_0/y_b = .20$ .

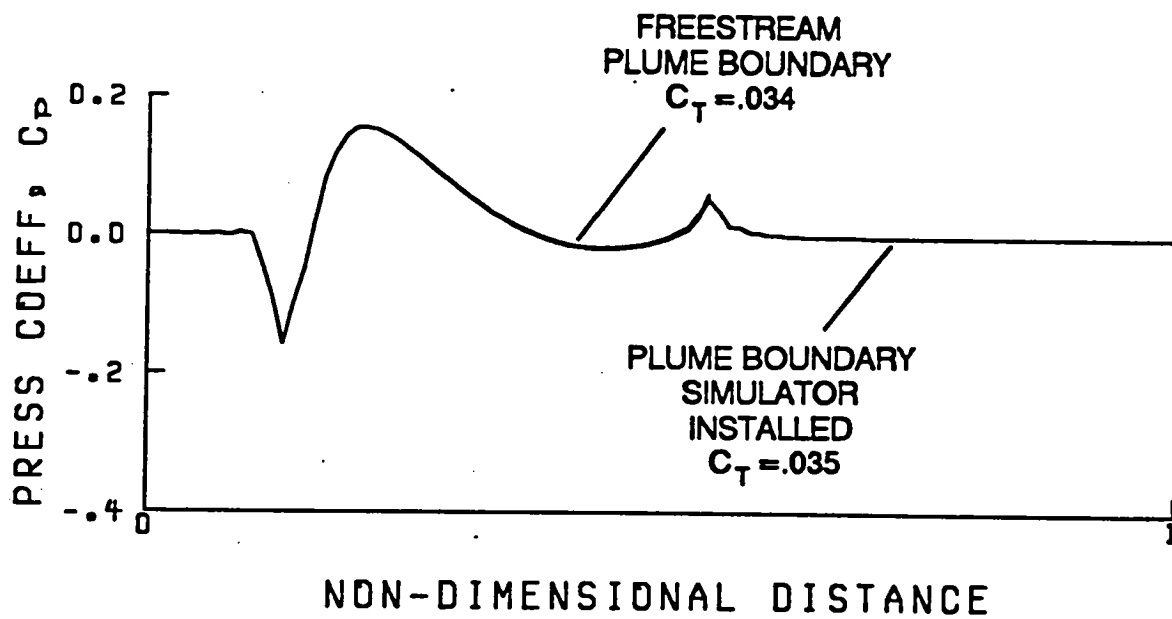
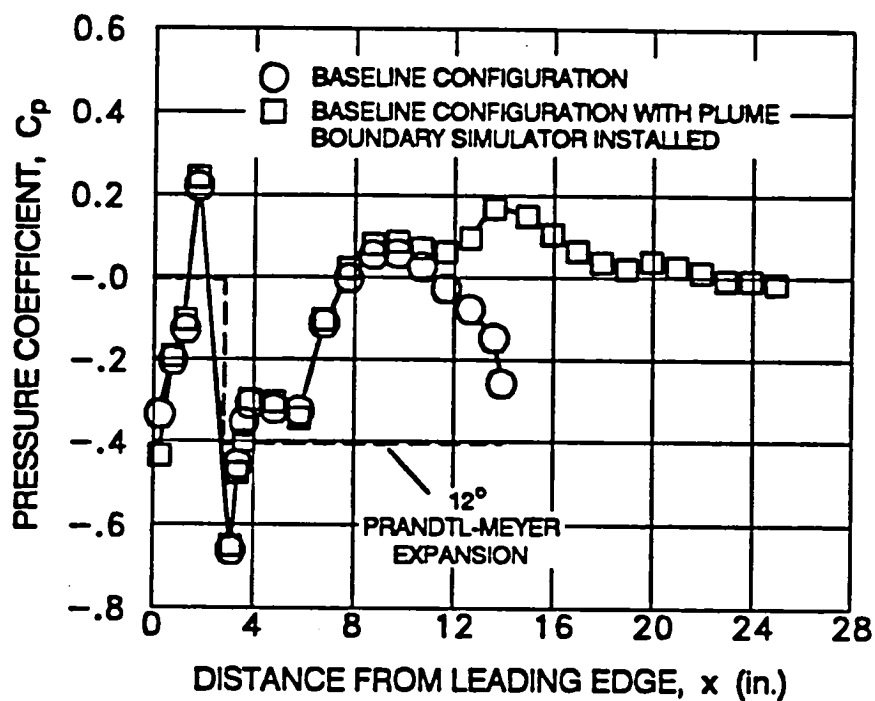
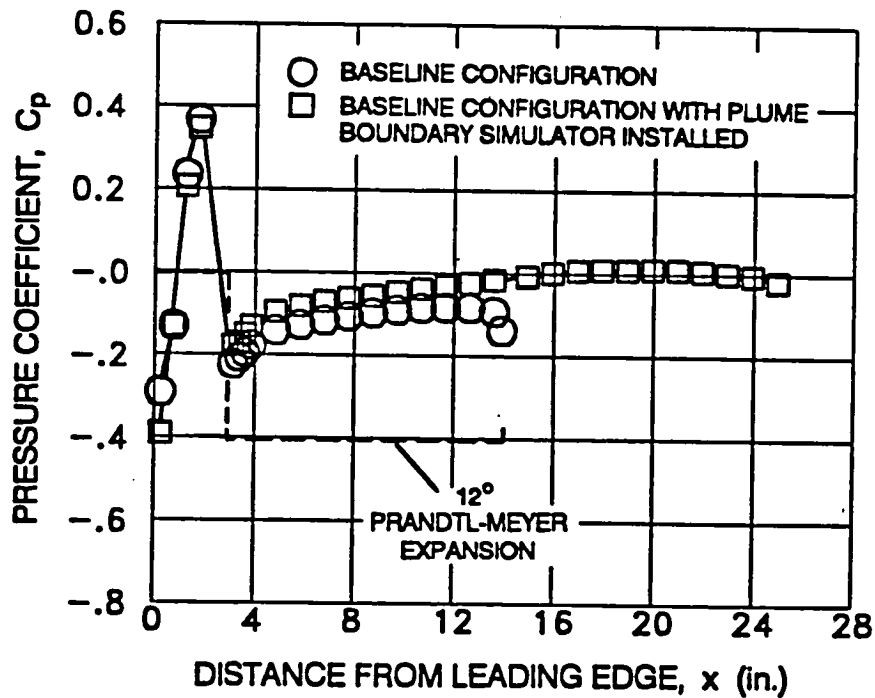


Figure 4-38. Comparison of wall pressure distributions, total heat added corresponds to  $\phi_{\text{corr}} = .45$ ,  $y_0/y_b = .20$ .

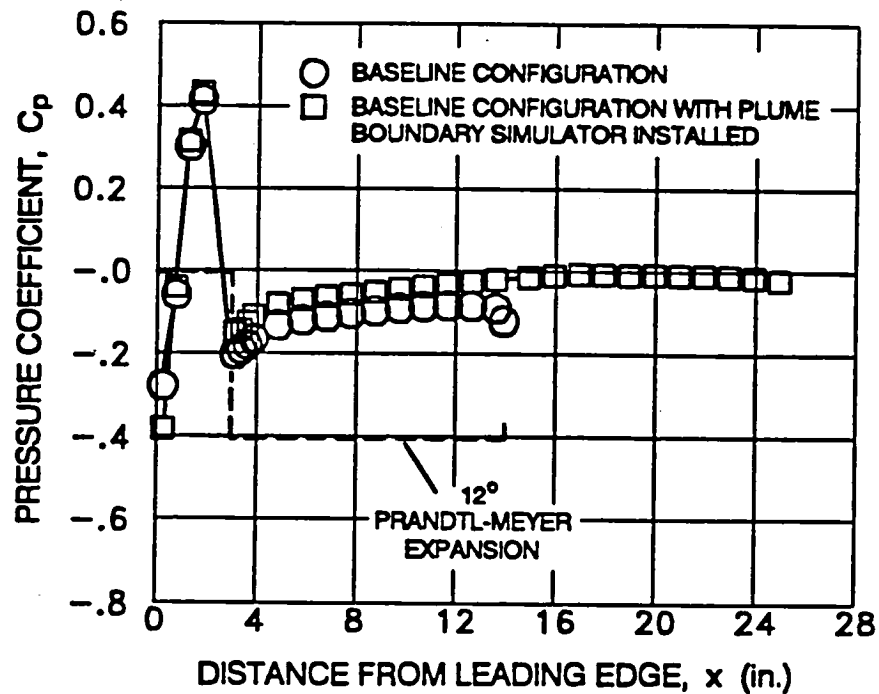


a) Fuel off;  $p_0=8$  psia.

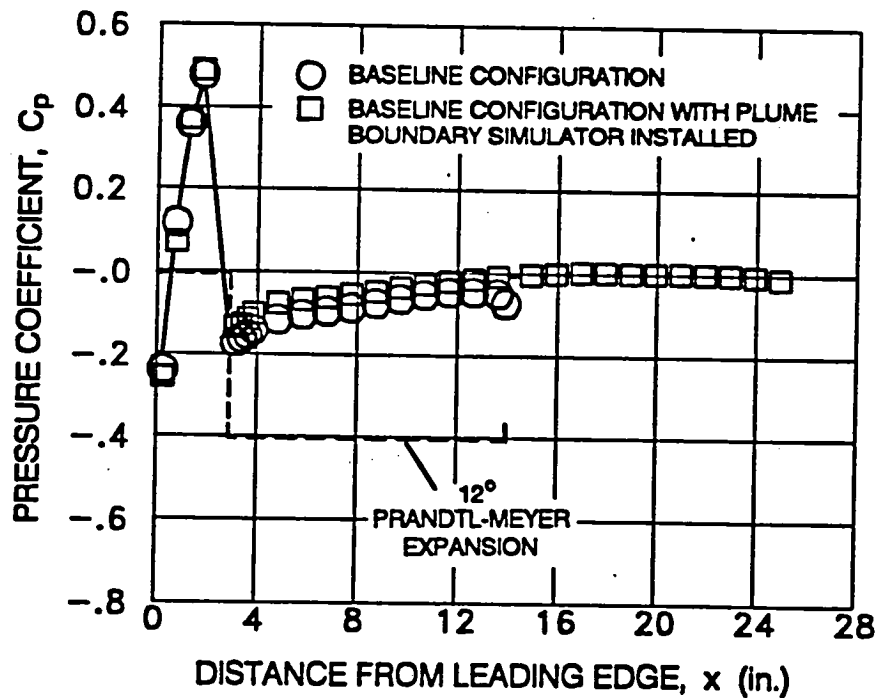


b)  $p_t=250$  psia,  $p_0=12$  psia ( $\phi_{corr}=.30$ ).

Figure 4-39. Effect of plume boundary simulator on centerline pressure distributions.



c)  $p_f = 375$  psia,  $p_0 = 8$  psia ( $\phi_{corr} = .67$ ).



d)  $p_f = 375$  psia,  $p_0 = 4$  psia ( $\phi_{corr} = 1.36$ ).

Figure 4-39. Concluded.



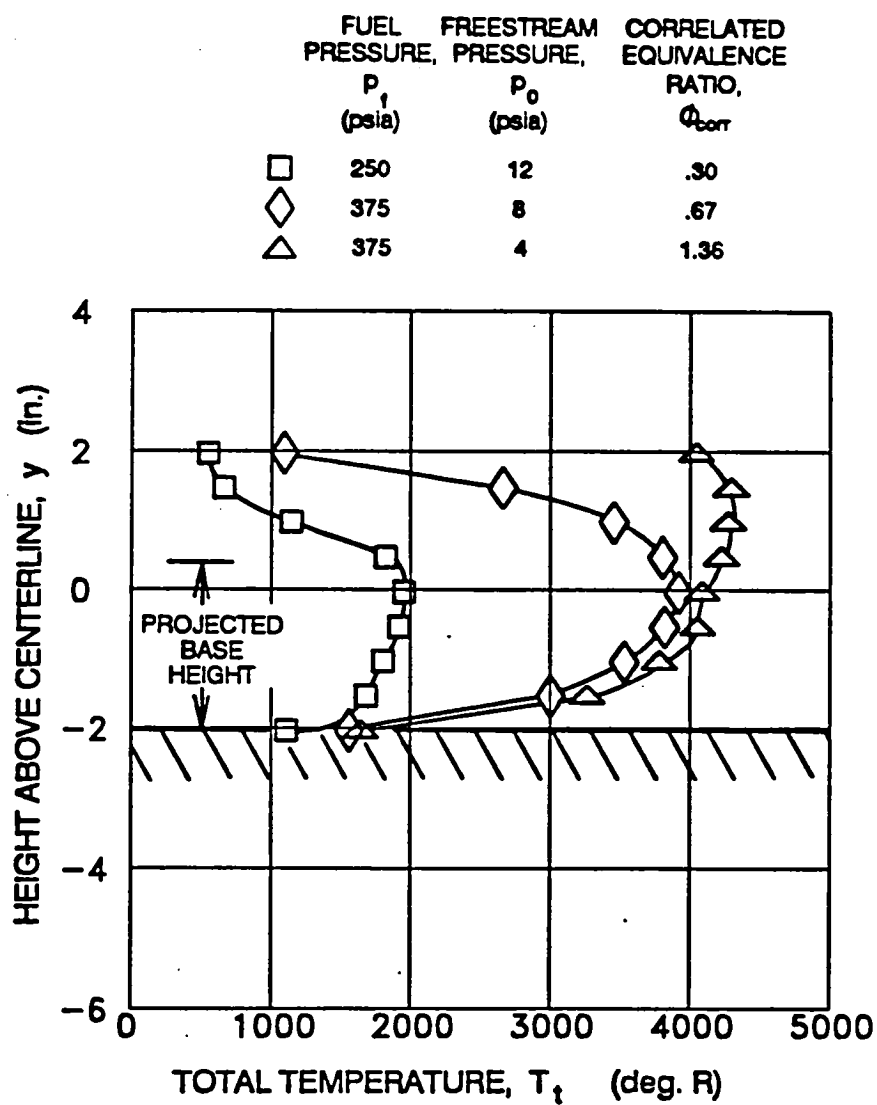


Figure 4-40. Total temperature profiles with plume boundary simulator installed; configuration 2.

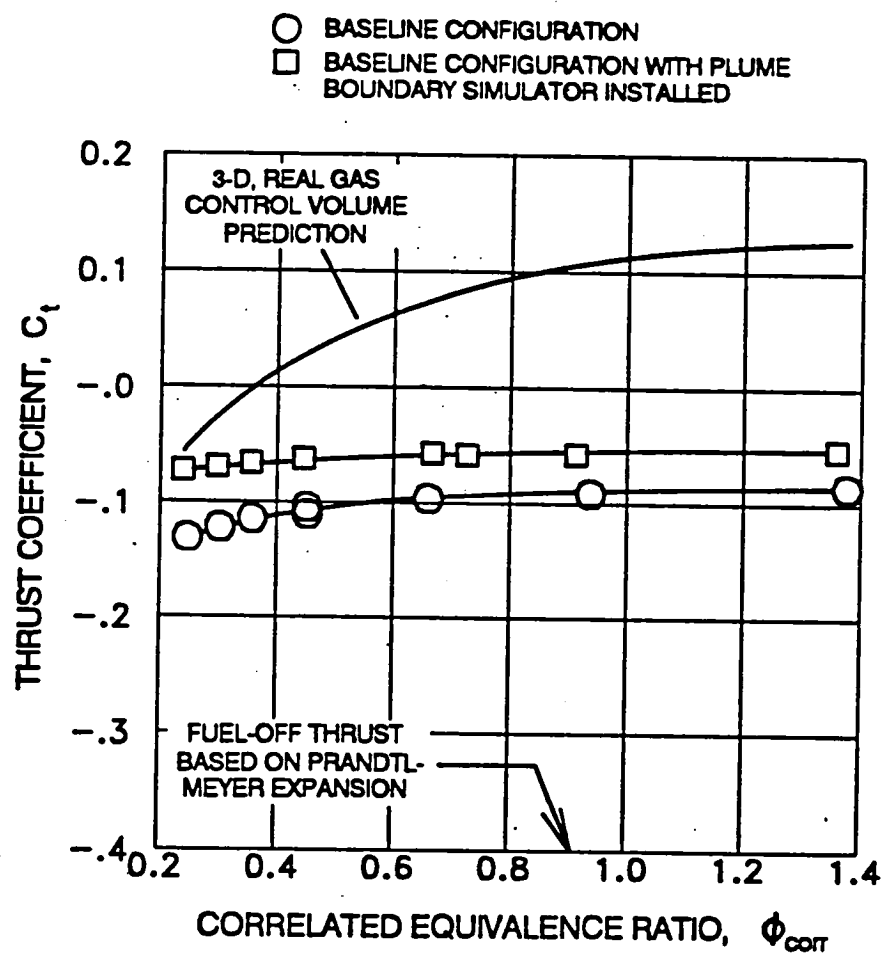


Figure 4-41. Effect of plume boundary simulator on thrust coefficient.

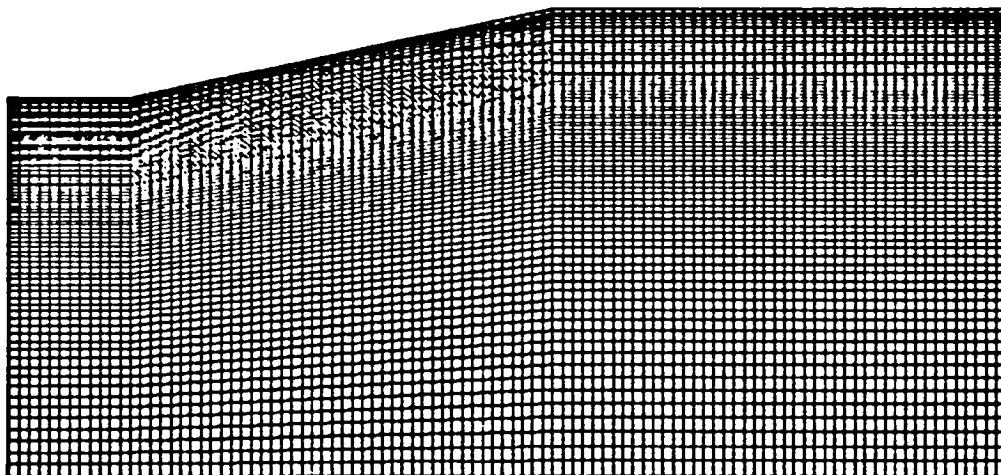


Figure 4-42. Grid used to evaluate effects of free-jet boundary (100 x 80 nodes).



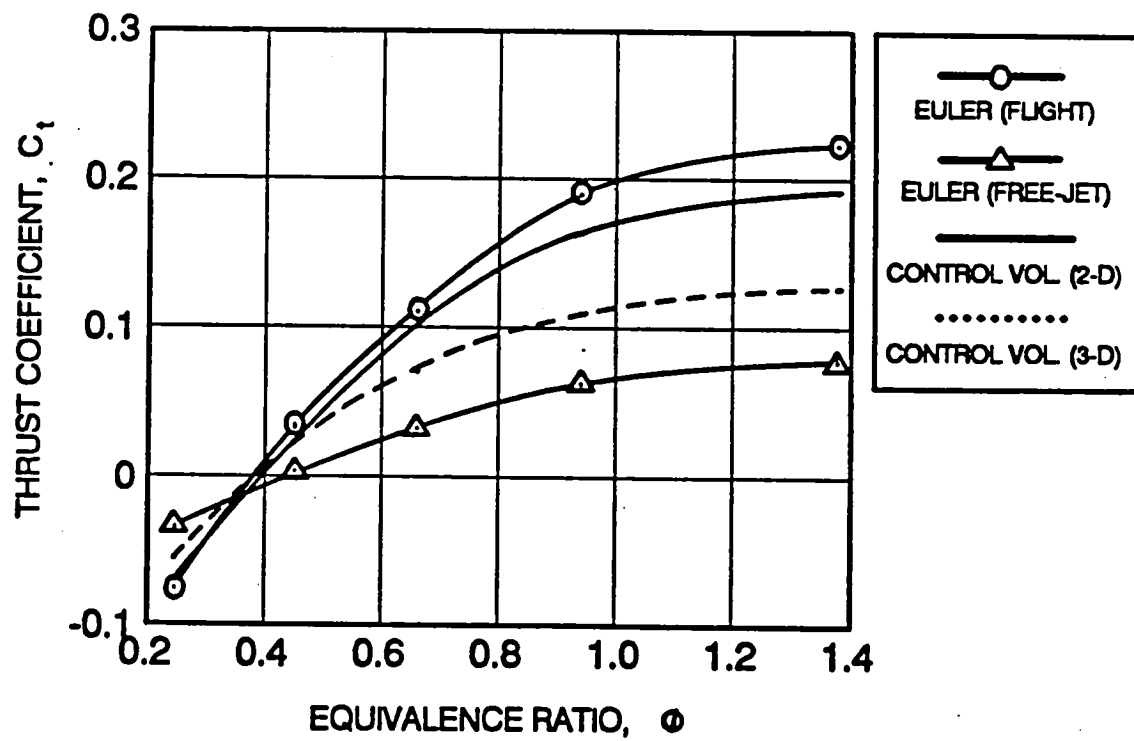


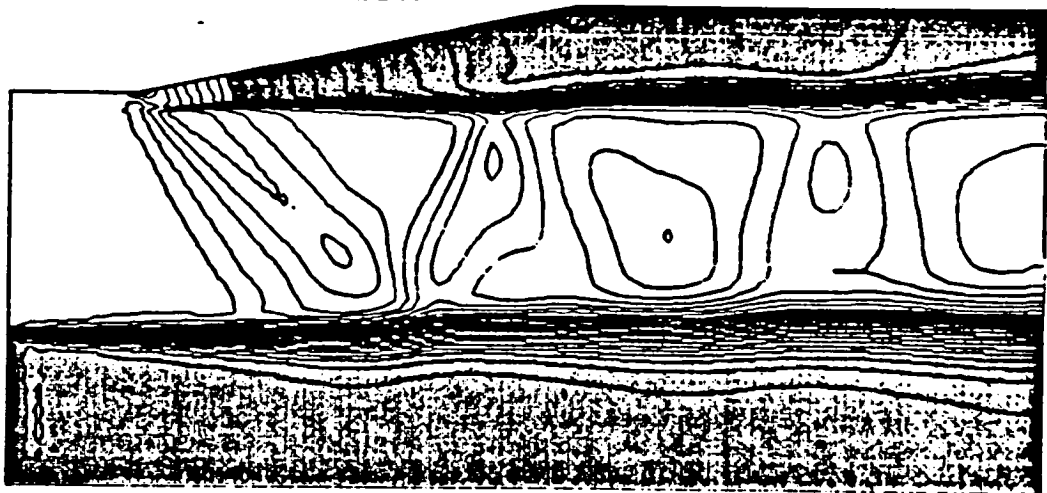
Figure 4-44. Effect of free-jet boundary on calculated external burning thrust coefficient.

SHADED REGIONS  
DENOTE SUBSONIC FLOW



a) Flight boundary.

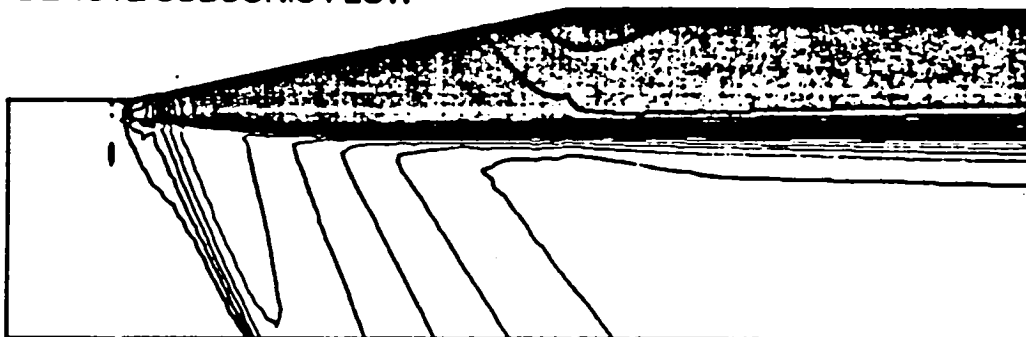
SHADED REGIONS  
DENOTE SUBSONIC FLOW



b) Free-jet boundary.

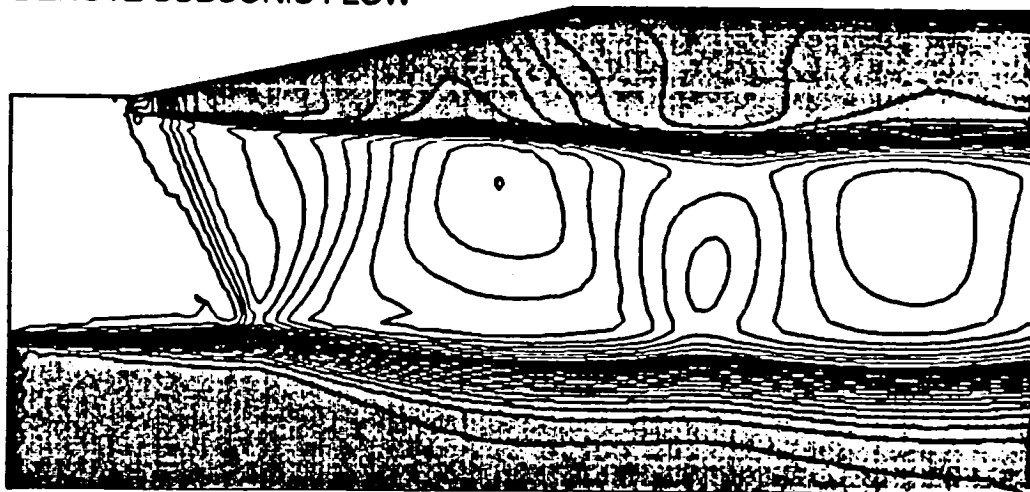
Figure 4-45. Comparison of Mach number contours at low heat addition corresponding to  $\phi_{\text{corr}} = .25$ ,  $y_0/y_b = .20$ .

SHADED REGIONS  
DENOTE SUBSONIC FLOW



a) Flight boundary.

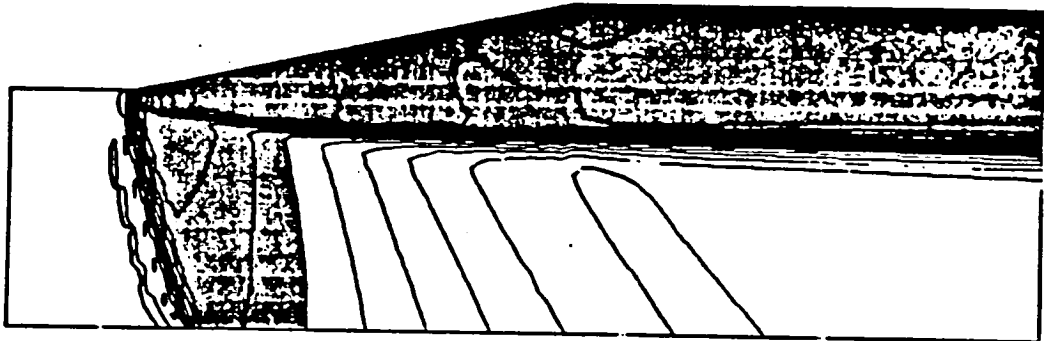
SHADED REGIONS  
DENOTE SUBSONIC FLOW



b) Free-jet boundary.

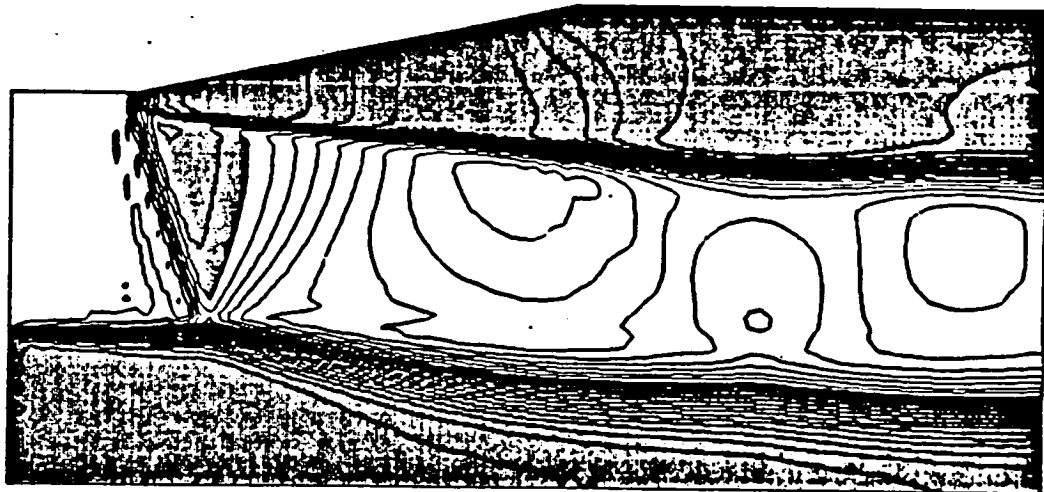
Figure 4-46. Comparison of Mach number contours at low heat addition corresponding to  $\phi_{\text{corr}} = .66$ ,  $y_0/y_b = .20$ .

SHADED REGIONS  
DENOTE SUBSONIC FLOW



a) Flight boundary.

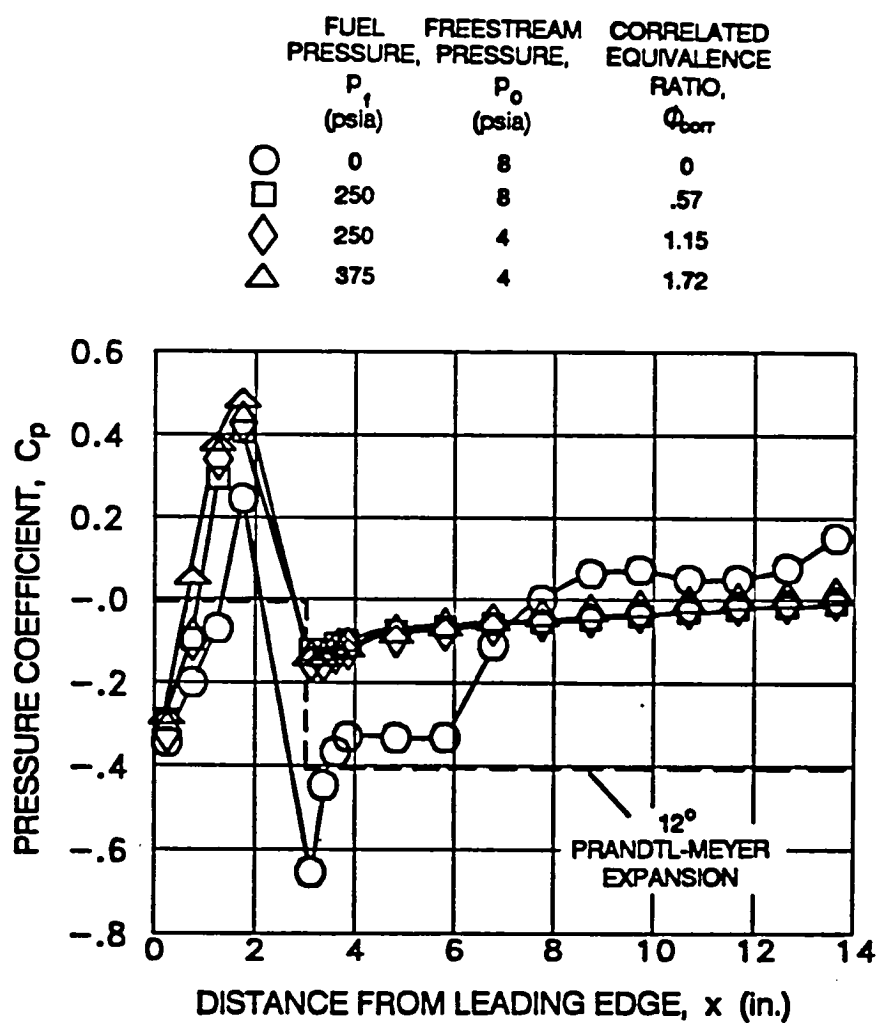
SHADED REGIONS  
DENOTE SUBSONIC FLOW



b) Free-jet boundary.

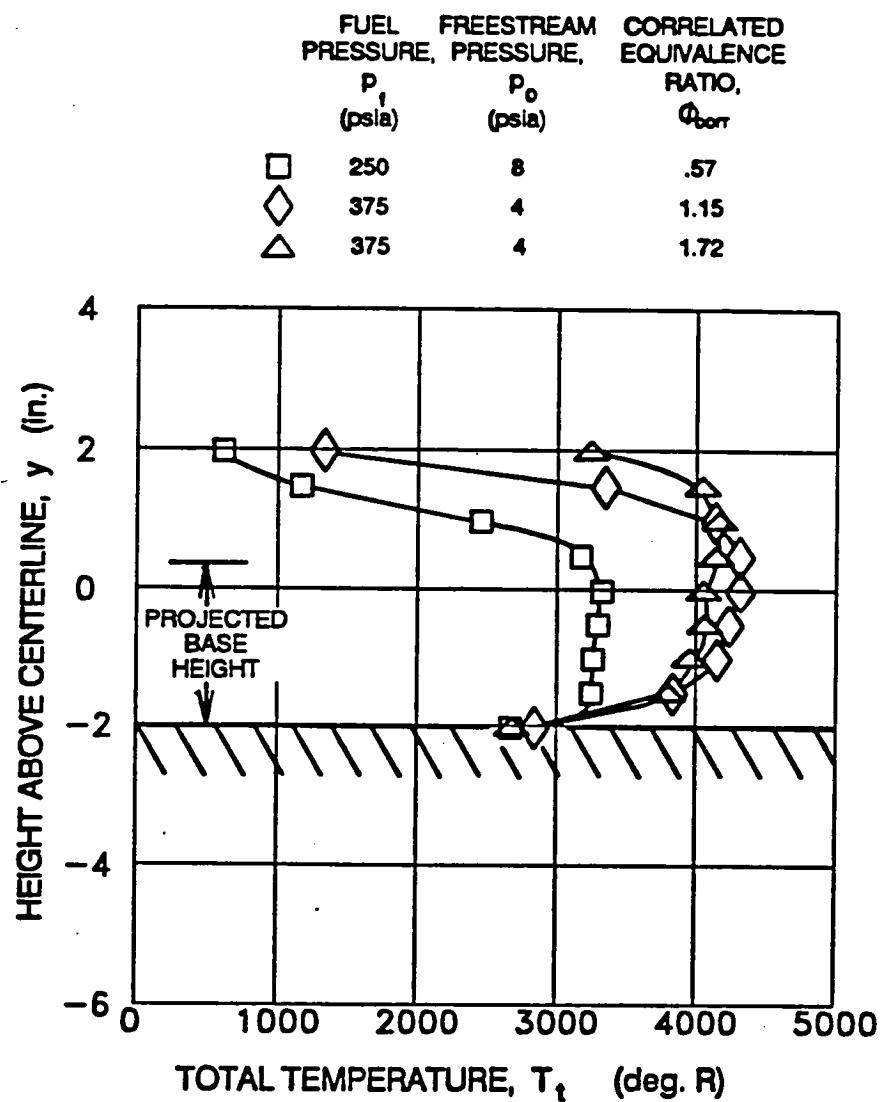
Figure 4-47. Comparison of Mach number contours at high heat addition corresponding to  $\phi_{\text{corr}}=1.38$ ,  $y_0/y_b=.20$ .





a) Centerline pressure distributions.

Figure 4-48. Results for 56 injector model; configuration 3.



b) Total temperature profiles.

Figure 4-48. Concluded.

ORIGINAL PAGE  
BLACK AND WHITE PHOTOGRAPH

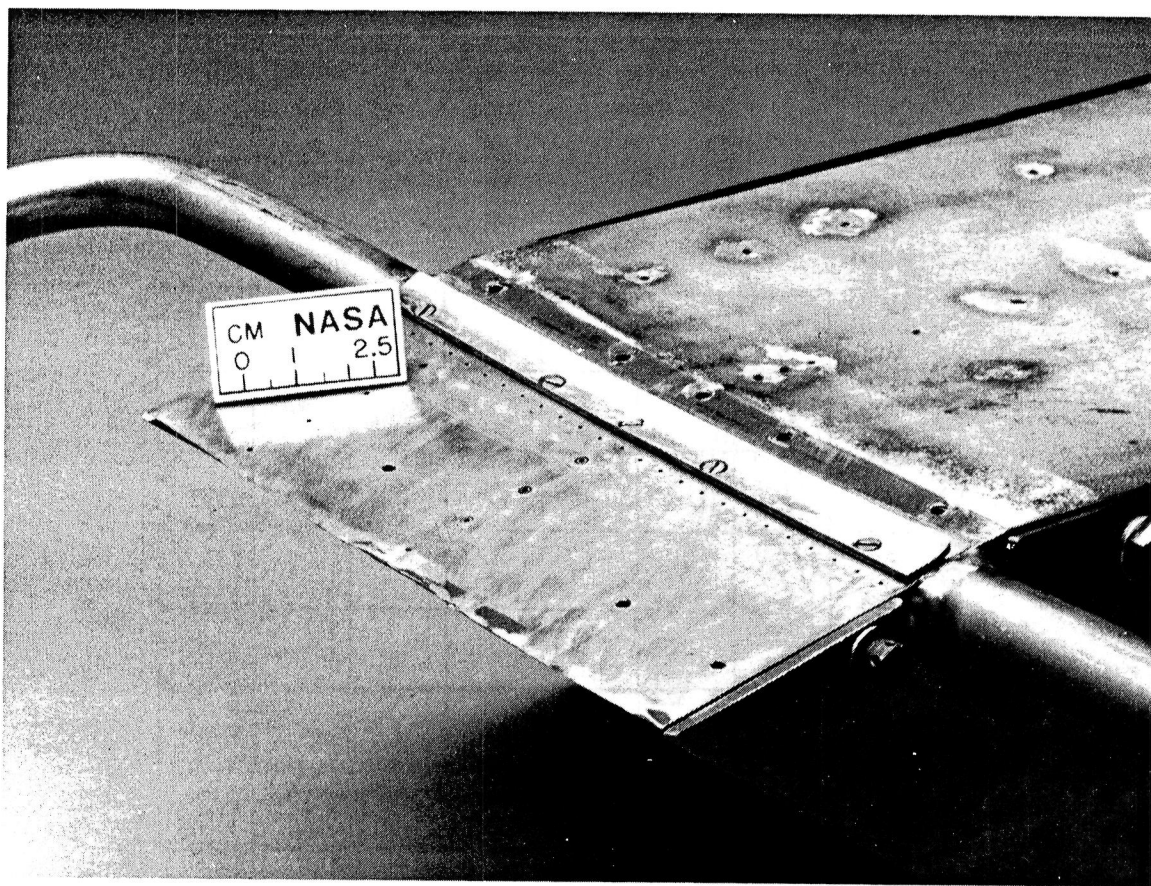
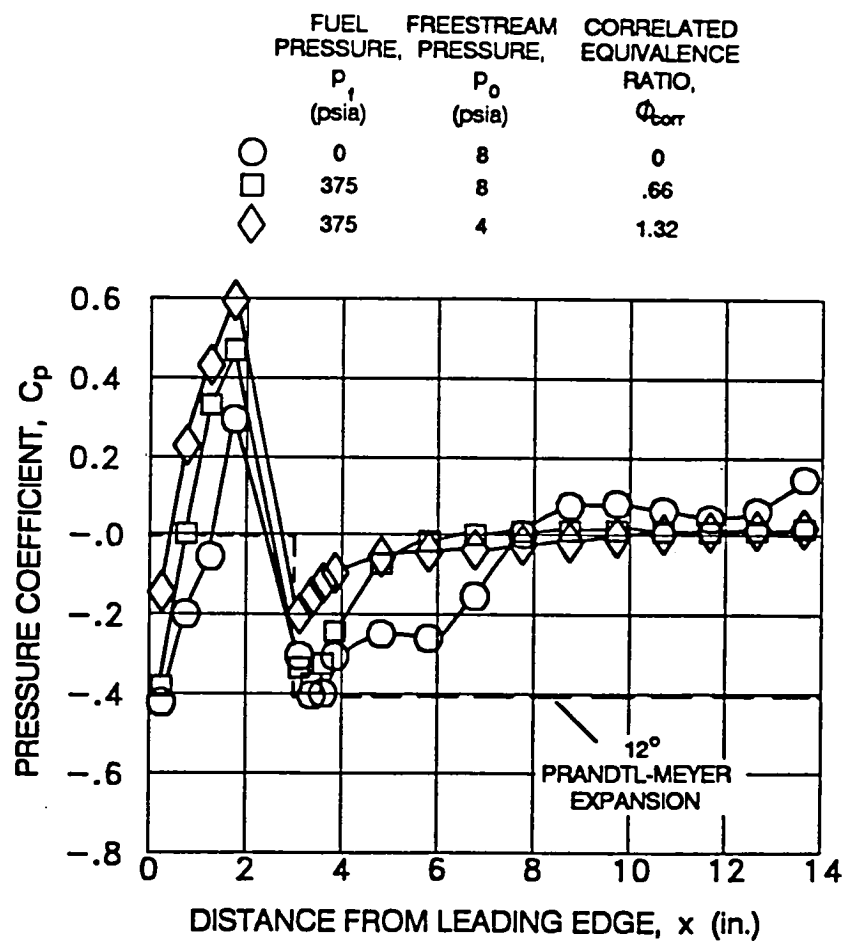
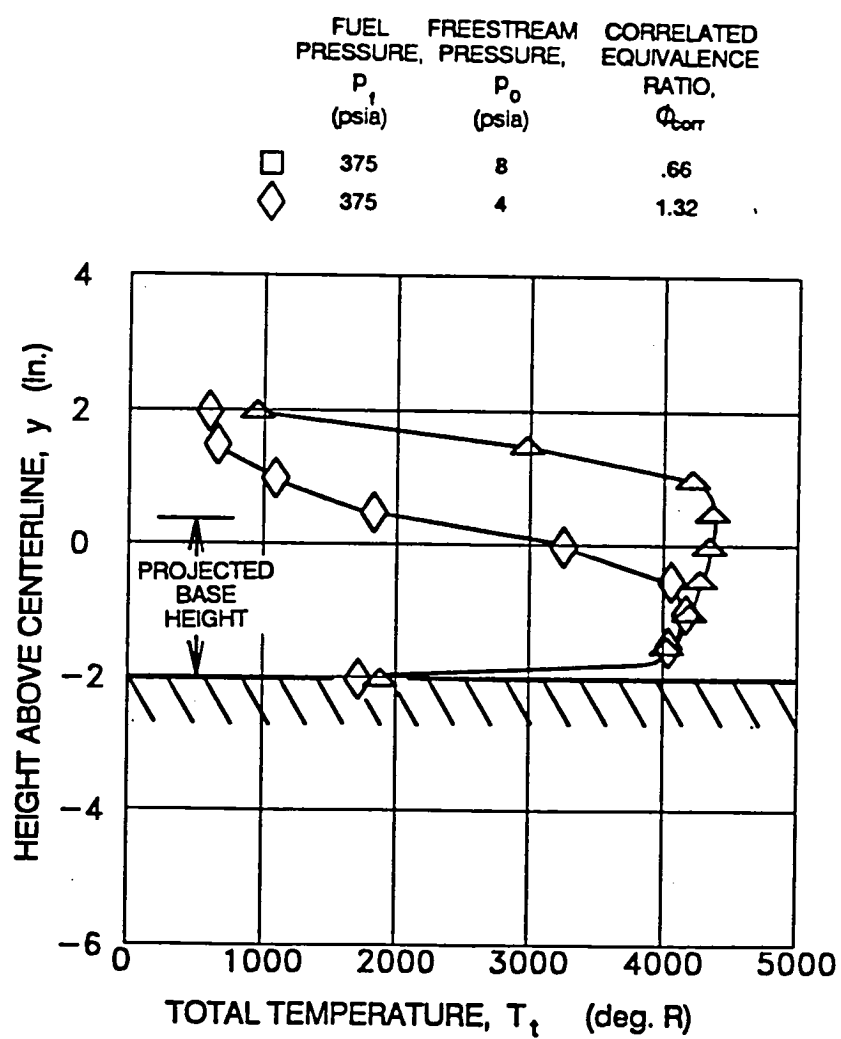


Figure 4-49. 26 injector model with upstream injection and flameholding; configuration 7.



a) Centerline pressure distributions.

Figure 4-50. Results with upstream injection and flameholding; configuration 7



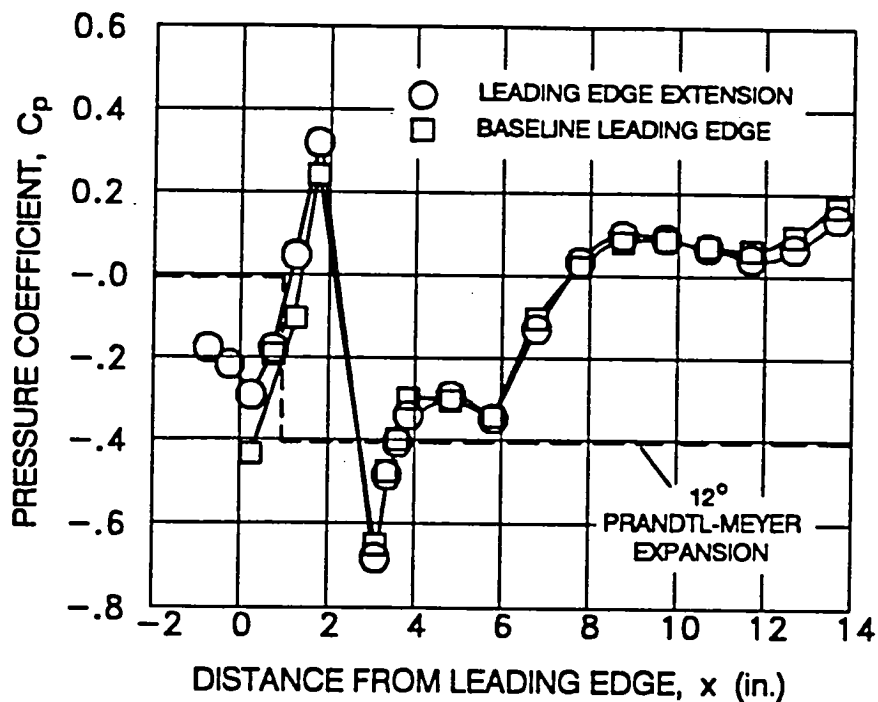
b) Total temperature profiles.

Figure 4-50. Concluded.

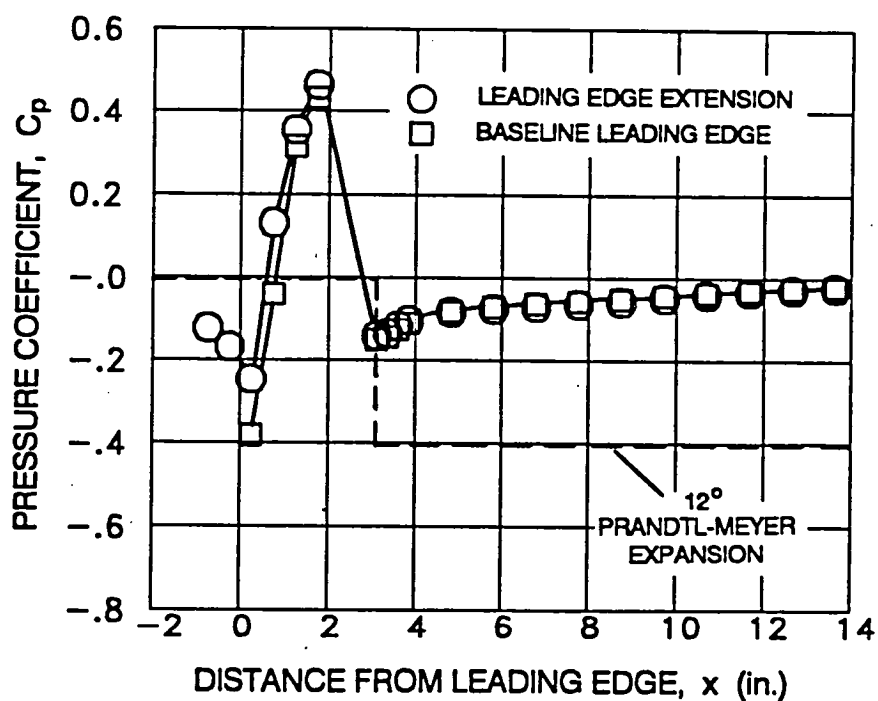
ORIGINAL PAGE  
BLACK AND WHITE PHOTOGRAPH



Figure 4-51. 26 injector model with leading edge extension installed (flameholder not installed).

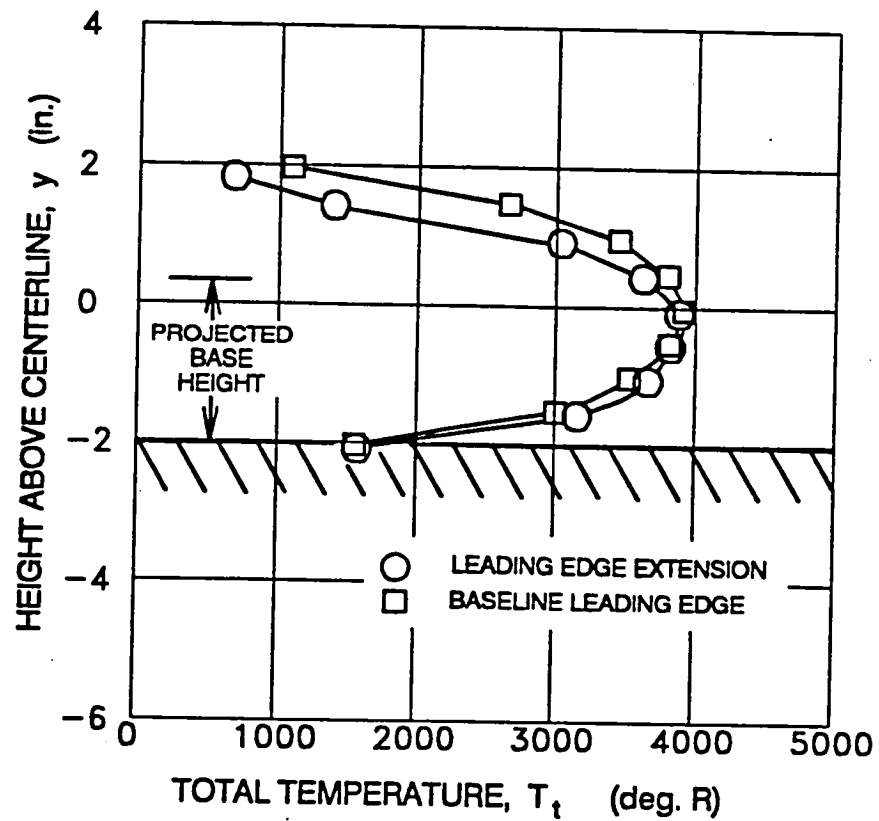


a) Comparison of centerline pressure distributions with fuel off;  $p_0=8$  psia.



b) Comparison of centerline pressure distributions with external burning;  $p_f=375$  psia,  $p_0=8$  psia ( $\phi_{\text{corr}}=.65$ ).

Figure 4-52. Effect of leading edge extension and upstream injection (configurations 2 and 8).



c) Comparison of total temperature profiles;  $p_t=375$  psia,  $p_0=8$  psia ( $\phi_{corr}=.65$ ).

Figure 4-52. Concluded.



ORIGINAL PAGE  
BLACK AND WHITE PHOTOGRAPH

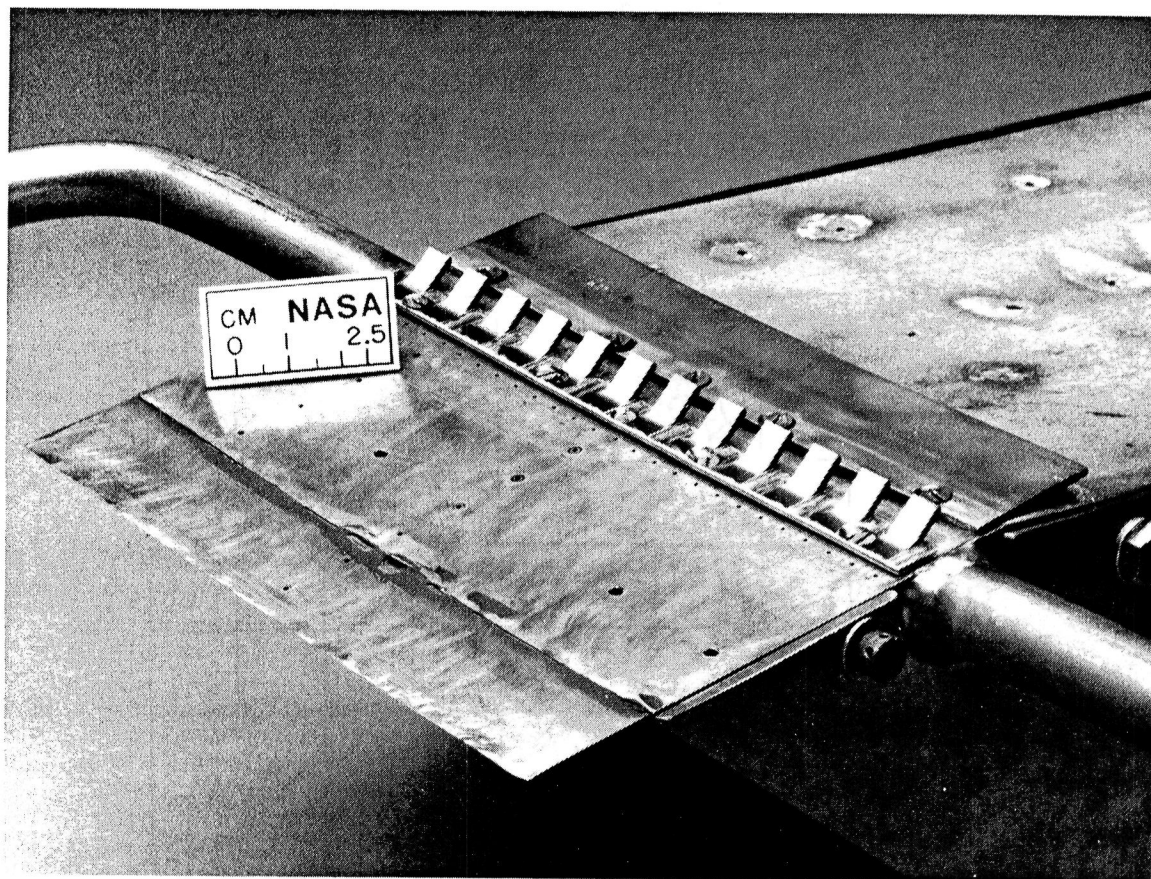
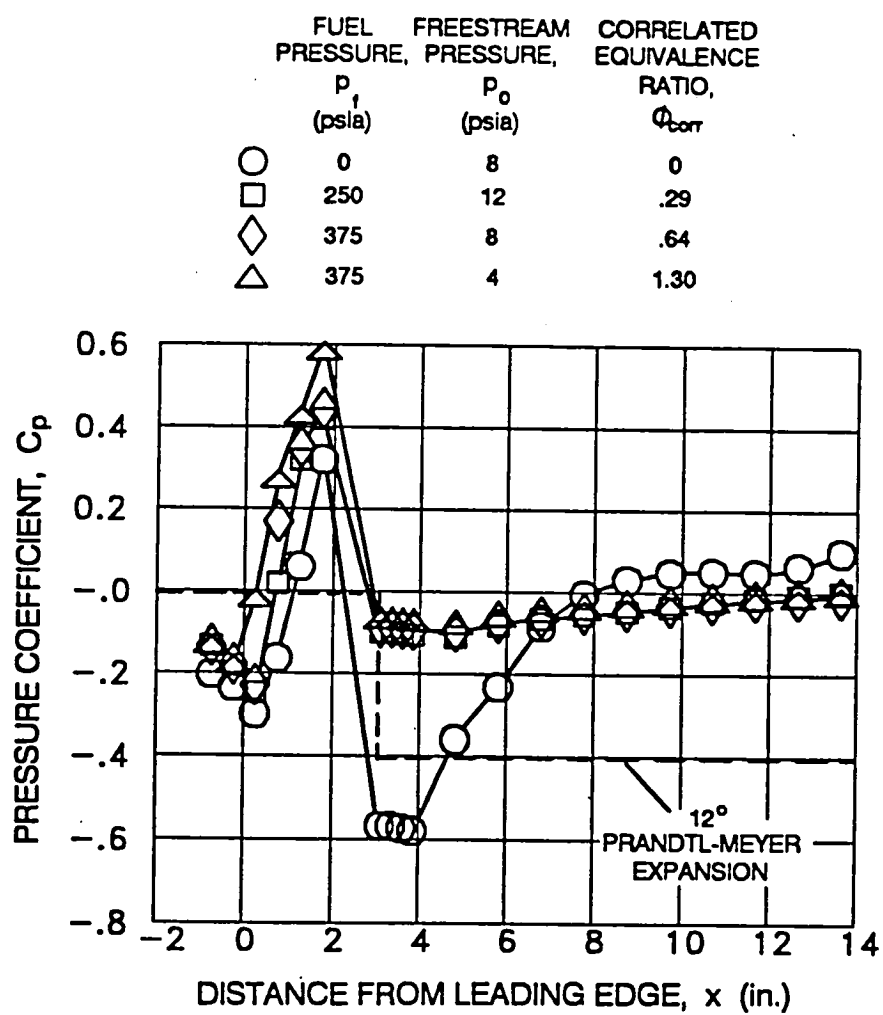
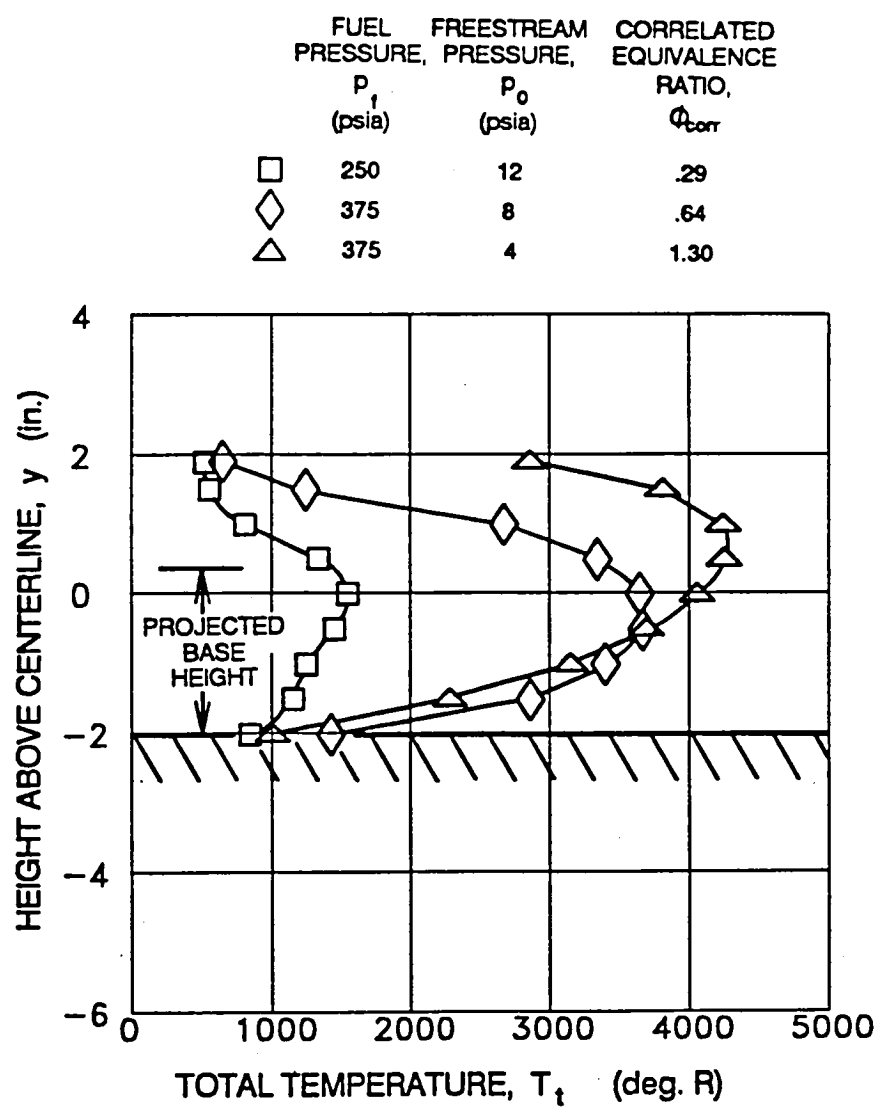


Figure 4-53. 1/4" serrated flameholder; configuration 10.



a) Centerline pressure distributions.

Figure 4-54. Results with 1/4" serrated flameholder; configuration 10.



b) Total temperature profiles.

Figure 4-54. Concluded.

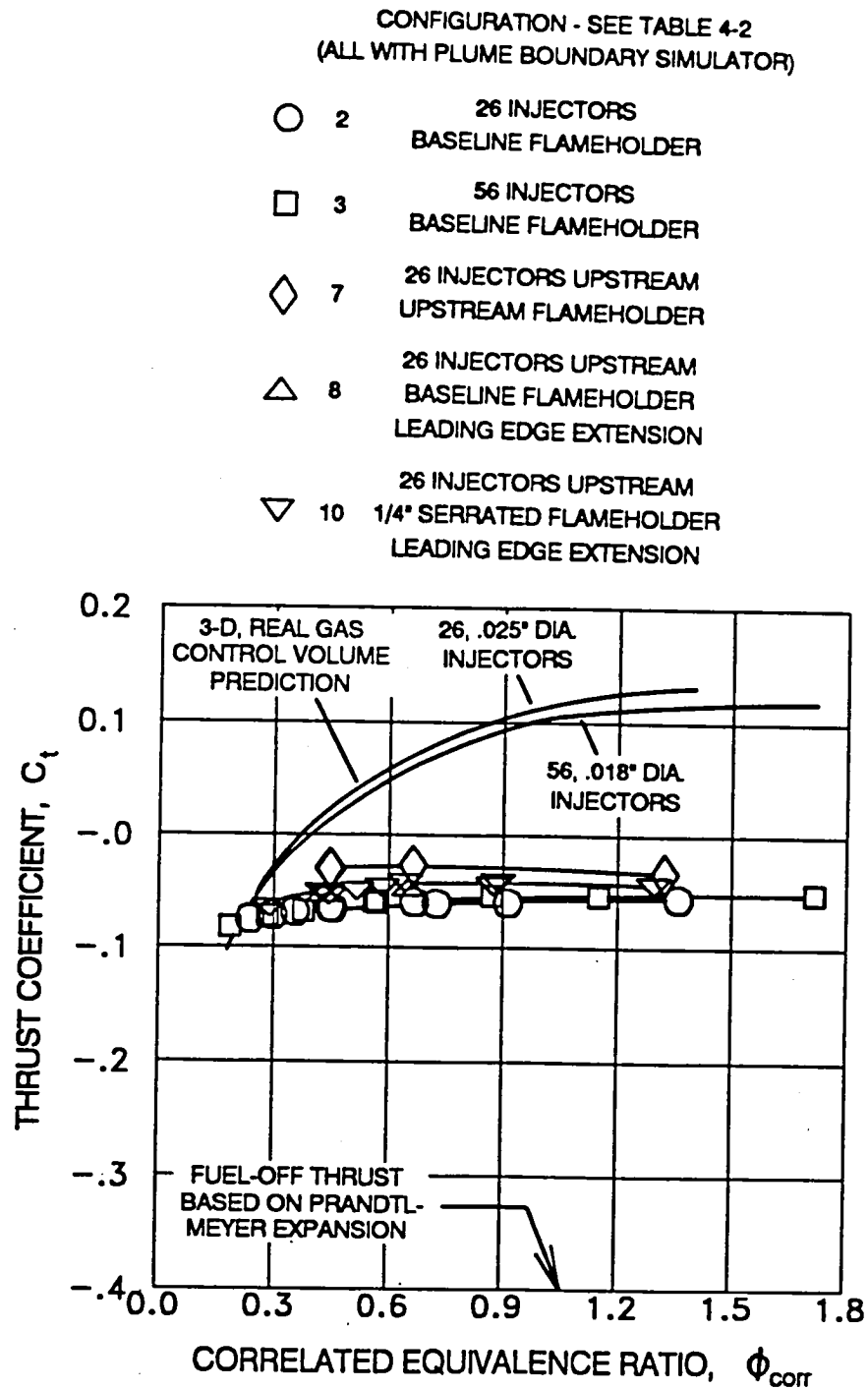
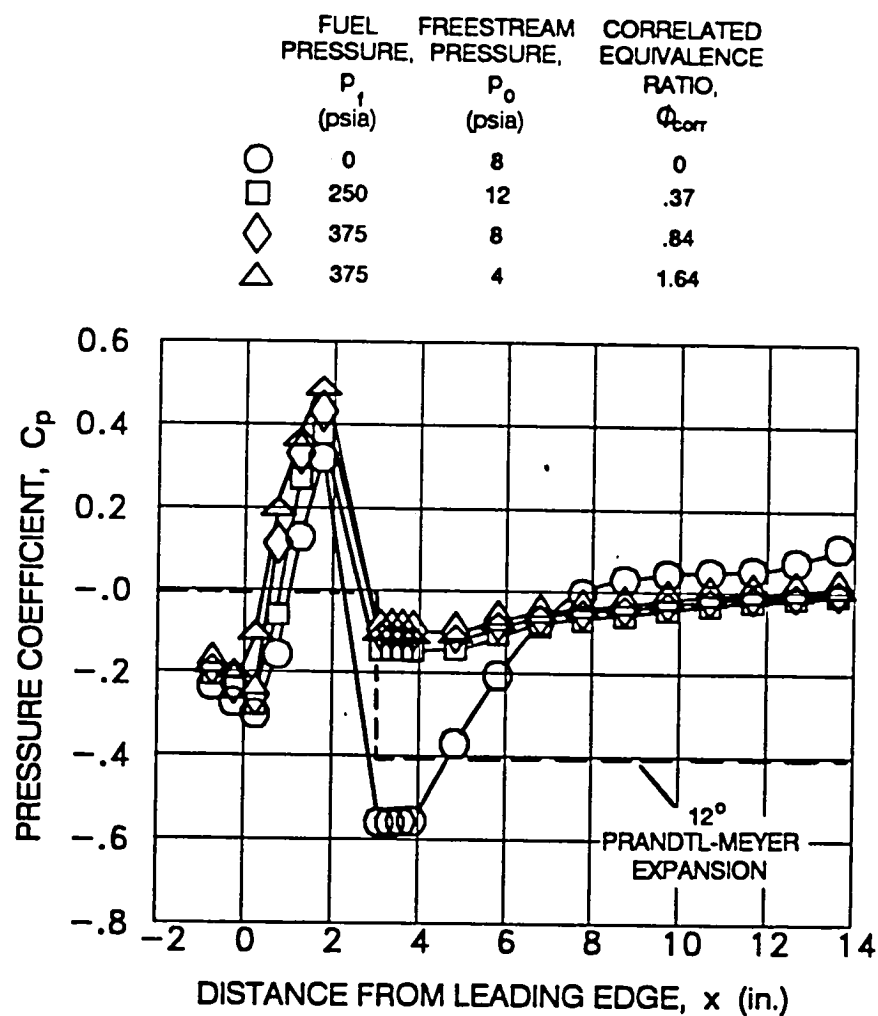
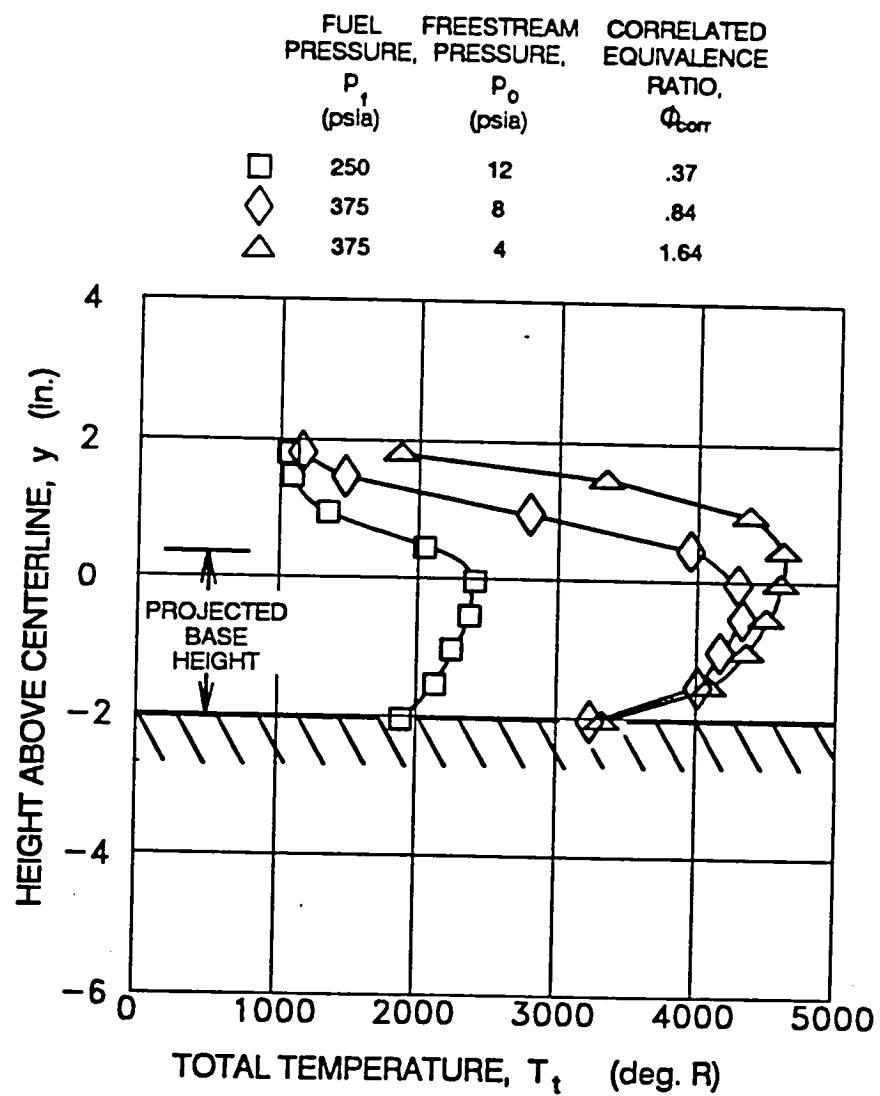


Figure 4-55. Thrust coefficient comparison for alternate configurations.



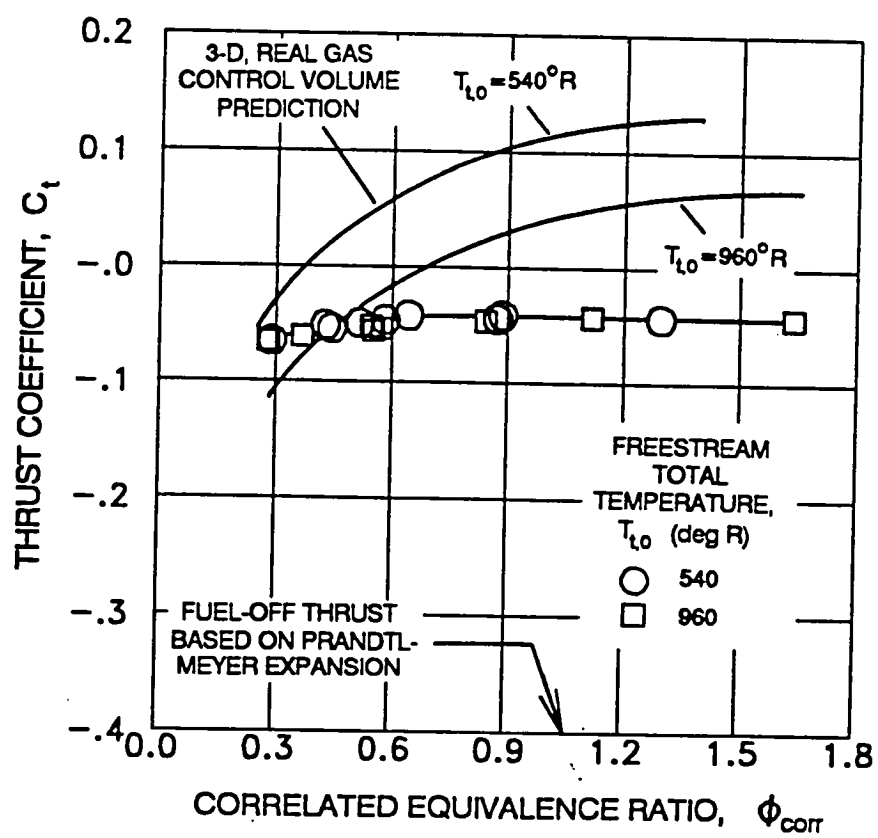
a) Centerline pressure distributions.

Figure 4-56. Results for configuration 10 with heated freestream;  
 $T_{t,0} = 960$  R.



b) Total temperature profiles.

Figure 4-56. Continued.



c) Thrust coefficient.

Figure 4-56. Concluded.

ORIGINAL PAGE  
BLACK AND WHITE PHOTOGRAPH

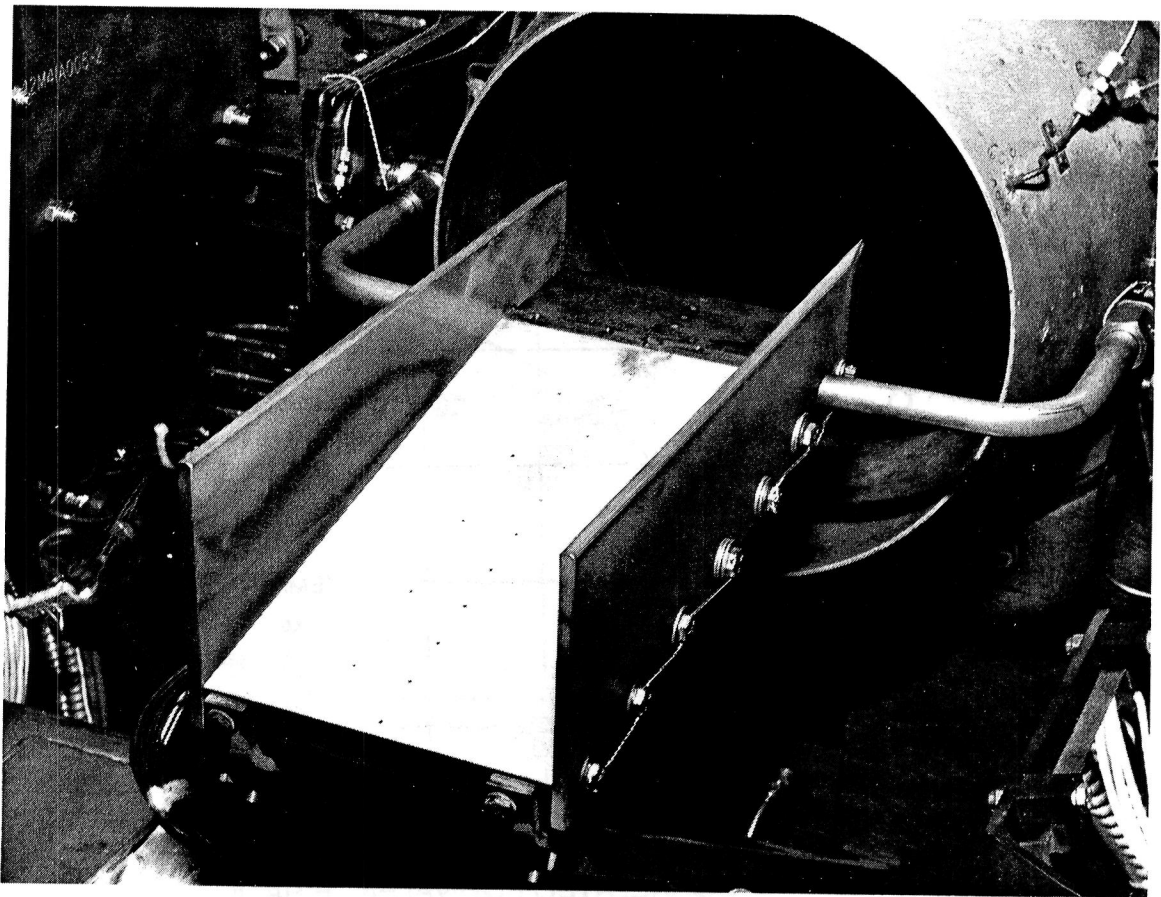
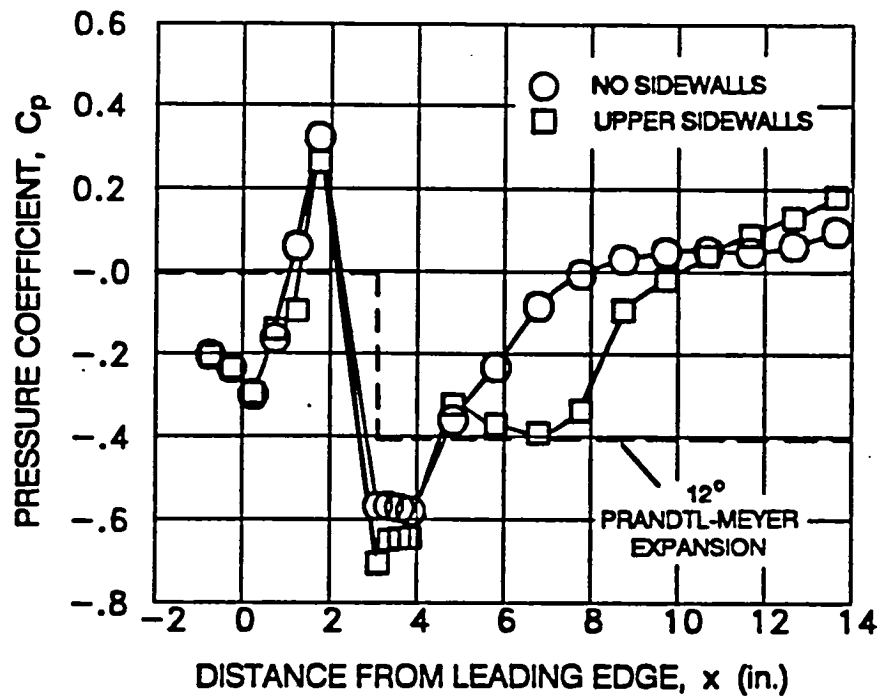
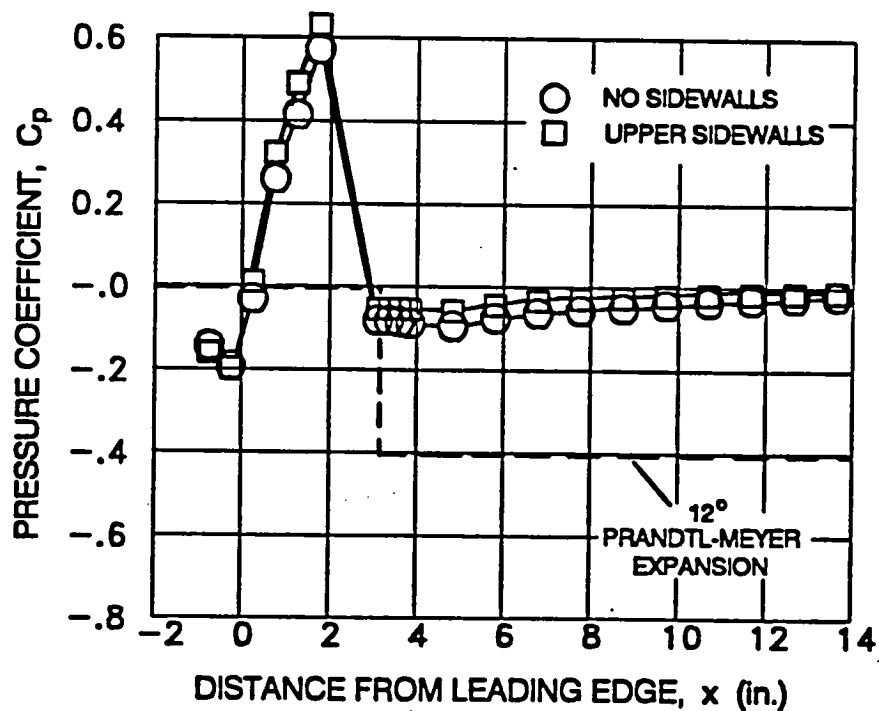


Figure 4-57. Upper sidewall installation (baseline flameholder shown).



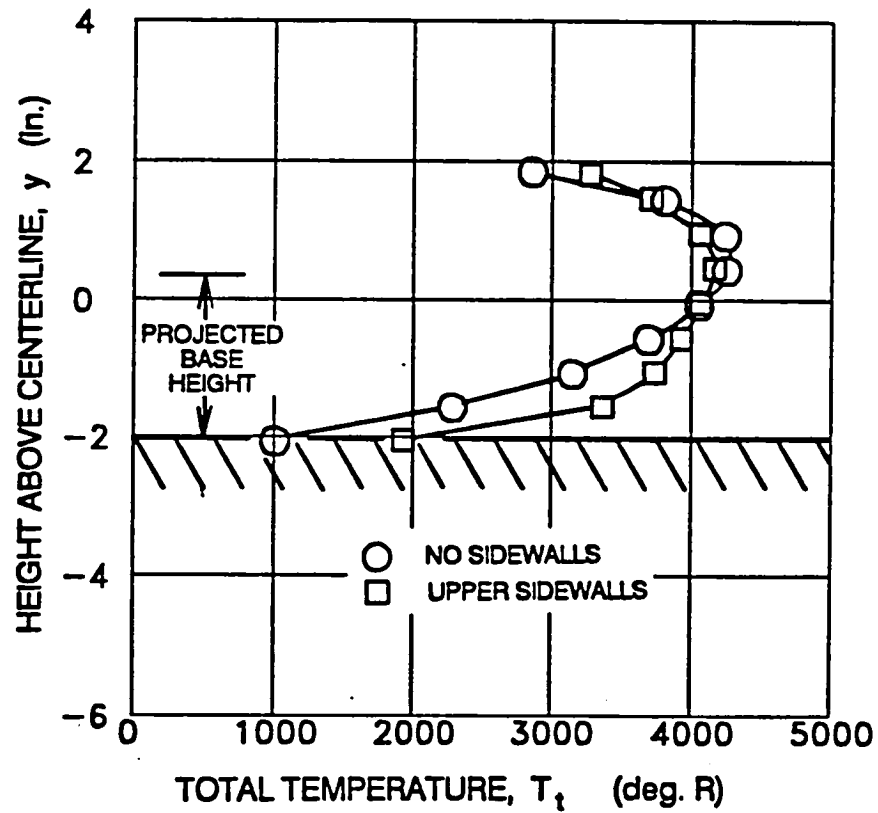


a) Comparison of centerline pressure distributions with fuel off;  $p_0=8$  psia.



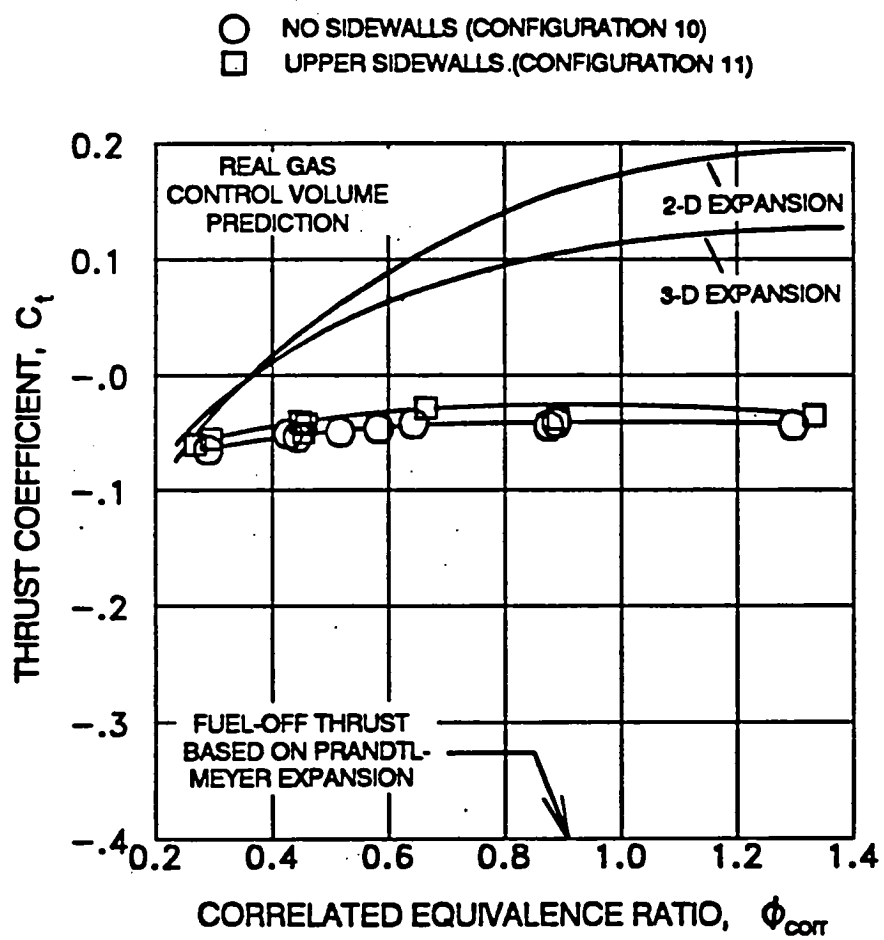
b) Comparison of centerline pressure distributions with external burning;  $p_t=375$  psia,  $p_0=4$  psia ( $\phi_{corr}=1.33$ ).

Figure 4-58. Effect of upper sidewalls on configuration 10 performance.



c) Comparison of total temperature profiles;  $p_f=375$  psia,  $p_0=4$  psia ( $\phi_{corr}=1.33$ ).

Figure 4-58. Continued.



d) Comparison of thrust coefficients.

Figure 4-58. Concluded.

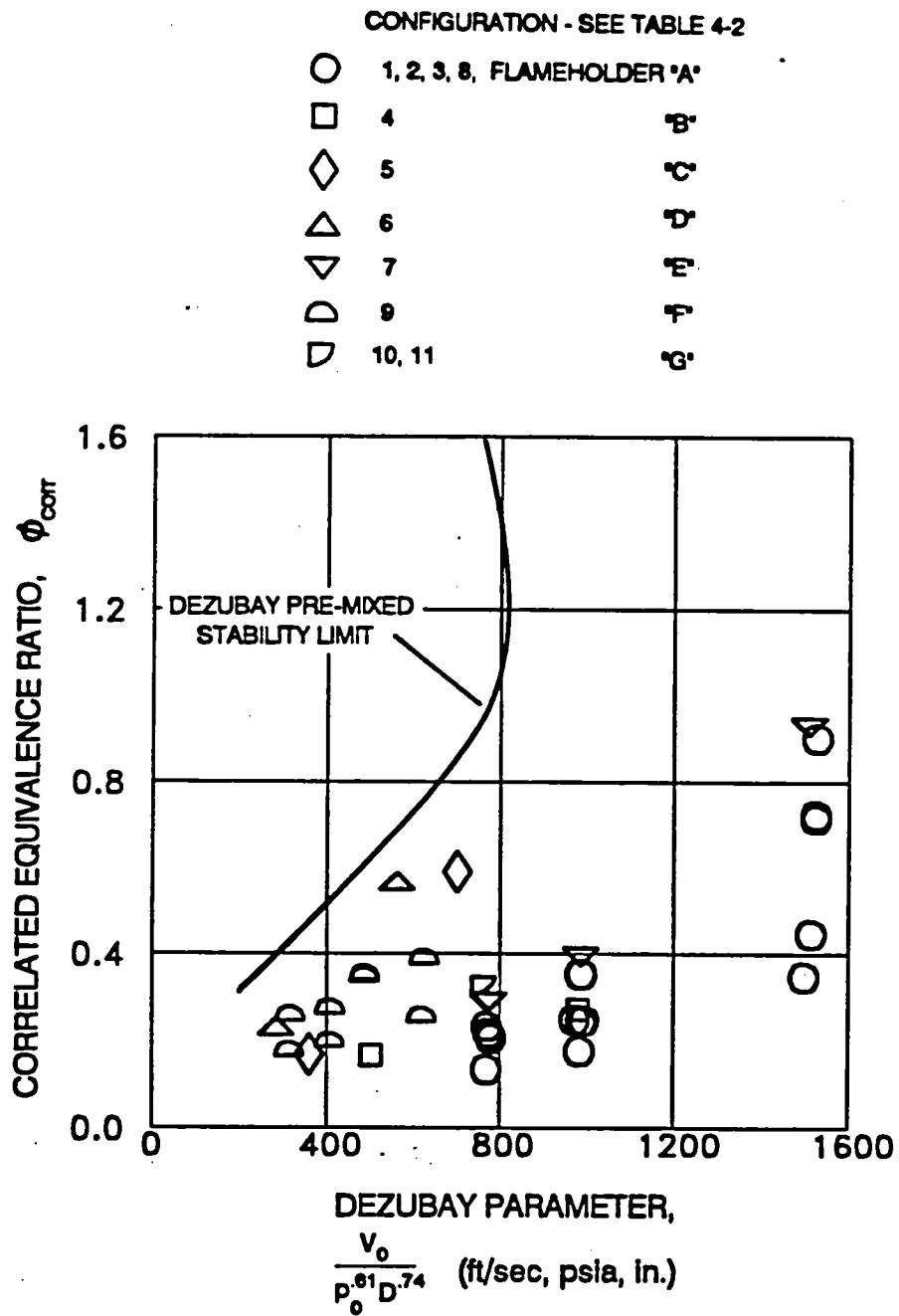
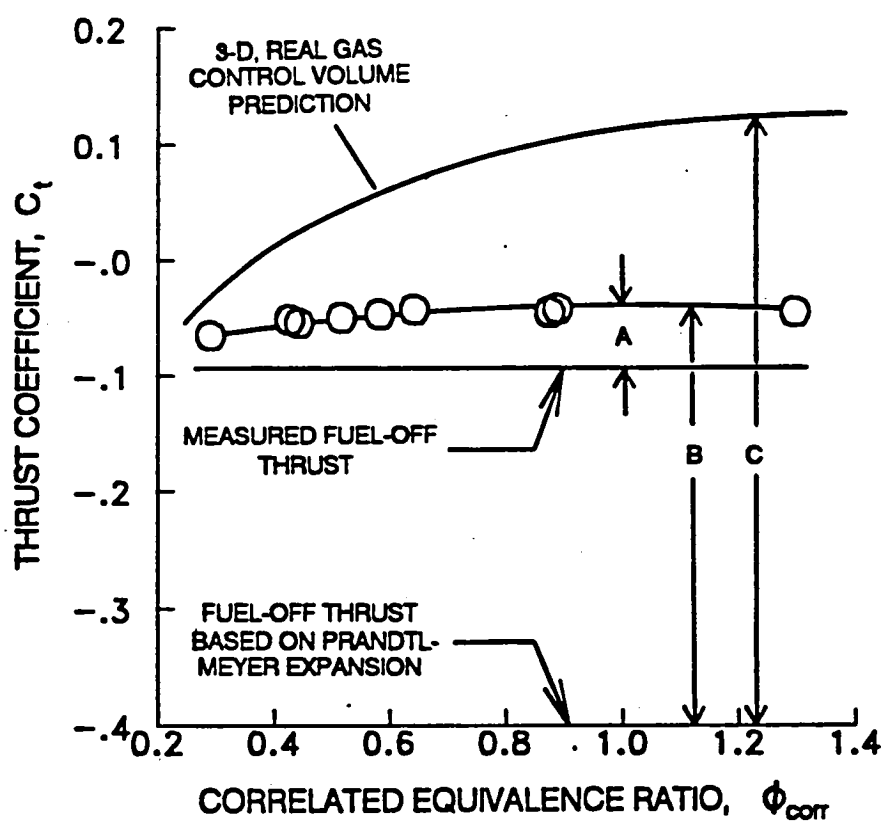


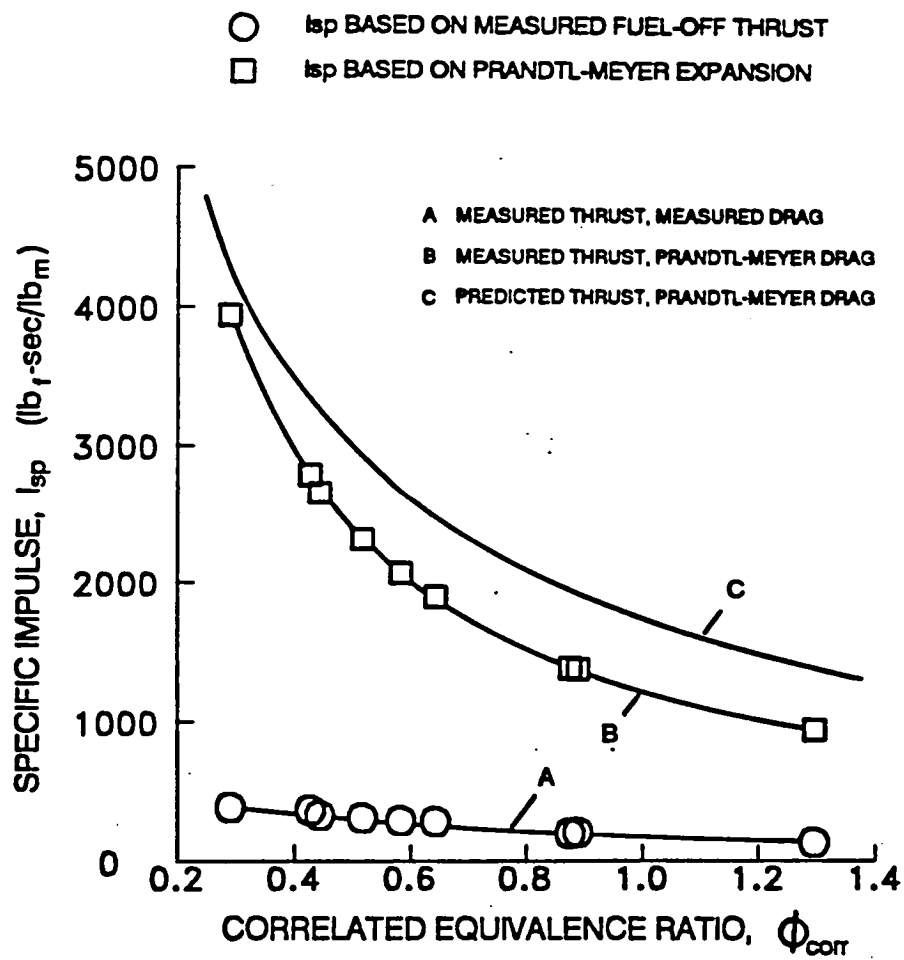
Figure 4-59. Expansion ramp flameholding, all flameholder configurations.



a) Thrust coefficient.

Figure 4-60. Demonstrated performance for configuration 10.

C-4



b) Specific impulse.

Figure 4-60. Concluded.



# REPORT DOCUMENTATION PAGE

Form Approved  
OMB No. 0704-0188

Public reporting burden for this collection of information is estimated to average 1 hour per response, including the time for reviewing instructions, searching existing data sources, gathering and maintaining the data needed, and completing and reviewing the collection of information. Send comments regarding this burden estimate or any other aspect of this collection of information, including suggestions for reducing this burden, to Washington Headquarters Services, Directorate for Information Operations and Reports, 1215 Jefferson Davis Highway, Suite 1204, Arlington, VA 22202-4302, and to the Office of Management and Budget, Paperwork Reduction Project (0704-0188), Washington, DC 20503.

1. AGENCY USE ONLY (Leave blank)		2. REPORT DATE January 1992	3. REPORT TYPE AND DATES COVERED Technical Memorandum	
4. TITLE AND SUBTITLE Experiments and Analysis Concerning the Use of External Burning to Reduce Aerospace Vehicle Transonic Drag			5. FUNDING NUMBERS  WU-763-01-21	
6. AUTHOR(S) Charles J. Trefny				
7. PERFORMING ORGANIZATION NAME(S) AND ADDRESS(ES) National Aeronautics and Space Administration Lewis Research Center Cleveland, Ohio 44135-3191			8. PERFORMING ORGANIZATION REPORT NUMBER  E-6789	
9. SPONSORING/MONITORING AGENCY NAMES(S) AND ADDRESS(ES) National Aeronautics and Space Administration Washington, D.C. 20546-0001			10. SPONSORING/MONITORING AGENCY REPORT NUMBER  NASA TM-105397	
11. SUPPLEMENTARY NOTES Report was submitted as a dissertation in partial fulfillment of the requirements for the degree Doctor of Philosophy to the University of Maryland, College Park, Maryland 20742 in 1991. Responsible person, Charles J. Trefny, (216) 433-2162.				
12a. DISTRIBUTION/AVAILABILITY STATEMENT  Unclassified - Unlimited Subject Category 07			12b. DISTRIBUTION CODE	
13. ABSTRACT (Maximum 200 words)  The external combustion of hydrogen to reduce transonic drag has been investigated. A control volume analysis is developed and indicates that the specific impulse performance of external burning is competitive with other forms of airbreathing propulsion and depends on the fuel-air ratio, freestream Mach number, and the severity of the base drag. A method is presented for sizing fuel injectors for a desired fuel-air ratio in the unconfined stream. A two-dimensional Euler analysis is also presented which indicates that the total axial force generated by external burning depends on the total amount of energy input and is independent of the transverse and streamwise distribution of heat addition. Good agreement between the Euler and control volume analysis is demonstrated. Features of the inviscid external burning flowfield are discussed. Most notably, a strong compression forms at the sonic line within the burning stream which may induce separation of the plume and prevent realization of the full performance potential. An experimental program was conducted in a Mach 1.26 free-jet to demonstrate drag reduction on a simple expansion ramp geometry, and verify hydrogen-air stability limits at external burning conditions. Stable combustion appears feasible to Mach numbers of between 1.4 and 2 depending on the vehicle flight trajectory. Drag reduction is demonstrated on the expansion ramp at Mach 1.26, however force levels showed little dependence on fuel pressure or altitude in contrast to control volume analysis predictions. Various facility interference mechanisms and scaling issues were studied and are discussed.				
14. SUBJECT TERMS External burning; Transonic drag reduction			15. NUMBER OF PAGES 294	
			16. PRICE CODE A13	
17. SECURITY CLASSIFICATION OF REPORT Unclassified	18. SECURITY CLASSIFICATION OF THIS PAGE Unclassified	19. SECURITY CLASSIFICATION OF ABSTRACT Unclassified	20. LIMITATION OF ABSTRACT	







3 1176 01422 6576

**DO NOT REMOVE SLIP FROM MATERIAL**

Delete your name from this slip when returning material to the library.

NAME	DATE	MS
<i>Gentile</i>	<i>9-95</i>	<i>352</i>